The structural architecture of seismogenic faults, Sierra Nevada, California; implications for earthquake rupture processes

James David Kirkpatrick MGeol. (Hons.)

Thesis presented for the degree of Doctor of Philosophy (Ph.D.)

University of Glasgow

Department of Geographical and Earth Sciences

April 2008

Dedication

For Mum and Dad, who have made anything and everything possible.

Abstract

Earthquake ruptures along tectonically active faults nucleate predominantly at depths of 5 to 12km in the crust, so the portions of faults that slip in these events cannot be directly observed. The geometry and composition of seismogenic faults controls the nucleation, propagation and termination of the earthquake rupture process. This study aims to place constraints on the geometry and composition of seismogenic faults by examining ancient faults exhumed from the depths at which earthquakes are observed to nucleate.

Faults exposed in the Sierra Nevada, California, show that the internal architecture of earthquake faults is heterogeneous at a variety of scales. Field and microstructural observations are used to describe in detail the architecture of two pseudotachylyte-bearing fault systems in the Granite Pass region of Sequoia and Kings Canyon National Park; the Granite Pass fault (GPF) and associated faults, and the Glacier Lakes fault (GLF) and faults that splay from the GLF. The GPF and sub-parallel faults are 1 to 6.7km long with left-lateral strike-slip displacements up to 80m. The GPF and GPF-parallel faults have architectures that are heterogeneous along strike. They are composed of one to four fault core strands containing cataclasites and ultracataclasites that cross-cut early localised crystal-plastic deformation. Slip surfaces developed at the edges of, within and between fault cores are defined by pseudotachylytes and cataclasites with thicknesses of ~0.01 to 20mm. Fault-related subsidiary structures are developed on either side of fault cores, and comprise damage zones with widths orthogonal to the fault of up to 30m. The GLF and splay faults have architectures that are more homogeneous along strike. These faults are composed of a tabular volume of heavily fractured and altered host rock between approximately planar fault core strands. The fault cores are centimetres wide and contain cataclasites and foliated cataclasites that are cross-cut by pseudotachylytes. Fault-related damage is limited in extent to several metres beyond the bounding fault cores. The GLF contains additional cataclasites, ultracataclasites and pseudotachylytes in a fault core strand within the tabular zone of fractured rock.

Thermochronologic analyses of the host rock granodiorite, combined with previously published palaeogeobarometry and apatite fission track data, define the temperature and pressure changes associated with cooling and exhumation of the pluton. The P-T conditions prevalent during the deformation history of the GPF fault system are evaluated by relating recrystallisation mechanisms in quartz to temperature, showing that the early stages of deformation occurred at temperatures of 450 to 600ºC. Dating of pseudotachylytes by the K-Ar isotopic method suggests subsequent brittle deformation took place at temperatures <350ºC and pressures ≤150MPa. A model for the architecture of the GPF architecture therefore has well constrained environmental controls, and should be transferrable to faults with comparable deformation histories.

Small faults (cumulative displacements <1m) in the Mount Abbot Quadrangle, 55km north of Granite Pass, have been examined to illustrate the processes associated with the earliest stages of slip in the Sierra Nevada faults. The faults have branched or straight fault traces. Pseudotachylytes in branching faults show that these faults accumulated displacement in high velocity slip events, rather than by quasi-static fault growth. Branching faults without pseudotachylytes contain chlorite breccias interpreted to have formed in response to slip along faults with elevated pore fluid pressure. Straight faults also likely underwent slip events, but contain cataclased chlorite and epidote, suggesting low fluid pressures during slip. The small faults show that fluid-rock interactions are critical to fault geometry, and that lateral structural heterogeneity is established after small finite displacements.

Field and thin section observations of exhumed seismogenic faults show that fault architecture and fault rock assemblage are critical to the earthquake rupture process. The heterogeneous composition of slip surfaces in the GPF faults imply that melt lubrication cannot account for all of the dynamic slip weakening as there are no continuous pseudotachylyte generation surfaces through the fault zones. Multiple slip weakening mechanisms must have been active during single rupture events. Slip weakening mechanisms also change at a given point on the fault in response to continued deformation. Splay faults at the GLF termination suggest that structural complexity observed at the terminations of fault surface traces can also be expected at depth. The off-fault damage at the termination of the GLF will change the bulk elastic properties of the host rock and must be accounted for in models of rupture propagation beyond fault terminations, or across geometrical discontinuities. Additionally, aftershock distributions and focal mechanisms may be controlled by the geometry of structures present at fault terminations.

Table of Contents

List of Figures

Chapter 1

Chapter 2

Chapter 3

Chapter 4

Chapter 6

Chapter 7

List of Tables

Chapter 3

Chapter 4

Chapter 5

Chapter 6

Acknowledgements

First and foremost I'd like to say a massive thank you to Zoe for all the help she has given me with so many things during the past few years, for finding me a PhD, and for sending me to California when it wasn't really the most sensible thing to do. I also owe a big thanks to Tim for having an open door, spending time looking down microscopes and helping me in the quest for zeolites. Equally, Cristina has been a massive help with my thermochron work and I have to say thanks to her for voluntarily taking extra apatites and zircons into her life. Kate's help with theses and zircons has been invaluable. I'd also like to thank John Gilleece for preparing thin sections expertly, Les Hill for taking great photos of rocks, and Peter Chung for helping me out with the probe and SEM. The thermochronology analyses in this study would not have been possible without the help of Jim and Paul at SUERC.

Special thanks must go to Nick, a one-time professional field assistant. His work and unswerving dedication to the cause in the face of pain, hunger, extreme physical exertion, mosquitoes, snow blizzards, bears, and relentless peanut butter tortillas was exceptional. I'd also like to thank my fellow postgrads over the past few years for lengthy discussions over coffee and/or beer concerning all things except pseudotachylytes, in particular Duncan, who has also been an excellent flatmate, Dan, who has done more than most to keep me on the straight and narrow, Aisling, Paul, Sally and Fernando. Thanks to all my friends and family, especially my brother, who have helped massively over the past few years, as well as all the years previously. Thanks to Kris for drinking so many coffees, and for being generally amazing.

Thanks to the National Park Service and the National Forest Service in California for fieldwork and sampling permits. This study was funded by a Glasgow University scholarship.

Declaration

The material presented in this thesis is the result of the independent research undertaken by myself between October 2004 and January 2008. This work was supervised by Dr. Zoe Shipton and Dr. Tim Dempster. All previously published and unpublished work by other authors referred to in this thesis is given full acknowledgement in the text.

James Kirkpatrick

January 2008

1

Introduction

Faults are structural discontinuities in the Earth's crust that accommodate strain imposed by plate tectonic motions by accumulating displacement. Much of the displacement in the upper portions of the actively deforming crust is accomplished through earthquake rupturing, where relative displacement of the crust on either side of a fault is achieved in sudden, cataclysmic events (Sibson, 1989). Gilbert (1883) was amongst the first to demonstrate the necessary relationship between earthquake ruptures and geologic faults. He mapped small fault scarps cutting Pleistocene sediments in the Basin and Range province, Utah and Nevada, and recognised similar structures along larger faults at the base of the Wasatch Range, Utah. By comparison with scarps formed during the Owens Valley, California earthquake of 1872, he concluded that relative displacement of the crust occurs when an earthquake ruptures a geologic fault.

The inter-dependence between earthquakes and faulting has subsequently been demonstrated by numerous works utilising a variety of techniques. Observations of surface ruptures associated with strike-slip faults show that the majority of earthquakes end at geometric complexities in fault traces, including fault terminations (DePolo *et al.*, 1991; King and Nabelek, 1985; Wesnousky, 2006). The macro-scale physical properties of faults therefore control to some extent the size of earthquake ruptures (e.g. Aki, 1979; Segall and Pollard, 1980; Sibson, 1989). Rupture propagation is also observed to decelerate in regions of structural complexity (Andrews, 2005; Aydin and Du, 1995; Barka, 1996). The precise geometry and composition of localised slip surfaces are thought to significantly influence the initiation (Segall and Rice, 2006) and subsequent propagation of earthquake ruptures (e.g. Rice and Cocco, 2007). Field and experimental investigations into the localisation of slip during rupture propagation show that the composition of the material in the slipping zone is both a product of seismic slip, and controls to a large extent the rupture process (Chester and Chester, 1998; Chester *et al.*, 2005; Wibberley and Shimamoto, 2005).

The purpose of this study is to examine faults that have been exhumed from seismogenic depths to investigate how the physical characteristics (assemblage and geometry of deformation products) of faults control the earthquake rupture process. Equally, the study aims to evaluate how earthquakes have imposed deformation onto the fault structure. The study will revisit previously identified left-lateral strike-slip faults in the Sierra Nevada, California, that have been exhumed from depths of 5-12 km (Evans *et al.*, 2000), the depths that earthquakes are observed to nucleate (e.g. Sibson, 1983). The faults are ~1 to >8km long, with cumulative displacements on the order of tens of metres. Scaling relations suggest that the faults could have experienced earthquakes up to around magnitude 6. Ancient earthquakes that ruptured the faults were therefore of a restricted magnitude range, though the larger ruptures would have broken to, or near to the Earth's surface, rupturing the majority of the brittle crust.

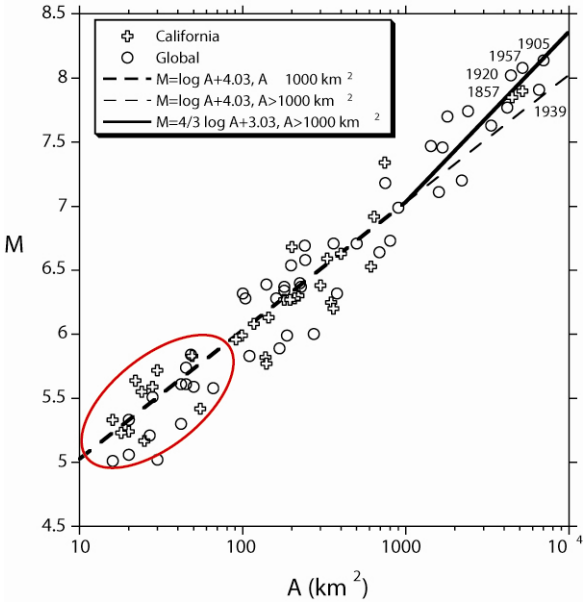

Figure 1. Graph showing the relationship between earthquake rupture area, A, and magnitude for continental strike-slip earthquakes (from Hanks and Bakun, 2002; data from Wells and Coppersmith, 1994). The data show that for magnitudes less than ~7 the magnitude scales with rupture area. The red ellipse indicates the range of possible earthquake magnitudes that could have occurred on the faults described in this study. Areas are calculated assuming circular ruptures occurring on faults with lengths less than the thickness of the seismogenic crust (15 to 20km, cf. Hanks and Bakun, 2002).

Primary data will comprise field, microscope and scanning electron microscope observations of faults and their related structures. These data will provide important constraints on the physical properties of fault zones from seismogenic depths. Specific objectives of the investigation include:

- Defining the internal architecture of fault zones in crystalline rocks that have been exhumed from seismogenic depths and describing in detail the assemblage of deformation products that make up the fault zones.

- Using micro-scale observations to determine the deformation mechanisms that accommodated displacement at the grain scale, and how they changed through the period of fault activity.

- Developing understanding of what controls the architecture of a fault, in particular the influence of the properties of the deformation environment (temperature, lithostatic pressure etc.) and the role of fault-hosted fluid flow.

- Inferring which properties of fault structures are the products of seismic activity, and how they might be used to constrain rupture processes.

This work builds on data previously gathered by Evans *et al.* (2000; see Chapter 2 for a detailed discussion of their work). Some of the results and interpretations gathered in this study are contained in Kirkpatrick *et al*., manuscript in press (Kirkpatrick, J. D., Z. K. Shipton, J. P. Evans, S. Micklethwaite, S. J. Lim, and P. McKillop (2008), Strike-slip fault terminations at seismogenic depths: Structure and kinematics of the Glacier Lakes fault, Sierra Nevada, J. Geophys. Res., doi:10.1029/2007JB005311, in press, accepted 18 January 2008). At the time of submission of the thesis, four further manuscripts are in preparation: 'The structural architecture of seismogenic faults in igneous rocks', Kirkpatrick J. D. and Shipton Z. K. (utilising data primarily from Chapters 3, 4 and 6 to detail the controls on the architectures of the Granite Pass and Glacier Lakes suites of faults), 'Fault structure, slip, and fluid flow interactions; insights from small faults in the Mount Abbot Quadrangle, California', Kirkpatrick J. D. and Shipton Z. K. (based on Chapter 5), 'Heterogeneous fault properties in exhumed seismogenic faults; implications for earthquake slip weakening mechanisms', Kirkpatrick J. D. and Shipton Z. K. (containing observations from Chapters 3 and 4 that demonstrate slip weakening mechanisms are spatially and temporally heterogeneous in the Granite Pass suite of faults), and 'Pseudotachylytes; rarely generated, rarely preserved or rarely reported? Implications for earthquake rupture processes', Kirkpatrick J. D. and Shipton Z. K.

1.1 Structure of the thesis

This chapter will introduce some of the concepts associated with structural geology that are fundamental to the analysis and interpretation that are undertaken in the study. In particular the basis for the description of faults as seismogenic structures is addressed. Chapter 2 introduces the locations and lithologies of the two field areas in the Sierra Nevada, and provides some geological background.

Chapter 3 presents the results of fieldwork in the Granite Pass study area. Kilometre-scale structures are defined and the architectures of two faults, the Granite Pass and Glacier Lakes faults, are described in detail. Cross-cutting relations in the field and contrasting architectures suggest that the Granite Pass fault pre-dates the Glacier Lakes fault. Chapter 4 presents thin section and scanning electron microscope observations of samples from three of the faults in the Granite Pass area.

The results of fieldwork in the Mount Abbot Quadrangle are presented in Chapter 5, which focus on five faults with small cumulative displacements (≤1m). The geometry and fault rock assemblage of the faults are shown to be different, and potential reasons for the differences are discussed.

Chapter 6 presents the results of thermochronologic analyses of a suite of minerals from the host rock in the Granite Pass area, the Pyramid pluton. Results of isotopic dating of pseudotachylytes are also included, and the variations in temperature and lithostatic pressure are correlated with deformation mechanisms. Chapter 7 discusses the controls on the architecture of the Granite Pass fault, the implications of the field and thin section observations for some earthquake rupture processes, and summarises the main conclusions arising from the study. Recommendations for further work are discussed in Chapter 8.

1.2 Describing faults

1.2.1 Brittle deformation (frictional)

Faults develop in response to plate tectonic forces, and produce a wide range of deformation products. In the brittle crust, pressure-dependent frictional behaviour predominates and results in fracturing and cataclasis at all scales. According to Anderson's theory of faulting (Anderson, 1942), faults form at predicable angles with respect to the principal stress directions that define the far-field (tectonic) stress regime.

Brittle faults form at 25 to 30º to the most compressive principal stress direction (σ_1). Assuming a vertical intermediate principal stress (σ_2) for near-surface faults allowed Anderson to classify the three major classes of faults that result from the three most common principal stress directions; normal, reverse, and strike-slip. Strike slip faults will be the focus of this study.

Previous work has shown that exhumed strike-slip faults are composed of a variety of differently deformed rocks (Figure 2); a fault core of intensely cataclased material tens of centimetres to metres thick is often embedded in a damage zone containing distributed fractures, subsidiary faults and micro-fractures (Caine *et al.*, 1996; Chester and Logan, 1986; Schulz and Evans, 2000; Wilson *et al.*, 2003). Within the fault core, the majority of displacement accommodated by the fault is frequently localised onto a narrow zone (millimetres or less). This zone is sometimes referred to as a slip surface (Caine *et al.*, 1996), a slipping zone (Shipton *et al.*, 2006), a prominent fracture surface (Chester and Chester, 1998) or a principal slip surface (Rice, 2006). The complicated array of terminology associated with this component of a fault is derived from the field geologist's recognition of a polished slickenside, which might display slickenlines, as a surface across which relative displacement has occurred. However, at some scale of magnification, the material that comprises the slickenside must have a thickness. Surfaces by definition have no thickness and so a contradiction arises that the studies mentioned above have sought to eradicate. For the sake of simplicity, this study will use the term slip surface when referring to any zone across which relative displacement occurs. Frequently a slip surface will be described as having a thickness of tens of millimetres.

The structural architecture of a fault, or fault zone, describes the arrangement of the three components of variably damaged rock defined from exhumed faults (Chester and Logan, 1986). Caine *et al.* (1996) showed that the different components of the fault architecture have different mechanical and permeability properties and suggested that a model of three fault zone components can account for a wide variety of architectures depending on whether all or any of the components are present in a fault, and the extent to which each of the components of the fault is developed (Figure 2). The three component model therefore expects faults to be inherently different. Caine *et al.* (1996) also suggested that there are a number of parameters that control the style of fault architecture that are either intrinsic properties of the fault (e.g. lithology, displacement, length, 3D geometry, fluid-fault rock interactions) or extrinsic properties of the deformation environment (i.e. temperature, lithostatic pressure, differential stress, time-averaged strain rate).

Deformation accompanying brittle faulting produces characteristic random-fabric fault rocks in which fracturing and cataclasis cause the host rock minerals to fragment, and generally reduce in grain size with progressive deformation (e.g. Sibson, 1977). The terms used to describe brittle fault rocks in this study are proto-cataclasite, cataclasite and ultracataclasite (see section 3.7.1.3 for further information on their classification). Fault breccias described in thin section (Chapter 4) are likely equivalent to proto-cataclasites identified in outcrop. Pseudotachylytes (see below) are a special class of brittle fault rock that contain randomly oriented clasts in an amorphous or neo-crystalline matrix (e.g. Magloughlin and Spray, 1992). As well as containing a random fabric (i.e. no systematic grain shape foliation), brittle fault rocks can be defined as they contain fractured grains which have a large range in grain size and typically sharp, straight edges (e.g. Blenkinsop, 1991). This is important for identifying foliated cataclasites, which are brittle fault rocks that do have foliations and are therefore not random fabric (Chester *et al.*, 1985). Note also that processes such as pressure solution also occur during brittle deformation that do not necessarily induce fracturing.

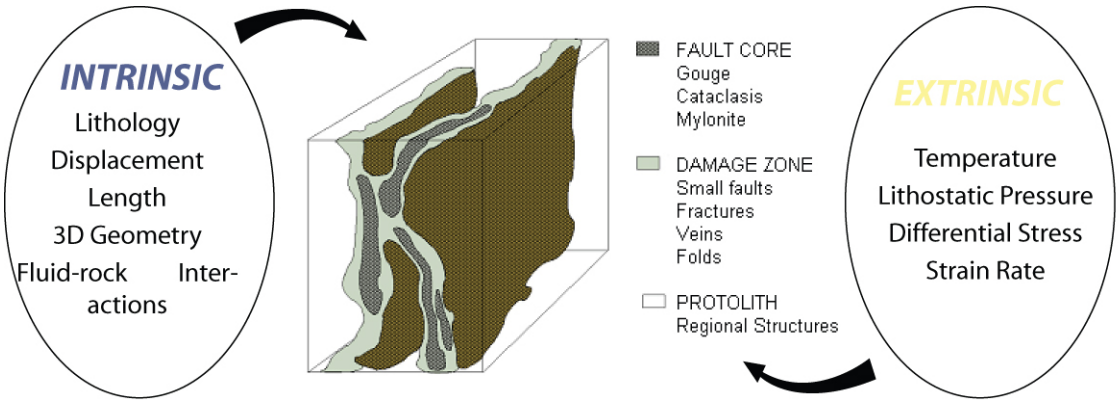

Figure 2. The three component fault zone architecture model (from Caine *et al.*, 1996). The architecture of a fault describes the arrangement of the fault core(s), slip surface(s) and damage zone (centre). Note that each component may or may not be developed in a fault zone. A number of parameters control the style of fault architecture that are either intrinsic properties of the fault or extrinsic properties of the deformation environment.

1.2.2 Crystal-plastic deformation (viscous)

At higher temperatures, grain-scale deformation is achieved through intra-crystalline deformation mechanisms by movement of lattice defects. Intra-crystalline deformation is dependent upon temperature and strain rate, and changes in grain shapes occur by three principle mechanisms; dislocation creep, and diffusion creep and grain boundary sliding (the latter two of which act together). For a given mineral, the dominant mechanism is dependent on the temperature, differential (flow) stress and strain rate that characterises the deformation. Different minerals are sensitive to each mechanism under different

conditions due to the crystallographic control on dislocation migration and diffusive mass transfer. Experimental and theoretical studies have defined flow laws for these three deformation mechanisms for some minerals. Flow laws relate strain rate to steady-state flow stress, temperature and material parameters. Investigating intra-crystalline deformation mechanisms is not the focus of this study, but deformation mechanisms with well-constrained deformation conditions for certain minerals will be applied to natural fault rocks as they can act as useful temperature gauges.

Deformation that occurs by dislocation creep is termed crystal-plastic deformation. Dislocation creep accommodates strain as dislocations move through the crystal lattice of a mineral along slip systems. Slip systems intersect in any mineral, and inevitably dislocations become tangled, leading to strain hardening. A form of recovery must therefore operate if progressed strain can occur at the same flow stress; one important manner in which dislocation density is decreased is the migration of vacancies in the crystal lattice to a dislocation tangle, which displace the tangle and allow it to climb to a new slip system. During deformation, dislocation generation and annihilation processes compete. After deformation has stopped, dislocations tend to become arranged into an equilibrium state with the shortest possible lengths of dislocations in the lattice. Planar arrangements of dislocations in a particular slip system, known as subgrain boundaries, can form. Subgrain boundaries separate portions of a mineral with slightly different crystallographic orientations. Grain boundary migration is another mechanism by which the dislocation density in a deformed mineral can reduce. Where two grains with differing dislocation densities are juxtaposed, the mineral with the lower density grows at the expense of the mineral with the higher density.

Dynamic recrystallisation, whereby small new grains replace old grains resulting in an overall change in the grain size, shape and orientation, operates by these two processes. There are three different recrystallisation mechanisms: bulging and grain boundary migration recrystallisation (induced by grain boundary migration), and progressive subgrain rotation recrystallisation. Results of experimental deformation of quartz (Hirth and Tullis, 1992) have been combined with observations of syn-kinematic quartz veins from a shear zone adjacent to a syn-tectonic contact metamorphic aureole (Stipp *et al.*, 2002). Stipp *et al.* (2002) calculated temperature variations in the metamorphic aureole from equilibrium mineral assemblages in the shear zone metasedimentary rocks, and correlated the temperature variation in the shear zone with the deformation mechanism (Figure 3). With increasing temperature, bulging recrystallisation gives way to subgrain

rotation and subsequently grain boundary migration recrystallisation. Identification of the characteristic microstructures of each of the dynamic recrystallisation mechanisms (for reviews of microstructures see Passchier and Trouw, 2005; and Stipp *et al.*, 2002) in thin section can be used to infer the temperature of deformation by comparison with the results of Stipp *et al.* (2002).

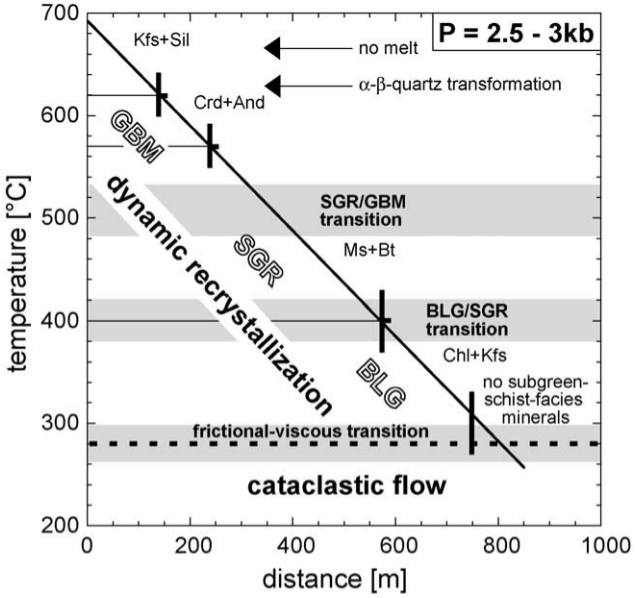

Figure 3. Temperature regimes of the dislocation creep deformation mechanisms from Stipp *et al.* (2002). Distance refers to the distance from the pluton that caused the contact metamorphism in the shear zone sediments.

Experimental work has also focused on feldspars, which deform by dislocation creep at higher temperatures than quartz due to the ease of fracture along cleavage planes (Tullis and Yund, 1985; Tullis and Yund, 1987). The transition from brittle fracture to crystal-plastic deformation in feldspars is affected by the composition of the minerals and subgrains, grain size and the presence of water (Tullis and Yund, 1987). Additionally, the microstructural textures that result from the two types of deformation are not easy to distinguish as cataclasis induces sub-micron fracturing, which can look like subgrain development when viewed with an optical microscope, and survivor grains, or augen, display little internal deformation (McLaren and Pryer, 2001; Tullis and Yund, 1987). Consequently, using feldspar recrystallisation mechanisms as temperature gauges is more complicated than for quartz (e.g. Pryer, 1993). Using a combination of reported experimental work and observations of naturally deformed feldspars, Passchier and Trouw (2005) summarise four key temperature regimes for the deformation of feldspars: below 400ºC feldspars deform by brittle fracturing and cataclastic flow resulting in angular grains with strong intra-crystalline brittle fractures, bent cleavages and twins. Minor dislocation glide is possible at temperatures between 400 and 500ºC, but deformation is predominantly

brittle. Tapered deformation twins, patchy undulose extinction and flame perthites may be developed but core-mantle structures are not. Dislocation climb becomes important at temperatures of 450 to 600ºC, and bulging recrystallisation results in nucleation and growth of new grains. Mantles of new subgrains develop around augen that have sharp edges. Above 600ºC dislocation climb and recovery predominate in feldspars and subgrain rotation and bulging recrystallisation mechanisms are active. Core-mantle structures occur, and have diffuse boundaries between augen and subgrains.

1.3 Pseudotachylytes

Tectonic pseudotachylytes are the product of extreme comminution, wear, and melting due to frictional heating along a sliding interface (Sibson, 1975; Spray, 1992; Spray, 1995; Wenk *et al.*, 2000). Pseudotachylytes are typically dark, have an aphanitic or glassy matrix and contain few lithic clasts. As such, they can be difficult to distinguish from other fault rocks such as ultracataclasites or ultra-mylonites. Generally, evidence for a melt origin for a particular sample is required for positive identification of pseudotachylyte (Magloughlin and Spray, 1992). However, experimental studies show that comminution is a necessary precursor to melting, and therefore pseudotachylytes are intimately associated with non-melt origin cataclasites (e.g. Curewitz and Karson, 1999; Rowe *et al.*, 2005). Recent studies have also demonstrated that extreme comminution and 'mechanochemical' processes can produce textures characteristics of pseudotachylytes often attributed to a melt origin (Lin, 1996; Ozawa and Shigeru, 2007).

The magnitude of heat necessary to achieve melting means that pseudotachylytes are accepted as an indicator of localised slip at seismic velocities, and so they record ancient seismic activity in an exhumed fault zone (Cowan, 1999; Sibson, 1975). Sibson (1975) demonstrated that pseudotachylyte vein geometries fall into two categories; relatively planar veins that are continuous for many metres across which shear displacement is evident, and irregular, shorter (often centimetres in length) veins which have little or no shear displacement. He interpreted these geometries as generation surfaces (across which rapid friction sliding occurred), and injection veins containing melt squeezed from the generation surface. Exposures of pseudotachylytes in fossil seismogenic faults are unique in preserving direct evidence of the dynamic processes that operate during such transient events as earthquakes. As such, pseudotachylyte-bearing faults are used to elucidate earthquake processes from field observations (Barker, 2005; Di Toro et al., 2005a; Di Toro

and Pennacchioni, 2004; Di Toro et al., 2005b). Pseudotachylytes are therefore important fault rocks that have a range of significant implications for the study of seismic processes.

The difficulty in correctly identifying pseudotachylytes prompted Magloughlin and Spray (1992) to propose a series of criteria by which pseudotachylytes could be distinguished in thin section, based on a review of pseudotachylyte literature:

1. quenched vein margins;
2. variation in microcrystallite textures and/or size with respect to the vein margin;
3. vesicle and amygdales;
4. newly recrystallised high-temperature mineral phases within a vein;
5. dendritic microcrystallite habits;
6. the presence of abundant sulphide droplets;
7. spherulites;
8. melting effects in clasts within the pseudotachylyte;
9. certain recrystallisation features;
10. certain systematic chemical relations between a pseudotachylyte and the host rock.

Magloughlin and Spray (1992) suggest that the presence of one or more of these criteria in a fault rock is indicative of the rock having a melt origin rather than a cataclastic origin. These criteria are used in this study as a basis for identifying pseudotachylytes, and in particular differentiating them from comminuted ultracataclasites. Previous studies have described in detail the structure and composition of microlites, interpreted as crystallites that form by nucleation and growth from the melt during quenching (e.g. Maddock, 1983). However, the term ‘microlite’ has precedence of usage as a mineral species name (Shepard, 1835). A wide range of terms exist for describing very small crystals in glassy rocks such as pitchstone, rhyolite and basalt. For simplicity, such crystals are referred to as microcrystallites in this study.

Physical models show that pseudotachylytes can be generated during moderate to large earthquakes (i.e. coseismic slip >1m) if the thickness of the slipping zone is of the order of a few millimetres (Kanamori and Heaton, 2000; Sibson, 2003). Field and microscope studies demonstrate that slip is frequently localised onto zones sufficiently narrow to induce the temperature elevation required for melting during earthquakes of this magnitude (Shipton et al. 2006; Sibson 2003). Given the frequency with which such magnitude events occur in modern tectonically active regions, pseudotachylytes might be expected to be widespread in crustal sections exhumed from seismogenic depths i.e. 5-15km (Jeffreys, 1942; McKenzie and Brune, 1972). However, compared to other fault rock types, there appear to be a limited number of reports of pseudotachylytes in studies of exhumed fault zones, and for this reason they are considered to be "rare" fault rocks (Magloughlin and Spray, 1992; Sibson, 2003). Sibson (2003) and Sibson and Toy (2006) suggest that the apparent scarcity of pseudotachylytes is either because pseudotachylyte material is rarely generated, or because it is rarely preserved in recognisable form.

1.4 The slip-weakening model of an earthquake rupture

An earthquake occurs when the strength of a fault diminishes more rapidly than the tectonic forces that are imposed on the system are relaxed. When this happens, stored elastic strain energy and gravitational energy are released and drive processes such as frictional heating along a sliding interface, and radiation of seismic waves. One model that relates the macro-scale energy budget of an earthquake rupture to the physical processes of earthquake slip is the slip weakening model (Andrews, 1976; Ida, 1972; Kanamori and Heaton, 2000; Kanamori and Rivera, 2006). In the slip weakening model, the initial static strength of a fault is exceeded, initiating slip. As slip increases, the strength of the fault decreases to a steady-state dynamic value, and remains at that value until slip stops. Slip continues until the driving forces are relaxed to levels below the dynamic shear strength of the fault. The rate of strength reduction is characterized by a critical displacement, the slip-weakening distance (D_c). To achieve the physical breakdown in strength of a fault, an energy input is required to break material bonds and create a rupture surface. This energy is the fracture energy, E_G. E_G is actually a composite term that can involve many physical processes that consume energy, including plastic yielding and micro-cracking in the breakdown zone at the rupture front and off-fault fracturing. Energy is also consumed by frictional heating along the sliding rupture surface (E_H), and is emitted as radiated seismic waves (E_R). The slip weakening model can be expressed as (Kanamori and Rivera, 2006):

$$E_t = \Delta W = E_R + E_H + E_G,$$ **Equation 1**

where E_t is the total energy released which is equal to the net work done (ΔW). This expression can be represented graphically (Figure 4). The relative magnitude of each of the energy sinks is unclear, though E_R, which can be measured seismologically, has been estimated as around 5 to 20% of E_t (McGarr, 1999). From a geologic perspective it is likely that E_G and E_H are indistinguishable (Shipton *et al.*, 2006). The slip weakening model paradigm is inherent to the subsequent analysis and interpretation of geologic structures in this study.

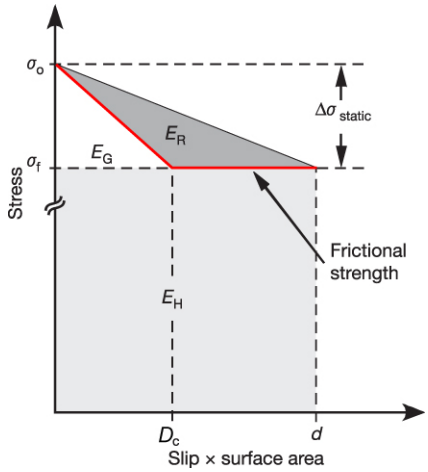

Figure 4. A graphical representation of the slip weakening model relating the partitioning of energy between fracture energy (E_G), frictional energy (E_H) and radiated energy (E_A) to the stress acting on the fault (σ). The change in fault strength is highlighted in red, modified from Chester *et al.* (2005).

1.5 Slip weakening mechanisms

The dynamic reduction in the strength of a fault can be caused by reducing the coefficient of friction across the rupture surface. The decrease in strength is a non-instantaneous process that must have some foundation in the physical properties of a sliding interface. For natural faults, a number of mechanisms have been proposed by which the slip weakening during frictional sliding is achieved, which are summarised below.

1.5.1 Thermal pressurization

Assuming co-seismic slip is localised to a slipping zone of finite thickness that contains a fluid-saturated, permeable material, the shear strength of the fault (τ) is given by:

$$\tau = f(\sigma - p),$$ **Equation 2**

where σ is normal stress, f is the (steady state) friction at slip rate V, and p is the pore pressure. Frictional heating induced by slip would cause the fluid in the slipping zone to expand. If the slipping zone is confined or has extremely low permeability so that expanding fluid cannot immediately escape then thermal expansion of the fluid increases the pore pressure (p) and for approximately constant σ reduces the shear strength (Andrews, 2002; Bizzarri and Cocco, 2006; Lachenbruch, 1980; Mase and Smith, 1984; Mase and Smith, 1987; Rempel and Rice, 2006; Rice, 2006; Rice and Cocco, 2007; Sibson, 1973; Wibberley and Shimamoto, 2005). Continued slip may have the effect of progressively heating the pore fluid which continues to expand causing the shear strength to progressively reduce towards zero. If CO_2 is dissolved in the pore fluid, liquid/vapour phase transitions may add to the increase in pre pressure (Mizoguchi *et al.*, 2007). Studies using inferred slipping zone thicknesses and permeability measurements of fault core ultracataclasite or fault gouge have shown that thermal pressurization is likely to occur (Wibberley and Shimamoto, 2005), and that estimates of the fracture energy of earthquake ruptures agree with seismologically determined values if thermal pressurization is operative (Rice, 2006). Recent investigations have highlighted that pore pressure can exceed the normal stress in the region surrounding the slip surface if wall rock types with different permeabilities are juxtaposed, and potentially cause hydrofracturing (Vredevoogd *et al.*, 2007).

1.5.2 Elastohydrodynamic lubrication

Lubricated ball-bearings are used to minimise frictional wear between mechanical moving parts in industrial applications. Brodsky and Kanamori (2001) suggested that an analogous mechanism could be operative during earthquake faulting. They showed that for two rough surfaces separated by a slipping zone composed of a matrix of granular material containing interstitial fluid, the resistance to sliding is reduced below the static friction by two effects; fluids present between solid-solid contacts (e.g. micro-scale asperities in the wall rock roughness or particle-particle contacts in the slipping zone) mean that the effective friction at the contact is a function of the fluid viscosity not the coefficient of friction between the solids, and the relative displacement of the rough wall rock surfaces strains the interstitial fluid causing an increase in the effective normal stress acting on the slipping zone and elastic deformation of the wall rock asperities.

Brodsky and Kanamori (2001) envisage the slipping zone as a granular slurry, in which the matrix of solid fragments is a fluidized cataclasite or a melt containing lithic clasts, between wall rocks that are significantly less porous. Using suitable parameters for slurry

viscosity, wall rock roughness and wall rock elastic properties they tested their formulation for earthquakes of a range of sizes. They concluded that elastohydrodynamic lubrication effects are likely active in combination with other slip weakening mechanisms such as melt lubrication and thermal pressurization, but that elastohydrodynamic lubrication is significant in moderate to large events.

1.5.3 Acoustic fluidization

Small wavelength, high frequency waves are emitted during earthquake rupture propagation that may be energetic enough to elastically deform the wall rock in the direction perpendicular to rupture propagation (Melosh, 1979; Melosh, 1996). This deformation could cause the effective normal stress acting upon a fault to be transiently diminished, enabling slip to occur at low shear stresses. Melosh (1996) assumes that a fault is composed of a cohesionless fault core, which behaves like a non-Newtonian fluid instead of a coulomb solid when the acoustic vibrations are generated. He uses an energy balance to show that the stress fluctuations associated with the vibrations can exceed the overburden load (normal stress), and achieve an order of magnitude reduction in the coefficient of friction. The vibrations are regenerated by a feedback process in the fault core whereby elastic failure of the core material releases a proportion of the stored elastic strain energy in the form of waves with a similar spectrum of wavelengths.

1.5.4 Flash heating

The frictional resistance to sliding across a rough interface between two solids is a function of the response of the asperities in the surfaces of the solids to sliding (e.g. Dieterich, 1978; Rice *et al.*, 2001). According to rate and state frictional constitutive laws, frictional strength increases with the time that asperities are in contact as the cohesion between asperities increases with progressive bonding at the atomic scale. However, when forced to shear, the asperity contacts generate intense localised heating during the lifetime of the contact (Rice and Cocco, 2007). If the sliding velocity is great enough a thin layer at the asperity contact's surface is heated, which causes a thermally-activated reduction in the frictional strength.

1.5.5 Melt lubrication

If frictional sliding generates sufficient heat to melt the wall rock surfaces then a resulting layer of melt could act to lubricate the fault surface as the viscosity of the melt would be

less resistant to sliding than a solid-solid frictional resistance (Jeffreys, 1942; McKenzie and Brune, 1972). Theoretically, friction-induced melts (pseudotachylytes) can be generated during moderate to large earthquakes (coseismic slip >1m) if the slipping zone is of the order of a few millimetres thick (Kanamori and Brodsky, 2004; Kanamori and Heaton, 2000; Sibson, 2003). Studies of exhumed faults show that slip is frequently localized onto principal displacement zones 1 mm to 10 cm thick (Shipton *et al.*, 2006; Sibson, 2003) implying that pseudotachylytes should be widespread in crust exhumed from seismogenic depths, i.e. 5-15 km.

Recent experimental work utilising high velocity rock friction (HVRF) apparatus have successfully induced frictional melting along a sliding surface (Di Toro *et al.*, 2006; Hirose and Shimamoto, 2003; Hirose and Shimamoto, 2005a; Hirose and Shimamoto, 2005b; Lin and Shimamoto, 1998). Measurements of the frictional resistance to sliding during these experiments show that there are two phases in the evolution of friction during slip that correspond to differences in the geometry of the melt along the slipping zone. During the early stages of slip, melt patches are discontinuous and are associated with strengthening of the fault. Subsequently, as melt patches coalescence into a continuous molten layer, slip weakening is achieved and the friction drops to the dynamic level. Hirose and Shimamoto (2005a) suggest that the higher values of friction due to small melt patches may act as a brake to prevent ruptures from developing into high slip events. However Fialko and Khazan (2005) showed that such viscous breaking is only likely to be significant at low values of normal and shear stress and therefore will occur for depths of less than ~5km.

1.5.6 Silica gel formation

Goldsby and Tullis (2002) and Di Toro *et al.* (2004) report a significant velocity-dependent reduction in the frictional resistance to sliding of quartz-rich samples at both sub-seismic and seismic velocities (>1mm s^{-1}), room temperature and normal stress (σ_n) = 5MPa. They inferred that the slip-weakening behaviour was due to the formation of a layer of silica gel; flakes of amorphous silica are produced through wear processes along the sliding interface that adsorb water from atmospheric humidity to produce a gel. The experimental results suggest that the silica-water mix displays the thixotropic behaviour of a gel, giving a slip weakening distance for this mechanism on the order of 0.5 to 1m. Extrapolation of the data implies zero friction at seismic slip rates (~1m s^{-1}). However, the gel-like phenomenon reported by Di Toro *et al.* (2004) has only been observed for novaculite (a quartzite) in which the silica content is ~100%. Other rock types including granite, albite and gabbro are thought to display similar velocity-weakening behaviour, but the only

direct evidence of gel formation (solidified flow-like textures coating the sliding interface) has been observed for novaculite.

1.5.7 Normal interface vibration

Brune *et al.* (1993) showed that as well as a dynamic reduction in friction, the strength reduction of a fault during slip weakening can be achieved by decreasing the normal stress acting across the rupture surface (see Equation 2). They observed macroscopic separation across the sliding interface between two foam blocks during stick-slip experiments caused by normal interface vibrations. Since separation was achieved, the normal stress acting on the sliding interface was overcome, and sliding occurred at low shear stress. Brune *et al.* (1993) went on to suggest that since most of the translational motion in their experiments was achieved when the interface was 'open' i.e. a separation had occurred, the frictional heat generation would be much less than expected.

2

Geologic Setting

2.1 Introduction

Two field areas were visited during fieldwork for this study; the Granite Pass region of Sequoia and Kings Canyon National Park, and the Bear Creek drainage area in the Mount Abbot Quadrangle (Figure 5). Granite Pass is located ~9km to the north of the south fork of the Kings River, and is accessible from the Copper Creek trailhead at Roads End, highway 180. The Bear Creek drainage area is situated to the south of Lake Thomas Edison, around 55km north of the Granite Pass area. Both study areas are in the central part of the Sierra Nevada mountain range, and lie predominantly at elevations in excess of 3000m.

The two study areas were chosen primarily because excellent exposures exist due to recent glaciation and climate at altitudes greater than 3000m. Faults are common in the areas, and the Mount Abbot Quadrangle in particular has been the focus of numerous previous investigations (see below). The faults cut relatively isotropic granitoids, and are thought to have been active at seismogenic depths (e.g. Pachell and Evans, 2002; Segall *et al.*, 1990). Isotropic crystalline host rocks are useful for studying earthquake rupture processes as complexities in these processes induced through juxtaposed lithologies can be ignored, while the rocks are still representative of the basement lithologies in which many earthquakes nucleate. Though the faults exposed in the study areas are relatively immature compared to plate-boundary faults (smaller lengths and total displacements; see Figure 1), the segmented nature of mature faults suggests that the insights into fault-earthquake interactions are generic to all faults (e.g. Sibson, 1989). Field observations from the two study areas therefore provide detail of fault geometry, composition and inferred deformation processes of seismogenic faults beyond that which may be collected utilising only geophysical techniques or deep drilling. The rigid-body exhumation of the Sierra

Nevada batholith means that the faults have been exhumed without significant associated deformation, preserving the characteristics that developed at depth.

The purpose of this chapter is to provide a geological context for the structural analyses undertaken in this study by giving an overview of the Sierra Nevada batholith emplacement subsequent exhumation. The lithology and previous fault-related studies for each of the two study areas will then be reviewed.

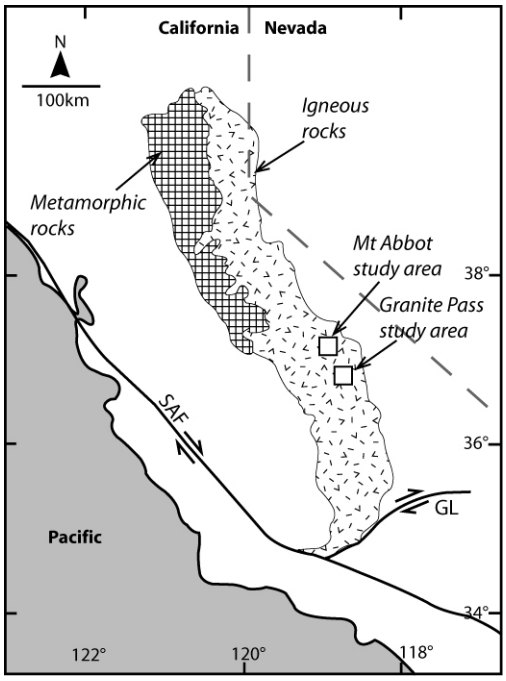

Figure 5. Map of California and western Nevada showing the localities of the two study areas. SAF = San Andreas fault, GL = Garlock fault (modified from Pachell and Evans, 2002).

2.2 Emplacement and exhumation of the Sierra Nevada batholith

The Sierra Nevada batholith is a continuous chain of plutonic and interspersed metamorphic rocks that represent one part of a continental magmatic arc which stretches the entire length of the west coast of North America (Bateman, 1992; Moore, 1978). The batholith is exposed today at altitude in the Sierra Nevada mountain range. The range is strongly asymmetric comprising a gentle western slope and steep eastern escarpment. Several regional-scale trends in the age and composition of the plutonic rocks have been defined from field mapping and extensive geochronologic analyses. In general plutons are more mafic (tonalitic) in the west, and become more granitic towards the east. A transverse gradient is also present in the ages of plutons; voluminous plutonism began in the western part of the batholith ca. 125Ma, subsequent to which plutonism migrated

steadily east until its conclusion in the Late Cretaceous (Chen and Moore, 1982; Evernden and Kistler, 1970; Stern *et al.*, 1981).

The following generalized tectonic history for the petrogenesis of the Sierra Nevada batholith is summarised from Saleeby (1999). In the Late Palaeozoic, the western margin of the North American plate was truncated by a transform plate boundary between continental orogenic terranes and oceanic lithosphere of the Panthalassa oceanic plates (Figure 6). Oblique convergence across the plate boundary initiated melange formation and obduction of oceanic crust units. Early Mesozoic time (Late Triassic-Early Jurassic) was characterized by the onset of arc magmatism and crustal imbrication, though phases of extension and ignimbrite eruption indicate the tectonic evolution during this period was complex. Strike-slip motion was partitioned onto intra-arc structures, which possibly utilised the initial plate transform boundary, and multiple, concurrent subduction zones may have been active. Marine conditions dominate the sedimentary record throughout the Sierra Nevada region until the Late Jurassic Nevadan orogeny caused crustal thickening and uplift.

During the Cretaceous, voluminous batholithic magmas were emplaced. Magmatism migrated eastward in time, with subduction zone-derived magmas emplaced in the west, and increasingly more crustal-derived components emplaced towards the east. The axial portion of the batholith, where conditions were hottest, was the locus of steeply oriented, discrete zones of ductile shearing. The majority of the rocks of the central Sierra Nevada were emplaced in the Late Cretaceous (Evernden and Kistler, 1970), in the eastern part of the batholith, and the Rosy Finch shear zone may represent a portion of the axial shear system active at the time (cf. Tikoff and de Saint Blanquat, 1997).

By the end of the Cretaceous, magmatism had ceased to be active and cooling of the crustal column as well as equilibration of an eclogite facies mafic root probably caused thermal subsidence. Recent seismic refraction studies indicate that the root to the batholith has been lost (Wernicke *et al.*, 1996). Upper mantle xenoliths entrained in Cenozoic volcanic rocks suggest that the eclogite root was replaced by mantle asthenosphere some time around 3 to 8Ma (Ducea and Saleeby, 1998; Ducea and Saleeby, 1996; Manley *et al.*, 2000). This may have occurred in response to regional extension in the lower lithosphere caused by the neotectonic motion of the Pacific plate, and has led to renewed a buoyancy effect causing range uplift and tilting, resulting in an asymmetric transverse topographic profile, and rapid incision by the major transverse streams (Jones *et al.*, 2004).

Additionally unroofing of up to approximately 15km of sediment from the batholith since the cessation of magmatism is likely to have also driven renewed uplift of the modern mountain range.

Specific geobarometric and geochronologic data that provide a basis for interpreting the timing and depth of faulting, and exhumation history of the study areas are discussed in Chapters 5 and 6.

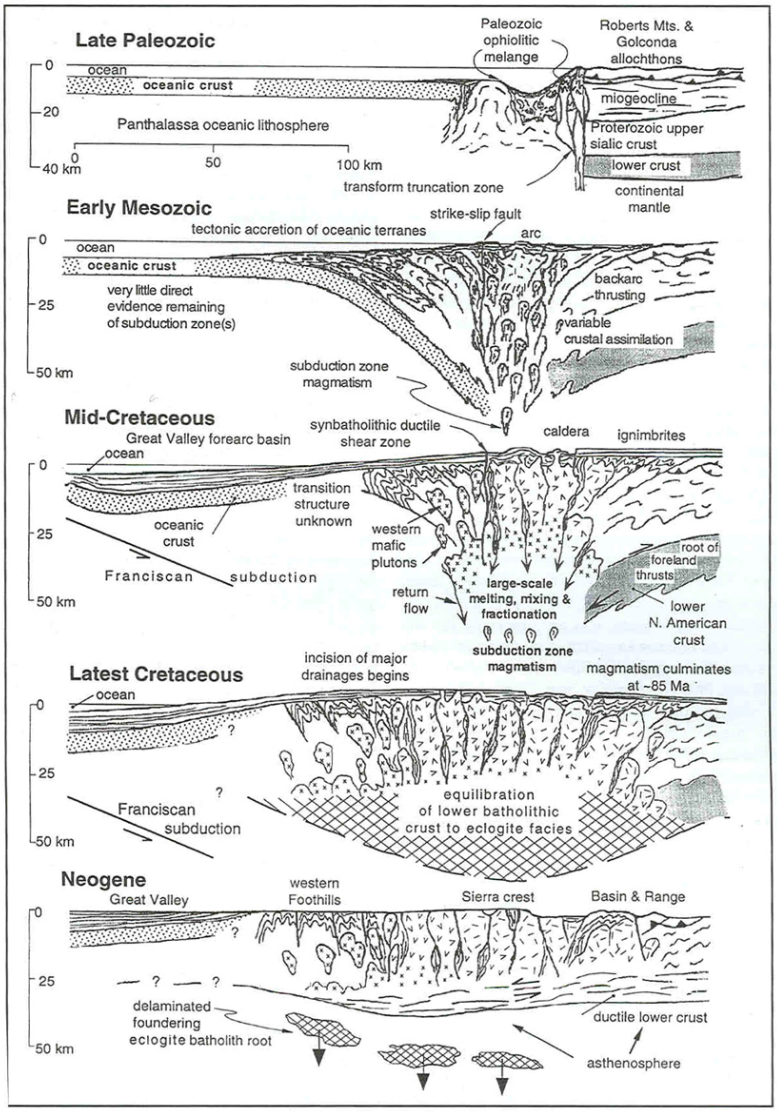

Figure 6. Generalized model describing the tectonic evolution of the Sierra Nevada batholith. For discussion, see text (from Saleeby, 1999).

2.3 Overview of the Granite Pass area

The area was first described by Moore (1978) during regional geologic mapping at 1:62 500 scale in the Sierra Nevada conducted by the USGS. Moore (1978) defined the lithologic units in the study area, which are primarily granites and granodiorites with

occasional tuffs and mafic plutonic rocks (diorites, tonalites, hornblende gabbros), and used cross-cutting relations to determine the relative ages of the units (Figure 7). The majority of the structures described in this study are within the Pyramid pluton, a dark granodiorite with some granite, quartz monzo-diorite and quartz diorite. Moore also described two systems of nearly vertical joints and cracks, one trending N70ºE and one trending approximately north-south, that formed after the plutons cooled to temperatures at which they were largely brittle. Joints of the more prominent N70ºE system are described as 'consistently showing a small amount of left-lateral shear', and as being mineralised with quartz and epidote.

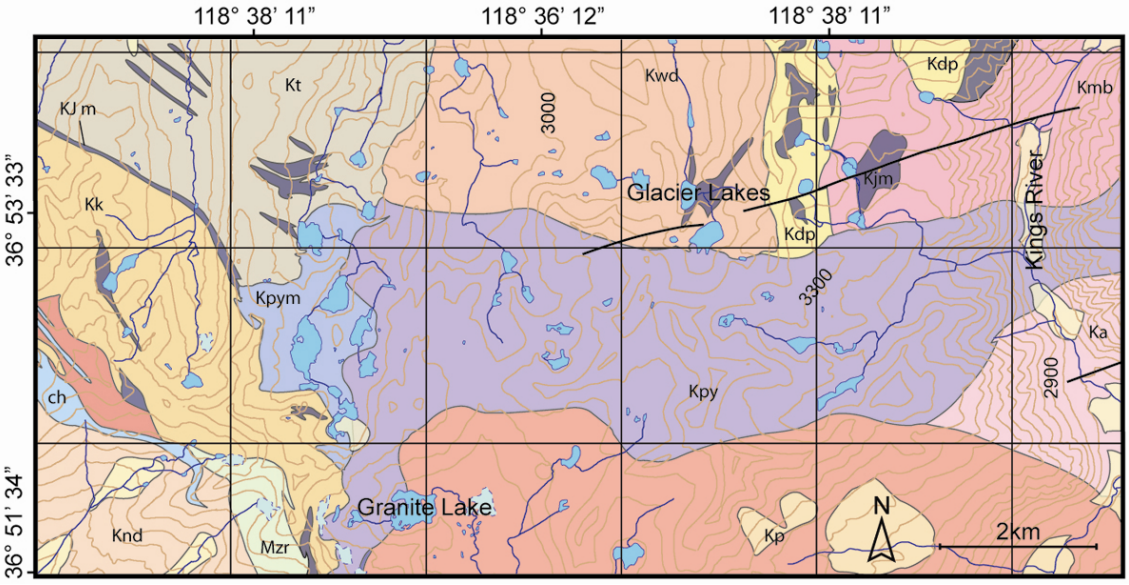

Figure 7. Geologic map of the study area showing lithologic units present and geologic structures, digitized from Moore (1978). Kjm = mafic plutonic rocks, Kt = granite of Tehipite Dome, Kwd = granodiorite of White Divide, Kdp = granite of Dougherty Peak, Kmb = granodiorite of Muro Blanco, Ka = Arrow pluton, Kp = Paradise pluton, Kpy = Pyramid pluton, Kpym = Pyramid pluton western mafic facies, Mzr = Metarhyolite tuff, Knd = granodiorite of North Dome, ch = calc-hornfels, Kk = Kennedy Lakes pluton, black lines are faults.

Evans *et al.* (2000) used air-photo analysis and fieldwork to define a series of geologic structures within the study area (Figure 8). Their work identified two principal faults, the Glacier Lakes fault (the northern fault described by Moore (1978), see Figure 7) and the Granite Pass fault, together with a series of splay faults emanating from the Glacier Lakes fault and striking 20-40º to the trace of the main fault in a counter-clockwise orientation. The Glacier Lakes fault was identified as a nearly pure left-lateral strike-slip fault with ~55m of slip at its western end (see Figure 8). The map pattern of the splay faults was therefore interpreted as a left-stepping zone of horsetail structures that formed at the termination of the Glacier Lakes fault in a similar way to splay fractures around small faults observed in the Sierra Nevada (e.g. Lim, 1998). Evans *et al.* (2000) rejected the possibility that the splays formed part of a stepover between two coeval faults (i.e. the

Glacier Lakes and Granite Pass faults) based on petrologic and structural observations, and speculated that the Glacier Lakes fault may terminate because of the presence of the Granite Pass fault.

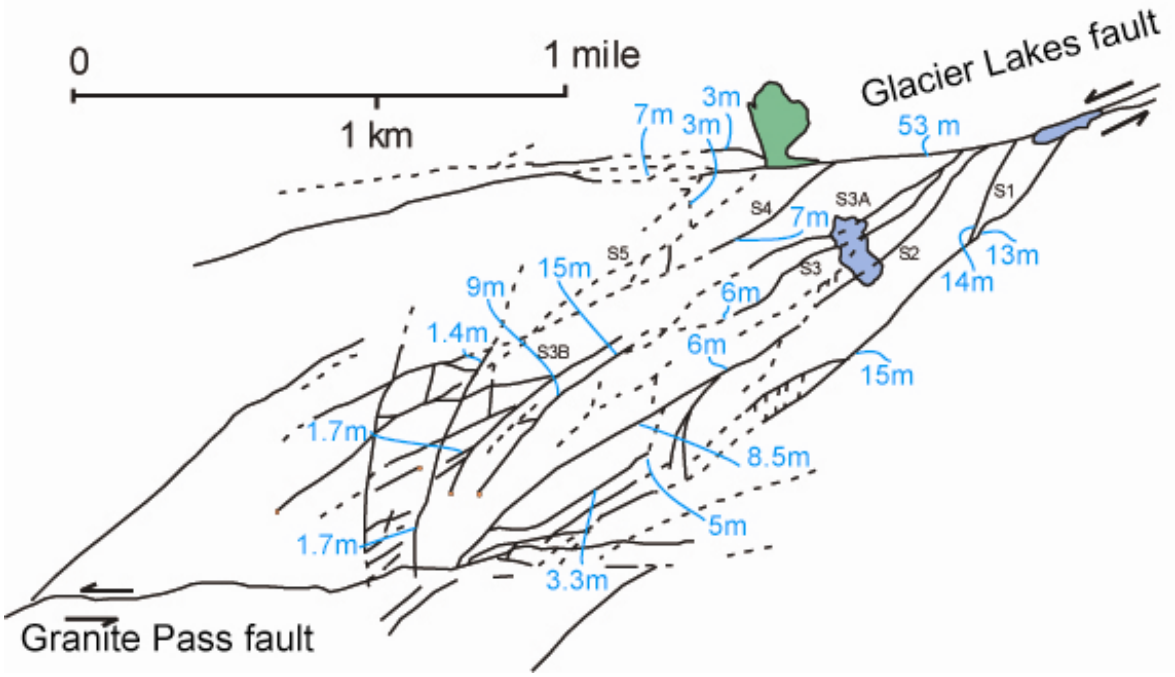

Figure 8. Simplified map of the Glacier Lakes fault, Granite Pass fault and splay faults in the Granite Pass area of Kings Canyon National Park, California (from Evans *et al.*, 2000). Green areas are meadows, and blue seasonal lakes that are prominent in air photos. Circles at the ends of fault traces imply the trace terminates, magnitudes of slip are given in metres. The splay faults (S_x) are labelled after Evans *et al.* (2000).

The western termination of the Glacier Lakes fault was studied in detail by Evans *et al.* (2000), who showed that slip on the Glacier Lakes fault decreases markedly beyond the splay faults to the west. The amount of slip on individual splay faults is variable, but the cumulative slip across all of the splay faults shows a smooth triangular profile (Figure 9). Evans *et al.* (2000) pointed out that the cumulative slip profile for the splays is similar to slip profiles observed for single faults, and suggested that this similarity was brought about over time as slip was systematically bled-off the main Glacier Lakes fault onto the system of splays. Slip vector rakes measured for the Glacier Lakes fault and the splays show a degree of variability, but the main fault rakes are mostly close to strike-slip, whereas the splay faults are generally more oblique (Figure 10). Other than the splay faults, Evans *et al.* (2000) concluded that the Glacier Lakes fault displayed little evidence for the presence of a damage zone that might represent the wake of a 'palaeo-process zone'.

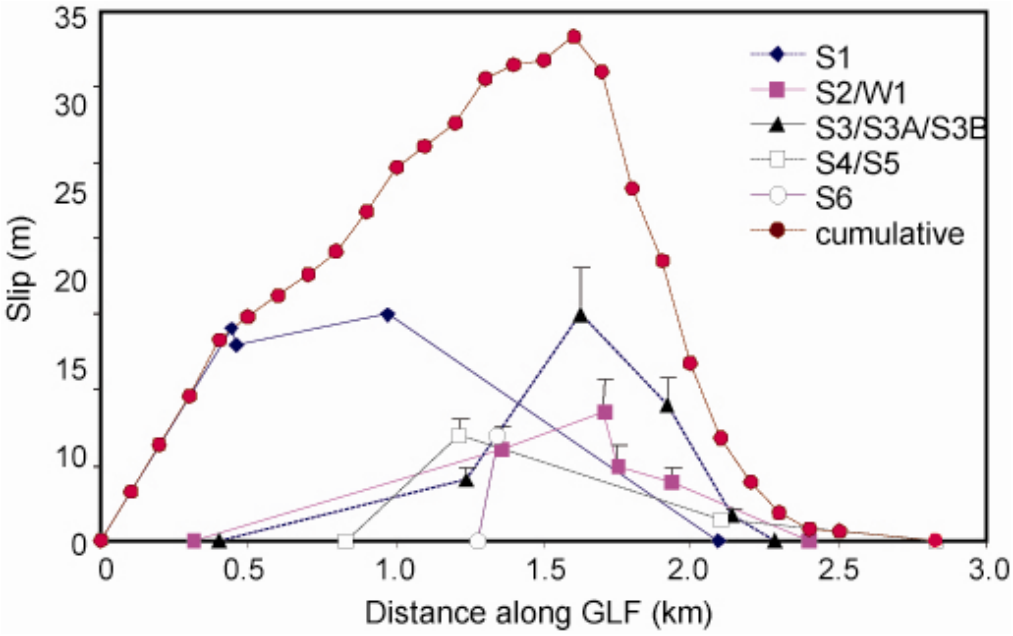

Figure 9. Slip profiles measured for individual splay faults (labelled in Figure 8) and a cumulative profile constructed parallel to the trend of the GLF. Error bars are an estimate of slip where no measurements are available. From Evans *et al.* (2000) .

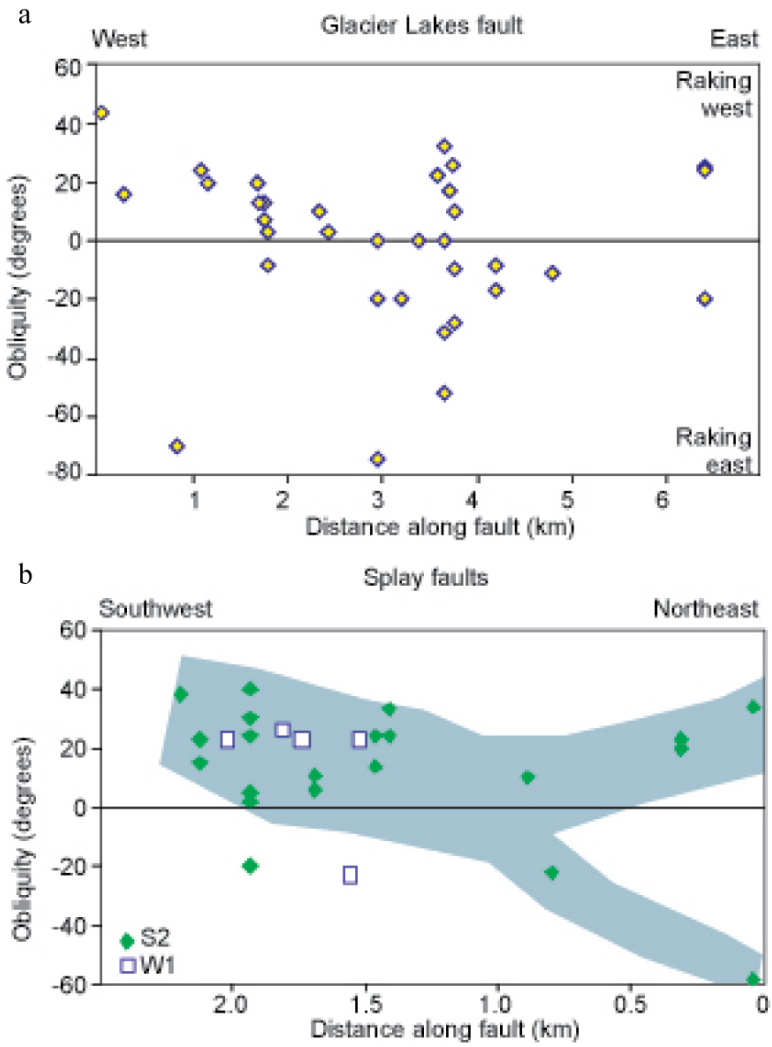

Figure 10. Slip vector rakes for a. the main trace of the Glacier Lakes fault, and b. splay faults S_2 and W_1, as labelled in Figure 8 (both from Evans *et al.*, 2000).

2.4 Overview of the Mount Abbot Quadrangle

The Mount Abbot Quadrangle was mapped at 1:62 500 scale by Lockwood and Lydon (1975) as part of the same regional geologic mapping campaign as Moore (1978). The quadrangle contains numerous elongate, NW-striking plutons, predominantly of Cretaceous age (Stern *et al.*, 1981). Pluton contacts are steeply dipping, and the relative sequence of emplacement is complex. Late stage aplite dykes cut through plutons and across pluton contacts. This study focuses on the Bear Creek drainage area. All of the field observations are from faults in the granodiorite of Lake Edison, a fine- to medium-grained biotite-hornblende granodiorite (Lockwood and Lydon, 1975). Fractures including dykes, joints, and small faults are ubiquitous throughout the pluton.

Numerous previous studies have focused on joints and faults in the Mount Abbot Quadrangle. Segall and Pollard (1983a) analysed the lengths and spacing of joints and derived a method for estimating the magnitude of tensile stress required for joint initiation and growth. Segall and Pollard (1983b) showed that small faults in the area had nucleated on the pre-existing cooling joints by comparing the geometry and mineral assemblage characteristics of joints and faults. Martel *et al.* (1988) analysed the geometry of oblique opening mode fractures observed to develop near the ends of small faults, and showed that these structures link small faults end to end and side to side. This insight prompted Martel (1990) to develop a model to describe the evolution of large (up to ten or more kilometres long with hundreds of metres displacement) faults from the population of cooling joints. He termed large faults compound fault zones. The model proposed by Martel (1990) will be referred to in this study as the fracture linkage model (FLM). Pachell and Evans (2002) conducted fieldwork and thin section analysis of a fault of comparable scale to compound fault zones, the Gemini fault zone, and concluded that the Gemini fault zone likely developed by linkage of structures derived from the local population of cooling joints.

Many other studies have arisen from the Mount Abbot Quadrangle exposures, including analyses of mylonitic fabrics developed at contractional jogs in small faults (Burgmann and Pollard, 1992; Burgmann and Pollard, 1994), nucleation of shear zones on aplite dykes (Christiansen and Pollard, 1997), combined mechanical modelling and detailed mapping of small faults and secondary fractures (Martel and Boger, 1998), and combined kilometre-scale mapping and mechanical analyses (d'Alessio and Martel, 2004). These studies are introduced and discussed in more detail in Chapter 5.

3

Field Mapping of Fault Zone Architectures

3.1 Introduction

Field investigations of exhumed faults provide significantly more detailed descriptions of fault geometry, composition and kinematics than is possible by analysing faults active at depth with geophysical techniques. Defining these parameters is critical to a number of aspects of fault behaviour. Investigations into earthquake rupture processes require information about the thickness of the coseismic slipping zone (Rice, 2006), the composition and permeability of fault rocks (Wibberley and Shimamoto, 2005), and the amount of fault-related damage that comprises a fault zone (Chester *et al.*, 2005). Faults are known to influence fluid flow through the crust as fault zones provide contrasting permeability properties to their host rocks (e.g. Rowland and Sibson, 2004). Fault-hosted fluids may also control to an extent the deformation processes that operate during slip events (Brodsky and Kanamori, 2001) and change fault rock composition and rheology (Jefferies *et al.*, 2006).

Previous work in the Granite Pass study area defined two strike-slip faults on the order of kilometres long, and suggested that these faults had been exhumed from seismogenic depths (Evans *et al.*, 2000). Fieldwork undertaken as part of this study used the preliminary work of Evans *et al.* (2000) as a basis for investigating several aspects of faults that developed at the depths that earthquakes are observed to nucleate. A key aspect to the investigation is to establish the relationship between the Glacier Lakes and Granite Pass faults described by Evans *et al.* (2000) to determine whether the Glacier Lakes fault terminates in the study area, or whether the splay faults between the two faults represent a stepover between two coeval faults. Few studies have described the architecture of strike slip faults with trace lengths of several to tens of kilometres (Pachell and Evans, 2002). The two structures of this scale in the Granite Pass area appear to be distinguished by different fault rocks (mylonites and ultracataclasites for the Granite Pass fault, and

cataclasites for the Glacier Lakes fault) and provide an opportunity to document the architecture of the faults, and contrast their inferred deformation histories. In particular describing the arrangement of the fault core, damage zone and slip surface components will constrain many of the fault properties pertinent to earthquake rupture processes and fluid flow characteristics.

This chapter aims to define the structural units present in the Granite Pass study area at the kilometre-scale. Field data will be used to define a new system of faults and to assess the relationships between the different faults. Outcrop-scale observations provide detail of the internal architecture of the faults, and will be used to constrain the geometry and composition of the faults by defining fault cores, slip surfaces and damage zones following the terminology of Caine *et al.* (1996). The Glacier Lakes fault and the Granite Pass fault will be compared to show whether their observed cross-cutting relations are also reflected in the style of faulting.

3.2 Methodology

The study area is part of ortho-rectified air photos of the geologic quadrangles Slide Bluffs (SE), Marion Peak (SW and SE), Cedar Grove (NE), and The Sphinx (NE and NW), as well as an older series of non-rectified photos of the same regions, all of which are available from the USGS. Air-photo analysis was conducted prior to the period of fieldwork to examine the accuracy of the published maps of the area (Evans et al., 2000; Moore, 1978), and to define key localities in the area where the relations between structures present could be examined. Topographic base maps of the study area were produced in Glasgow from DEM data at 1/3 arc second resolution with an accuracy of 10m acquired from the National Elevation Dataset, available via the USGS Seamless Data Distribution service. Additional data describing the hydrologic features of the study area were downloaded from the USGS National Hydrography Dataset. The ARC GIS software package was then used to combine both geo-referenced datasets, and to produce contours of the land surface, label the horizontal datum with both UTM and latitude-longitude coordinate systems (derived from the NAD83 geo-reference information attached to the DEM data) and export maps at a variety of scales.

Fieldwork primarily involved mapping the geologic structures in the study area at kilometre-scale and collecting data to define fault zone architecture at outcrop-scale. Mapping was accomplished by tracing structures along strike from outcrop to outcrop, recording each successive location at which the feature of interest was exposed with a

hand-held GPS device, which utilised the UTM coordinate system. Satellite coverage of the area resulted in an accuracy of ±5m for the GPS-recorded positions. This method was also used to ortho-rectify the maps of Evans *et al.* (2000), which were published without a reference frame (see Figure 8). Orientation data were collected and recorded wherever structures were suitably exposed using a compass-clinometer. Measurements used the left hand rule convention, and all data reported in this study follow the same convention. Structural orientation data collected in the field have been analysed using StereoNett version 2.46 (Duyster, 2000), and the method of Fisher (1953) has been used to characterize the statistical properties of a population of vector data (see Appendix 3 for detailed explanation of the statistical analyses). Total slip at a given point is calculated by using offset pluton boundaries and aplite dykes. Where exposed, the intersection of two dykes was used to define a piercing point to directly measure the total displacement. Offset pluton boundaries and single dykes could also be used to define the displacement where slip vectors were measured from slickenlines on exposed slip surfaces.

Exposures in the Granite Pass study area are typically ice-scoured granite pavements or small (less than around ten metres) steep exposures in grassy slopes. The area is at high elevation (around 3000m) and is snow-covered during the winter. The resulting vegetation is dominated by grassy areas, as well as trees in stream gullies and at lower elevations (<3000m). Exposures suitable for studying fault rocks are therefore limited in extent, and are spaced infrequently; regions in between useful outcrops are not exposed at all due to vegetation cover. The structural analysis undertaken in this study is therefore necessarily restricted to the extent of natural outcrops, and the results presented in this chapter may be subject to bias imposed by the distribution of well-exposed rocks.

Outcrop-scale maps of fault zones were produced using a baseline mapping technique. Once the area of interest within an exposure was identified, a reference line was placed over the outcrop by fixing a measuring tape across the outcrop. The orientation of the tape and the orientation of the surface exposure being mapped were measured so that the data collected during the mapping would be spatially oriented. A 1m square transect was constructed from a wooden frame with strings cutting the frame every 20cm dividing the metre square into 25 smaller squares (Figure 11). The metre square was placed with one edge aligned with the reference tape and a copy of the structures within each of the small squares defined by the string was made onto squared paper at an appropriate scale by measuring line lengths within the 20cm squares with a ruler. The metre square would then be moved along the reference tape to the adjacent metre and the structures again mapped.

Once the structures either side of the reference line had been completed, the tape used as a reference line was moved laterally by 2m, keeping the new reference line parallel to the original. In this way, maps of outcrops covering areas up to around 300m^2 at scales of up to 1:20 were formed with estimated accuracies of ±2cm associated with spatial measurements.

Figure 11. Photograph showing the construction of a baseline map using a reference line (tape), and a 1m square transect.

The spatial distribution of structures within fault zones was also analysed by utilising one-dimensional transects across entire fault zones. 1D transects quantify parameters such as fault zone thickness and fracture density within faults, and are relatively quick to produce in comparison to maps. Transect sites were selected where the exposure of the fault zone was generally good over a large cross-strike distance, though total exposure of large fault zones was never found. The transects were constructed by placing a measuring tape approximately perpendicular to the trend of a fault zone, though local relief dictated the amount of plunge of the tape. A zero point for each transect was established within the fault zone and the occurrence of structures recorded where they intersected the tape in both directions defined by the tape azimuth. Parameters collected to describe each structure include the type of structure, the orientation, thickness, amount of offset, fill composition, alteration and/or mineralization products present, whether any intersections with other structures were observed and whether any ductile fabrics were developed in association with the structures. Transects finished either where exposures ended or where the frequency of structures had obviously decayed to the background level defined by the frequency of cooling joints away from fault zones (measured separately), or to zero.

A similar method was used to produce structural logs taken through fault zones, in which the orientation and composition of the various fault zone components were described in detail and the relation between the different components represented. A tape was placed across an exposure of a fault zone and its orientation measured. Logs were then constructed onto squared paper to allow thicknesses of different fault zone components to be represented. Structural logs were produced where excellent exposure allowed detailed analysis of a portion of a fault zone, but exposures were always limited in extent so that structural logs likely do not sample the entire fault zone. Sites at which structural logs were constructed for a particular fault zone were selected solely on the occurrence of good exposure allowing a significant number of fault zone components to be studied.

Sampling the variety of deformation products present within the field area was essential to allow subsequent microscope and Scanning Electron Microscope (SEM) analysis (see Chapter 4). Oriented samples were collected using a rock chisel and 5lb hammer and then wrapped with tape to prevent damage during transport back to Glasgow. Permission to use a hand-held coring device was requested from the National Park Service but use of any mechanical device is strictly prohibited due to the noise pollution generated. Sampling sites were therefore selected according to whether or not collecting a sample was possible; joints or other fractures in the rock face were a necessary pre-requisite to enable a piece of rock to be extracted. Sampling was further moderated by the remoteness of the study area as all samples were either manually carried out of the field area or packed out by mule along with the field equipment. The cumulative weight of samples that could be transported was therefore a limiting factor.

3.3 Identification criteria for fault zone components

Caine *et al.* (1996) demonstrate that the fault rocks that comprise the different components of the conceptual model of fault zone architecture vary greatly between different geologic settings. Delimiting the components in the field therefore requires the deformation elements that comprise the fault zone components to be identified. This section outlines the manner in which the fault cores, slip surfaces and damage zones of faults in the study area have been defined.

Within a fault zone, one or more fault cores accommodate most of the displacement (Caine *et al.*, 1996). In the study area, the distribution of displacement across a fault zone can rarely be established as displacement indicators are uncommon. Slip magnitude is often high so correlating dyke fragments across a fault zone can be problematic. The

identification of fault core material is therefore most often based upon the presence of the products of the deformation processes that act to accommodate displacement. Brittle cataclasis results in random-fabric breccias and cataclasites, and ductile shear produces foliated mylonites (Sibson, 1977). Where these fault rocks are present a high magnitude of deformation can be inferred and the geometry of a fault core defined by the distribution of the fault rock.

Slip surfaces are commonly intricately associated with fault cores (e.g. Chester and Logan, 1986). A slip surface is frequently a zone of some finite thickness containing intensely strained rock across which relative displacement occurs, rather than a 2D plane (e.g. Sibson, 2003; see section 1.2 for a discussion). According to this definition, a slip surface and fault cores may be indistinguishable, for example if a fault is composed of only one PSZ then the slip surface could also be considered a fault core. However, within a fault zone it is generally apparent that localised slip surfaces can be identified within, at the edge or away from fault cores. It is essential to the understanding of slip mechanisms that the coseismic slipping zone thickness be delimited as best as possible (e.g. Rice and Cocco, 2007), and so where distinct slip surfaces can be identified within fault zones in the study area, their properties have been measured.

Defining slip surfaces in the field is problematic in the study area due to the scarcity of displacement indicators in the granitic lithology. However, it is possible to infer relative displacement across distinct slip surfaces from a number of lines of evidence. Fault-related pseudotachylytes are the cooled remnants of melt generated along a sliding interface due to frictional heating during a slip event (Shand, 1916; Sibson, 1975). Pseudotachylyte generation surfaces (the coseismic slipping zone) thus represent surfaces across which slip events have occurred. Slickenlines, striations and corrugations present on exposed fracture surfaces are commonly used as indicators of relative displacement occurring across the fracture surface (e.g. Doblas, 1998). Previous investigations of faults in crystalline rocks have identified narrow bands of extremely comminuted cataclasite as zones across which slip has been accommodated (Chester and Chester, 1998; Shipton *et al.*, 2006). Such slip surfaces are most obvious in thin section, but are observed in the study area where displacement indicators are present as narrow (most often millimetres in thickness) seams of highly comminuted cataclasite or ultracataclasite.

Damage zones are defined as the volume of rock surrounding a fault core containing fault-related subsidiary structures (Chester and Logan, 1986). Delimiting a fault damage zone

therefore requires identification of the types of subsidiary structures that are developed about a fault, and the extent to which they occur. Cooling joints are an inherent feature of the host rock plutons in the study area (Moore, 1978), and these structures are present in the host rock regardless of whether a fault zone is nearby or not. Extra attention is therefore required to distinguish fault-related structures from cooling joints in the analysis of fault damage zones in this study. Previous workers have defined the damage zone as the volume of rock in which the frequency of structures is elevated compared to where no faults are present (Schulz and Evans, 2000; Wilson *et al.*, 2003). A similar approach is adopted in this study whereby a 'background' level of deformation is defined by using 1D transects to measure the frequency of cooling joints away from faults, and interpreting elevated frequencies of subsidiary structures around faults as damage zones.

3.4 Kilometre-scale structural analysis

This section will present an overview of the geologic structures in the study area at the kilometre-scale (see Appendix 1). The structures are grouped based on the results of previous work in the area (Evans *et al.*, 2000) to facilitate description of the data; regional cooling joints, the Granite Pass fault (GPF), Glacier Lakes fault (GLF) and a series of faults newly identified during fieldwork will all be described separately. Locality numbers referred to in the text are from the numbering system used in the field. Appendix 2 contains a list of localities with grid references, and all localities are shown in Appendix 1. The genetic significance of the groups of structures will be addressed in the discussion section of this chapter.

3.4.1 Regional cooling joints and reactivated joints

Cooling joints are an inherent feature of the plutonic rocks in the Sierra Nevada (Figure 12a). Cooling joints are here defined as mode I fractures, and reactivated joints as fractures that are parallel to joints, with the same geometry and mineral assemblage, but with small (up to tens of centimetres) amounts of shear offset that has deformed of the fracture fill (cf. Segall and Pollard, 1983b). Fractures are rarely exposed for their entire lengths, though traces are observed to be tens to hundreds of metres long. The macro-scale geometry of the fractures is simple; they have straight traces without significant geometrical discontinuities. Orientation data have been collated from 1D transects throughout the study area (Figure 12b). The transects record the properties of cooling joints where the transect continues beyond the limit of fault-related deformation. 136

measurements define a mean cooling joint orientation of 075/75S, with α_{95} = 3.8º. The spherical variance for the population of joint orientations is 0.091.

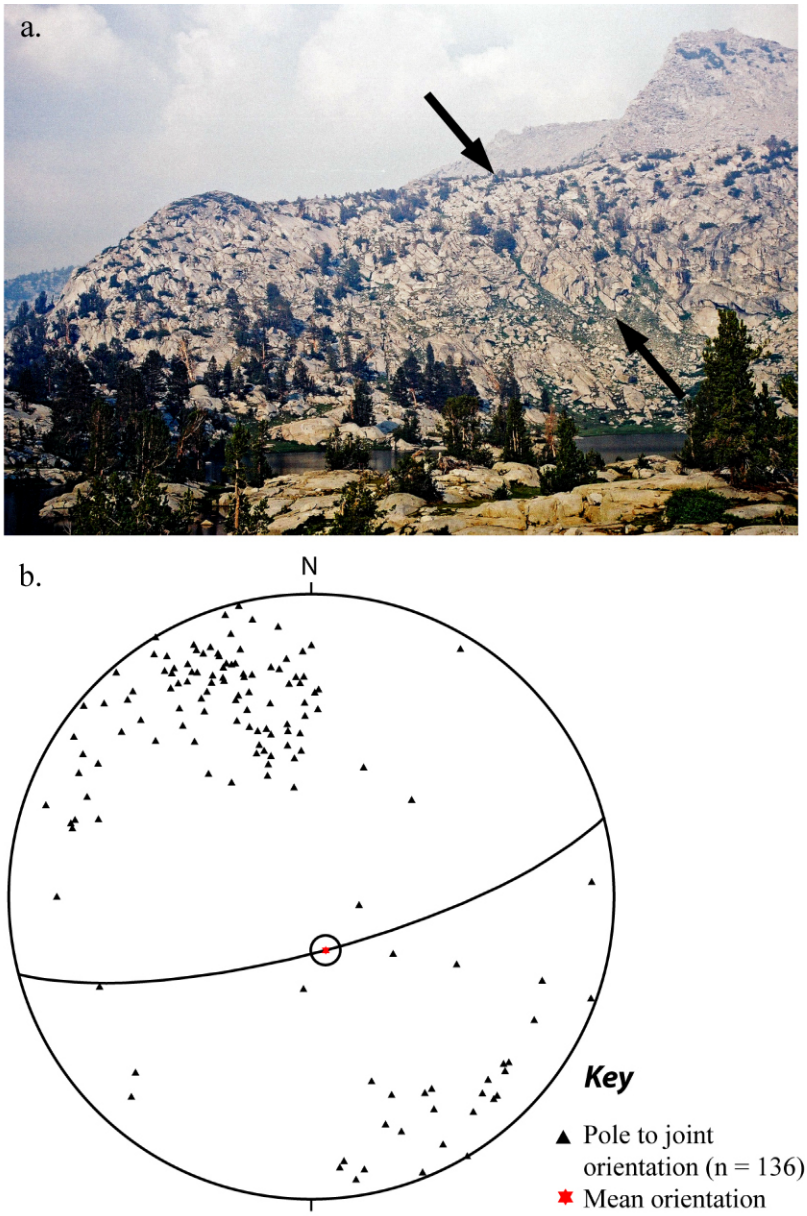

Figure 12. Cooling joints are an inherent feature of the plutonic rocks in the Sierra Nevada. a. Photograph of the cliff to the east of two-fingered lake that contains abundant fractures, typical of the study area rocks, arrow indicates joint orientation. b. Stereonet (equal area, lower hemisphere projection) showing poles to measured cooling joint orientations and a great circle representing the mean orientation. The α_{95} confidence ellipse is shown.

Some of the fractures in the study area are opening-mode fractures (joints), across which there is no shear displacement. These fractures can be recognised where host rock crystals on either side of the fracture can be re-aligned across the fracture aperture. Opening mode fractures are nearly always mineralised with granular epidote and/or chlorite, though sometimes the fractures are too narrow to contain any discernable mineralisation. Fragments of wall rock are often present within fracture traces as sub-angular to sub-

rounded clasts of wall rock minerals that are ≤4mm in length. Fracture traces are generally ≤10mm wide, are straight or slightly wavy on a metre-scale, and are observed to cut individual crystals, as well as following crystal edges in some cases. Individual traces are sometimes comprised of en-echelon segments that form acute angles counter-clockwise when measured from the overall trend of the fracture. En-echelon segments are ≤30mm long, and ≤1mm wide and overstep by tens of millimetres. Fracture traces may change along strike from single traces to en-echelon segments and vice-versa. Joints generally have associated alteration halos ≤70mm in width, in which feldspars are bleached white.

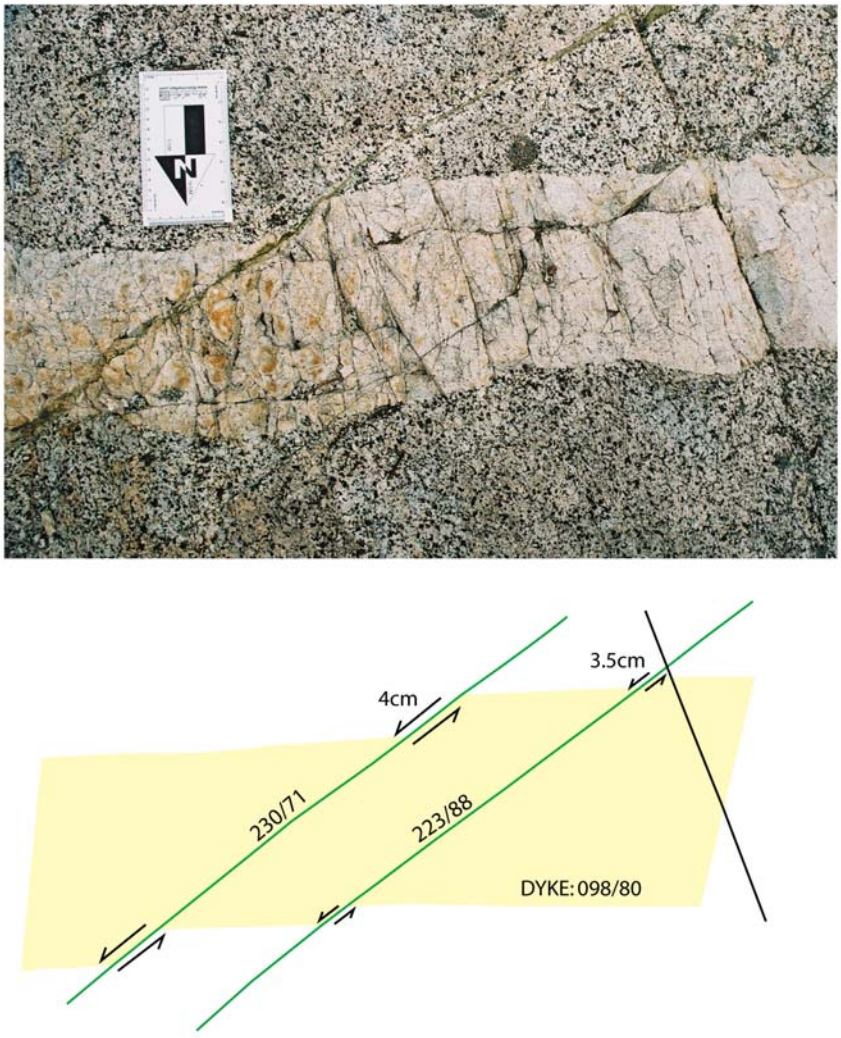

Figure 13. Photograph and interpretive sketch of a pair of small fractures at locality 4 that left-laterally offset an aplite dyke. The sheared fractures are mineralised with epidote and chlorite. A north-south trending, opening mode fracture that is not mineralised is present on the right hand side of the image.

Reactivated joints are fractures that display many of the characteristics of opening mode cooling joints may also display small amounts of shear displacement (Figure 13). The magnitude of shear displacement ranges from centimetres to tens of centimetres, and is nearly always in a left-lateral sense. These shear fractures are up to several centimetres in

width and contain epidote and chlorite mineralisation, as well as abundant clasts of sub-angular to sub-rounded wall rock minerals. Lenses of more clast-rich material are present in some exposures, juxtaposed against epidote or chlorite-rich, clast-poor material. Reactivated joints also frequently contain quartz mineralisation in the form of lenses tens of centimetres long, and up to 25mm wide, containing euhedral quartz crystals up to 5mm in size. Alteration halos accompany reactivated joints in the same way as opening mode fractures, and have similar magnitude thicknesses. Shear displacement is evident at small bends in some fractures, where the fracture aperture is wider due to a releasing-bend morphology. Restraining bends seem to be associated in an increase in the width of the alteration halo accompanying the fracture to 70 to 120mm.

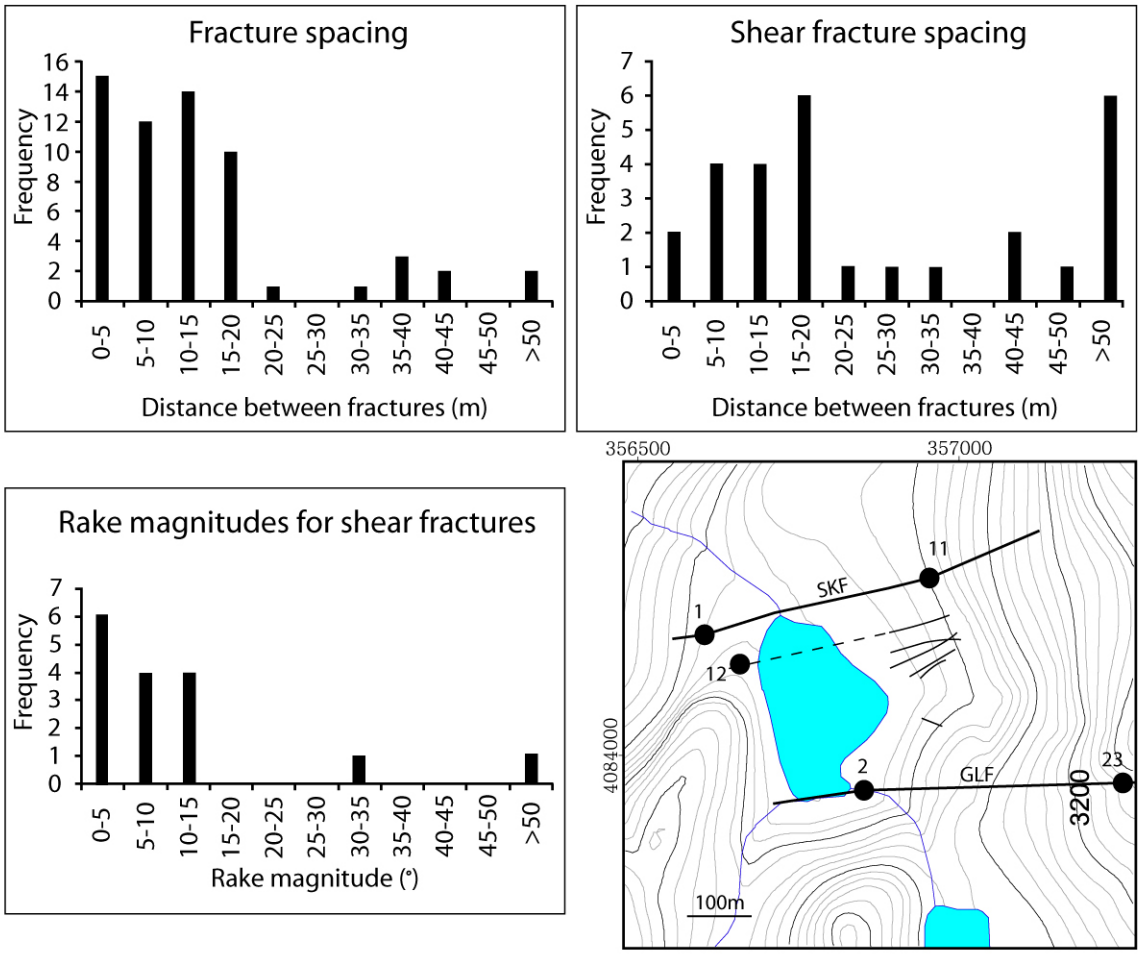

Figure 14. Histograms of fracture spacing (all fracture types), shear fracture spacing, and rake magnitudes for shear fractures sampled during transects between localities 11 and 2, and to the north of locality 17. The map shows shear fractures mapped between localities 2 and 11. SKF and GLF refer to Skeeter fault and the Glacier Lakes fault (see below) and are shown for reference. Blue area (centre) is a seasonal lake that is known as Shortie's Meadow and numbers are locality numbers (see Appendix 1).

Two transects through portions of the area in which no major structures are mapped show that overall fracture spacing (considering both opening mode and shear fractures) is mostly

on the order of 1-20m, and that fractures are rarely spaced further apart than this (Figure 14). However, reactivated joint (shear fracture) spacing shows a higher proportion of fractures that are spaced >20m apart. This is reflected in a map of the area between localities 11 and 2 (Figure 14), which shows shear fractures. One fracture that intersected the transect may be projected along strike across the meadow (blue area in Figure 14), and has a displacement of 1.75m at locality 12.

The 'background' level of deformation in the study area comprises opening mode cooling joints and reactivated joints that have similar geometries to cooling joints, but sheared mineral assemblages. These fractures may be spaced more than 50m apart, but the vast majority are spaced closer than 20m, and many less than 5m apart. Therefore some spatial variation is inherent in the fracture frequency in the background deformation.

3.4.2 The Granite Pass fault (GPF)

The GPF crops out as dark-coloured, deformed rocks that allow the trace of the fault to be accurately mapped. The GPF has a simple macro-scale geometry, with a trace length of ~6.7km that is not interrupted by any stepovers or significant geometrical discontinuities (see Appendix 1). The total fault length remains unconstrained as the terminations of the fault in both the east and the west have not been identified. However, the fault is likely to be at least 8km long. As is evident from the fault trace pattern the fault orientation strikes east-west and dips to the south. Fifty seven measurements of the fault orientation collected in the field define a mean fault plane orientation of 087/64ºS, with α_{95} = 5.9º (Figure 15). A spherical variance of 0.087 indicates a relatively small amount of scatter in the measured orientations. The displacement across the GPF is difficult to establish in the field due to a lack of well exposed piercing points. However, a large mafic inclusion near locality 28 was left-laterally offset by ~80m by the GPF, which represents the maximum observed displacement for the GPF.

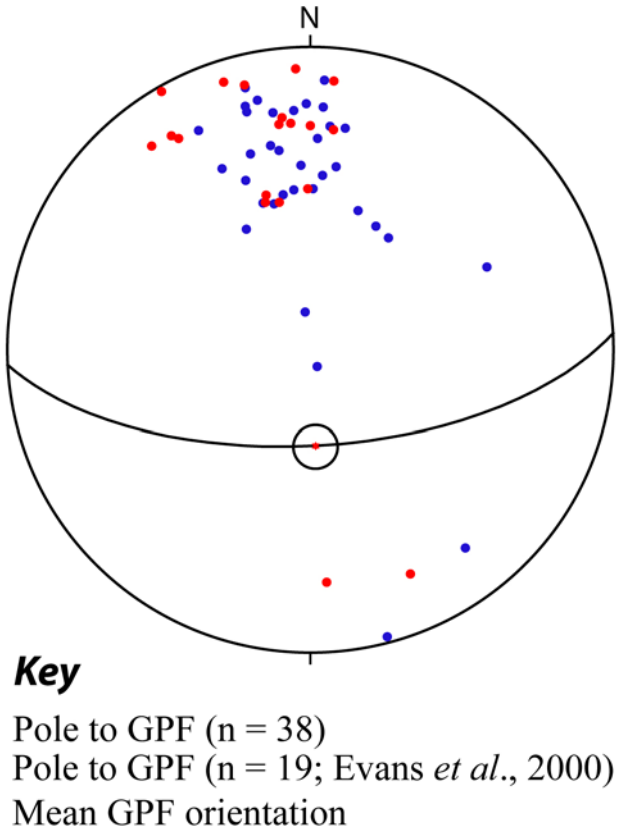

Figure 15. Stereonet (equal area, lower hemisphere projection) showing poles to GPF fault orientations (fault core and slip surfaces) and a great circle representing the mean fault orientation. The mean GPF slip surface orientation (red star) and the α_{95} confidence ellipse are shown.

3.4.3 The Glacier Lakes fault

The GLF frequently forms a prominent gulley in the study area (Figure 16). The GLF has a trace length of 8.2km, though this is a minimum estimate as the eastern termination of the fault was not identified during fieldwork (see Appendix 1). Air-photo reconnaissance suggests that the fault continues further to the east than has been mapped, and is likely to be at least 9.9km long. The mean GLF orientation, as defined by 35 measurements collected in the field, is 086/84ºS with α_{95} = 5.9º (Figure 17). The spherical variance of the sampled GLF orientations is 0.054, indicating that the orientations are tightly clustered. Slip on the GLF (see Figure 9) was measured in a number of places by Evans *et al.* (2000), but reaches a maximum left-lateral displacement of 125m where Moore (1978) mapped an offset pluton boundary to the east of Glacier Lakes (Figure 7).

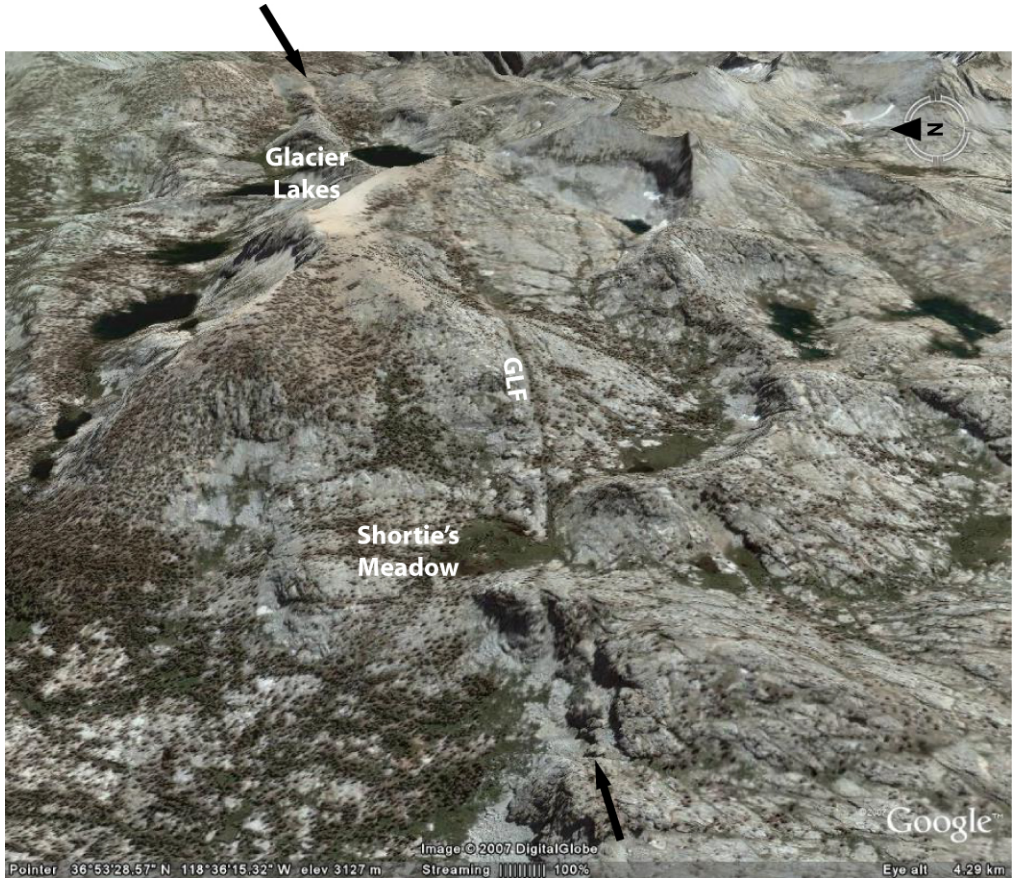

Figure 16. The trace of the GLF forms a prominent gulley in the study area (between arrows). A Panorama of the study area taken from Google Earth emphasizes the outcrop style of the fault (view to the East). No scale bar is shown because the perspective of the view causes foreshortening, but the distance from Shortie's Meadow to Glacier Lakes is around 2.5km (see Appendix 1).

The termination of the GLF in the west is confirmed where the boundary between the Pyramid and adjacent, older Kennedy Lakes plutons (Moore, 1978) is not offset. The GLF terminates at its western end in a series of smaller faults that splay counter-clockwise from the main trace of the GLF in a NE-SW orientation. These splay faults are present in the extensional quadrant for the left-lateral GLF, have lengths of 0.44-3km, and form a zone of secondary faulting ~1.4km wide. The splay faults have a mean orientation of 239/85NW, and form dihedral angles with the GLF ranging from 13-60° with an average of 39° (Figure 17). The compressional quadrant to the north of the GLF does not exhibit any macro-scale deformation structures. All of the splay faults cut and displace dykes with a left-lateral to oblique sense of slip. In five places, the splay faults are observed to cross-cut and displace the GPF (splay faults S_m, S_4, S_2 and S_1 – two strands; see Appendix 1 for labels), indicating that the GPF is an older structure.

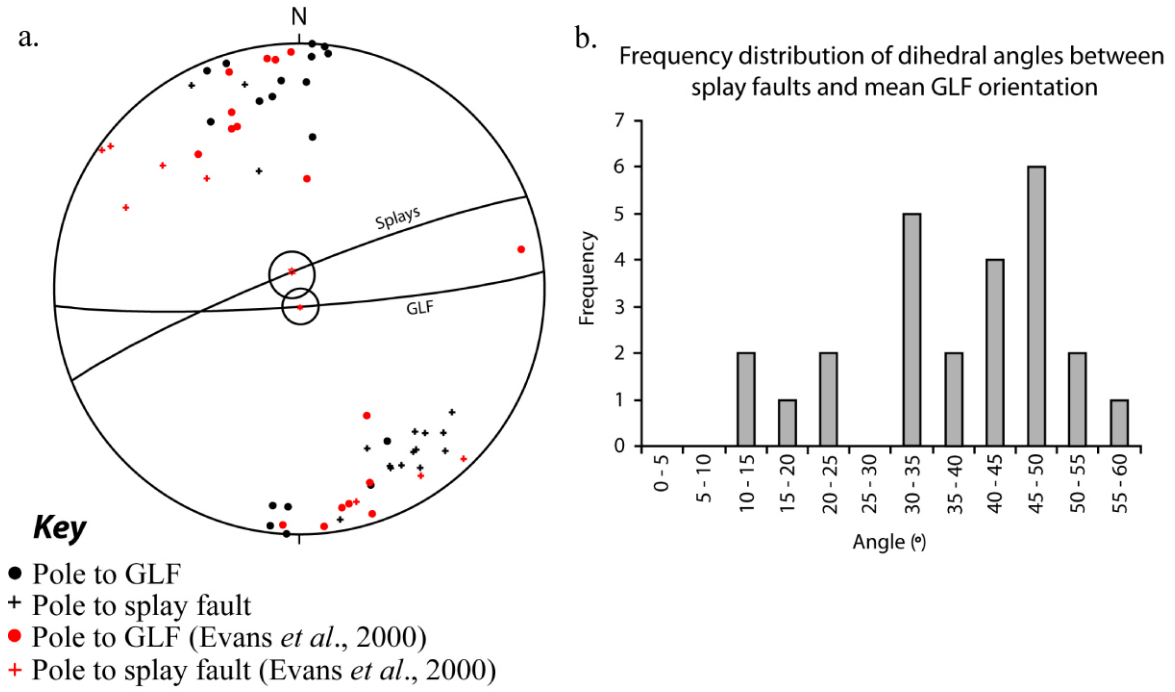

Figure 17. The orientation of the GLF and splay faults. a. Stereonet (equal area, lower hemisphere projection) showing poles to fault orientations and great circles representing mean fault orientations for the GLF and splays. b. Histogram of angles between measured splay fault orientations and the calculated mean of the GLF orientations.

Figure 18. Photograph looking to the west along strike of the southern strand of the GLF in the Glacier Lakes region towards Goat Crest (arrow, see also Appendix 1). The intersection of the two GLF fault strands is not accessible due to the cliff behind Glacier Lakes (below the skyline to the right of Goat Crest in the photo).

The macro-scale geometry of the GLF is complicated in two places by the presence of two adjacent fault strands. The fault located immediately to the south of Glacier Lakes (see Appendix 1) comprises a zone up to around 5m wide of deformed rock that intersects the GLF to the west of the Glacier Lakes. This southern fault trends in a direction close to east-west, whereas the GLF trend changes at the intersection of the two faults to slightly

more towards northeast-southwest in the Glacier Lakes region. Fieldwork and air-photo interpretation suggest that the southern fault in the Glacier Lakes region may be part of the GLF system. However, the nature of the intersection is difficult to establish as the relief at the point of intersection is extreme (Figure 18). The significance of the southern strand also remains unclear as the continuation of the fault to the east was not mapped.

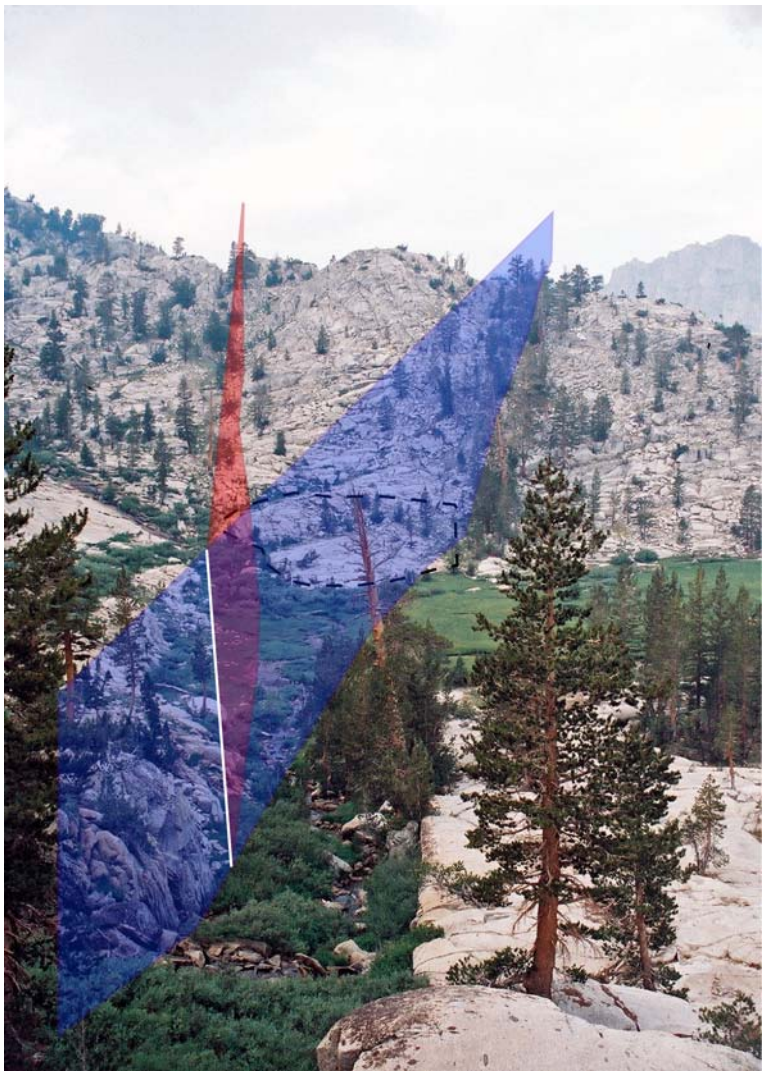

Figure 19. Photograph taken from locality 13 viewed towards the west, with super-imposed GLF fault planes projected above the ground surface showing the two strands of the GLF (the traces form densely vegetated gullies). Dashed area is locality 24 (see Figure 33).

The trace of the GLF splits into two strands near locality 24 (Figure 19, see also Figure 33). Other than the exposure at locality 24, neither of the two GLF strands is well exposed, though both are expressed as characteristic gullies enabling the fault traces to be defined as far west as the ridge near 0356510 4083580 (see Appendix 1). Further to the west than the ridge, the relief becomes very steep, so direct observation of the GLF in this region is impossible. A combination of air-photo interpretation and field reconnaissance suggests

that the two strands coalesce near grid reference 0356000 4085900. The GLF therefore has two sub-parallel strands for ~1km of its trace to the west of locality 24.

3.4.4 Newly-identified faults

Five new faults were identified in the study area (see Appendix 1, Table 1). These faults have similar macro-scale properties and so are described below as a group. The newly identified faults are named Skeeter fault, which is located to the north of the trace of the GLF, Little Lake (LLF), Snowy, Kinobe and Gilley faults, which are located between the GLF and GPF. They are characterized by simple macro-scale geometries, with traces that are not complicated by step-overs or other discontinuities. Mapped trace lengths for the faults range from ~1 to 3.5km, though none of the tips of the faults could be defined in the field so the total lengths remain unconstrained. Displacements were recorded for three of the faults. Two dykes with different orientations defined a piercing point at locality 11 that was left-laterally offset by 21.7m by Skeeter fault. A piercing point was also used to calculate a left-lateral offset of 36m for the LLF near locality 17. An offset dyke at locality 37 showed apparent left-lateral offset of 19.4m for Kinobe fault. Kinobe fault is cross-cut and displaced by ~2m in a left-lateral sense by one of the splay faults from the GLF at locality 34.

Fault	Trace Length (km)	Displacement (m)	Mean Orientation
Skeeter	1.36	21.7	086/76S (n=12)
Little Lake	2.28	36	084/62S (n=11)
Snowy	2.26	?	055/64S (n=5)
Kinobe	3.49	19.4	083/54S (n=10)
Gilley	0.98	?	076/87S (n=1)

Table 1: Summary of the names and properties of the newly identified faults in the study area. Lengths are mapped trace lengths, displacements are all left-lateral and calculated from piercing points, except for Kinobe fault where the displacement is apparent.

All of the new faults have similar trends, which are reflected in the measured orientations of the structures (Figure 20). The faults strike approximately east-west and dip ~50-80º to the south, with the exception of Snowy fault which trends slightly more towards northeast-southwest. However, only five orientations were measured for Snowy fault, so the mean orientation calculated from this small number of data points is not significant. An analysis of the combined orientation data for the newly identified faults shows that the mean orientation for the population is 080/65S, with α_{95} = 6.4º. The spherical variance of the

combined data is 0.071, indicating that there is very little scatter in the measured orientations of the newly identified faults. The mean orientation of the newly identified faults is very similar to the mean of the GPF (087/64S).

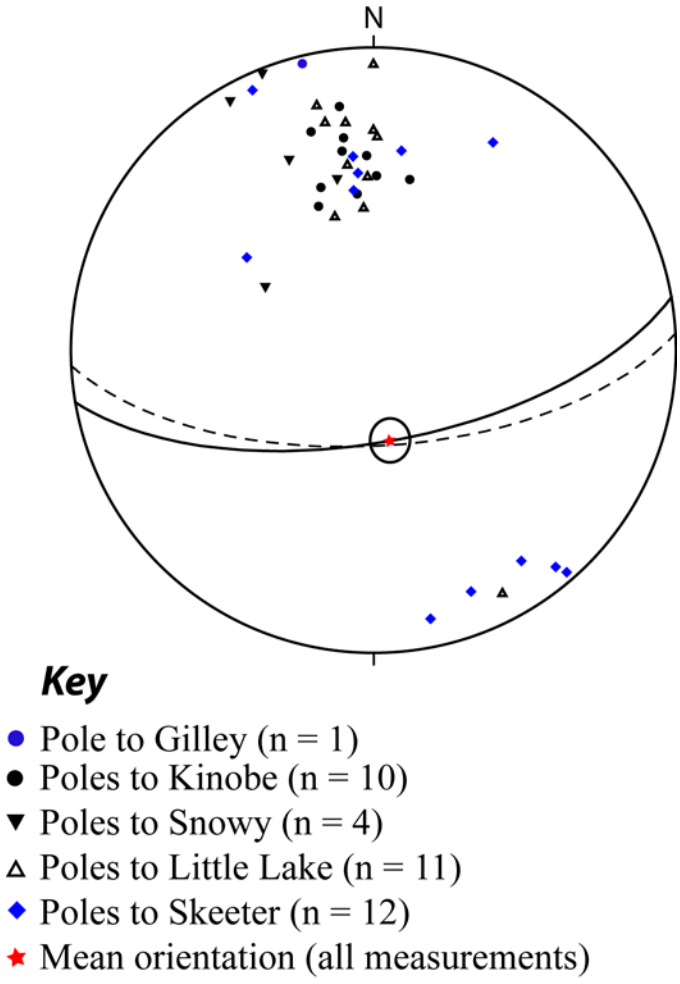

Figure 20. Stereonet (equal area, lower hemisphere projection) showing poles to measured fault orientations for the newly identified faults, and a great circle representing the mean orientation of all of the measurements of the newly identified faults (dashed great circle is the mean GPF orientation for comparison).

3.5 Fault zone architecture

Outcrop-scale field data and hand specimen-scale observations will be used in this section to characterize the fault zone architecture of the two principal structures in the study area, the GPF and the GLF (and splays), as well as the series of newly identified faults. For each of the faults, the overall style of the fault-related deformation will be presented in order to assess the nature of the fault zone architecture, and the fault zone components present within the faults will then be described in turn.

3.5.1 The Granite Pass fault

3.5.1.1 General appearance

The GPF is exposed as outcrops containing dark coloured, deformed rocks that often stand proud with respect to the local landscape. The fault has a complex internal structure evidenced by an extremely changeable appearance between outcrops (Figure 21). The irregularity inherent in the fault zone is expressed as a variable fault zone thickness (measured orthogonal to the fault orientation) that contains inconsistent numbers of fault zone components, which have differing properties between outcrops.

Figure 21. The GPF has a changeable appearance between outcrops. a. The GPF at locality 21 is composed of intensely deformed, but cohesive fault rocks that stand out against the host granodiorite (clipboard for scale is 30cm long). b. The GPF at locality 29 contains fault rocks that are paler in colour and are much more friable.

A series of structural logs taken through exposures of the GPF demonstrate the variable nature of the fault zone (Figure 22). The GPF is composed of up to three fault core strands between and outside of which there are a variety of subsidiary fractures comprising a damage zone. Slip surfaces are difficult to define directly in the field due to the lack of offset markers. However, relative displacement across surfaces or zones can be inferred from a number of lines of evidence (see section 3.3), indicating that multiple slip surfaces are present, and that these have a complex geometry.

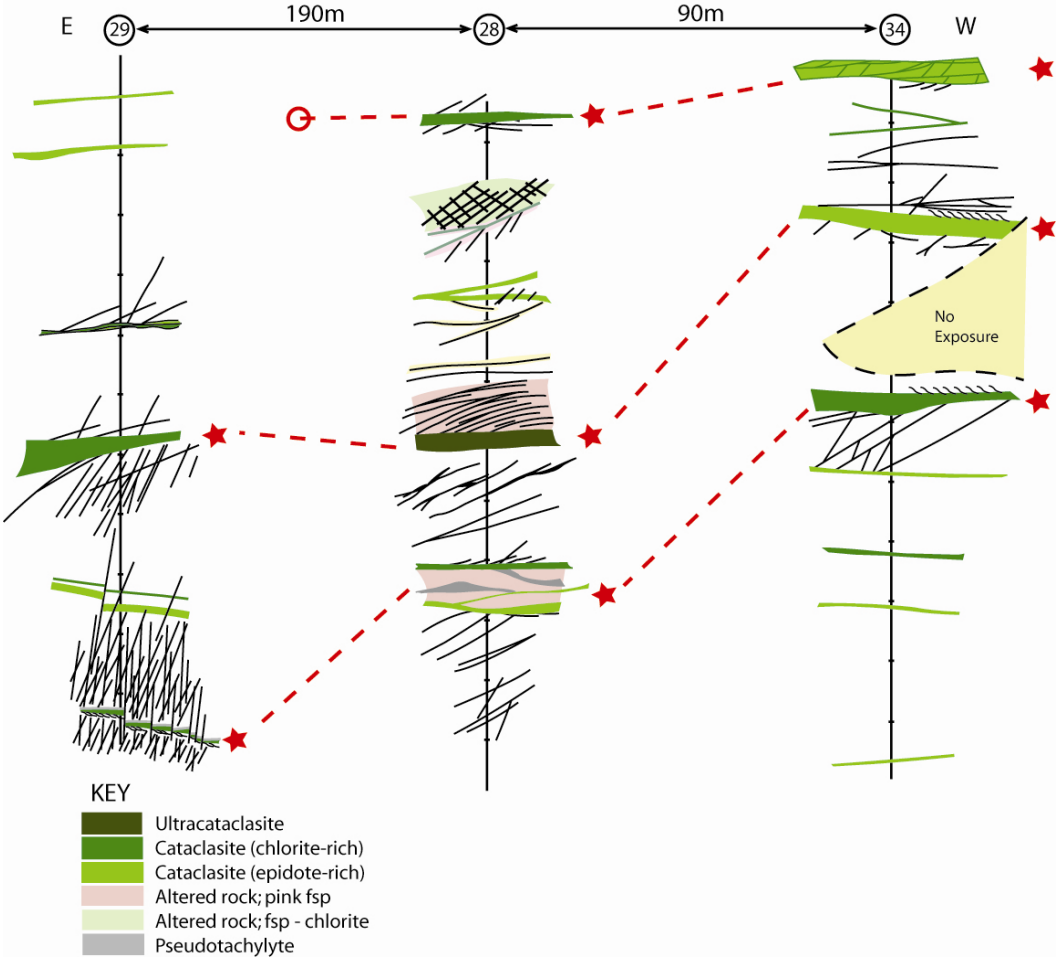

Figure 22. Structural logs taken through the GPF at localities 28, 29 and 34, ticks on vertical axes define intervals of 1m. In each log fault core strands containing cataclasites and ultracataclasites are defined by stars. Fault core strands could be traced along strike so were correlated between logs, but were too poorly exposed to describe in detail. The southern-most strand (top) terminates between localities. Fractures that comprise the damage zone are shown by black lines.

The three logs that comprise Figure 22 are taken from localities (from west to east) 34, 28 and 29 where the GPF is well exposed, though it is unlikely any of the transects have sampled the entire cross-strike width of the fault zone due to the limited extent of the exposures. As the localities are at approximately the same elevation, these distances may be considered as distances along strike of the fault zone. Several significant differences in the GPF architecture can be inferred from the logs; at localities 34 and 28 three fault core strands are present, whereas at locality 29 there are only two, the distances between fault core strands vary along strike, the thickness and composition of the fault core strands change along strike, and the number, distribution and type of subsidiary fractures is different between outcrops. The variation in the number and physical properties of the fault core strands is significant as the strands could be traced through poor exposure between outcrops and be correlated with one and other. The observed changes that have occurred between the outcrops from which the logs were taken therefore reflect genuine

changes in the fault architecture along strike, rather than changes made apparent by differences in exposure.

The structural logs demonstrate that fault zone components within the GPF have a heterogeneous geometrical arrangement. The number, type, and properties of the components that make up the fault zone at any given point can change significantly within 100m distance along strike.

3.5.1.2 Slip surfaces

Pseudotachylytes in the GPF are exposed as narrow (≤10mm), planar surfaces that are metres long and are oriented sub-parallel to the fault zone with infrequent associated high angle veins that are a few centimetres in length. The geometry of the pseudotachylytes correlates well with previously described tectonic pseudotachylytes, and the planar surfaces are interpreted to be generation surfaces with high angle injection veins (e.g. Di Toro and Pennacchioni, 2004; Sibson, 1975). Some narrow veins form a network of interconnected slip surfaces with an overall thickness of around 15mm. All pseudotachylyte veins have sharp edges, are aphanitic, grey to black and display colour banding where thicker. Pseudotachylyte generation surfaces can be traced laterally for several metres, though this distance is most often limited by exposure. At the scale of the exposure, the surfaces have simple geometries; they rarely branch or interconnect. Pseudotachylytes are most often associated with cataclasites, but are also observed to cross-cut mylonites and undeformed host rock. Within the GPF, pseudotachylytes cross-cut fault cores, as well as protolith away from fault cores (Figure 23). Slip surfaces defined by pseudotachylyte generation surfaces are thus distributed throughout the fault zone and are not necessarily associated with fault core strands. The observed pseudotachylytes in the GPF at locality 28 are spaced 2-8m apart.

Slickenlines and striations observed on exposed fracture surfaces within the GPF display rakes that are predominantly strike-slip. Slickenlines are defined by elongate trails of aligned chlorite crystals, which may be oriented approximately parallel to similarly aligned corrugations (up to a centimetre amplitude) in exposed fracture surfaces. Slip surfaces defined by seams of extremely comminuted fault rock are common within the GPF. The comminuted material is composed of extremely fine grained (<<0.5mm) material that is often grey or grey-green, and which contains very few visible clasts. Seams of this material are present in fault core strands within cataclasites and ultracataclasites (see below), and in some cases between juxtaposed fault rock types. Some fault core strands

have slip surfaces at one or both edges that are typically 5-10mm thick, with a maximum observed thickness of 25mm. Slip surfaces located at the edges of fault cores have simple geometries that approximate the fault core strand; they are approximately planar over the distance of exposure. Within cataclasites and ultracataclasites slip surfaces are common and are intrinsically related to the macro-scale shear fabrics present within the fault rocks (see below). Internal slip surfaces to cataclasites and ultracataclasites have complex geometries that frequently inter-connect.

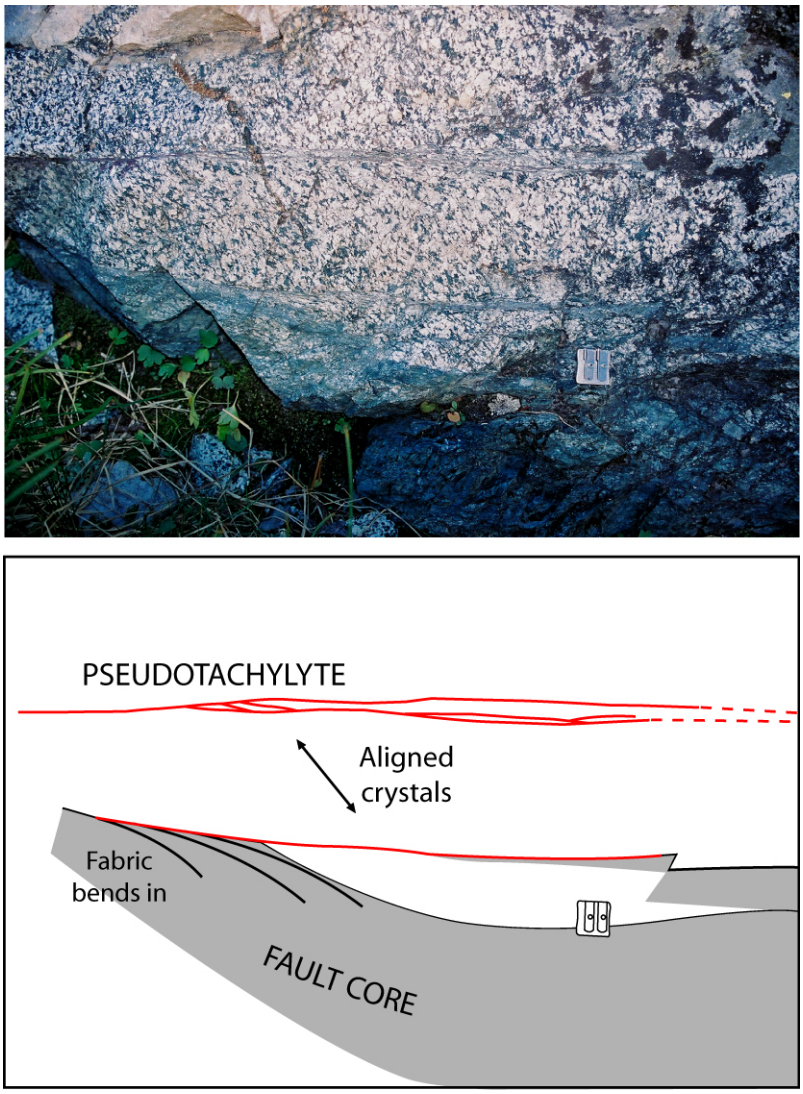

Figure 23. Part of the outcrop containing the GPF at locality 31 showing sub-parallel trending pseudotachylyte veins (red) cross-cutting host rock (top) and at the edge of the fault core which is composed of mylonites and cataclasites (the grey areas are the most intensely deformed fault rocks). A bend-in fabric (see below) is juxtaposed against host rock in which a weak fabric is defined by aligned crystals by the central pseudotachylyte (pencil sharpener for scale is 2.5cm across).

3.5.1.3 Fault core

The GPF contains fault core material in strands oriented sub-parallel to the overall fault zone orientation (Figure 24, also see Figure 22). Fault core strands are continuous along

strike for at least tens of metres, but are discontinuous at the scale of the entire fault zone (i.e. hundreds of metres to kilometres). The strands range in thickness from centimetres to several metres, with order of magnitude thickness variations occurring over lateral distances of tens of metres. Fault core strands are generally non-planar in plan view, often having a wavy morphology, and have sharp edges with the adjacent rock. In some cases, fault core strands are asymmetric with one side marked by a sharp planar boundary with the host rock (slip surface), and on the other side material grades laterally into less deformed rock within the fault zone. Alteration of the surrounding protolith often, but not ubiquitously, accompanies a fault core strand. Two colours of alteration are dominant; 1. pale pink where plagioclase feldspar has changed from milky white in colour to pink, or 2. white where plagioclase and alkali feldspar are bleached and dark coloured biotites and hornblendes are replaced completely with chlorite. These colour changes occur in zones up to 50mm wide on either side, or in some cases on one side only, of a fault core strand.

Figure 24. An example of a fault core strand within the GPF defined by intensely deformed cataclasites. The fault core thickness in this case is around 8cm. Associated with slip surfaces and damage zone fractures (compass for scale is around 10cm long).

The deformation elements that comprise fault core strands in the GPF are commonly cataclasites. The GPF cataclasites vary from lightly fractured or brecciated protolith (proto-cataclasites) to cataclasites, and intensely deformed ultracataclasites. Mylonites defined by foliated protolith may also be present. These fault rocks are frequently juxtaposed so that an individual fault core strand may contain several different types of deformation element (e.g. Figure 25). Fault core strands containing ultracataclasite often show no systematic spatial distribution or relationship between the deformation elements, instead any deformation element may be found at the edge or near the centre of a strand,

and be juxtaposed with any other element. However, fault cores that are composed primarily of cataclasites sometimes have more comminuted, or finer grained, material at the edges of the strand. Typically a fault core strand with this geometry has a total thickness up to tens of centimetres, with millimetres to several centimetres of finer material generally lacking clasts at one or both edges. The central and thickest portion of the fault core strand may contain green cataclasites or mylonites.

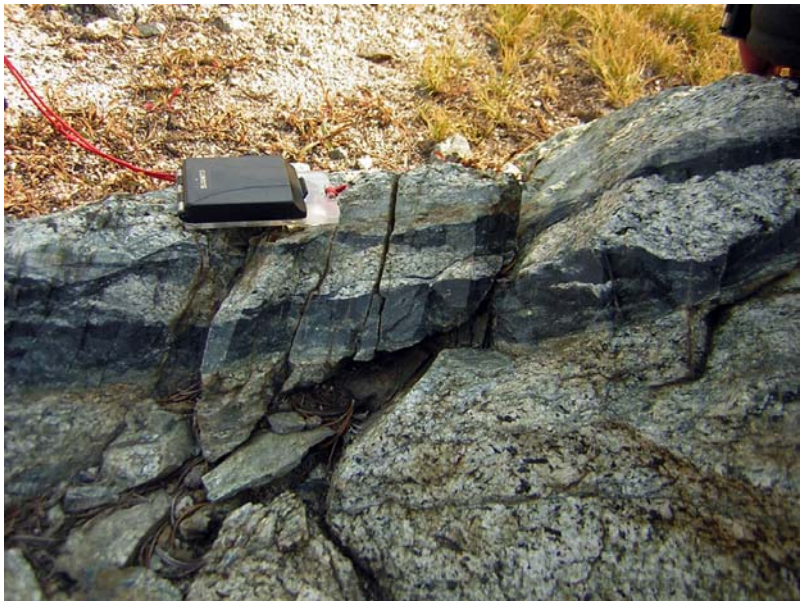

Figure 25. An example of a fault core strand from the GPF that contains multiple, juxtaposed deformation elements. Cataclasites are pale to grey-green and ultracataclasites are very dark grey to black. Compass-clinometer is 10cm for scale.

Proto-cataclasites are here defined as fault rocks in which the protolith mineral assemblage, crystallinity and fabrics are maintained, but which are pervasively fractured. The fractures in proto-cataclasites are most frequently opening-mode, but may also involve shear fractures with centimetres of displacement. In some cases lenses of fracture-bounded proto-cataclasites are encompassed within cataclasites or ultracataclasites. Fractures within proto-cataclasites are always mineralised with chlorite and epidote, range in thickness from <<1mm to ~1mm, and often have morphologies that appear to follow crystal edges. Alteration of the protolith may accompany proto-cataclasite development, where feldspars are altered to either bright white, or pink as described for alteration halos around fault cores (above). Fracture spacing defines the degree of cataclasis that these fault rocks have undergone; fractures spaced several to ten millimetres apart define lightly fractured protolith, but fractures spaced up to a few millimetres apart indicate a larger degree of deformation, and are close to becoming comminuted cataclasites.

Cataclasites within the GPF are grey-green, fault rocks containing clasts with a range of grain sizes within a finer grained matrix (Figure 26). The proportion of clasts within cataclasites ranges from 80% to around 25%, with the number of clast-clast contacts decreasing as the proportion of matrix increases. Individual clasts are up to ~10mm in size and are often multi-crystalline aggregates derived from the wall rock or fragments of single crystals from the host rock. Clasts may also be composed partly of epidote and chlorite where these minerals are present along intra-clast fractures. Lenses or pods of more or less comminuted cataclasite may also be present within a cataclasite seam. The clasts are contained within a matrix of extremely fine grained crystalline material that is often grey-green. Matrix material grain size ranges from too small to identify in hand specimen to ~0.5mm. The matrix frequently displays shear fabrics in hand specimen that are defined by compositional variation between different layers and lenses, and resemble slip surfaces where through-going zones of highly comminuted material can be identified.

Figure 26. Photograph of sample GPF6 showing proto-cataclasite (pale grey, right), cataclasite (grey-green, left), and ultracataclasite (very dark, centre).

Ultracataclasites in the GPF are aphanitic (i.e. grain size is generally too small to distinguish with a hand lens), cohesive, crystalline fault rocks. They are extremely dark green to grey-black, and are composed of cohesive matrix material containing rare clasts. Clasts are rounded, pale coloured minerals (quartz and feldspars) up to 0.5mm in diameter and give the ultracataclasites a speckled appearance when examined closely. Some faint variations in the colour of the ultracataclasites are defined by lenses and layers of clast content (Figure 27). Darker lenses are clast free, and appear to be 100% ultracataclasite matrix material. Lighter lenses are composed of similar material to the most highly comminuted cataclasites, being extremely fine-grained (<<1mm), with occasional clasts of pale minerals up to 0.5mm in diameter. In places the lenses within the ultracataclasites

define fabrics that are geometrically similar to S-C fabrics in ductile shear zones and some cataclasites (e.g. Chester *et al.*, 1985; Vernon *et al.*, 1983). The pale lenses in particular are often lozenge-shaped and contain a grain shape preferred orientation with long axes oriented approximately parallel to the edges of the ultracataclasites.

Figure 27. Photograph of specimen GPF5 showing juxtaposed cataclasites and dark-coloured ultracataclasites. Inset: the variable composition of the ultracataclasite is defined by lenses and layers of clast content.

Mylonites can be recognised within the GPF where the protolith has developed a schistosity defined by aligned inequant mineral grains. Primary foliations are generally absent from the host granodiorite in the study area, except where a weak alignment of hornblende is present. The presence of a schistose fabric is therefore indicative of localised ductile deformation. Within the GPF, the fabric elements that define schistose fabrics are flattened and rotated hornblende, quartz and feldspars giving the rock a grain shape preferred orientation. The intensity of the schistose fabric varies from slightly aligned, undeformed grains to strongly aligned, extremely flattened and sheared grains, and in places the deformation is so intense that the original mineral assemblage of the protolith cannot be recognised. The schistosity is commonly oriented at a high angle (≤70º) to slip surfaces, which consistently truncate the fabric. However, in some cases the fabric may become more pronounced approaching a slip surface (see Figure 23) so that the orientation

of the fabric elements rotates towards being parallel to the slip surface. Where such a bend-in geometry is observed, the intensity of the fabric increases.

3.5.1.4 Damage zone

Subsidiary structures around the GPF fault zone have a higher intensity of deformation within the fault zone than the level defined by the regional cooling joints (Figure 22). As these subsidiary structures are absent in regions away from faults, they represent the damage zone of the GPF.

Structural logs show that subsidiary structures are present both between and outside of the fault core strands. However, as the logs are limited in length, they are unlikely to have traversed the entire fault zone width. 1D transects taken through the fault zone at localities 18, 19, 20 and 28 were therefore used to delimit the lateral extent of the damage zone, and to analyse the distribution of subsidiary structures within the GPF (Figure 28). The localities selected for 1D transect analyses were better exposed over a broader area than the structural log sites. All structures recorded during the transects are included in this analysis, and are equally weighted, although the presence of fault core strands is indicated for reference.

Two fault core strands at locality 20 define the GPF. The fracture frequency calculated from 1D transect results is highest in the vicinity of the fault core strands, reaching a peak at 34 fractures per metre (frs/m), and maintaining a level of around 10frs/m for a lateral distance of 8m. This elevated fracture frequency is due to the presence of highly fractured and altered protolith associated with the fault core strands. Further away from the fault core strands, the fracture frequency is lower, ranging from 0-5frs/m. A fracture frequency elevated above the background level (see section 3.3) is therefore associated with the GPF, representing a fault-related damage zone. At locality 20 the fault zone width, measured orthogonal to the fault plane, which encompasses all of the fault zone components is therefore at least 10m wide. A lack of exposure to the south of the most southerly fault core strand observed means that the fault zone width measured at locality 20 is likely a minimum value. Several other peaks in the fracture frequency at around 5frs/m are present in the transect results. Those at -7m and 14m may be part of the fault zone as they are in relatively close proximity to the zone of fault core-related damage. If this is the case, it would mean that the fault zone width could be greater than 26m.

The transect through the GPF at locality 19 shows that the fault contains at least three fault core strands at this locality. Fracture frequency is highest close to the fault core strands as a series of fractures splay from the strands, though the maximum observed fracture frequency (7frs/m) is lower than that observed at locality 20. High fracture frequency occurs on both sides of the fault core strands, and is maintained above the background level at this locality for ~16m lateral distance. The fault zone width at locality 19 may therefore be 16m, though poor exposure to the south of the zone of fault-related damage means that this is again a minimum estimate. However, the maximum fault zone width at locality19 is likely 21m as the fracture frequency decreases significantly outside of the poor exposure.

At locality 18 at least three fault core strands are also present within the GPF. Poor exposure immediately to the south of the most southerly of the observed fault core strands restricted the range over which the data could be collected. To the north of the fault core strands, the fracture frequency is high (9frs/m maximum). These closely spaced fractures delimit a zone of host rock that is broken into fracture-bounded blocks of approximately equal size (~10cm in width) within which the rock is pervasively altered. Away from the fault core strands, the background fracture frequency is much lower, showing that the fault zone width is at least 25m at locality 18. A poorly exposed, shallow gulley immediately to the north of the zone of elevated fracture frequency contains disassociated blocks of rock similar to those exposed close to the fault core strands, suggesting that the fault zone may be wider, and that 25m is a minimum estimate.

The 1D transect at locality 28 could only be collected to the south of the well exposed portion of the fault zone described in the fault core logs (see Figure 22). The transect is a continuation of the FC log from the same locality, and shows that there is one more fault core strand present in the GPF than those recorded in the log, taking the total observed to four. The transect data also show that the highest fracture frequency of 10frs/m occurs close to the fault core strand, and that the fracture frequency associated with the GPF is higher than the background level at this locality. This is consistent with the schematic representation of the subsidiary fractures in the fault core log, which are significantly more frequent than the background level of 1-2frs/m. An estimate of the fault zone width at locality 28 is difficult due to the limited transect data, but combining observations from the fault core log and 1D transect shows that fault-related damage delimits a minimum width of 17.5m.

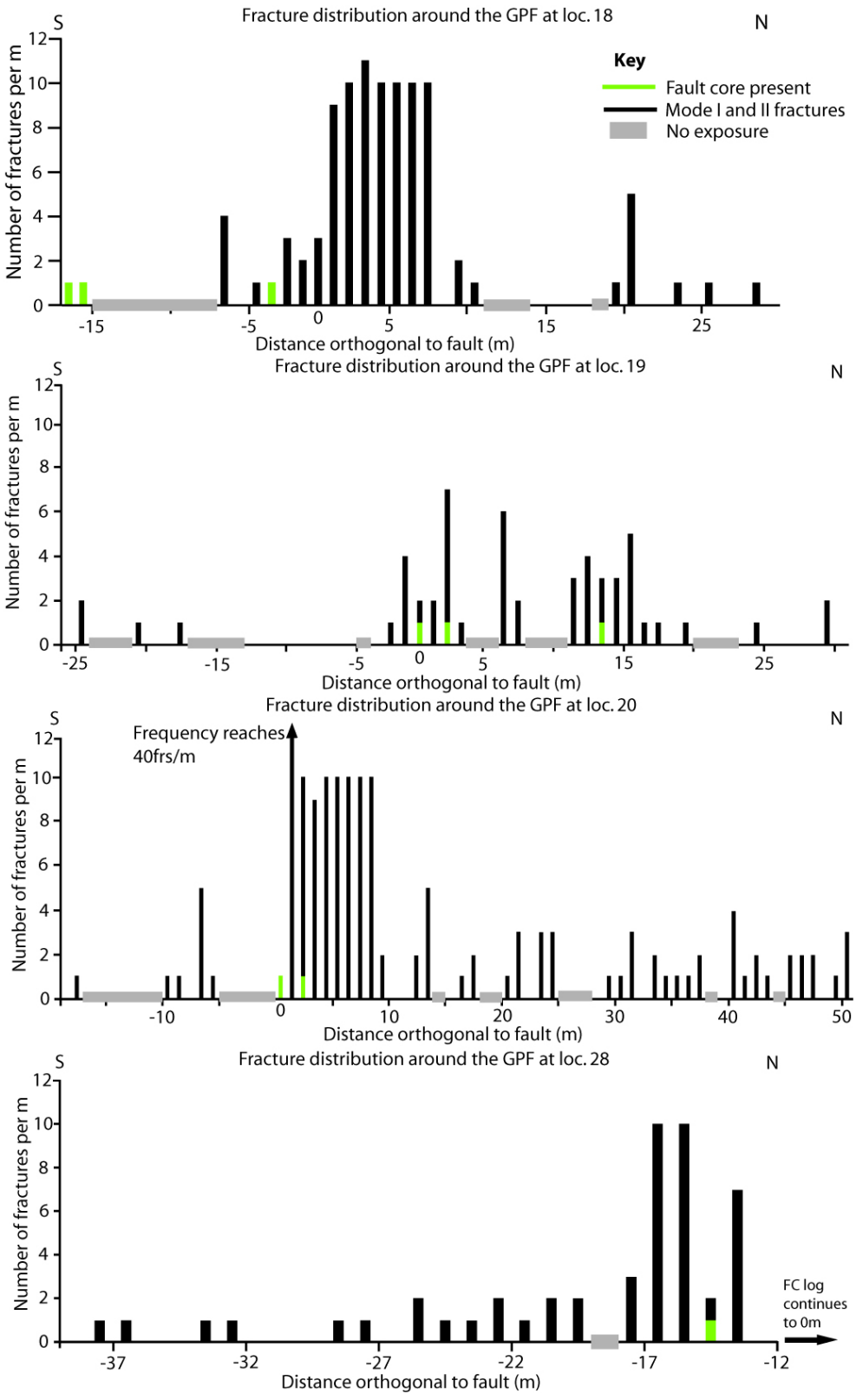

Figure 28. The results of 1D transects through the GPF at localities 20, 19, 18 and 28. Transect data are presented here in the form of histograms of fracture frequency against distance orthogonal the fault zone. Note difference in scales. Due to the method of arbitrarily choosing the start point for a transect (i.e. 0m) somewhere in the middle of the fault zone, the lateral distance measurements should only be considered as a scale.

A number of patterns significant to the GPF architecture are evident from the data collected in each 1D transect (Figure 29). The number of fault core strands varies along

strike, and the types of structures within the damage zones vary between transect sites (see below). Although some of the variability is likely due to the limitations of exposure, the GPF is characterized by a highly variable architecture. Along-strike changes in damage zone architecture are also expressed in the distribution of orientations of the observed structures; structures dip more to the south at locality 19 than locality 20, the damage zone structures at locality 18 have developed with more dispersed strike directions than at 19, and at locality 28 the structures have a greater range of dips than at 18. In each case, except for locality 28, the damage zone structures are oriented counter-clockwise to the fault core orientations, and the structures within the fault zones are asymmetrically distributed.

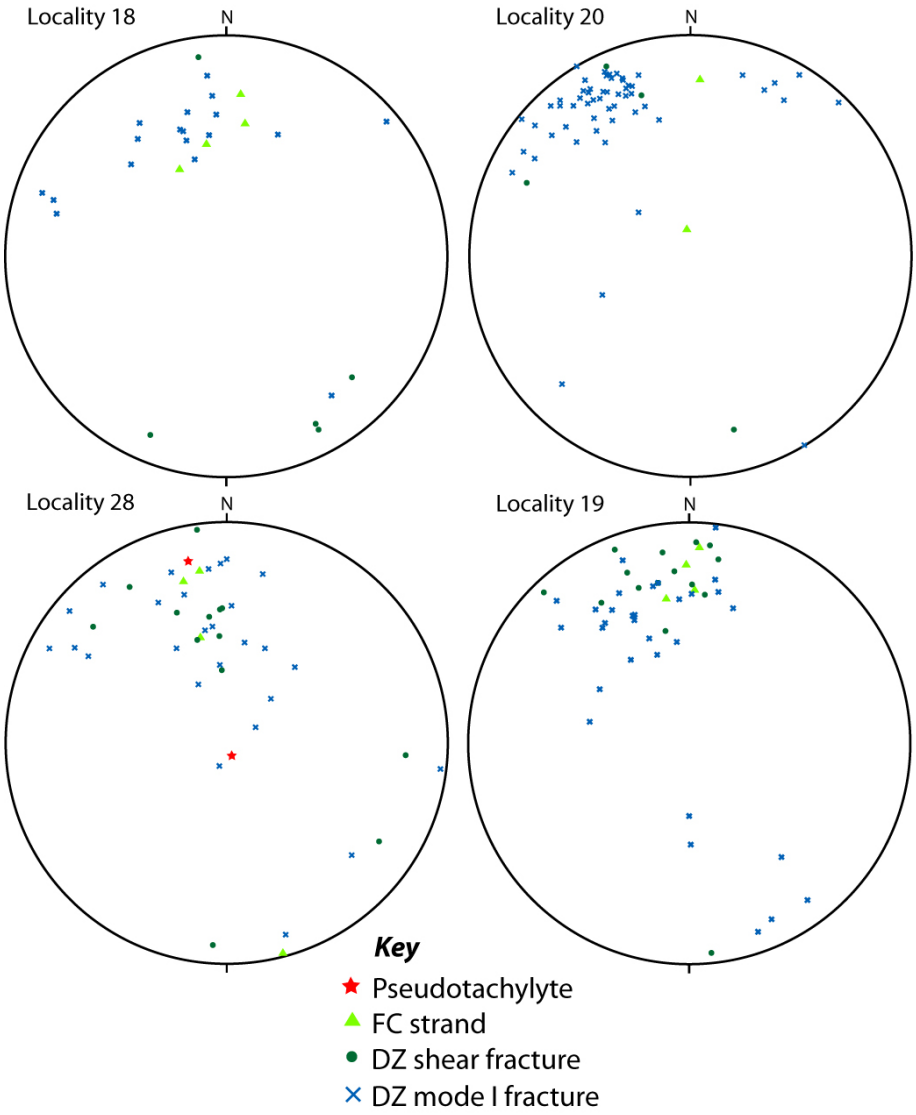

Figure 29. Stereonets showing poles to measured orientations of the fault zone components for the four 1D transects taken through the GPF.

The GPF damage zone contains different types of structures that are equivalent to the deformation elements within the fault cores. Opening mode fractures are common and can

be identified where the edges of crystals in the host rock can be correlated across the fracture. Opening mode fractures mostly have a straight or slightly wavy morphology, are 0.1m to greater than 1m long, and have apertures of <1mm to 10mm that narrow gradually towards zero at the tip. Opening mode fractures may bifurcate, forming branched, or tree-like, arrangements of small (tens of centimetres long) fractures. The fractures are frequently filled with extremely fine grained, granular epidote and chlorite, which may be laminated parallel to fracture margins or mixed along strike. Fractures may also be filled with a black mineral (that may be chlorite) or be too thin to have any type of mineral fill. Alteration of the surrounding rock can accompany opening mode fractures forming zones up to 70mm wide that can be symmetrically or asymmetrically distributed about the fracture. In some cases (e.g. locality 18) opening mode fractures are extremely closely spaced within zones of fractured rock that are up to 5m thick. In these places fractures occur every few centimetres, are often mineralised and have regular orientations that define fracture-bounded blocks of protolith that is often pervasively altered.

Arcuate fractures are present at locality 28. These fractures splay from a fault core strand and have broad, curved traces that bend back towards the fault core, intersecting with the fault core several metres along strike (Figure 30, see also Figure 22). Evidence for arcuate fractures being entirely opening mode is rare, only a few fractures were observed where host rock minerals could be correlated across the opening, but no direct evidence for relative shear displacement across the fractures was observed. The fractures are spaced 2-10cm apart and frequently intersect each other, or branch from one to another. Arcuate fractures have apertures of up to 10mm, and are filled with crystalline, dark grey to black, aphanitic material that resembles pseudotachylyte present elsewhere in the same outcrop. Although the dark aphanitic material resembles pseudotachylyte, the fractures contain insufficient features unique to pseudotachylyte to positively identify the material as such. In some cases narrow ribbons of quartz mineralisation accompany the dark aphanitic material, and quartz may also be the only type of mineral fill in a fracture. The host rock cut by the arcuate fractures is pervasively fractured and altered containing friable, pink plagioclase throughout the rock and abundant epidote mineralisation along the tightly spaced, fine fractures.

Shear (mode II) fractures are also present within the damage zone of the GPF. Shear fractures are 1-35mm thick, at least 1m long, and exhibit slickenlines where a fracture surface is exposed. Slickenlines are generally defined by elongate aggregates of chlorite crystals, and have a range of orientations within the fault zone. Cohesive fracture fills of

either epidote or chlorite are common, though often laminated or patchy assemblages of the two minerals are present. Clasts or lenses of host rock minerals may be contained within shear fractures. Comminuted wall rock may be present as sub-rounded to angular clasts up to 5mm in size, which in some cases have aligned long axes defining a shear fabric.

Figure 30. Photograph of the arcuate fractures at locality 28, view approximately parallel to the slip vector (to the west). The fractures splay from a fault core strand (lower right), and form a broad arc before rejoining the strand several metres along strike.

3.5.2 The Glacier Lakes fault

3.5.2.1 General appearance

In general the GLF is less well exposed than the GPF, but shows limited variability in fault architecture along strike. The GLF fault trace is frequently expressed as a gulley in which fault rocks are sometimes exposed, particularly near the edges. The GLF gulley can be used as a proxy for the fault zone thickness as deformation is limited beyond the gulley walls; the width of the gulley ranges from approximately 10m to 60m. However, the gulley becomes wider where the splay faults intersect the GLF, and so the observed widths of the gulley may not reflect solely the GLF fault architecture.

At locality 2, the fault is partly exposed in a stream-cut gulley (Figure 31). The northern edge of the fault zone is defined by a sub-vertical wall formed of a fault core strand that is parallel to the overall fault zone orientation. To the north of the fault core strand, few fault-related fractures appear to be present. To the south of the strand (in the gulley) is a zone of highly fractured and altered protolith that is at least 2m thick. There is no further

exposure of the fault until the opposite side of the gulley, which is defined by a wall of host rock parallel to the fault core strand.

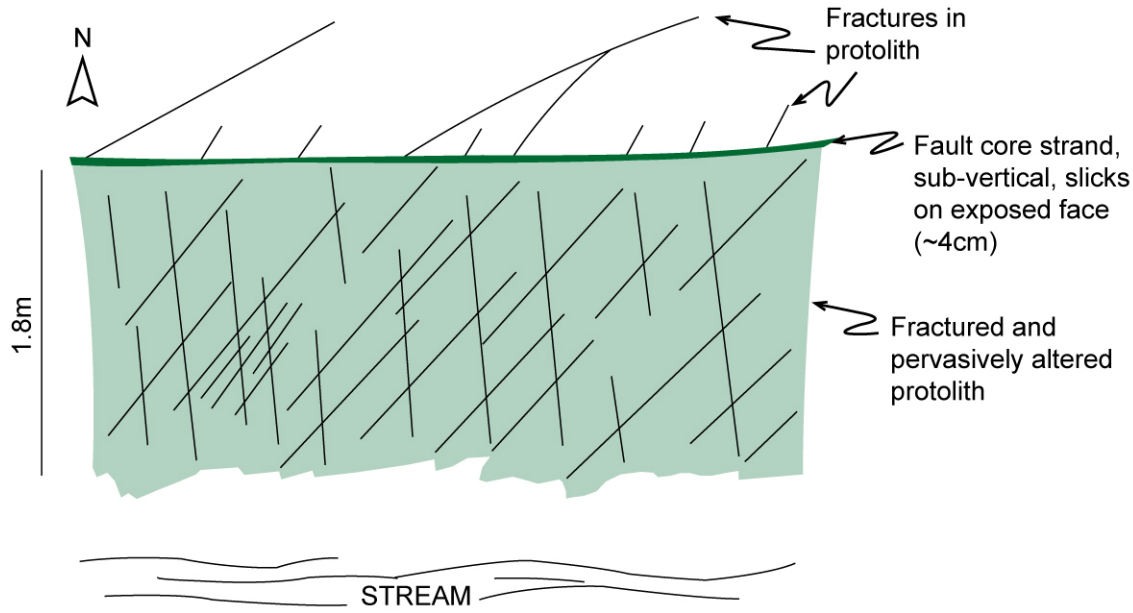

Figure 31. Sketch (plan view) of the GLF exposure at locality 2 showing the architecture of the fault zone. A planar fault core strand is present at the north edge of the fault zone with highly fractured and altered protolith immediately adjacent to the south.

The GLF is also exposed ~375m to the east of locality 2 at locality 23 where the fault gulley is not stream-filled (Figure 32). The northern edge of the fault is defined by a fault core strand ~7.5cm in thickness that again forms a sub-vertical wall to the gulley. To the north of the gulley wall are fractures, up to metres in length that splay from the fault core strand. To the south of the fault core strand is ~1.5m of highly fractured protolith, which grades into another fault core strand to the south. This strand forms a zone of intense deformation around 1.2m thick in total. To the south of the second strand is a further 7m of poorly exposed, fractured protolith, before another fault core strand 0.4m in thickness is present. The southern extent of the fault gulley is marked by a shorter, more irregular sub-vertical wall.

The consistent nature of the geomorphic expression of the GLF and the two exposures within the fault gulley suggest that intense deformation including fault core strands and highly fractured, pervasively altered host rock might be present along the entire length of the fault zone. The GLF fault zone is bounded by approximately planar fault cores that are sub-parallel to the overall fault zone orientation. Beyond the lateral extent of the fault gulley, the intensity of deformation appears to drop off rapidly.

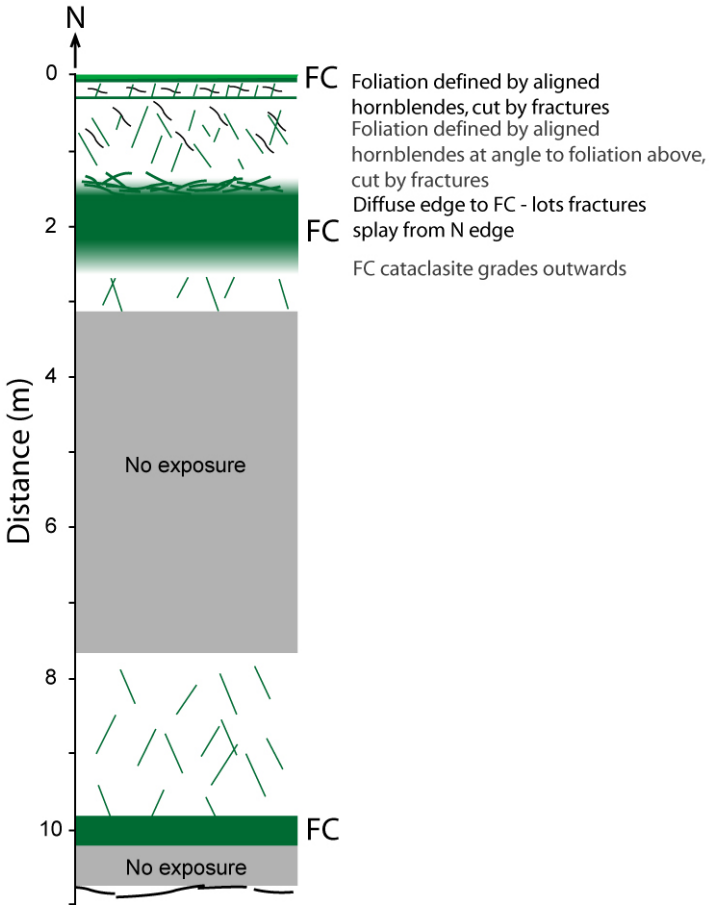

Figure 32. Structural log through the GLF at locality 23 showing the internal fault architecture. Fault cores (FC) are composed of cataclasites, green lines represent brittle fractures, black lines indicate the orientation of foliations in the fault zone rocks.

An exception to the generalised fault zone architecture for the GLF described above is the portion of the fault that is well exposed at locality 24 (Figure 33). As previously discussed (section 3.4.3), the GLF splits into two fault strands in the vicinity of locality 24. The fault at this locality is exposed on a planar, glacially-scoured pavement. The northern of the two fault strands is composed of a fault core that ranges in thickness from 0.08m to 0.2m, which has few related subsidiary structures, though the exposure is limited to the north of this fault strand. The southern fault strand comprises two fault cores that are up to 0.1m thick, and which have a complex network of associated subsidiary structures. Both fault strands form topographic gullies in the hill to the west of locality 24. At this locality the GLF comprises several fault core strands that have an intricate network of subsidiary structures.

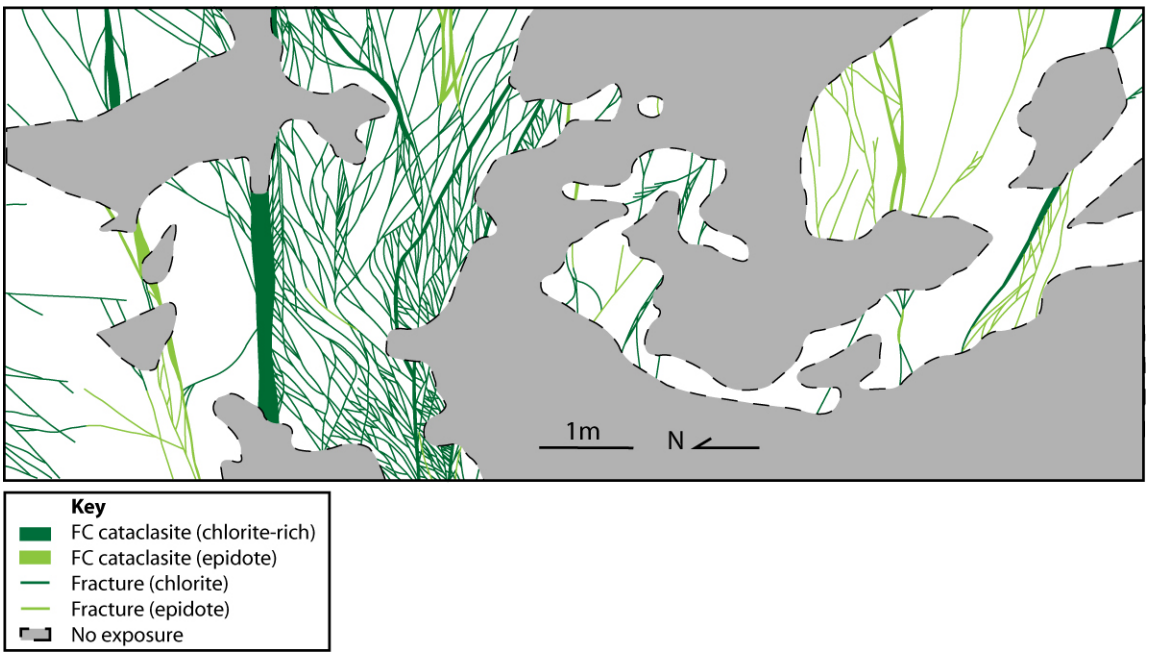

Figure 33. Base map of the exposure of the GLF at locality 24 showing the fault cores developed into three fault strands as well as numerous subsidiary structures.

3.5.2.2 Slip surfaces

Slip surfaces are present within the GLF as polished surfaces on which slickenlines are developed, and as seams of extremely comminuted material. Pseudotachylytes were not observed within the GLF in the field (though pseudotachylytes are evident in thin section, see section 4.4.3). Slickenlines are composed of aligned chlorite and epidote crystals and are present on exposed fracture surfaces. The fracture surfaces may also be corrugated, with amplitudes of millimetres to a few centimetres, which were used to infer slip vector orientations in some cases. Exposed fracture surfaces are most frequently present at the edges of fault core strands due to incision of the fault gulley. Few slickenline data were collected during fieldwork due to the limited exposure of the fault zone, though slickenlines exposed at localities 2 and 23 all rake ≤10º, consistent with the observations of Evans *et al.* (2000), which show GLF slickenlines are predominantly sub-horizontal (Figure 10).

Seams of extremely comminuted material are present within the GLF, across which relative displacement can be inferred. The seams are frequently present within fault core strands, as well as separating domains of fractured and altered protolith away from fault core strands, and are up to 10mm in thickness. The material within these slip surfaces is greyish green or pale green, extremely fine grained (≤0.5mm) and contains rare clasts of feldspar and quartz that are rounded and ≤1mm. Slip surfaces tend to be located towards

the edges of fault core strands, but also form acute angles to the fault core edge in places, giving the slip surfaces an inter-connected geometry.

3.5.2.3 Fault core

The GLF contains fault core material localised in strands. The strands are sub-vertical and are located at the edges of the fault zone, as well as within the fault zone. Individual strands cannot be traced for more than 5m along strike in the field due to limited exposure. However, the northern bounding fault cores at localities 2 and 23, 375m apart, may be the same strand as they occupy the same relative position within the fault zone and are part of the same fractured wall rock-fault core pattern present at both exposures. Fault core strands range in thickness from ~4cm to ~1.8m, and tend to be planar in plan view. Most strands have sharp edges, though the thickest strand observed (at locality 23) has gradational transitions on both sides, which occur over tens of centimetres.

The fault cores within the GLF are composed of pale green or greyish green cataclasites (Figure 34). Cataclasites are made up of clasts of protolith minerals that are present in a granular chlorite and epidote rich, matrix that gives the fault rocks their colour. Clasts range in size from <1mm to 8mm and are rounded to sub-angular. Cataclasites contain disordered domains, or lenses, of material with different clast-matrix ratios and/or maximum clast size. Matrix-rich domains (70-90% matrix) generally have smaller, more rounded clasts, with clast size increasing as the proportion of matrix decreases. Slivers of less comminuted material, in which the protolith mineral assemblage can be recognised, are also present in some cataclasites. These domains of variably deformed fault rock are ~5mm to ~10cm wide and are juxtaposed across slip surfaces defined by extremely comminuted material. Less fractured cataclasite is present at the edges of fault core strands that have gradational transitions from cataclasites to fractured protolith. The gradational change in fault rock follows a pattern of cataclasite grading laterally into less comminuted cataclasite, then extremely fractured protolith in which blocks of undeformed rock are present several centimetres in width (similar to the proto-cataclasite in the GPF), to fractured protolith in which undeformed protolith is present in blocks tens of centimetres in width. Ultracataclasites are not observed in the GLF.

Schistose fabrics indicative of ductile deformation are present within the GLF fault zone. The fabrics are defined by aligned, elongate minerals, most notably hornblende, and are consistently cross-cut by brittle fractures. The foliations within the ductile fabrics are

weak i.e. the original crystal habits are not sheared (as in the GPF, see section 3.5.1.3), and do not increase in intensity towards slip surfaces.

Figure 34. Photograph of sample GLF4 showing greyish green cataclasites from the internal fault core strand of the GLF at locality 23 (see Figure 32).

3.5.2.4 Damage zone

The GLF is associated with a large number of fractures. The structural log at locality 23, combined with the exposure at locality 2, indicate that the subsidiary structures are abundant within the fault gulley of the GLF. Fractures present between the bounding fault core strands are spaced around 2 to 10cm apart, giving the rock a shattered appearance. The closely spaced internal fault zone fractures are consistently oriented at high angles to fault core strands, where exposed. However, qualitative observations suggest that the fracture frequency diminishes rapidly beyond the fault core strands.

One-dimensional transects at localities 2 and 22 provide an indication of the distribution of GLF fault-related subsidiary structures. Transect data at locality 2 (Figure 35) could only be collected to the north of the fault gulley due to lack of exposure to the south of the gulley. The southern edge of the fault core strand in the northern wall of the fault gulley was selected as a start point for the transect. The results of the transect show that the maximum fracture frequency sampled by the transect is 3frs/m, immediately adjacent to the fault core strand and the fault gulley. The fracture frequency remains elevated for approximately 3m to the north of the GLF gulley, beyond which the fracture frequency reduces to a background level of 0-1frs/m. Fault related structures therefore extend the GLF fault zone for an extra 3m beyond the width of the gulley. At locality 2, and also locality 23, the fractures in the wall rock adjacent to the northern fault core strand of the

fault zone are present in 2 distinct orientations; one set comprises fractures up to several metres long that form angles of <30º with the fault core strand, and another set of fractures are up to tens of centimetres long and form angles of ~50º with the fault core (see Figure 31 and Figure 32).

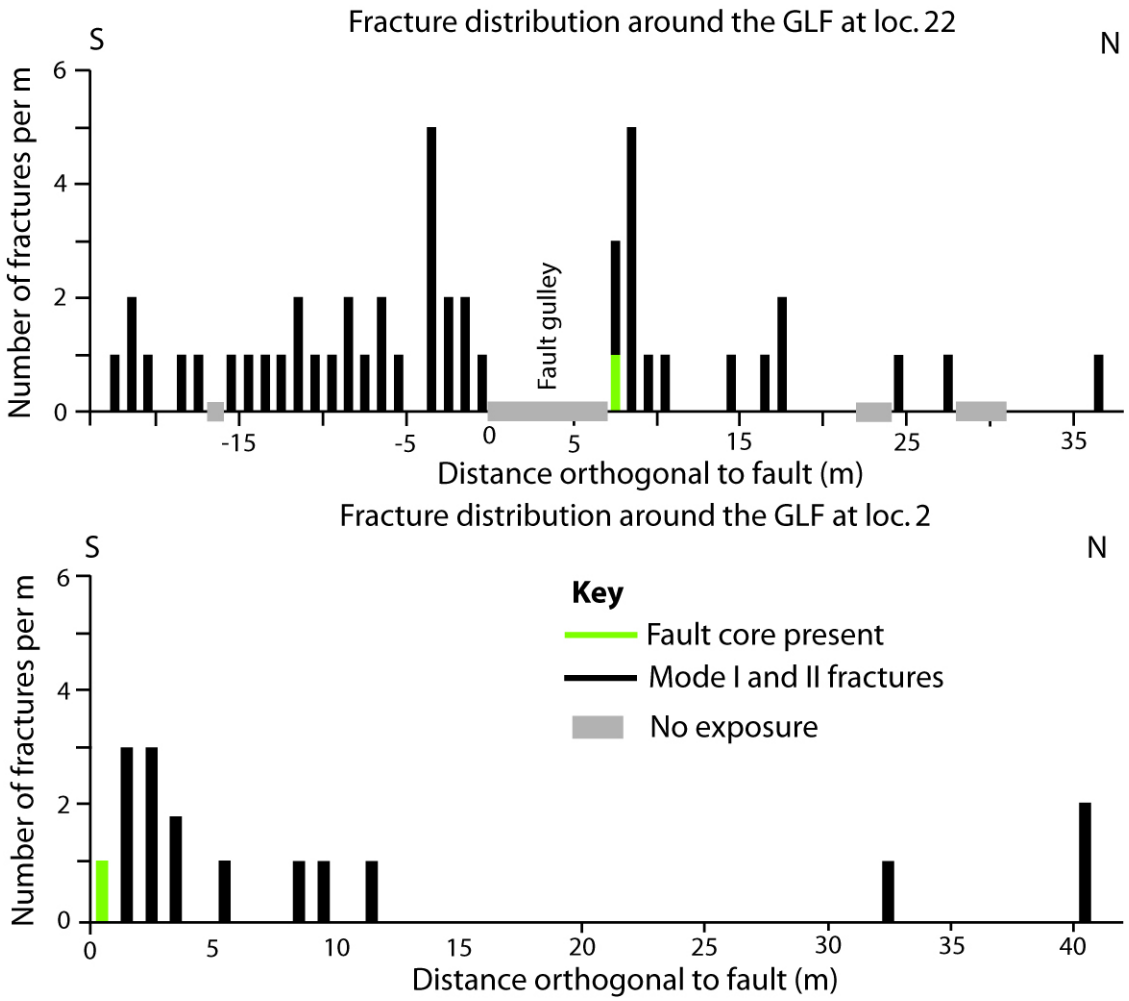

Figure 35. 1D transect results at 2 and 22 in the form of histograms of fracture frequency against distance orthogonal to the fault zone.

The GLF at locality 22 forms a pronounced, grass-filled gulley in which the fault is not exposed. One fault core strand is present at the north edge of the gulley, representing the most deformed rock at this locality. 1D transect results show that the maximum fracture frequency at locality 22 is 5frs/m immediately adjacent to the fault core strand, and also near the south edge of the fault gulley. The zones of high fracture frequency are ~1-2 m wide, beyond which the fracture frequency decreases to around 1-2frs/m, which is the background level at this locality. The internal architecture of the GLF is not exposed at locality 22, so the maximum observed fracture frequency and the distribution of subsidiary structures within the fault zone cannot be completely evaluated. However, the presence of elevated fracture frequency adjacent to the fault core strand at the edge of the fault gulley

which then decreases to the background level within a short lateral distance is similar to the distribution of fractures at the edge of the GLF fault zone at locality 2. The peak in data at the southern edge of the fault gulley at locality 22 is therefore likely to be the southern edge of the fault zone, though a southern bounding fault core is not exposed. If this is the case, then the total fault zone width of the GLF at locality 22 is approximately 13m.

3.5.3 GPF-parallel faults

The similarity in the orientations, lengths, and magnitudes of observed slip for the newly identified faults and the GPF suggests that these faults are closely related. This section will use observations combined from all of the newly identified faults in order to show that the architectures of the faults are alike, and to describe in detail the style of fault architecture of the GPF-parallel faults.

3.5.3.1 General appearance

The GPF-parallel faults form zones of variably deformed, greyish green or dark green deformed rock. The architecture of the faults is characterized by one to three fault core strands contained within a damage zone of subsidiary fractures. The geometry of the faults varies along strike, incorporating differing numbers of fault core strands, as well as changing dimensions of individual fault cores. A structural log taken through the LLF at locality 17 shows that three fault core strands are contained in a volume of fractured rock at least 3.5m thick (Figure 36). Approximately 300m along strike to the west, the fault is exposed in a cliff section, where it is composed of a single strand of fault core material that changes in thickness from 0.3-1.8m within ~30m along strike distance. Though the total fault zone width is difficult to establish in the cliff exposure due to the nature of the exposure, it seems that both the fault zone width and the number of fault core strands change along strike.

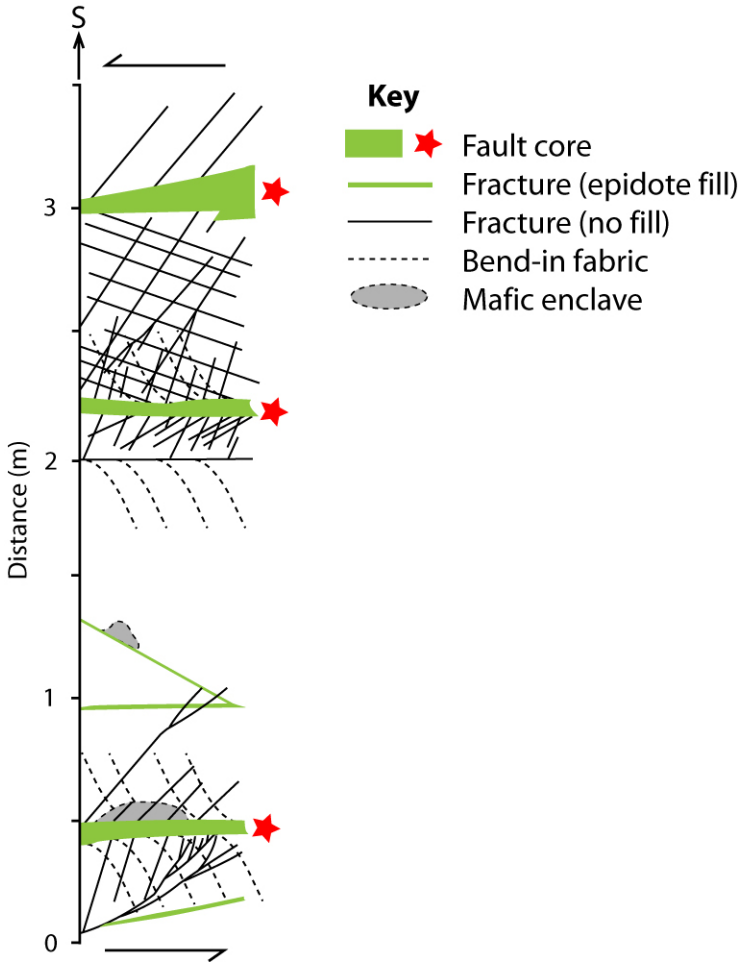

Figure 36. Structural log through the LLF at locality 17 showing the internal architecture of the fault. Three fault core strands are marked by stars, and are contained within a volume of deformed rock.

Skeeter fault is exposed at locality 1 where the fault comprises three fault core strands (the Southern, Middle and Northern stands), as well as numerous subsidiary structures, in a similar way to the LLF at locality 17. At locality 1, the three fault core strands are spaced several metres apart, but the consistently high level of deformation in the regions between the strands suggests that they are components of a single fault zone. The fault zone width of Skeeter fault at locality 1 is on the order of several tens of metres in width. Approximately 375m to the east at locality 11, Skeeter fault is composed of two main fault cores, with a series of subsidiary structures in between. The overall fault zone width at locality 11 is around 10m (see section 3.5.3.4). The fault zone at locality 11 is narrower overall than at locality 1, and has one fewer fault core strand.

The exposures of Skeeter and the LLF at localities 1 and 17 respectively show that the geometry of the newly identified faults changes along strike and between exposures as the number of fault core strands is different. One exposure of the LLF at locality 14 demonstrates how the changing fault core strand geometry might affect the other fault zone

components (Figure 37). At this locality, two fault core strands have a similar trend and run sub-parallel through the exposure until one strand changes orientation and the strands become further apart. Subsidiary fractures are abundant between the strands when they are close together, but diminish in number rapidly as the strands become further apart. The pattern of subsidiary structure frequency being dependent on fault core spacing is a fundamental characteristic of the new fault architectures.

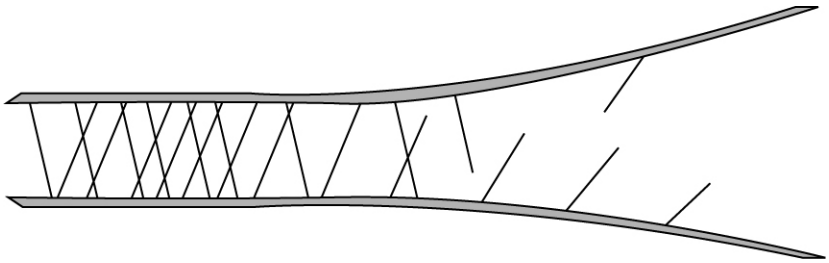

Figure 37. Schematic representation of the two fault core strands at locality 14 and the spacing controlling the fracture density.

3.5.3.2 Slip surfaces

Pseudotachylytes define slip surfaces in two of the newly identified faults in the study area; the Little Lake fault and Skeeter fault. Pseudotachylytes are present in the cliff exposure of the LLF 300m to the west of locality 17 where the outcrop contains a series of interconnected generation surfaces that clearly truncate a dyke fragment (Figure 38). The amount of slip across any of the pseudotachylytes cannot be measured as there are no displacement indicators. Injection veins accompany one of the generation surfaces, and are asymmetrically distributed about the generation surface. Pseudotachylyte veins in this outcrop range in thickness from ~0.5-4mm and are frequently curved. The veins are black or grey with sharp edges, and have a glassy appearance. The interconnected generation surfaces cross-cut undeformed host rock, weakly mylonitic host rock and limited cataclasites. The outcrop also contains a 20cm thick band of dark grey to black, aphanitic deformed rock, and may also be pseudotachylyte (Figure 38). The band is cut by a series of later fractures, and also contains a shear fabric defined by flattened and sheared lenses of the dark material.

Figure 38. A photograph of the pseudotachylytes present in the LLF in the cliff section 300m to the west of locality 17 (pen for scale is approximately 15cm). The sketch of the outcrop (top) shows the pseudotachylyte veins (highlighted in red) that are typical of a generation surface - injection vein geometry (aplite dyke fragment is highlighted in yellow).

Pseudotachylytes are abundant in the exposure of Skeeter fault at locality 1. In the southern fault core strand multiple generation surfaces ≤20mm thick with many accompanying injection veins give the rock a brecciated appearance in places (Figure 39). In this strand, pseudotachylyte veins are all grey to black, though wide veins tend to be either homogeneous black, or display colour banding that may comprise several differently coloured bands. Lithic clasts are visible within veins in the outcrop that are ≤3mm, rounded and in some cases are multi-crystalline aggregates. Veins overprint cataclasites and undeformed host rock. Differences in colour, colour banding patterns, and cross-cutting relations suggest that more than one generation of veins is present in the rock where the brecciated fabric is developed.

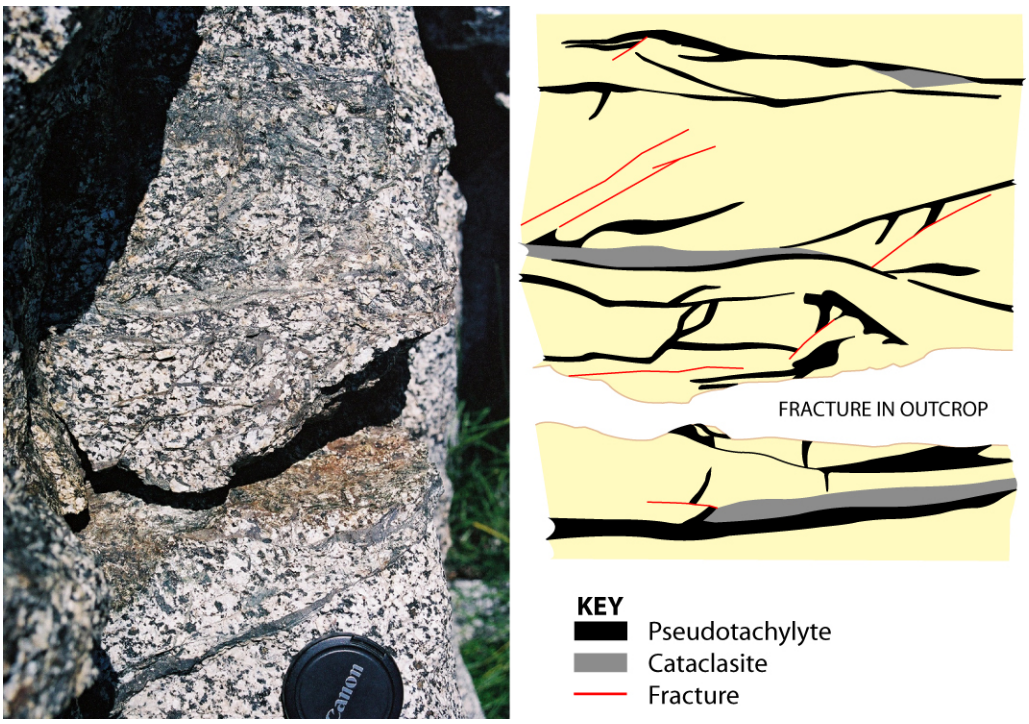

Figure 39. Photograph and interpretive sketch of pseudotachylytes present in the southern fault core strand within the Skeeter fault at locality 1. Pseudotachylytes can be indentified from generation surface – injection vein geometries, as well as the cohesive, dark, aphanitic material in the veins. In this outcrop the pseudotachylytes are distinct as they consistently cross-cut cataclasites and the igneous texture of the host rock.

The northern strand of Skeeter fault at locality 1 contains pseudotachylytes where the fault core strand thickness reduces to less than 1cm (Figure 40). The pseudotachylytes in this part of Skeeter fault are glassy, dark grey, aphanitic and contain rare rounded clasts of feldspar. Generation surfaces are evident, located at the edge of the fault core strand, from which injection veins branch off into the wall rock as well as in towards the centre of the fault core strand. The generation surfaces in this exposure are 0.19-1.22mm thick, within a fault core that ranges from 5-13mm in thickness. Pseudotachylytes cross-cut extremely comminuted cataclasites within the fault core (see section 3.5.3.3), and are present at the cataclasite-wall rock contact where they clearly truncate crystals in the wall rock.

Slip surfaces defined by pseudotachylytes are closely associated with fault core strands. In Skeeter fault, pseudotachylytes are localised within an extremely fault core strand (the narrow section of the northern fault core strand), forming at the edges of the strand. Pseudotachylytes are also dispersed throughout wider fault core strands (e.g. the southern fault core strand). However, the LLF pseudotachylytes are associated with a single fault core, but generation surfaces are frequently outside of the fault core. In the LLF the generation surfaces cut less deformed rock or undeformed protolith, despite having a similar orientation to the fault core strand.

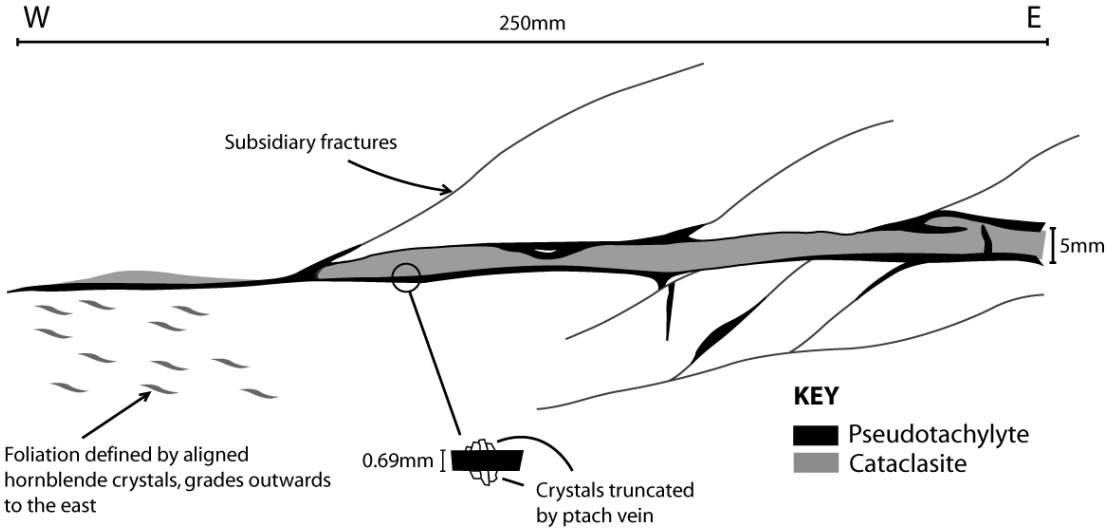

Figure 40. Sketch of the pseudotachylyte-bearing fault core where it is narrowest in the northern strand in Skeeter fault at locality 1.

Slickenlines are present on some exposed fracture surfaces in the newly identified fault zones. Elongate aggregates of chlorite and epidote define rakes that are close to strike-slip. Slip surfaces are also inferred to be present at the edges of some fault core strands where seams of extremely comminuted fault rock approximate the fault core edge (Figure 41). These slip surfaces are generally <10mm in thickness and are composed of chlorite and epidote rich cataclasites. The cataclasites are consistently fine grained, with clast size ranging from aphanitic to ~2mm, and contain clasts of feldspar and quartz that are rounded or sub-rounded. Often, the cataclasite seams are filled with clast-free epidote or chlorite, with inter-layered lenses of comminuted protolith minerals.

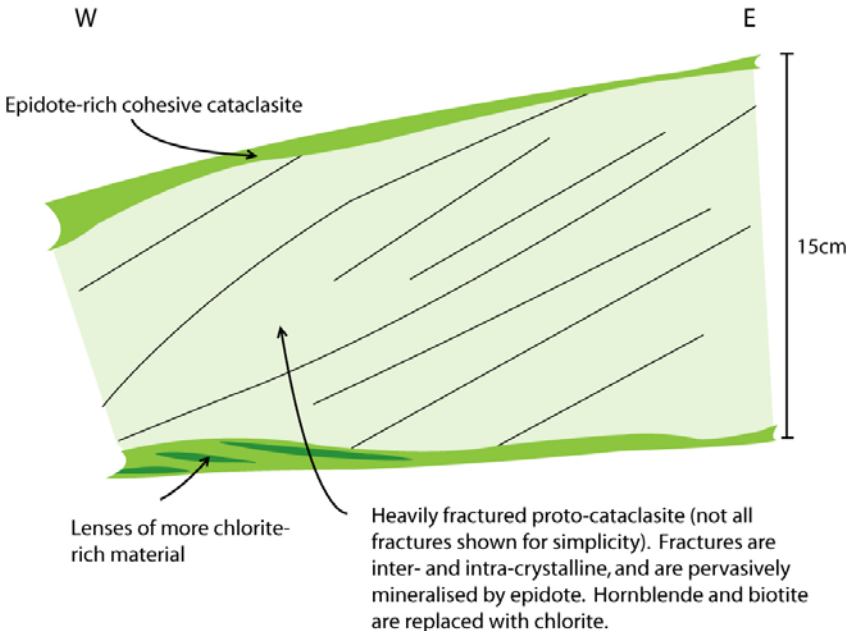

Figure 41. Plan view of a fault core strand at locality 1 emphasising the presence of slip surfaces at the edges of the strand. The most comminuted material is localised at the edges of the strand. Note that the damage zone elements have not been included for simplicity.

3.5.3.3 Fault core

The GPF-parallel faults in the study area are composed of 1-3 fault core strands that contain the most intensely deformed material in the fault zone. The strands have variable orientations due to their irregular geometry but generally approximate the orientation of the fault zone (Figure 36). Individual strands range in thickness from less than one centimetre to several tens of centimetres, with the maximum observed thickness for an individual strand of 1.8m. Strands are continuous along strike for tens of metres, and where exposed show that order of magnitude thickness changes can occur within tens of metres. The fault core strands have sharp edges that are often wavy where the thickness of a strand changes along strike. Alteration of the host rock frequently accompanies fault core strands, and is defined by white or pinkish feldspar crystals. Zones of alteration can be tens of centimetres wide on either side of a fault core strand and are thickest where two strands are close enough for alteration zones associated with each strand to merge into one large zone.

Deformation elements that comprise fault core material are most frequently cataclasites, with occasional mylonites. The geometry of the fault core strands appears to be related to the type of deformation elements developed within the strands. At locality 1, the northern fault core strand of Skeeter fault contains cataclasites where the thickness of the strand is several tens of centimetres, and highly comminuted cataclasites and pseudotachylytes where the strand is less than 1cm thick (Figure 42). A change in fault core thickness also correlates with a change in deformation element in the cliff exposure of the LLF 300m to the west of locality 17. Where the single fault core strand of the LLF is 1.8m thick, it is comprised of massive cataclasites, but where it is narrower mylonites and pseudotachylytes are developed along with highly comminuted cataclasites.

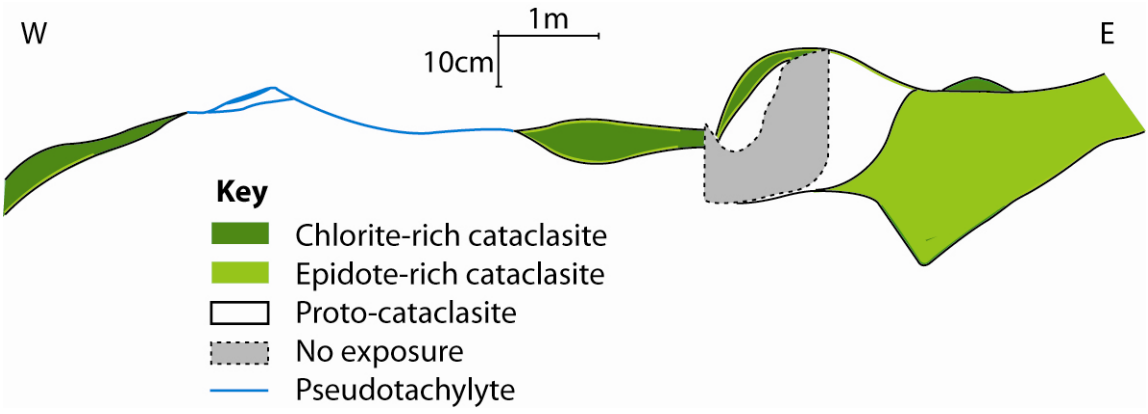

Figure 42. Baseline map of the northern strand of Skeeter fault at 1. Wider parts of the fault core are composed of cataclasites, whereas the narrower part is defined by pseudotachylytes (cf. Figure 40). More comminuted material is often localised at the edges of cataclasites, in a similar way to Figure 41. Note the vertical exaggeration to emphasise fault core thickness changes.

Cataclasites in the GPF-parallel faults range from proto-cataclasites to extremely comminuted cataclasites, which are foliated in places. Proto-cataclasites are lightly fractured protolith in which the original mineral assemblage is still identifiable. Within the fault cores, proto-cataclasites are generally pale or dark green due to pervasive alteration of hornblende to chlorite, and epidote mineralisation. Plagioclase and alkali feldspars within proto-cataclasites are often also altered, appearing to be milky white or pink. Fractures within these fault rocks are opening mode or shear fractures that cross-cut individual minerals, as well as frequently cross-cutting other fractures. Fracture surfaces are ubiquitously mineralised with chlorite and/or epidote. Some preferred orientation of fractures within proto-cataclasites may be present within fault cores, with fractures forming a fabric oriented at an acute angle counter-clockwise to the trend of the fault core strand. Minerals within proto-cataclasites vary from undeformed, to fractured with a jigsaw-like fragmentation, to comminuted. Zones of comminution are often present within proto-cataclasites, the geometries of which are always fracture-controlled.

Cataclasites (Figure 43) are composed of fragments of minerals from the protolith assemblage including feldspar, quartz, and rare hornblende, as well as abundant epidote and chlorite. Clasts in the cataclasites range in size from <<1 to ~6mm, are sub-angular to rounded, and are present within a matrix, which comprises 25-80% of the fault rock. Clasts can be aggregates of several crystals, and often contain healed intra-clast fractures. The matrix material within cataclasites is greyish green or dark green and is aphanitic. Variation in the clast-matrix proportions defines fabric domains within cataclasites. Domains are juxtaposed across narrow seams of extremely comminuted material that is always finer-grained and contains fewer clasts than the material within domains. Foliated cataclasites are developed in some domains (Figure 43) and are defined by the presence of a shear fabric consistent with left-lateral slip. Two shear sets may be defined corresponding to the R and P Riedel shears (see Figure 43). The fabrics within foliated cataclasites are similar in appearance to ductile fabrics developed in shear zones; elongate, lozenge-shaped clasts of chlorite, epidote and feldspar are aligned with sub-parallel long axes. These aligned clasts are ≤5mm long and have irregular, sheared shapes that contribute to the waviness apparent in the fabric. Domains of foliated cataclasites are also bounded by seams of much more comminuted material.

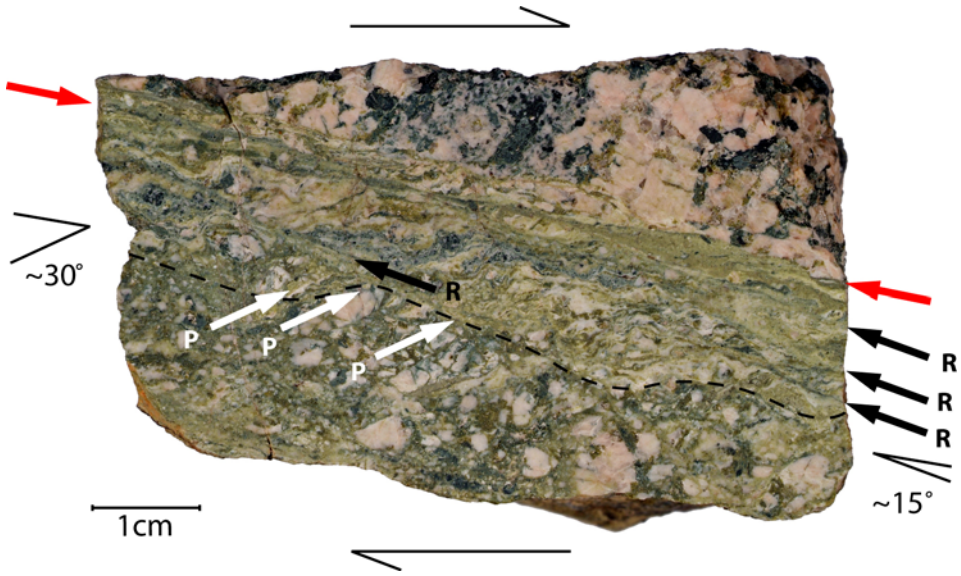

Figure 43. Photograph of a cut through hand specimen SK8 showing a cataclasite and a portion of wall rock. Two foliations are present corresponding to the R (black arrows) and P (white arrows) Riedel shear orientations (edge of the slipping zone is between red arrows for reference). Note that the foliation is consistent with left lateral shear, but this view is up into the cataclasite so the sense of displacement across the fault is reversed.

The most comminuted cataclasites in the newly identified faults are often associated with pseudotachylytes (see section 3.7.3.3). Highly comminuted cataclasites are dark grey or black, aphanitic, cohesive, and contain rare visible clasts of feldspars. Occasional zones of slightly coarser material in which greyish white grains <<1mm are discernable give the material a granular texture. The narrowest part of the northern strand of Skeeter fault at locality 1 contains these cataclasites, which are present in a narrow seam ≤5mm in width, and which are overprinted by pseudotachylytes (Figure 40). The fault core strand becomes wider along strike and so the extremely comminuted cataclasites are laterally associated with less comminuted material. In this exposure, the seam of more comminuted material dies-out into less comminuted cataclasite.

Mylonites are not extensively developed in the GPF-parallel faults but foliations defined by elongate, aligned protolith minerals are present in association with some fault cores. Mylonites tend to be present in small (up to tens of centimetres across) domains that are cross-cut by cataclasites or slip surfaces. Occasionally, foliations bend-in to slip surfaces.

3.5.3.4 Damage zone

Fault-related subsidiary structures associated with the GPF-parallel faults are present both between and outside of the fault core strands, and define the damage zones of the faults (e.g. Figure 36). A 1D transect taken at locality 1 shows the distributions of fractures within Skeeter fault at (Figure 44). Two fault core strands were sampled by the transect,

which are the along-strike extensions of the Southern and Middle fault core strands described in section 3.5.3.1. The fracture frequency within Skeeter fault at this locality reaches a maximum of 9frs/m to the north of the two sampled fault core strands. This zone of highly fractured rock is laterally equivalent to the Northern fault core strand of Skeeter fault, though poor exposure between the exposure of the northern strand (Figure 42) and the zone of highly fractured rock sampled by the transect means that the relationship between the two cannot be directly examined. The fracture frequency is lower (0-1frs/m) further away from the fault core strands and likely represents the background level of deformation. The total fault zone width of Skeeter fault at locality 1, as defined by the elevated fracture frequency in the 1D transect, is therefore ~27m. However, poor exposure immediately to the north of the northern limit of the transect means further deformation may be hidden, so the fault zone width may be greater.

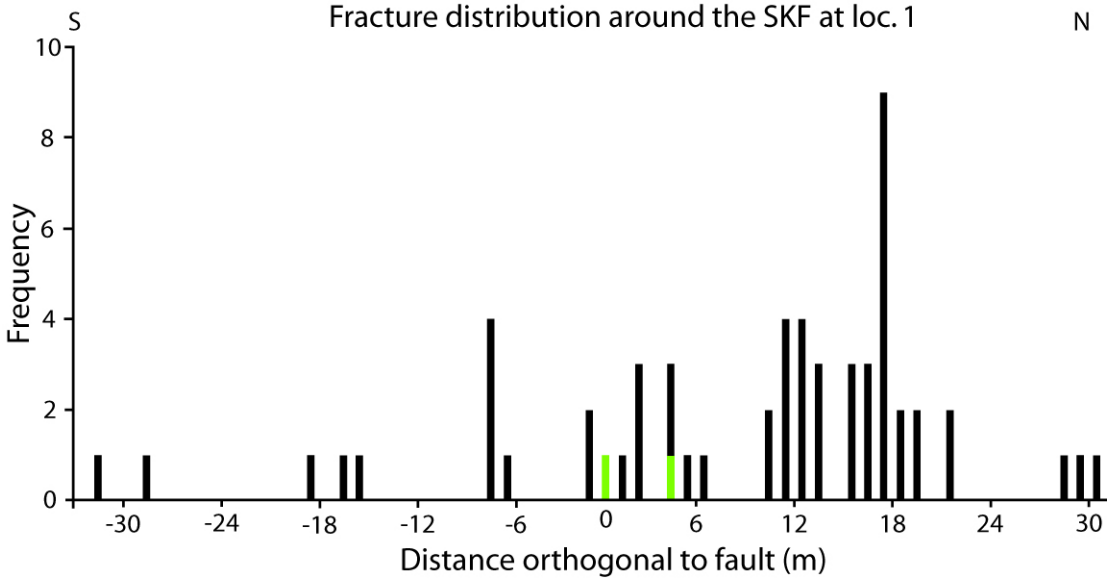

Figure 44. The results of a 1D transect taken through Skeeter fault at locality 1. The results are plotted as a histogram of fracture frequency (number of fractures per metre) verses lateral distance through the fault zone.

A map of the exposed subsidiary structures present within Skeeter fault at locality 1 elucidates further the geometry of the damage zone structures (Figure 45). The middle fault core strand of the fault is present in the centre of the map, from which many fractures splay in a counter-clockwise sense. Fracture traces are <1 to >10m long, and form a complex network of inter-connected structures. The highest frequency of fractures is present adjacent to the fault core strand within a zone ~2m wide. Some fractures are truncated at both ends by other subsidiary structures and so do not splay from the fault core strand. Within the zone of high fracture density, there appear to be two preferred orientations for the subsidiary structures; one at an acute angle to the trend of the fault core

strand and one sub-parallel. The fractures therefore define rhomb-shaped prisms containing relatively undeformed host rock.

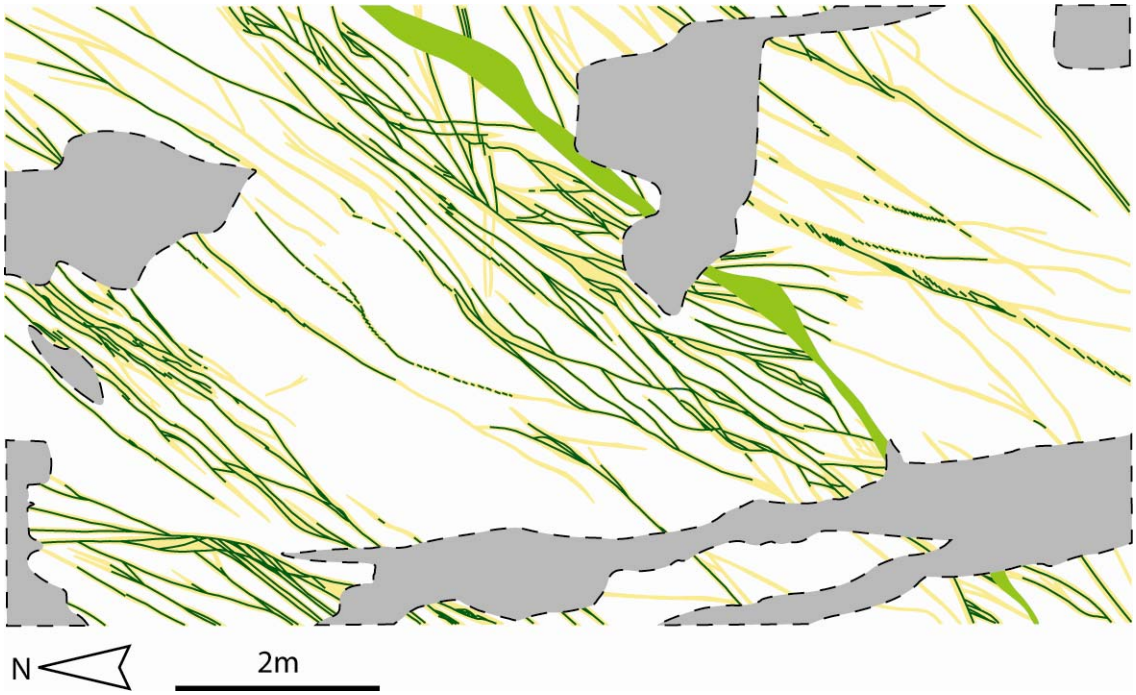

Figure 45. Map of part of the exposed portion of Skeeter fault at locality 1. The middle fault core strand (solid mid-green) is present in the centre of the map, from which many fractures splay (shown in green), and are associated with alteration of the host rock (the extent of which is shown in yellow).

The structures sampled by the 1D transect at locality 1 show a preferred orientation with the majority of fractures striking around ENE, and dipping relatively steeply; the mean orientation is 071/78S (Figure 46). The two fault core strands at this locality also dip steeply. The majority of the subsidiary structures within the fault zone make acute dihedral angles with the fault core strands. However, the two orientations of the subsidiary structures apparent in the map of the fault zone are not reflected in the transect data.

Many exposures of the GPF-parallel faults do not contain such well-developed subsidiary structures as those present at locality 1. For example, Snowy fault at locality 15 comprises a single fault core strand, with few subsidiary structures. However, though the subsidiary fractures are less numerous than those at locality 1, they are present, splaying from the edges of the fault core in a similar counter-clockwise sense. The fractures are up to 1m long, and the extent host rock cut by these fractures seems to control the width of the zone of alteration around the fault core.

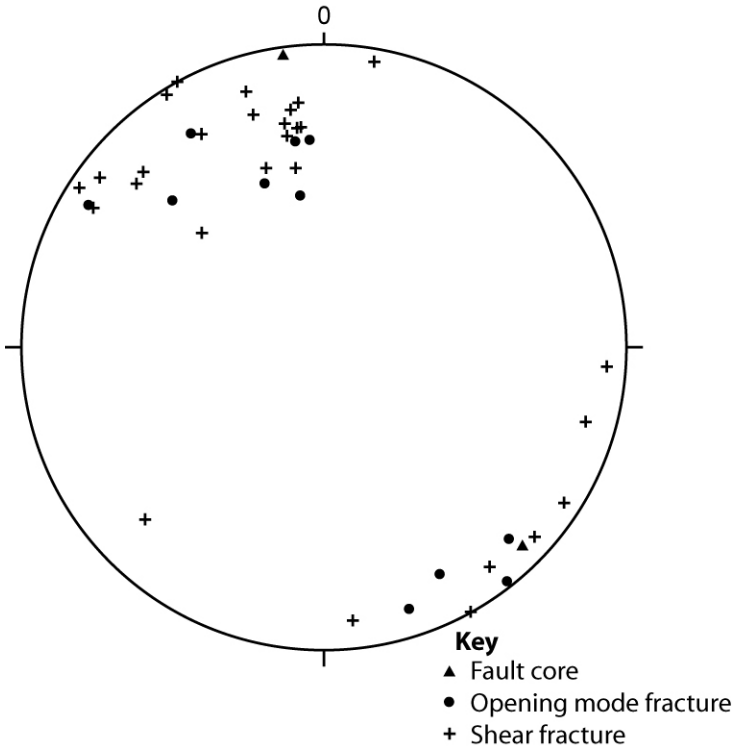

Figure 46. Stereonet of the pole to all the structures sampled by the 1D transect at locality 1.

The deformation elements that comprise the damage zones of the newly identified faults are opening mode fractures and shear fractures. In a similar manner to the GPF damage zone structures, opening mode fractures mostly have a simple morphology; they are straight or slightly wavy, are on the order of 0.1 to 1m long, with apertures of much less than one millimetre to several millimetres. Opening mode fractures are consistently filled with granular epidote and/or chlorite, and often have associated halos of altered protolith that may be up to 10cm in width for an individual fracture. Where several fractures are closely spaced, the alteration halos may coalesce into a single zone of alteration several tens of centimetres in width.

One fracture observed to splay from the Northern strand of Skeeter fault at locality 1 shows that opening mode fractures may also have a branching morphology (Figure 47). The fracture is approximately 1m long in total. It splays from the fault core strand and bifurcates several times in the direction away from the fault core. The branching angles are acute, and five branching levels may be recognised (branching levels are defined following Sagy *et al.*, 2001). The fracture is extremely thin (the aperture is much less than 1mm), so any mineralisation that may be developed is indistinguishable.

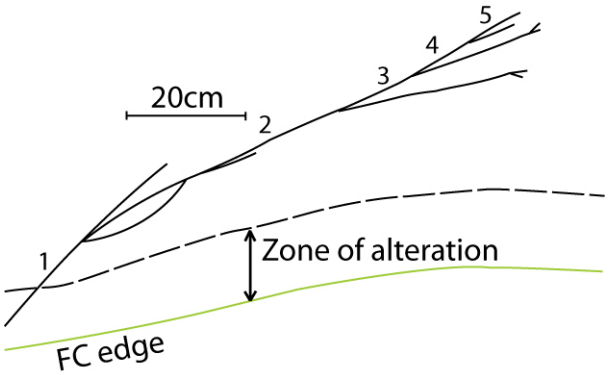

Figure 47. The branching fracture at 1. Branching levels are defined following Sagy *et al.* (2001).

3.6 Discussion

3.6.1 Joints

Field results show that opening mode fractures, interpreted as cooling joints by Moore (1978) and Bergbauer and Martel (1999), are ubiquitous throughout the extent of the Pyramid pluton. Some fractures with small (<1m) amounts of shear displacement are also present, along with the opening mode fractures. Based on the observations that parallel opening mode and shear fractures are present in the same outcrop, containing the same mineral assemblages which are deformed in shear fractures and that both types of fractures have similar alteration halos, these fractures likely originated as opening mode fractures which were subsequently reactivated. A similar conclusion was reached by Segall and Pollard (1983b) for joints and small faults in the Mount Abbot Quadrangle. It is also possible that some of the fractures developed as shear cracks. However, many of the fractures that display shear displacement are tens of metres long, and have displacements of millimetres. Compared to previously reported displacement and length data for small strike-slip faults (e.g. Peacock, 1991), these faults have accommodated significantly less displacement for their length suggesting that they initially formed as opening mode fractures with zero shear offset.

The fracture linkage model (Martel, 1990) predicts that faults in the Sierra Nevada grow by linkage of pre-existing joints. If the GPF or GLF developed by fracture linkage the orientations of the slip surfaces in the fault zones might be expected to be similar to the orientations of cooling joints and reactivated cooling joints in the vicinity of the faults. The distribution of poles to joint orientations clusters strongly around approximately ENE-WSW striking and dipping ~75ºS (close to the mean, see section 3.4.1), with a secondary cluster dipping ~50º (Figure 48). Comparison with the GPF shows that GPF slip surfaces

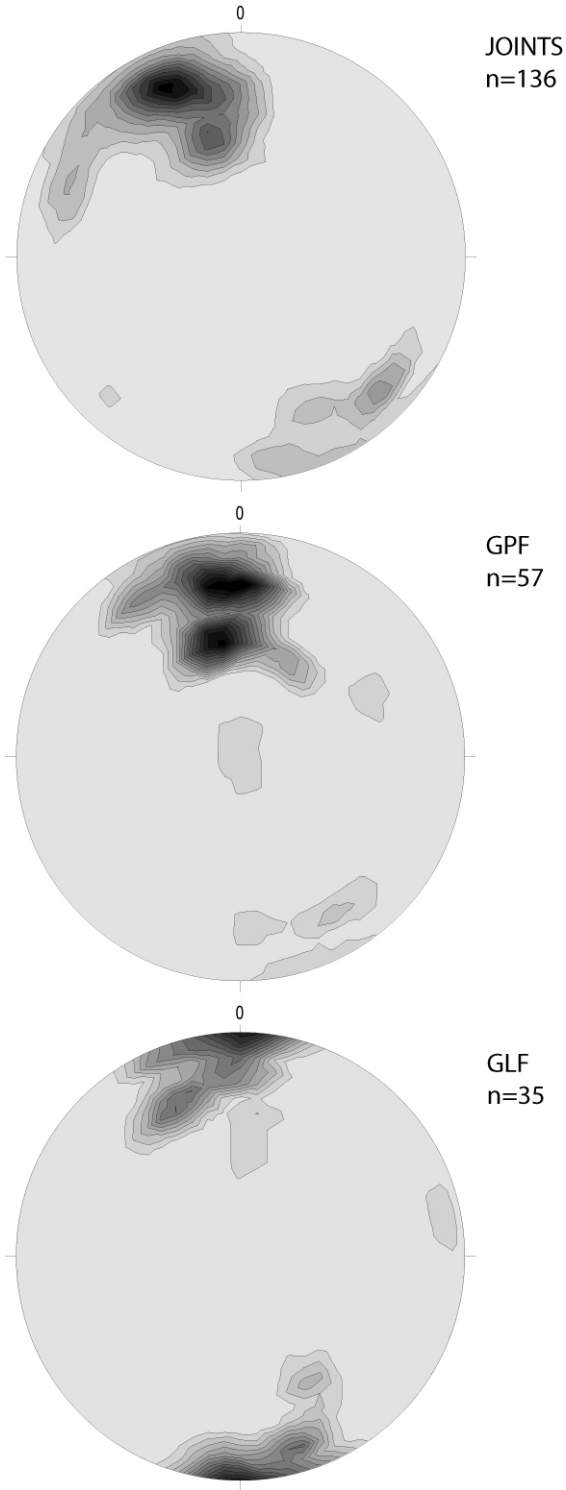

Figure 48. Contour plots of poles to cooling and reactivated joint orientations (top), and GPF (middle) and GLF (bottom) slip surface orientations. Lower hemisphere, equal area projection, contours are intervals of 1.

have a slightly bimodal distribution of orientations. One of the GPF clusters has a very similar orientation to the secondary cluster of joint orientations, and the other is rotated slightly from the main joint cluster. In general, the majority of GPF orientations fall within the range of orientations defined by the population of joints. The GLF poles to slip surfaces also show a slightly bimodal distribution of orientations. One cluster (the less

steeply dipping) is close to the main joint orientation cluster. However, the prominent east-west striking, nearly vertically dipping cluster of GLF slip surface orientations lies outside the range of joint orientations. The GLF therefore contains a significant proportion of slip surfaces that are not similar to the joint orientations, whereas the GPF slip surfaces are all similar to the range of joint orientations. The GPF is therefore more likely to have developed by linkage of the cooling joints.

3.6.2 Fault systems

The data presented in this chapter describe in detail the structures in the study area and are consistent with there being two distinct fault systems; the GPF and GPF-parallel faults, and the GLF and splay faults. The GPF and newly identified faults have many similar characteristics, suggesting that they share a common deformation history. The mean orientation of the GPF is slightly different to that of the mean orientation of the newly identified faults (Figure 49). However, the α_{95} confidence intervals for the two populations of orientation data overlap, indicating that the mean orientations of the GPF and the newly identified faults are statistically indistinguishable. A similar orientation for the faults might be expected if all of the structures in the system had developed in response to the same regional stress fields.

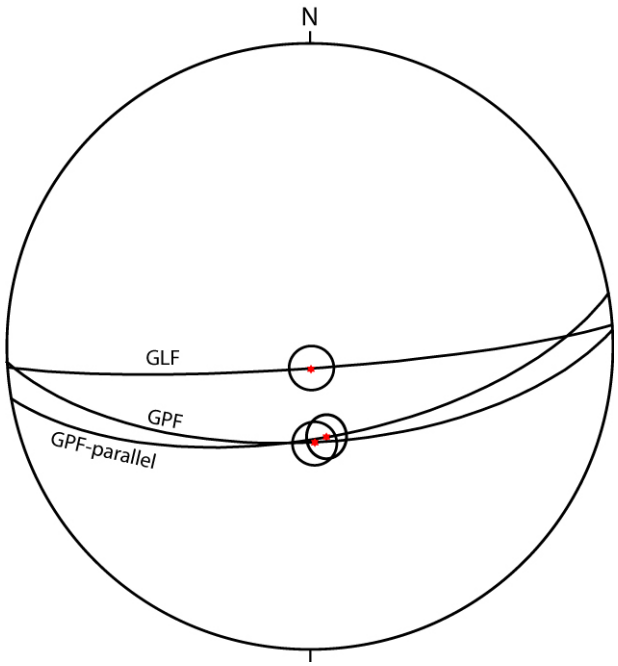

Figure 49. Stereonet (equal angle, lower hemisphere projection) showing the mean orientations (plunge and plunge azimuth of the maximum dip vector, red stars), and the α_{95} confidence ellipses of the GPF, newly identified faults, and the GLF.

The GPF is composed of up to four fault core strands, with fault-related subsidiary structures developed between and outside of the strands. A similar number of fault core strands were observed for the LLF at locality 17 (3 strands), and for Skeeter fault at locality 1 (3 strands), with fault-related fractures abundant at both localities. The macro-scale characteristics of the GPF architecture are therefore similar to those of the newly identified faults. However, some of the newly identified faults (e.g. Kinobe fault at locality 37) are composed of a single fault core strand with a limited number of accompanying subsidiary structures. Exposures of the GPF consistently show that the fault comprises several fault core strands, and never a single fault core. The architecture of the GPF is therefore different to the architecture of the newly identified faults exposed at some localities. The localities where the newly identified faults have multiple fault core strands correspond to the localities where the measured displacements for the faults are greatest. As the GPF also has a relatively high maximum observed displacement, the presence of multiple fault core strands may be a function of increased displacement.

Deformation elements present within the GPF include cataclasites, ultracataclasites and mylonites. Cataclasites and mylonitic fabrics are also present in the GPF-parallel faults showing that the faults contain similarly deformed rocks. Mylonites are well-developed in the GPF and in the GPF-parallel faults and show foliation orientations rotating into slip surfaces, with the intensity of the fabric increasing as the surfaces are approached. This 'bend-in' geometry suggests that both the GPF and the newly identified faults are characterised by left-lateral displacement that accumulated at least in part by crystal-plastic mechanisms, and which was subsequently overprinted by kinematically consistent brittle fracture. The faults must therefore all have been active during both ductile and brittle conditions.

The GLF and splay faults are part of a single fault system, with the splay faults branching off from the main trace of the GLF. There are no splay faults to the north of the GLF fault trace. The mean GLF orientation is distinct from both the mean GPF orientation and the mean of the newly identified faults as the α_{95} confidence interval of the GLF does not coincide with either of the intervals for the other faults. Orientation data collected from the splay faults show the splays form average angles of 39º to the GLF, and also that the orientations are significantly different to the GPF and newly identified faults.

Field observations demonstrate that the GPF and its associated suite of sub-parallel faults are consistently cross-cut by the splay faults from the GLF. The GPF and newly identified

faults are never observed to cross-cut the splays or the GLF. Mylonitic fabrics indicative of localised ductile deformation are present within the GLF, but are not observed with the pronounced bend-in geometry of the GPF. The GLF fabrics are developed in fracture-bounded terranes within the fault zone, but cannot be shown to be kinematically related to the GLF deformation.

The consistent cross-cutting relations between the two fault systems, together with the absence of ductile fabrics in the GLF fault zone, indicate that the GLF and related splays post-date the GPF. The splay faults at the western extent of the GLF therefore represent a termination structure, rather than a step-over between two coeval strike-slip faults. A similar conclusion was drawn by Evans *et al.* (2000), based on petrographic observations alone. The faults between the GPF and GLF provide planes of heterogeneous mechanical properties that could have influenced the GLF (e.g. Burgmann *et al.*, 1994). However, given that the GLF splay faults are observed to cross-cut and displace some of the GPF-parallel faults, it is unlikely that the GLF terminates because of the presence of the GPF.

The mean orientations of the GLF and the GPF show that the difference in the fault plane orientations is small; the GPF dips around 75º towards the south whereas the GLF is nearly vertical. The GPF may therefore have been in part coeval with, or reactivated by the GLF. Yin and Ranalli (1992) show that for a pre-existing plane of weakness, the reactivation of the anisotropy depends on its orientation with respect to the stress field. Assuming that the GLF was active under an Andersonian stress system (i.e. σ_2 vertical for a strike slip fault), the GPF would be favourably oriented for reactivation in a narrow range of orientations (Figure 50). Following Yin and Ranalli (1992), the pole to the mean GPF orientation has been related to the GLF stress regime by measuring the angles between the GPF pole and the inferred σ_1, σ_2 and σ_3 (Figure 50). The results show that the GPF, in its current orientation with respect to the GLF, would be favourably oriented for oblique-normal faulting under a GLF stress system. The inferred direction of normal faulting is down to the south east.

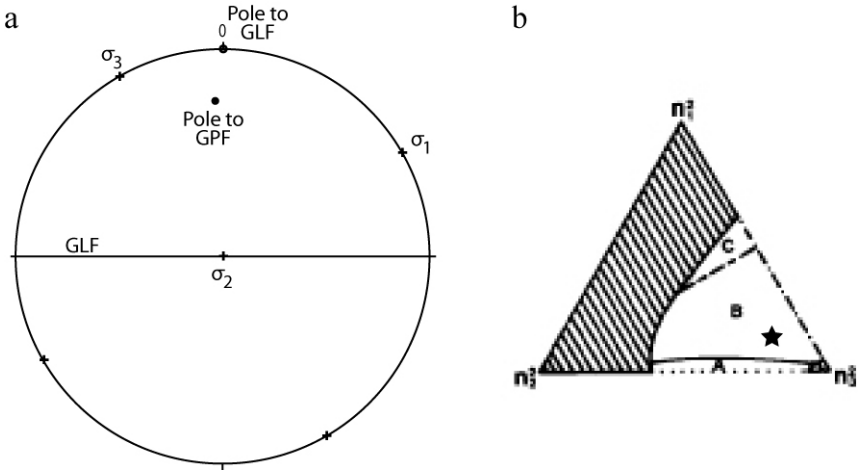

Figure 50. An analysis of the potential reactivation of the GPF by the GLF. a. The GLF is assumed to be a vertically-dipping, east-west striking left-lateral strike-slip fault that is active in an Andersonian stress system; σ_1, σ_2 and σ_3 are the orientations of the principle stress directions. b. Angles between the pole to the GPF and the principal stress directions have been used to calculate the parameters n_1, n_2 and n_3 of Yin and Ranalli (1992). The results are plotted on a triangular diagram (Yin and Ranalli, 1992; their Fig. 10) where zone A corresponds to normal-oblique faulting, B to oblique-normal, and C to oblique-thrust faulting where the first term denotes the predominant component of slip. The GPF (star) is favourably oriented for oblique-normal reactivation, with throw down to the south east. Calculations are for depth = 10km, cohesion = 75MPa, coefficient of steady-state sliding friction = 0.75, hydrostatic pressure and σ_2 = vertical stress.

3.6.3 Fault zone architectures

Data collected to describe the fault zone architectures of the faults have been collated to produce generic models for fault zone architecture for the GPF and GLF fault systems (Figure 51; Figure 52). The GPF architectural model is for a left-lateral strike-slip fault that is ~7km long, cutting crystalline basement rocks, and with around 80m displacement. The model is also expected to describe the architecture of the newly identified faults where the displacement magnitudes are high.

In the model, the fault zone is composed of 3 to 4 fault core strands that contain primarily cataclasites and ultracataclasites, overprinting mylonites developed in places in the wall rock. Fault core strands are oriented sub-parallel to the overall fault zone, but anastomose and bifurcate along strike. The strands range in thickness from around 10cm to several metres, with order of magnitude thickness changes occurring over lateral distances of tens of metres. Slip surfaces are developed within fault cores, at the edges of fault core strands and between the fault cores, accommodating a heterogeneous strain distribution across the fault zone. Slip surfaces are defined by pseudotachylytes, polished surfaces with slickenlines, and thin seams of extremely comminuted cataclasite. Fault-related subsidiary structures are present between fault core strands, which take the form of opening mode and shear fractures with a variety of morphologies. Between fault core strands, the spacing of

the subsidiary fractures is as little as several centimetres, resulting in fracture frequency on the order of tens per metre. Fracture frequency between fault core strands decreases as the strands get further apart. Subsidiary fractures are also developed outside the fault core strands, with fracture frequency reaching around 10frs/m, which is elevated above the background level for up to 10m. These fractures form acute angles with the fault core strands. The total fault zone width is variable along strike, but is typically around 30m.

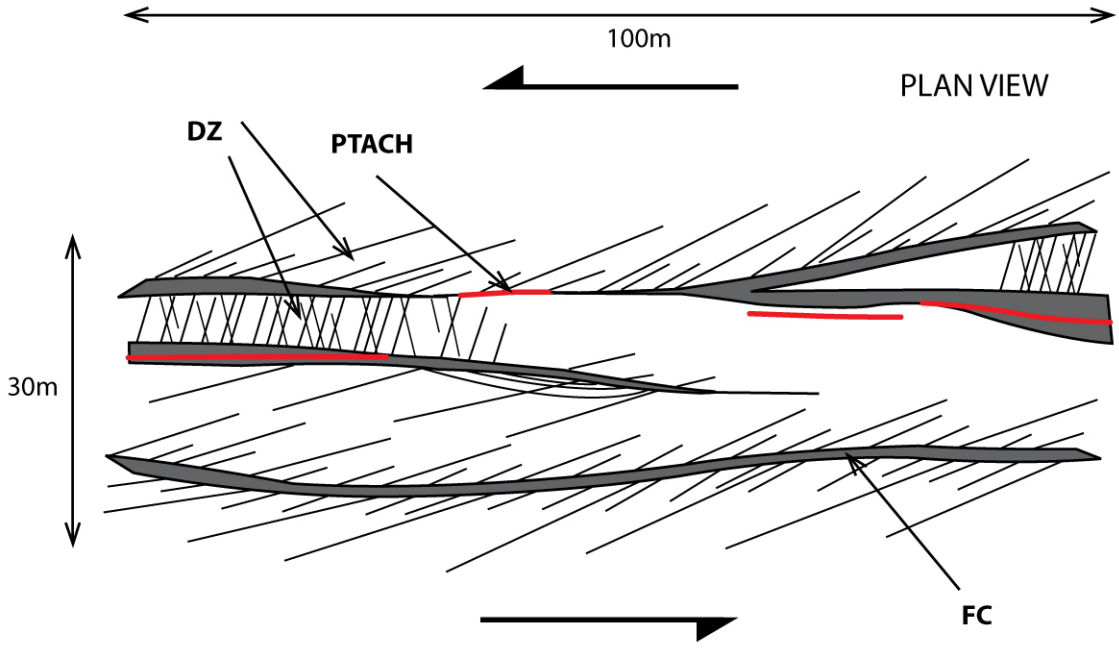

Figure 51. A plan view of the generalised fault zone architecture model for the GPF showing multiple fault core strands and abundant subsidiary structures between and beyond the extent of the strands. Scale bars show a typical fault zone width and the along strike distance over which lateral variations in the architecture might be expected to occur.

The GLF model architecture is based upon less field data, so the model is more schematic than the GPF. The GLF model describes a left-lateral strike-slip fault that is approximately 8km long, cutting crystalline rocks, and with around 125m displacement (Figure 52). In the model, the fault zone is composed of two planar bounding fault core strands that are centimetres thick and contain cataclasites. Between the bounding fault cores, additional fault core strands may be present that are tens of centimetres thick, and which are oriented parallel to the bounding fault cores. There are also abundant fault-related subsidiary structures, spaced 2 to 10cm apart producing a fracture frequency of tens of fractures per metre. Slip surfaces in the form of polished surfaces are present at the edges of the fault core strands, and also within the fault cores as seams of comminuted cataclasites. Outside the bounding fault cores, subsidiary structures are present in two distinct orientations; one at low angle (~30º) to the fault cores and one at higher angle (50º). The fracture frequency outside of the bounding fault cores is around a few fractures per metre, which decreases to

the background level within 1 to 2m. The fault zone width of the GLF model architecture is generally around 10 to 15m, though it may be wider at intersections with splay faults.

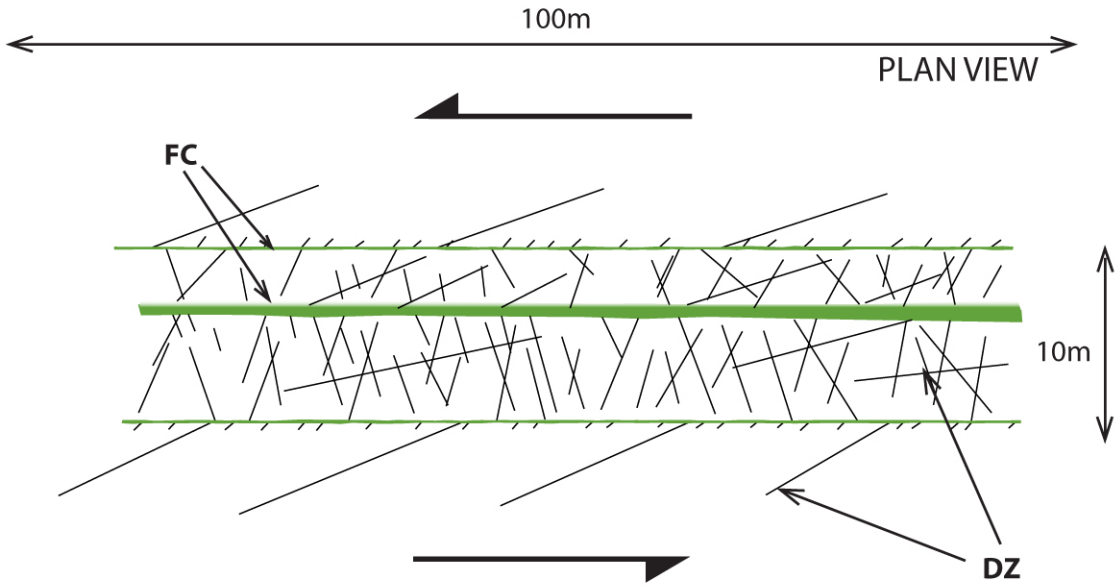

Figure 52. Representation of the generalized GLF fault zone architecture in which intense deformation is present between planar bounding fault core strands, beyond which deformation decreases rapidly.

The two fault zone architectures are similar in that both fault zones comprise fault cores of predominantly cataclasite that are present in strands, with associated subsidiary structures. However, several significant differences are present that distinguish the faults from each other. The GLF architecture is characterised by the presence of roughly planar bounding fault core strands. Such well-defined fault core strands close to the edges of the fault zone are not consistently present within the GPF. Fault core strands in the GPF are also frequently non-planar and bifurcate and anastomose along strike. In contrast to the extremely limited damage zone outside the GLF bounding fault core strands, the GPF damage zone may be diffuse and much wider than in the GLF. The fracture frequency within the GPF damage zones is also higher than in the GLF.

These specific differences between the two fault architectures give rise to some broad differences in the model architectures. The overall fault zone width of the GPF model is generally greater than the width of the GLF. This is primarily due to the greater number of fault core strands, but also due to the extensive damage zone outside the fault core strands. The GPF architecture is also more variable along strike than the GLF model architecture as the number of fault cores and the thicknesses of individual fault core strands are more changeable than in the GLF.

3.6.4 Comparison with the Gemini fault zone

The steeply-dipping Gemini fault zone exposed in the Mount Abbot Quadrangle is 9.3km long with a maximum left-lateral strike-slip displacement of 131m (Martel, 1990; Pachell and Evans, 2002). The fault cuts four plutons that are mechanically relatively mechanically homogeneous, and is inferred to have been active towards the base of the seismogenic zone (Pachell and Evans, 2002). As such, it is directly comparable with the larger fault zones analysed in this chapter (i.e. GPF and GLF).

The Gemini fault zone has been studied in detail by Pachell and Evans (2002). Their analyses of the fault trace and along-strike slip profile shows that the fault is composed of three ~3km long non-coplanar segments that are separated by slip minima. Each segment of the fault is locally sub-parallel to cooling joints developed in the host rock plutons. The western termination of the fault is geometrically analogous to a horsetail structure; a series of subsidiary faults 0.3 to 0.5km long splay counter-clockwise from the main trace of the fault. Field observations presented by Pachell and Evans (2002) show that the Gemini fault zone is composed of multiple brittle slip surfaces between two narrow bands (<5cm) of cataclasites that define a fault trough 2 to 15m wide. They observed fault rocks including mylonites, cohesive cataclasites and breccias and extensive sericite- and zeolite-filled veins, and demonstrated that early ductile deformation was overprinted by brittle deformation that occurred at sub-greenschist facies conditions. Although the Gemini fault zone does not scale directly from the small faults and simple fault zones described by Segall and Pollard (1983b) and Martel et al. (1988), Pachell and Evans (2002) concluded that the fault grew by linkage of the non-coplanar segments, which were likely controlled by pre-existing joints.

The Gemini fault zone is similar to the GLF in several respects. The length and magnitude of observed strike-slip displacement are very closely matched. The western terminations of the two faults are also comparable; subsidiary faults splay from both of the main fault traces into the dilational quadrants of the left-lateral faults. The internal character of the Gemini fault zone is better documented than that of the GLF. However, both faults are defined by fault troughs due to preferential erosion of highly fractured and deformed wall rock between bounding fault strands. Multiple fault strands are observed in places along the Gemini fault zone, which seem directly analogous to the multiple fault strands within the GLF at locality 23 (e.g. Figure 32). The only significant difference seems to be the segmentation of the Gemini fault zone. However, the GLF slip profile has not been

constructed for most of the eastern part of the fault so assessing the potential for slip minima is impossible.

In contrast to the GLF, the GPF shares few similar characteristics with the Gemini fault zone. The length and displacement magnitude for the GPF may be of the same order of magnitude as the Gemini, but as neither fault termination of the GPF is mapped, this remains uncertain. Equally, splay faults are not observed in association with the GPF but this may also be due to the absence of pertinent data for the GPF. However, the fault zone architectures of the GPF and Gemini faults do seem distinct; the GPF is not composed of a fault trough containing brecciated rock bounded by narrow fault strands. The GPF is therefore distinct from both the GLF and Gemini fault zone.

3.7 Summary

Field observations demonstrate that in addition to cooling joints, two systems of faults are present in the Granite Pass study area; the GPF and GPF-parallel faults, and the GLF and splay faults. The GPF system of faults contain pseudotachylytes and are characterised by a complex architecture in which multiple fault core strands and slip surfaces are associated with a broad (up to 30m wide) zone of fault-related damage. Orientation data indicates that the GPF may be genetically related to pre-existing cooling joints inherent to the host pluton. Fault core strands vary in thickness by an order of magnitude along strike, with thickness changes coinciding with the deformation product that locally defines the strand. The GLF and splay faults have a different architecture characterised by a volume of damaged host rock bounded by two fault core strands centimetres in thickness. Fault-related damage is limited to several metres in extent beyond the bounding fault strands. The GLF splay faults cross-cut the faults of the GPF system, suggesting that the GPF system is older. However, reactivation of the GPF during GLF deformation is possible assuming the GLF was active in an Andersonian stress system.

4

Microstructural Analysis of the Granite Pass Faults

4.1 Introduction

Many of the most important properties of faults for earthquake rupture processes (e.g. width of the coseismic slipping zone, thickness of structural units with differing permeability properties) are thought to be localised to the millimetre- or centimetre-scale. Constraining these parameters therefore requires observations of faults at thin section as well as outcrop scale. Grain-scale deformation is accomplished by a wide variety of mechanisms in natural faults, which produce different textures in fault rocks. These textures are indicative of the deformation conditions, as well as the type of slip, and so a suite of grain-scale observations will be distinctive to a fault.

This chapter aims to provide a detailed description of some of the deformation elements that make up the various fault zones in the Granite Pass study area. Microscope and SEM analyses will be utilized to determine the composition, geometries and deformation mechanisms of the various fault rocks from the GPF, SKF and the GLF. Observations of the deformation features and products of fluid flow will enable the deformation histories of the two systems of faults to be compared. Particular attention will be paid to slip-related structures within the GPF so that the mechanisms of slip and the slip weakening mechanisms that were active during co-seismic slip can be investigated.

4.2 Methodology

Oriented samples were collected in the field that were re-oriented in the lab in Glasgow for thin section preparation. Samples were marked and cut for thin section preparation along a plane with a specific orientation with respect to the fault from which the sample was collected. In general the plane perpendicular to the fault containing the inferred slip vector for that fault was chosen to display the maximum kinematic information, but several

samples were also prepared perpendicular to the slip vector to analyse changes that might occur up and down dip along a fault plane. Large (75 x 55mm) thin sections 30μm thick were prepared for all samples. Some sections were polished for SEM analysis, and some were covered for standard optical microscope analysis (Table 2). All samples were impregnated with blue resin during thin section preparation to highlight porosity in the samples, and provide a qualitative gauge for the relative permeabilities of the fault rocks.

Standard optical microscope and scanning electron microscope (SEM) images are presented in this chapter to describe the composition and textures in the samples. SEM analysis utilised an FEI Quanta 200F environmental SEM with secondary electron and back-scattered electron detectors in high vacuum mode. The installation is equipped with an EDAX Pegasus 2000 Energy Dispersive X-ray microanalysis (EDX) system enabling qualitative spot, line and map scans of chemical compositions.

Sample	Locality	Fault	Component	Orientation
GPP1	35	n/a	Host rock	n/a
GPF10	28	GPF	FC	2
GPF5	18	GPF	FC	2
GPF6	18	GPF	FC	2
GPF7	21	GPF	FC	2
GPF11	31	GPF	SS	1
GPF2	18	GPF	DZ	2
SK8	1	SKF	FC	2
SK9	1	SKF	SS	2
SK10	1	SKF	FC	2
GLF5	2	GLF	FC	2
GLF3	23	GLF	FC	2
GLF4	23	GLF	FC	2

Table 2. List of the samples analysed in this chapter showing the localities from which they were collected, the fault that the sample is from, the prominent fault zone components present within each sample (FC = fault core; SZ = slipping zone; DZ = damage zone), and the orientation of the thin section with respect to the inferred predominant slip vector at the sampling site (1 = perpendicular to the slip vector, 2 = perpendicular to the fault orientation and parallel to the slip vector).

An SEM works by directing a beam of electrons at a sample, which interact at an atomic scale with the material of the sample in a number of ways. Back-scattered electron (BSE) imaging uses electrons reflected back from the main electron beam by crystals at the sample surface. The characteristics of the back-scattered electrons depend on the crystal structure and chemical composition of the substance that the beam interacts with, and therefore carry information on the composition the sample. Atomic number, or Z-contrast, images are constructed by scanning the electron beam over an area of a sample. These

images are grey-scale, with different tones representing different mean atomic weights; in general brighter tones (closer to white) represent minerals that contain more elements with a high mean atomic number. The secondary electron emission detector captures electrons that are detached from the sample by the electron beam. This analysis is useful for studying the topography of a sample; as the thin sections were polished in this study, the SE detector was used to cross-check charge effects in BSE images due to cracks or pores inherent to the sample. EDX analysis measures the energy of X-rays emitted by atoms at the surface of a sample by the electron beam. Minerals can be recognised through the elements identified by the EDS detector, and correlated with the grey scale of BSE images. Labels showing the composition of different phases added to BSE images in this chapter have been determined by EDX analysis.

4.3 Host rock: the Pyramid pluton granodiorite

The faults in the study area cut crystalline plutonic rocks of Cretaceous age (Moore, 1978; see also Chapter 2). All of the sites from which samples of the GLF, GPF and GPF-parallel faults were collected are located within the Pyramid pluton. The mineralogy, textures and deformation features inherent in the host rock to the faults will be described in this section.

Moore (1978) described the Pyramid pluton as being composed of a dark granodiorite with some granite, quartz monzo-diorite and quartz diorite. The pluton is relatively homogenous, except in the vicinity of Volcanic Lakes, where the rock is dominated by a more mafic western facies. Sample GPP1 is an unoriented sample collected from locality 35 (see Table 2 and Appendix 1) where recent trail maintenance had created fresh exposure. The locality is as far away from mapped structures as was possible to define in the field, so is useful for defining the micro-scale background deformation.

Sample GPP1 is typical of the Pyramid pluton granodiorite consisting of inequigranular (1-10mm) plagioclase feldspar (~40%), quartz (~25%), orthoclase (~15%), biotite (~10%) and hornblende (~10%) with accessory titanite, zircon, apatite and opaques. In hand specimen large (≤6mm), euhedral biotites and acicular hornblendes (≤7mm), which are often clustered into small aggregates, are prominent in a groundmass of finer quartz (≤3mm) and feldspars (1-10mm) though the distinction between feldspars can be difficult where weathered. The rock lacks foliations or any fabrics other than the randomly oriented, interlocking crystals of a plutonic rock.

In thin section, quartz crystals are anhedral, filling irregular shapes between other euhedral minerals. Undulose extinction is ubiquitous, and is sweeping in some cases. Extensive recrystallisation by subgrain rotation and/or grain boundary migration has resulted in the development of numerous subgrains around the edges of some quartz crystals. Subgrains also comprise the entire volume of some crystals, giving quartz-rich portions of the rock an inequigranular, interlobate texture. Subgrain development is particularly pronounced where quartz crystals have been impinged by adjacent euhedral minerals (Figure 53). Intra-crystalline fractures are abundant in quartz, cross-cutting subgrain boundaries, but apparently lacking systematic orientations. The fractures contain small amounts of epidote mineralisation. Fluid inclusion trails are also present that are often sub-parallel and spaced as closely as ~0.1mm.

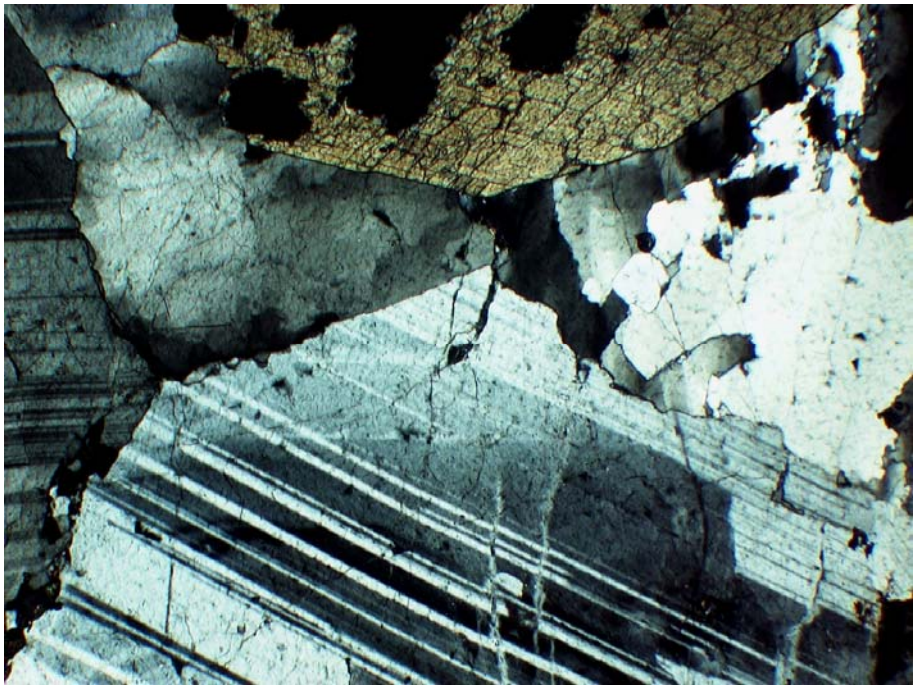

Figure 53. Quartz deformed by grain boundary migration recrystallisation consists of numerous sub-grains that account for nearly the entire volume of the mineral. The quartz is impinged on two sides by larger, euhedral hornblende (top) and plagioclase feldspar (bottom; XPL, field of view 3.1mm).

Plagioclase feldspar predominates over the alkali feldspars in thin section. Plagioclase feldspar forms euhedral, tabular to elongate crystals ≤10mm in length which have lamellar twinning. Larger crystals display strong oscillatory zoning and contain inclusions of biotite, hornblende, and euhedral apatite. Orthoclase microperthite with patches of microcline, with distinctive cross-hatch twinning, tend to form small (≤2mm), interstitial, subhedral crystals. Deformation twinning, healed intra-granular fractures filled in places with epidote, and fluid inclusion trails oriented approximately parallel to twin planes are common in the plagioclase feldspars. Myrmekites with characteristic vermiform quartz

and plagioclase intergrowths form around some plagioclase crystal edges where the plagioclase is adjacent to orthoclase (Figure 54). Alkali feldspars also display deformation twins, as well as occasional kink bands and healed intra-crystalline fractures.

Figure 54. Myrmekite developed in a plagioclase feldspar crystal showing characteristic vermiform intergrowths of quartz and plagioclase (XPL, field of view 1.6mm).

Biotite crystals exhibit characteristic brown to dark brown pleochroism, and appear to have a bimodal size distribution. Smaller (~1mm), crystals are consistently euhedral, though larger crystals (≤5mm) are often subhedral or anhedral, containing cleavage planes that are kinked, or slightly bent, and undulose extinction. Crystal edges are frequently straight parallel to the cleavage planes, and irregular orthogonal to the cleavage. Inclusions of small, euhedral apatite and zircon are common in the biotite crystals. However, intra-crystalline fractures are extremely rare, and fractures within adjacent minerals terminate against biotite crystal edges. Chlorite replaces portions of some biotites, generally around the edges of the crystals. Aggregates of extremely fine crystals that are probably epidote are localised in embayments in the irregular crystal faces of deformed biotite.

Prismatic hornblende crystals are ≤5mm and tend to be euhedral with straight edges where adjacent to feldspars, but are irregular adjacent to some quartz crystals. Large (≤0.5mm in length), blocky, opaque mineral inclusions are abundant, along with euhedral zircons. Pyroxene crystals are present towards the centre of some large hornblendes, which have replaced the original pyroxene. Hornblende is itself replaced by biotite and chlorite at the edges of some crystals. Fractures are frequently distributed throughout the crystals,

commonly oriented orthogonal to the dominant cleavage planes in the section of view. Undulose extinction is never developed in hornblende crystals.

A significant degree of deformation is observed in sample GPP1. Grain boundary migration recrystallisation, deformation lamellae and sweeping undulose extinction in quartz attest to deformation that occurred at medium to high temperatures (400-600ºC) and relatively low strain rates (Passchier and Trouw, 2005). However, quartz does not form elongate crystals or aggregates of recrystallised subgrains that might define a foliation. Feldspars and hornblende impinge recrystallised quartz, and are deformed exclusively by brittle fracture; undulose extinction is poorly developed or absent in these minerals. Though feldspar would also be expected recrystallise at temperatures greater than ~500ºC, mantles of feldspar subgrains are not developed around any feldspar crystals. The combined behaviour of quartz and feldspar suggests that the rock was homogeneously strained at temperatures around 400-500 ºC. Brittle fractures are ubiquitous throughout the sample, including both intra- and inter-crystalline fractures in quartz and feldspar (Figure 55), cross-cutting the recrystallisation textures. However, it is unclear how much of the fracturing is due to the sample preparation process; further SE analysis of a fractured surface of the sample (rather than cut surface, or thin section) is required to quantitatively establish the impact of thin section preparation for all samples.

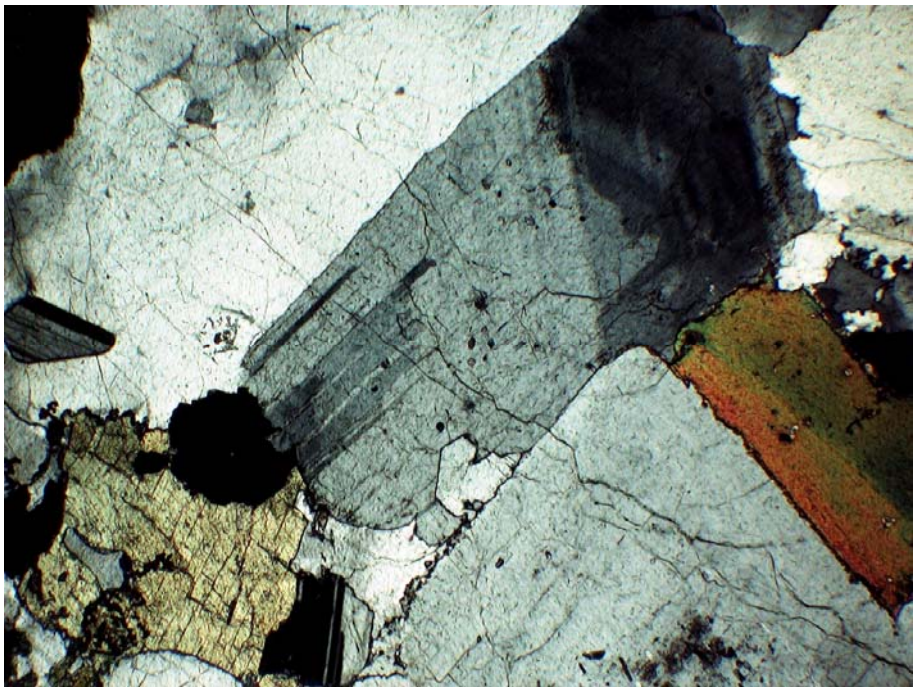

Figure 55. Inter-crystalline fractures cross-cutting the boundary between adjacent quartz and plagioclase feldspar crystals (XPL, field of view 3.1mm).

Epidote mineralisation in fractures within quartz and feldspars is evidence for fracture-controlled fluid flow within sample GPP1 under greenschist facies conditions. Chlorite replacement of biotite and hornblende tends to be localised around the edges of crystals, and minerals precipitated from fluids are also present along grain boundaries suggesting that fluid flow also occurred at grain boundaries. Aggregates of precipitated minerals are concentrated at irregularities induced by deformation especially in biotite. The fluid flow may therefore have been coeval with the deformation, though evidence for dissolution-precipitation is not observed.

4.3.1 The Pyramid pluton: summary

The Pyramid pluton granodiorite is composed of inequigranular (1-7mm) plagioclase feldspar (~40%), quartz (~25%), orthoclase (~15%), biotite (~10%) and hornblende (~10%) with accessory titanite, zircon, apatite and opaques. The observed textures that are indicative of crystal-plastic deformation, fracturing and fluid flow are the product of processes inherent to the host rock.

4.4 The Granite Pass fault

4.4.1 Cataclasites

Cataclasites are the primary constituents of fault cores within the GPF. As described previously (section 3.5.2.1) a variety of different types of cataclasites may be distinguished based upon the degree of comminution of the fault rock. Different cataclasites are frequently juxtaposed, and cataclasites are also juxtaposed against other fault core deformation elements.

Sample GPF10 is from the central fault core strand exposed at locality 28 (see Figure 22) which is composed of inter-layered cataclasites and ultracataclasites, but which lacks any obvious slip surfaces. Arcuate fractures splay from this fault core strand. The sample contains several cataclasites that have distinct colours and grain sizes. Prominent in thin section is a central zone of dark brown, predominantly aphanitic matrix material (~90%) that dies out within the section. SEM imaging of the central aphanitic zone shows that it is composed of a fine-grained (mostly ≤10μm) granular matrix enriched in epidote, titanite and magnetite. The zone is 0.2 to 1.5mm thick and contains layers of matrix material with slightly differing colours in which clasts 25 to 500μm long are composed of recrystallised quartz and feldspar. The long axes of the clasts define a grain shape fabric oriented ~30-

40º clockwise from the trend of the zone. Some lenses of matrix material, as well as occasional multi-crystalline clasts of recrystallised minerals, have asymmetric, mineral-fish shapes (Figure 56) that define an S-C' type fabric (Passchier and Trouw, 2005). Two fractures that are filled with euhedral chlorite (≤100μm) and massive quartz appear to splay from within the central aphanitic zone (Figure 56). These two fractures coalesce to form a single, wider fracture (0.2mm maximum thickness) within the section, but are otherwise undeformed. The edges of the central zone are sharp but irregular. The southern edge wraps around clasts within the adjacent cataclasite, but is diffuse and difficult to distinguish in places. Some clasts in the cataclasite to the north of the zone are sheared and smeared into the central zone, forming similar asymmetric shapes to the mineral-fish within the zone.

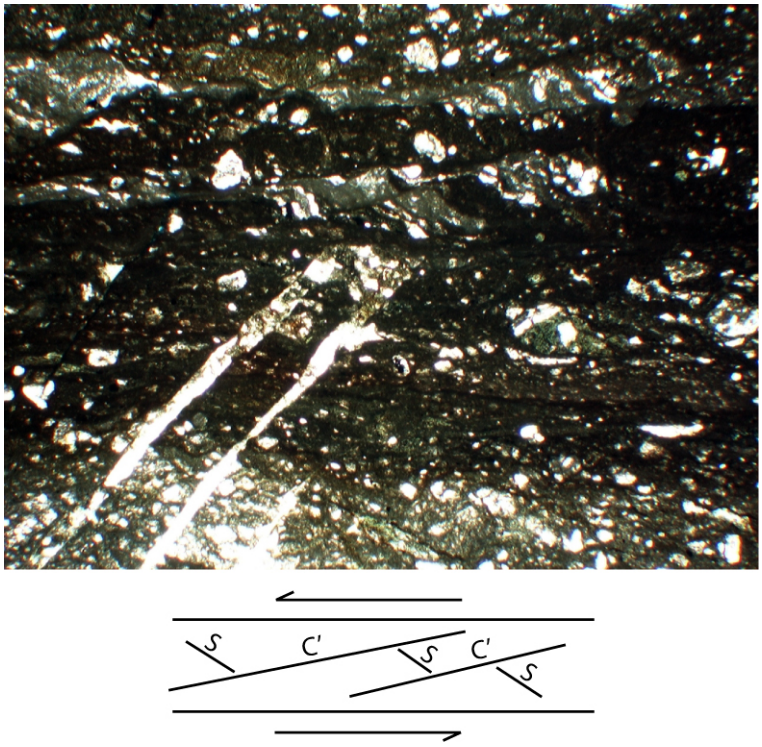

Figure 56. The central aphanitic zone of GPF10 contains ~90% matrix material. Lenses of matrix material, as well as some clasts have mineral-fish habits. The S-C' type fabric is consistent with left-lateral shear. Two chlorite and quartz filled fractures (lower left) that appear to have splayed from within the zone are otherwise undeformed (PPL, field of view 3.1mm).

The central aphanitic zone cross-cuts a more coarsely-grained fault breccia that is up to 2cm thick. The breccia contains random-fabric, angular to rounded clasts 30μm to 2.5mm long. Clasts comprise ~75% of the breccia and have a variety of compositions including fragments of previously generated pseudotachylyte, pseudotachylytes that are cross-cut by quartz-filled veins, clasts of previously formed cataclasite, fragments of quartz veins, and occasional fragments of single quartz plagioclase, and alkali feldspar. A grey-brown, aphanitic matrix is present between the clasts.

The wall rock to the fault breccia is an intensely deformed rock that contains a variety of deformation textures, which are cross-cut by numerous fractures indicative of a cataclasite. Alkali and plagioclase feldspar fragments in the wall rock cataclasite contain healed fractures in survivor grains that are surrounded by subgrains developed along grain boundaries bulging recrystallisation (Figure 57). The boundaries between survivor grains and mantles are diffuse. Quartz consistently displays sweeping undulose extinction and extensive recrystallisation by subgrain rotation and bulging recrystallisation mechanisms. The crystal-plastic deformation textures in the quartz and feldspars are cross-cut by brittle fractures that have broken the rock into fracture-bounded clasts ≤0.8mm long that are angular to sub-rounded. This cataclastic fabric is often difficult to distinguish due to the complexity of the textures within clasts. Matrix material is present between clasts that is chlorite rich, but generally aphanitic. Fractures filled with euhedral chlorite and quartz are present in the cataclasite, but are truncated at the cataclasite-fault breccia contact.

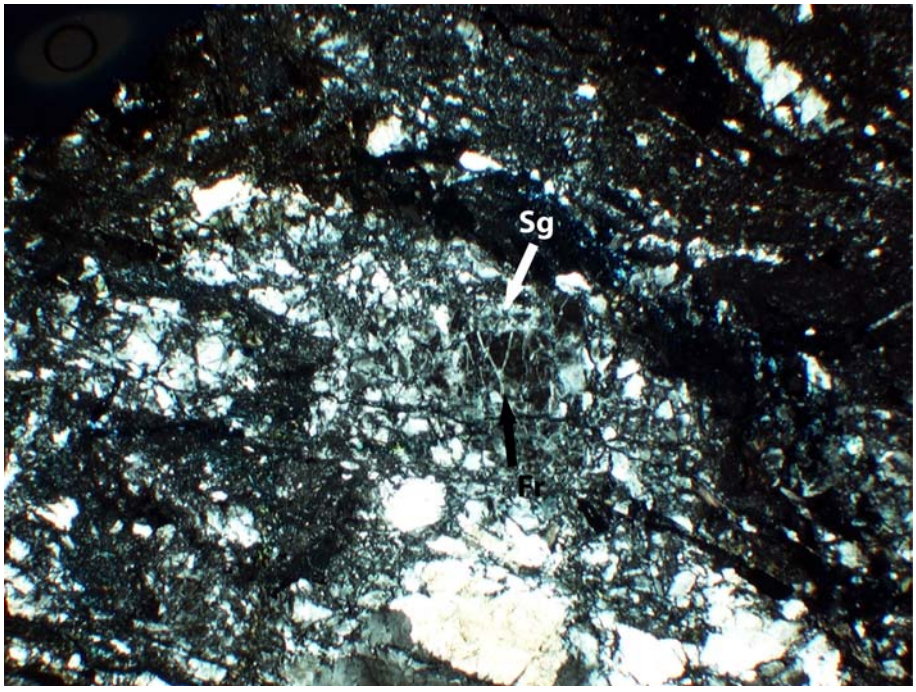

Figure 57. The wall rock to the fault breccia in sample GPF10 contains complex deformation textures. In this photomicrograph, an alkali feldspar crystal contains healed fractures (Fr) that are over-printed by subgrain rotation recrystallisation (Sg; XPL, field of view is 3.1mm).

The fault breccia - wall rock contact is sharp and approximately planar except for two significant irregularities that have similar geometries to injection veins associated with pseudotachylyte generation surfaces (Figure 58). The larger of these two structures has an aperture of 2mm, is at least 4mm long, and forms an angle of ~30º with the trend of the fault breccia-wall rock cataclasite contact in the plane of the section. The structure contains material that is composed of rounded to sub-rounded clasts (~80%) that are 0.1 to

0.3mm in length in a dark grey-brown aphanitic matrix. Fragments of pseudotachylyte, pseudotachylyte that is cross-cut by veins, and fragments comprising aggregates of dynamically recrystallised quartz and feldspar, and also some chlorite are present in the structure. The clasts define a random-fabric material that is directly connected to the fault breccia; the structure is filled with the same material that makes up the fault breccia. The smaller of the two irregularities is also filled with the same material as the fault breccia, but is narrower, forms a higher angle with the trend of the wall rock contact (~50º), and is longer (~8mm). A small pocket of aphanitic ultracataclasite material is present between the wall rock cataclasite and the fault breccia in one local embayment in the wall rock cataclasite edge, which is also truncated by the fault breccia.

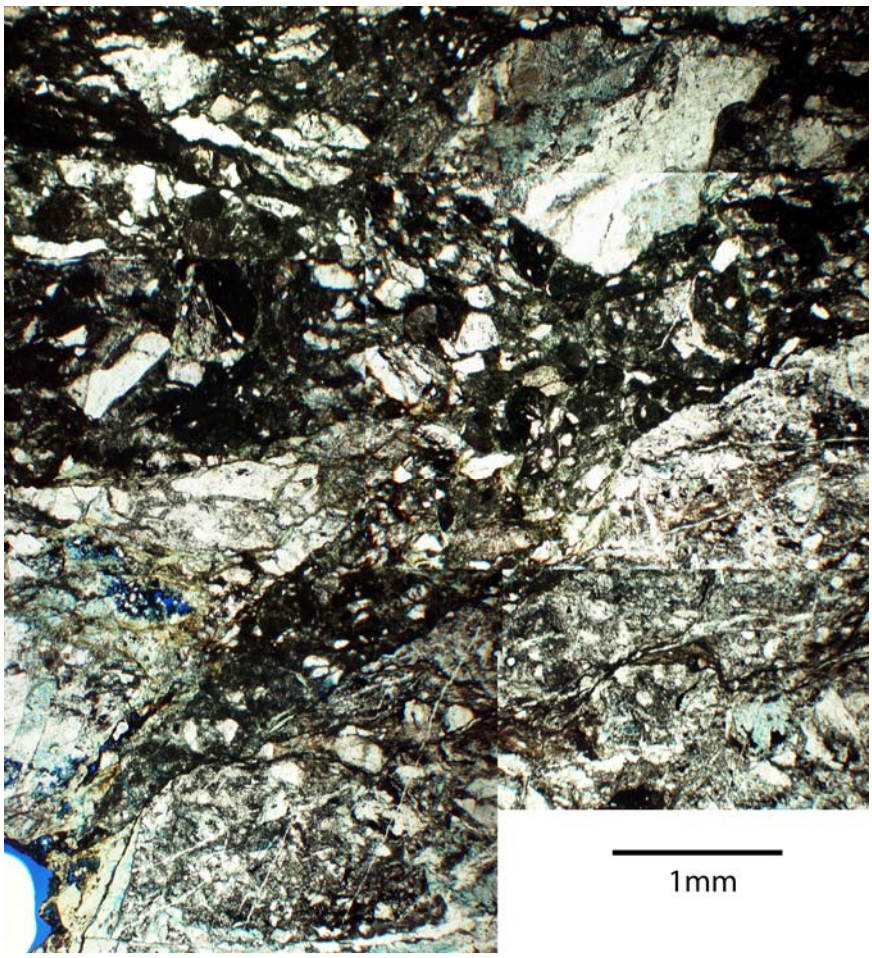

Figure 58. An irregularity in the fault breccia – wall rock contact has a similar geometry to an injection vein and contains the same material as that which comprises the fault breccia (PPL).

4.4.1.1 GPF10: summary

Cataclasites with varying degrees of comminution comprise all of the fault rock in GPF10. Cataclasites contain fragments of deformation products including pseudotachylytes and

recrystallised feldspars demonstrating the GPF has a deformation history involving crystal-plastic deformation, followed by multiple brittle slip events.

4.4.2 Ultracataclasites

Samples GPF5, GPF6 and GPF 7 contain greenish black material classified as ultracataclasite based on field and hand specimen observations (see section 3.5.1.3). Thin section observations show that the cataclasites are composed of clasts in a chlorite- and epidote-rich matrix (Figure 59). Clasts account for ~40% of the bulk ultracataclasites, but locally the proportion of clasts varies between <10 to ~80%, reflecting the lenses of more or less clast rich material described in section 3.5.1.3. Clasts are ~20μm to 4mm long, and around 90% of clasts are composed of quartz. Quartz clasts vary from angular or sub-rounded fragments of crystals that display undulose extinction or occasionally localised bands of subgrains developed by bulging recrystallisation to rounded aggregates of intensely recrystallised quartz. The rounded aggregates contain small (typically ≤50μm) subgrains occasionally surrounding cores of quartz that have sweeping undulose extinction. Clasts are also composed of altered plagioclase and alkali feldspar, epidote and opaque minerals.

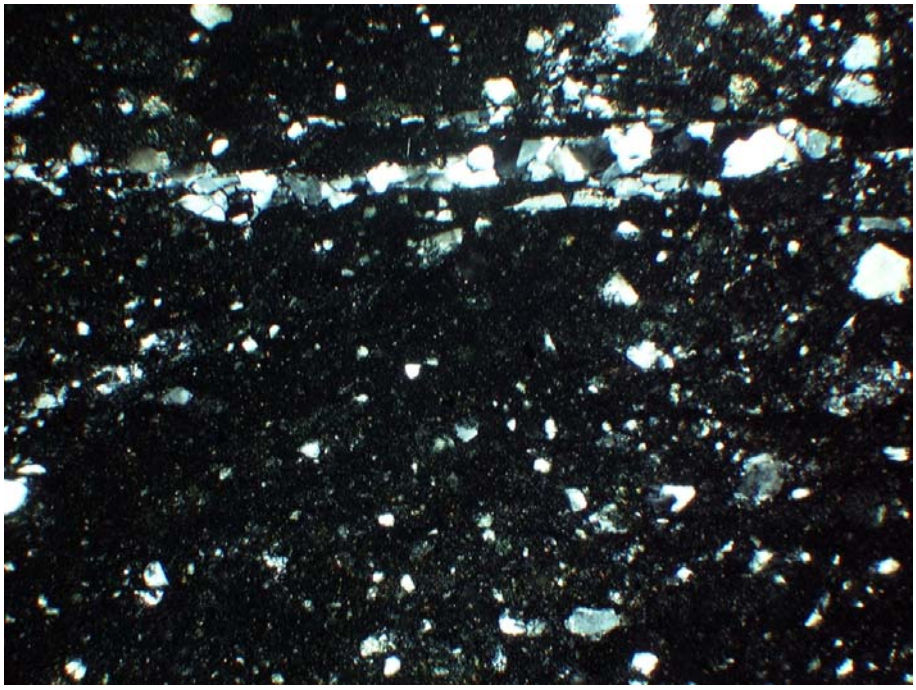

Figure 59. Photomicrograph of a typical texture of the ultracataclasites in the GPF. Note the quartz-filled vein that is undeformed near the top of the image (XPL, field of view 3.1mm).

The matrix in the ultracataclasites is composed primarily of chlorite or epidote, ≤5μm in size, along with quartzo-feldspathic material. Domains with chlorite-rich matrix appear to

cross-cut domains with epidote-rich matrix, which forms fragments of ultracataclasite within the ultracataclasite. These domains are around 0.2mm wide, and include clasts that have aligned long axes defining a weak shape fabric. The ultracataclasites are cross-cut by inter-connected shear fractures that truncate clasts, offsetting grain boundaries by <1mm. The fractures are thin (~10μm), are filled with chlorite, anastomose and are discontinuous at the scale of the thin section, having maximum lengths on the order of several centimetres. SEM imaging of the matrix shows that rounded to sub-rounded chlorite, quartz and alkali feldspar are the principal constituents of the matrix, which has a granular texture.

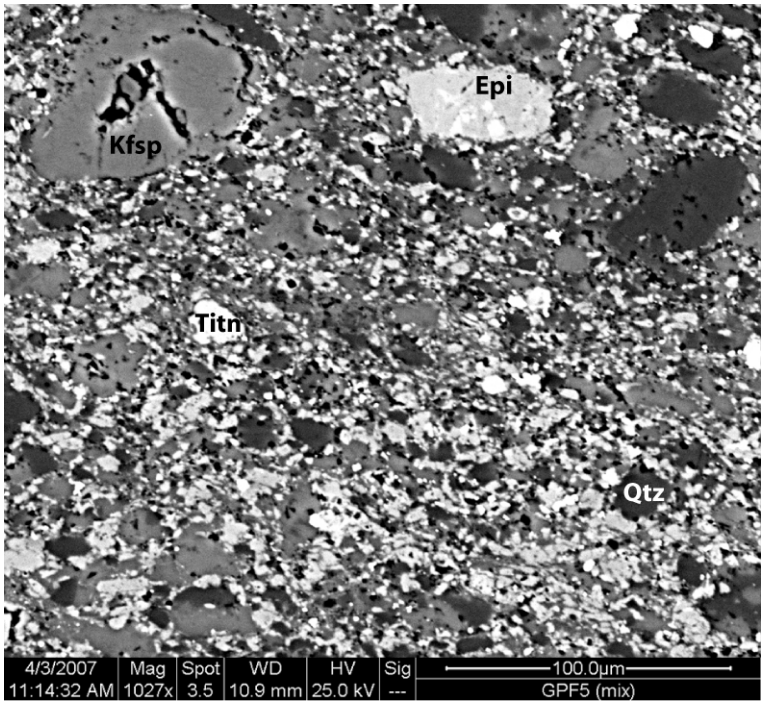

Figure 60. BSE image of the ultracataclasite matrix. The matrix is composed primarily of epidote (Epi), quartz (Qtz) alkali feldspar (Kfsp), and titanite (Titn).

The ultracataclasites are cross-cut by numerous veins that contain quartz and alkali feldspar, which are generally undeformed (Figure 59). The veins are opening mode fractures that are ~10μm to 750μm wide, which have a wide variety of orientations. The veins are irregularly-shaped, curved, and/or wavy and frequently form sigmoidal shapes where two non-coplanar segments join. Quartz in the vein contains occasional isolated fluid inclusions ~2μm in diameter. Fragments of ultracataclasite are incorporated into some veins.

Sample GPF6 contains ultracataclasites that are juxtaposed against pale proto-cataclasites (see Figure 26). Thin section analysis shows that the proto-cataclasites defined in hand specimen grade into ductiley deformed rock in which quartz and feldspar have undergone

extensive intra-crystalline deformation (Figure 61). Large (0.3 to 0.6mm) quartz crystals that contain sweeping undulose extinction and occasional deformation lamellae are separated by zones of quartz subgrains 20 to 50μm in diameter that likely developed by bulging recrystallisation. Subgrains displaying gradual transitions from subgrain- to grain-boundaries are developed around some of the larger quartz crystals indicating subgrain rotation recrystallisation. Some domains between larger quartz crystals contain approximately equigranular (50 to 150μm), polygonal grains that have straight edges and often form triple junctions. These subgrains may have developed by static recovery or annealing. Plagioclase and alkali feldspars also have subgrains 50 to 150μm along grain boundaries, and larger crystals show sweeping undulose extinction. Hornblende and biotite are rarely present in the ductiley deformed part of the rock, but are chloritized. The chlorite around crystal edges of hornblende and biotite forms tails of small (<10μm) crystals that are intercalated with the recrystallised quartz and feldspars. Internally biotites show little deformation with straight cleavage planes and some undulose extinction.

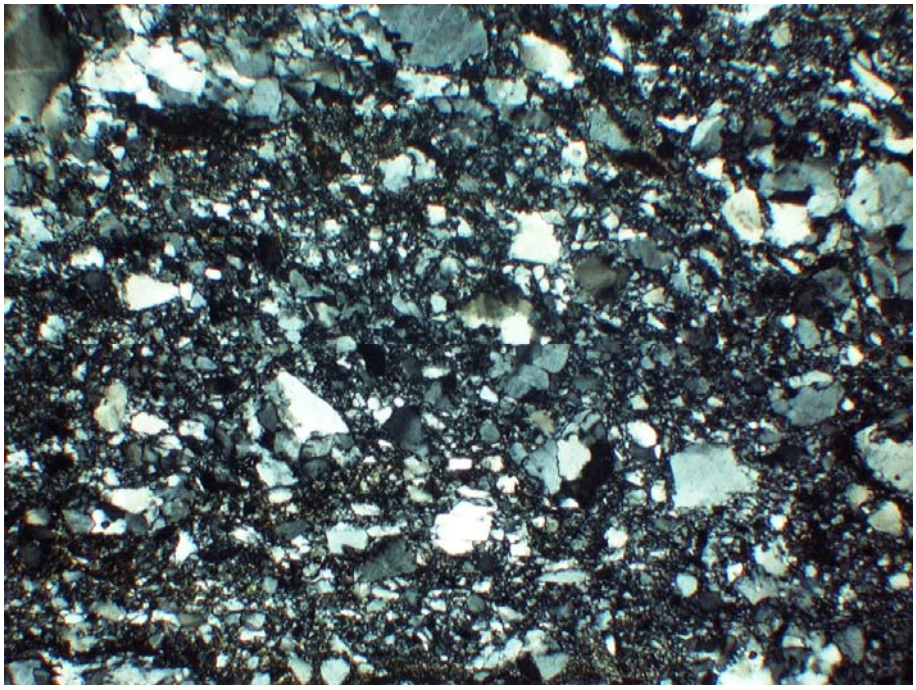

Figure 61. Ductile deformation of quartz in the rock adjacent to the ultracataclasite in sample GPF6 (XPL, field of view 3.1mm).

Shear fractures containing a material similar to the ultracataclasite matrix splay from within the ultracataclasites in two orientations into the domain of ductiley deformed adjacent rock. High angle fractures (50-60º) cross-cut lower angle (≤30º) fractures. Both sets of fractures are centimetres long and characteristically form triangular embayments in the ultracataclasite edge that localise onto narrow (0.05 to 0.2mm) slip surfaces containing epidote and angular fragments of the ductiley deformed rock. The fractures are apparent in

hand specimen, and the low angle set seem to curve back towards the ultracataclasite in a sidewall ripout geometry. Fragments of the ductiley deformed rock spall from the portions of material between the ultracataclasite and low angle fractures.

4.4.2.1 GPF ultracataclasites: summary

Ultracataclasites in the GPF are more comminuted that cataclasites, comprising up to 90% matrix material. Ultracataclasites contain large proportions of chlorite and epidote, and numerous quartz-filled veins that are sometimes undeformed. The ultracataclasites cross-cut intensely recrystallised quartz and feldspars in GPF6.

4.4.3 Slip surfaces

Field identification criteria show that slip surfaces are variously distributed throughout the GPF cross-cutting fault cores, forming at the edges of fault cores, and cross-cutting apparently undeformed host rock (see section 3.5.1.2). Sample GPF11 is taken from locality 31, and contains a portion of the upper pseudotachylyte generation surface shown in Figure 23. The sample therefore contains part of a slip surface that in the field appears to cross-cut apparently undeformed host rock.

In thin section, GPF11 contains a clearly defined zone of fault rock that includes pseudotachylytes, cataclasites and foliated cataclasites, which together comprise a deformed zone in which multiple slip surfaces are present (this deformed zone will hereafter be referred to as the slipped zone, in reference to the collection of deformed rocks that are inferred to have accommodated slip in this section only, and does not refer to individual slip surfaces; Figure 62). In the section the slipped zone varies in width from ~2.5mm to ~4.5mm. The edges of the slipped zone are sharp and well defined as intensely deformed cataclasites or pseudotachylyte generation surfaces are juxtaposed directly against largely undeformed wall rock. Within the slipped zone, the fault rocks show complicated cross-cutting relations between various pseudotachylytes and cataclasites. Outside the zone, deformation decreases rapidly so that the wall rock at the southern edge of the thin section is effectively undeformed.

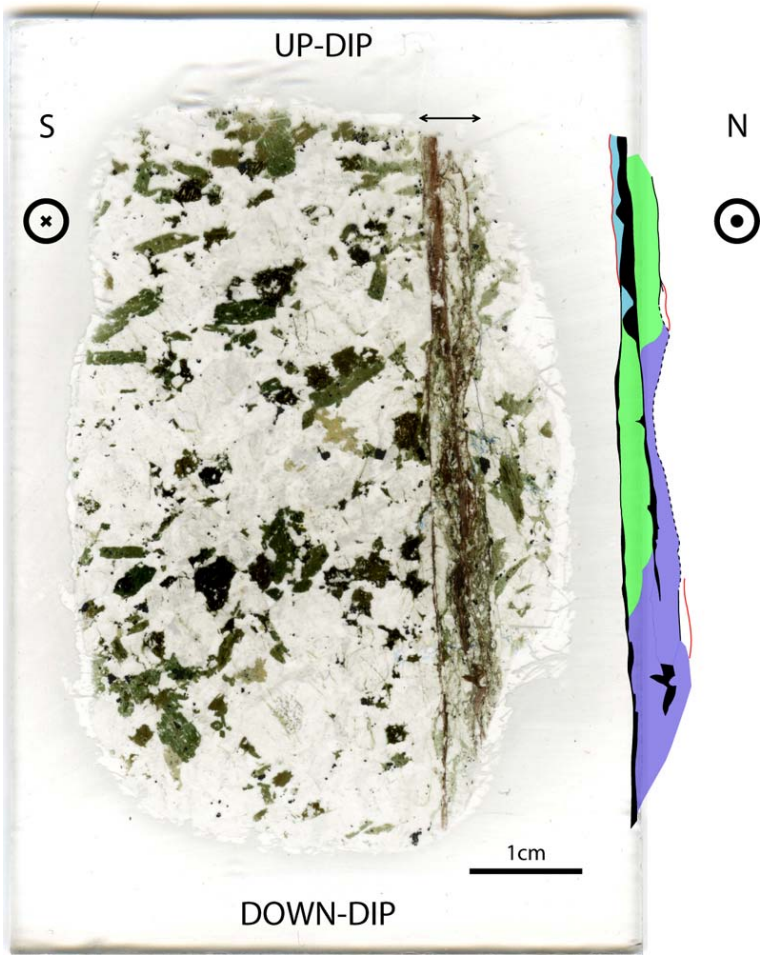

Figure 62. Scanned image of the thin section of sample GPF11 and an interpretive map of the slipped zone in this section (indicated by arrows). The map shows the complicated distribution of cataclasites (pale blue), foliated cataclasites (green), pseudotachylytes (green), pseudotachylyte breccias (dark blue), and isolated brittle slip surfaces (red).

The pseudotachylytes present in GPF11 have a complicated geometry and are often difficult to identify. The northern edge of the slipped zone is defined by a pseudotachylyte generation surface at the up-dip end of the section (see Figure 62) where the pseudotachylyte separates a foliated cataclasite from wall rock (Figure 63). This pseudotachylyte is typical of pseudotachylytes in the section; it is brown to pale brown (PPL), opaque in places, very thin (10µm to 0.25mm), and contains rare clasts. Where present, the clasts are rounded and embayed, and are composed of predominantly of feldspars, and also quartz. Injection veins up to 0.15mm in length frequently branch at high angles from the main surface. Occasional wedge-shaped pockets of cataclasite are present between the pseudotachylyte and the wall rock, localised in irregularities in the geometry of the wall rock edge. The main pseudotachylyte generation surface in this part of the section becomes indistinct ~3mm beyond a slight kink (right step), where several fractures branch from the main surface at low angles. The majority of the rest of the northern edge of the slipped zone is defined by cataclasite juxtaposed directly against wall

rock implying the presence of a slip surface (Figure 62), with pseudotachylytes possibly developed in places. However, there is insufficient evidence in thin section for their presence to be confirmed. Pseudotachylytes are present towards the down-dip end of the northern edge of the slipped zone, but are brecciated (see discussion below).

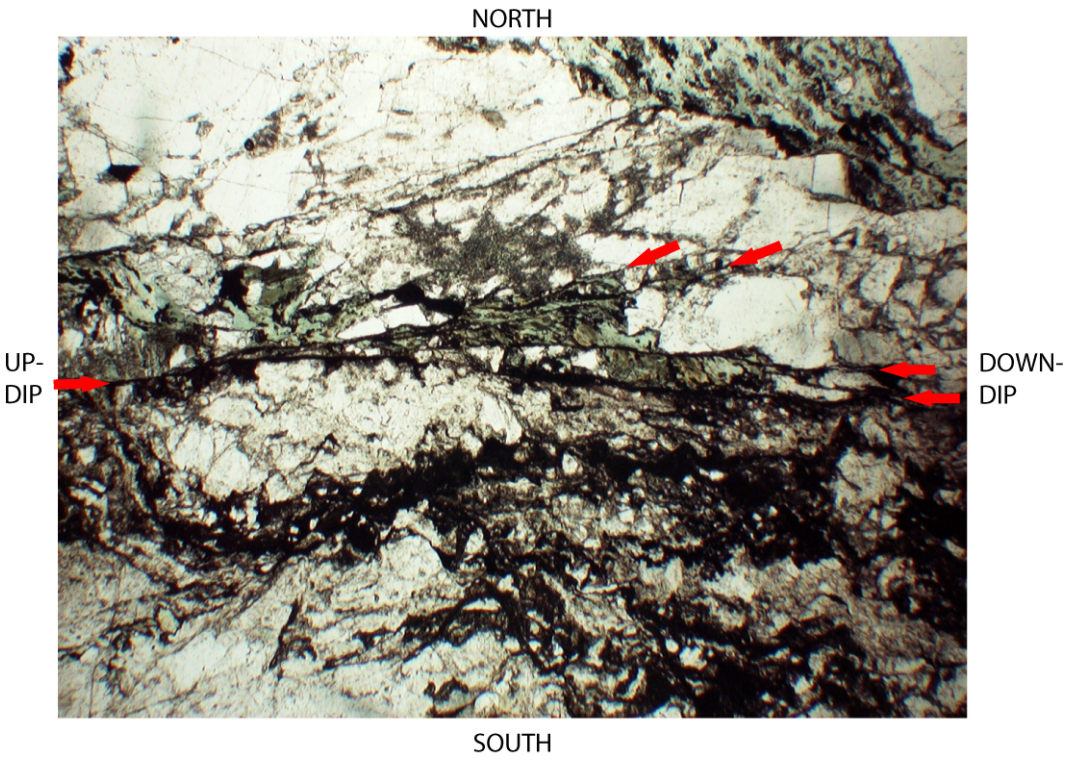

Figure 63. The pseudotachylyte that forms the northern edge of the slipped zone at the upper end of the section of GPF11. The pseudotachylyte generation surface is thin and straight with high angle injection veins, until a small right step in the surface where multiple fractures branch from the main surface (PPL, field of view 3.1mm).

The southern edge of the slipped zone is also delimited by a pseudotachylyte generation surface, which can be traced across the entire section. In the central and down-dip portions of the section, this pseudotachylyte forms a narrow (10μm to 0.25mm), slightly wavy vein with sharp edges and a varying thickness. Injection veins are rare and where present are very small (up to 0.7mm long). The southern pseudotachylyte generation surface generally separates foliated cataclasites from wall rock that displays little deformation. The geometry of pseudotachylyte is complicated in places where the vein branches into several sub-parallel, closely spaced slip surfaces along which melt is poorly developed (Figure 64). The slip surfaces subsequently coalesce back into a single pseudotachylyte vein. Chlorite replaces parts of the pseudotachylyte vein material, the distribution of which appears to reflect flow banding developed during the melt phase.

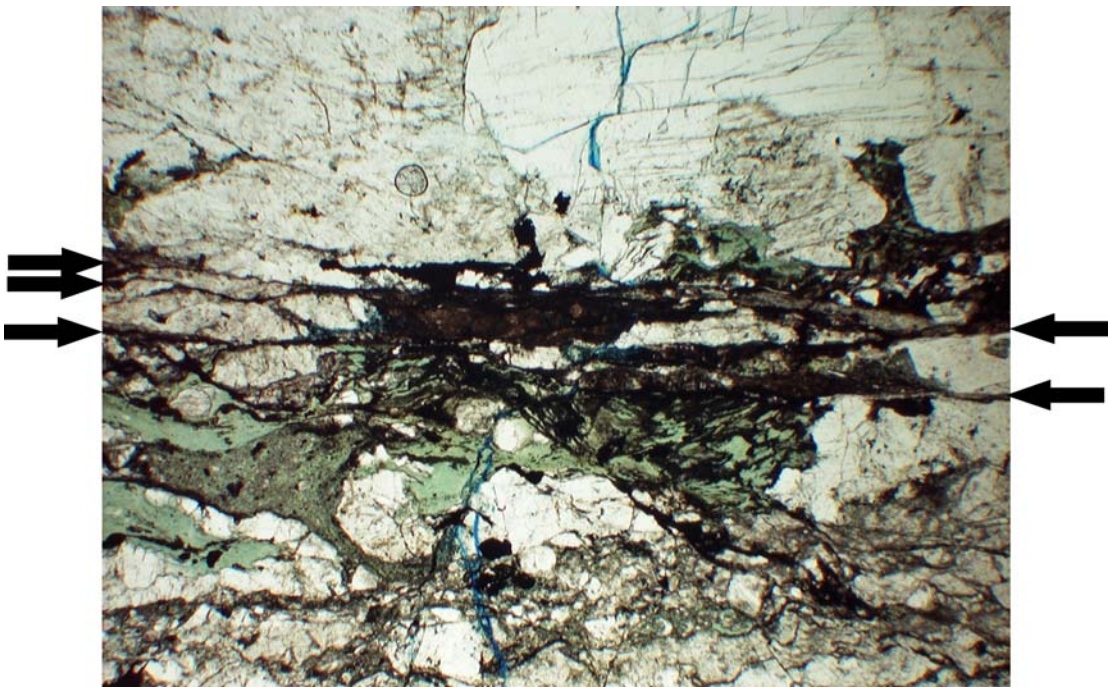

Figure 64. The southern edge of the slipped zone is defined by a pseudotachylyte generation surface that branches into sub-parallel slip surfaces (between arrows) along which melt is poorly developed (PPL, field of view 3.1mm).

The pseudotachylyte at the southern edge of the slipped zone appears to splay from a thicker, central pseudotachylyte vein in the up-dip part of the section (Figure 62). The central vein is brown to pale brown (PPL), with colour variation defining apparent flow banding, which is well developed parallel to the vein edges. Clasts in the central vein are rounded, up to 15μm to 0.5mm long and are composed of quartz, feldspars that are partly sericitized, and fragments of recrystallised quartz and feldspar aggregates. The northern edge of the central vein is sharp, with frequent embayments and several injection veins branching into the adjacent foliated cataclasite, which have exceptionally irregular geometries. In places the injection veins form compositional banding within the cataclasite that are not cut by brittle fractures within the cataclasite but resemble other dark brown compositional bands within the foliation. The southern edge of the central pseudotachylyte vein is defined by a sharp edge that cross cuts the adjacent unfoliated cataclasite in places, but is also diffuse in places so that the pseudotachylyte is difficult to distinguish from the cataclasite. One portion of the pseudotachylyte is brecciated in a fracture-bounded irregularity in the vein margin.

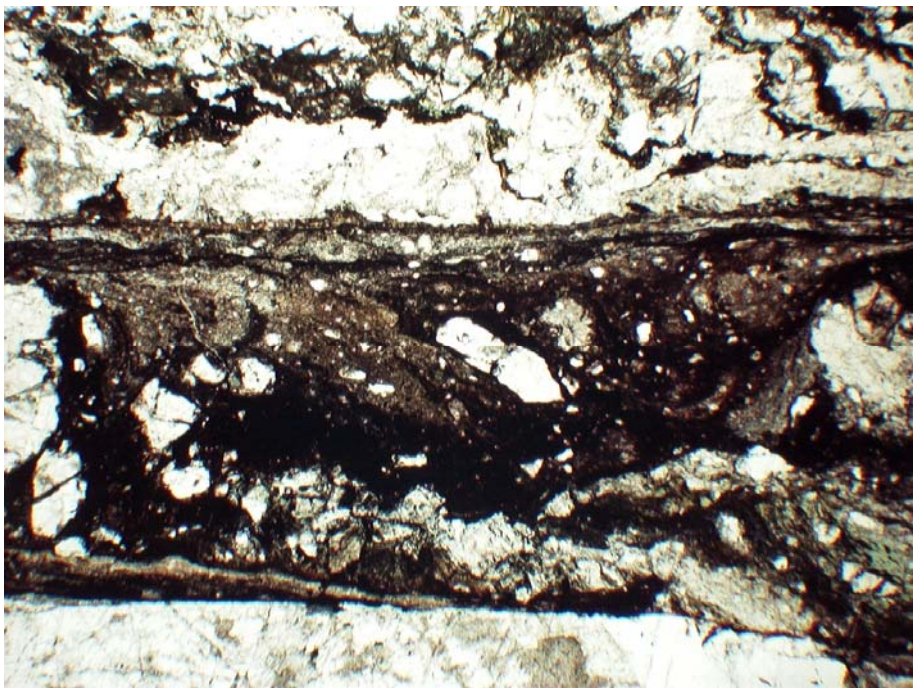

Figure 65. The central pseudotachylyte vein within the slipped zone in sample GPF11. The pseudotachylyte contains flow banding developed in an otherwise aphanitic groundmass (PPL, field of view 3.1mm).

The splay junction between the central and southern pseudotachylytes is complicated as the two pseudotachylytes are difficult to distinguish until they are separated by a significant thickness of foliated cataclasite. The foliated cataclasite between the twp pseudotachylytes seems to be intruded by both pseudotachylyte veins; the cataclasite is present as clasts in pseudotachylytes near the splay junction, and the transition from pseudotachylyte to cataclasite is gradual until the two pseudotachylytes localise onto narrow generation surfaces. Injection veins from both of the pseudotachylyte generation surfaces intrude the foliated cataclasite. The foliation within the cataclasite is defined by aligned shear fractures that form angles of ~30º with the trend of the generation surfaces in the plane of the section (Figure 66). These shear fractures truncate clasts within the cataclasite, but do not cross-cut the pseudotachylytes; in places the fractures appear to splay from the cataclasites.

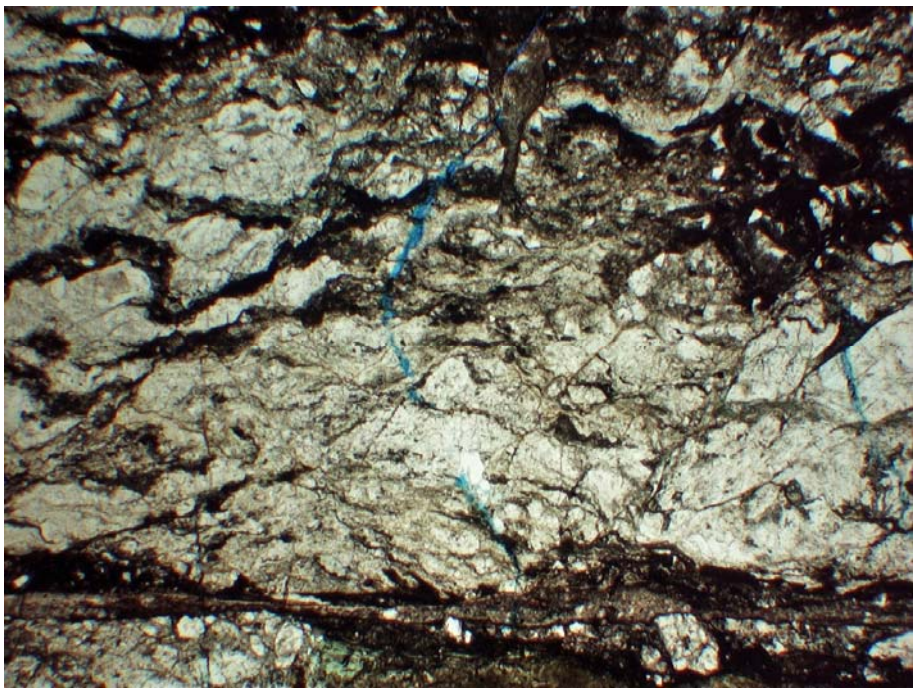

Figure 66. Foliated cataclasite developed between the southern and central pseudotachylyte generation surfaces of the slipped zone in sample GPF11. The foliation is defined by aligned shear fractures that truncate clasts in the cataclasite (PPL, field of view 3.1mm).

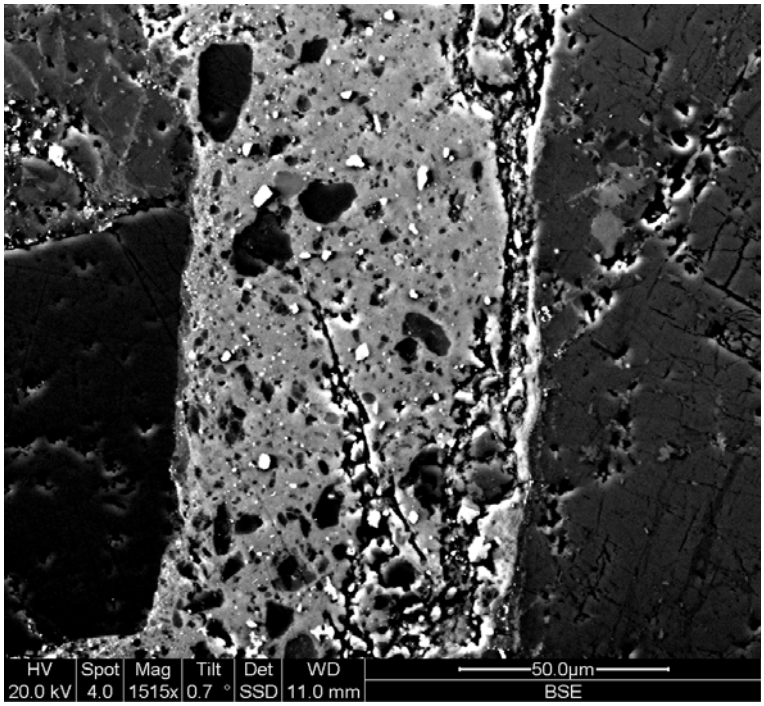

Figure 67. BSE image of the pseudotachylyte at the southern edge of the slipped zone in GPF11. Note the amorphous matrix that does not contain microcrystallites.

Microcrystallites are not visible in the groundmass of the any of the pseudotachylytes in thin section GPF11, even though the veins can be characterised as generation surfaces and injection veins based on their orientation with respect to the GPF. SEM analyses show that the pseudotachylytes are composed of lithic clasts in an amorphous groundmass (Figure

67). The groundmass is compositionally heterogeneous, comprising domains that are very similar to alkali feldspar or plagioclase feldspar, with variations in the titanite, magnesium, and sodium content, reflecting flow banding that can be recognised in thin section. Titanite, magnetite and sulphide droplets are abundant in the groundmass. However, the majority of the pseudotachylytes in the sample have an unusual texture due to an uneven topography to the thin section (e.g. see the right hand side of the pseudotachylyte vein in Figure 67). Analysing the structures and composition of the groundmass is therefore difficult or impossible.

Cataclasites are developed in a number of places in the section (see Figure 62). An unfoliated cataclasite is present between the central and northern pseudotachylytes in the down-dip end of the section. This cataclasite contains 80% clasts (25μm to 0.85mm) and is the coarsest-grained material in the slipped zone. The clasts are angular to sub-rounded and are composed of quartz, feldspar (sericitized in some cases), and multi-crystalline aggregates containing recrystallised quartz and feldspar. Some clasts contain fragments of pseudotachylyte, and fragments of pseudotachylyte with its wall rock (Figure 68). Chlorite is abundant in the matrix material within the cataclasite, along with extremely comminuted quartz and feldspar. The distinctive pseudotachylyte fragments characterise this cataclasite as a pseudotachylyte breccia, which can be traced into a foliated cataclasite where the fragments of pseudotachylyte are no longer discernable.

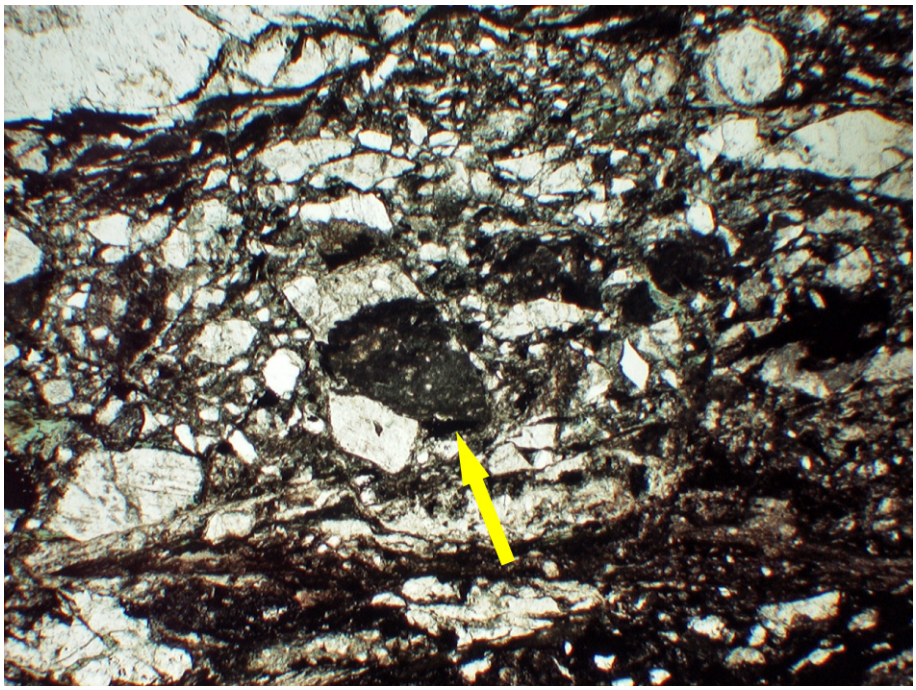

Figure 68. Fragment of pseudotachylyte and wall rock comprising a clast in the unfoliated cataclasite (yellow arrow; PPL, field of view 3.1mm).

The two pseudotachylytes that define the edges of the slipped zone are undeformed, and cross-cut the central foliated cataclasite and the unfoliated cataclasites. However, the undeformed cataclasite trends up-section into a foliated cataclasite which is intruded by injection veins from the central and northern pseudotachylytes. These injection veins appear to define compositional bands within the foliated cataclasite indicating that they are deformed by the cataclasite. The injection veins can mostly be traced back to the place where they branch from the main pseudotachylyte vein suggesting that slip on the pseudotachylyte generation surface may have been synchronous with the deformation of the foliated cataclasite. Pseudotachylyte fragments in the unfoliated cataclasite indicate that pseudotachylyte generation has occurred more than once along the slipped zone in GPF11. The pseudotachylyte fragments that also contain part of the wall rock to the pseudotachylyte show that deformation had preceded pseudotachylyte generation as the wall rock portions are composed of cataclasites.

The wall rock to the south of the pseudotachylytes and cataclasites contains limited evidence for alteration and deformation. Biotite and hornblende are partly chloritized around crystal edges and along cleavage planes and intra-crystalline fractures throughout the thin section. Plagioclase and alkali feldspars are both sericitized primarily along twin and cleavage planes. Sericitization has also occurred along some inter-crystalline fractures. Quartz crystals occasionally contain deformation lamellae, fractures and rare fluid inclusions. In general fractures in the wall rock do not show a consistent orientation. However, within around 10mm of the slipped zone, fractures are predominantly sub parallel (0 to 20º) to the pseudotachylyte at the edge of the zone and contain sericite. These fractures are tens of millimetres long, and appear to form sidewall ripout geometries where they curve back to the pseudotachylyte edge. Crystals of plagioclase feldspar and quartz within zones bounded by a sidewall ripout and a pseudotachylyte are more fractured than in the wall rock.

4.4.3.1 GPF11: summary

Slip surfaces are defined by pseudotachylytes, foliated cataclasites and cataclasites in the slipped zone of GPF11. Fragments of pseudotachylytes are present in some of the pseudotachylytes showing that multiple slip events were localised onto the slipped zone.

4.4.4 Damage zone

The damage zone of the GPF at locality 18 is partly comprised of fracture-bounded blocks of altered host rock that give the rock a shattered appearance. Sample GPF2 is an oriented sample taken from the shattered rock at locality 18. In the sample the altered host rock is cross-cut by numerous fractures that are filled with chlorite.

A thin section cut approximately perpendicular to the GPF fault core orientation at locality 18 and containing a slip vector that is assumed to be horizontal (orientation; 231/20ºN) shows that the rock is pervasively altered; hornblende and biotite are completely replaced with pseudomorphic chlorite, and plagioclase is extensively sericitized. Blue resin impregnated in the sample during thin section preparation is preferentially located in plagioclase crystals. The resin highlights abundant intra-crystalline fractures and also decorates inter-crystalline fractures in plagioclase and in adjacent minerals. Alkali feldspars are also often sericitized, though some crystals show little alteration. Alkali feldspars contain inter-crystalline healed fractures filled with alkali feldspar and small amounts of epidote (Figure 69). The healed fractures are opening mode and cross-cut earlier-formed fluid inclusion trails. The fluid inclusions do not show any consistent orientation in the section, though the healed fractures mostly trend approximately north-south. Where the healed fractures in alkali feldspar cross grain boundaries they turn into fractures that are not healed in plagioclase.

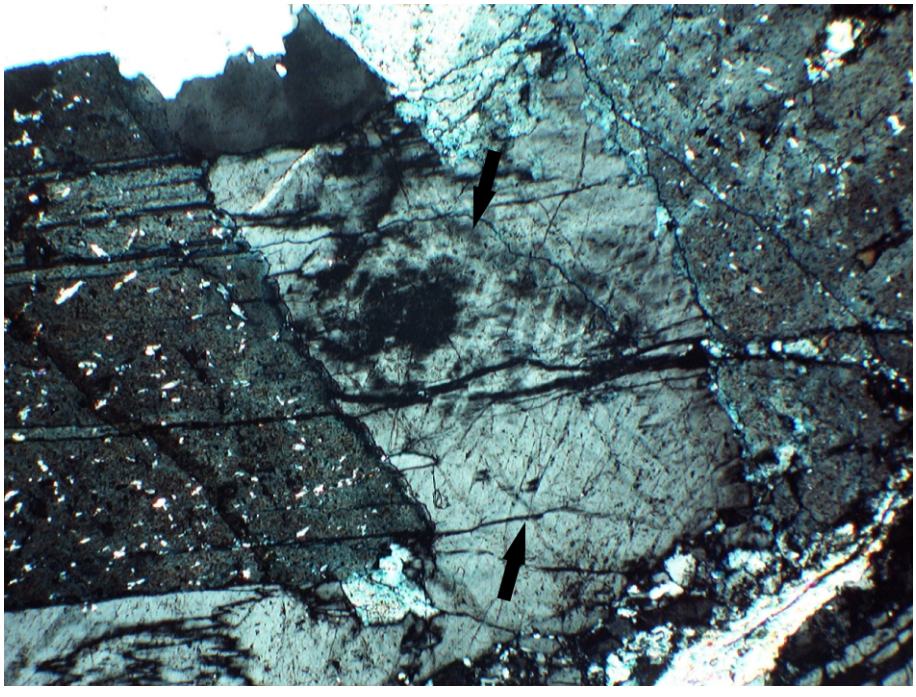

Figure 69. Inter-crystalline fractures that are healed in alkali feldspar cross-cut fluid inclusion trails, indicated by arrows (XPL, field of view 1.6mm).

Quartz in sample GPF2 ubiquitously shows sweeping undulose extinction and subgrains along grain boundaries that developed by bulging recrystallisation. Inter-crystalline fluid inclusion trails that cross-cut subgrain boundaries are abundant in quartz. Inter-crystalline fractures also cross-cut quartz grain boundaries but often terminate before crossing boundaries with different types of minerals.

Numerous brittle fractures cross cut the altered host rock in GPF2, which are centimetres long (Figure 70). The fractures have three predominant orientations; within the sample each orientation includes a shear fracture that cross-cuts the entire section. These main fractures (labelled 1, 2 and 3 in Figure 70) are accompanied by smaller, sub-parallel fractures distributed throughout the section. Fracture 1 intersects the section with a rake of ~50º from the north east. The fracture is slightly wavy and contains cataclased epidote ≤0.5mm and feldspar and quartz fragments ≤0.2mm that are cross-cut by chlorite. The chlorite in the central part of the fracture is olive green (PPL) with low interference colours, and is extremely fine-grained (10µm). Fracture 2 forms an angle of ~90º with fracture 1 and contains cataclased epidote fragments ≤5µm long. The fracture is straight but numerous euhedral epidote-filled veins branch off at high angles (sub-parallel to fracture 1). Smaller (≤5mm long) fractures in the same orientation as fracture 2 cross-cut the host rock, healed fractures in alkali feldspars and fractures in plagioclase, and fluid inclusions in quartz. Fracture 2 cross-cuts fracture 1, displacing it by ~1mm in a right lateral sense. Fracture 3 is also filled with cataclased epidote, but is slightly wavy and encompasses some slivers of the altered host rock where it is thicker (~1mm). One fracture in the same orientation as fracture 3 right-laterally displaces fracture 1 by ~0.4mm. Fractures 2 and 3 do not intersect in the section.

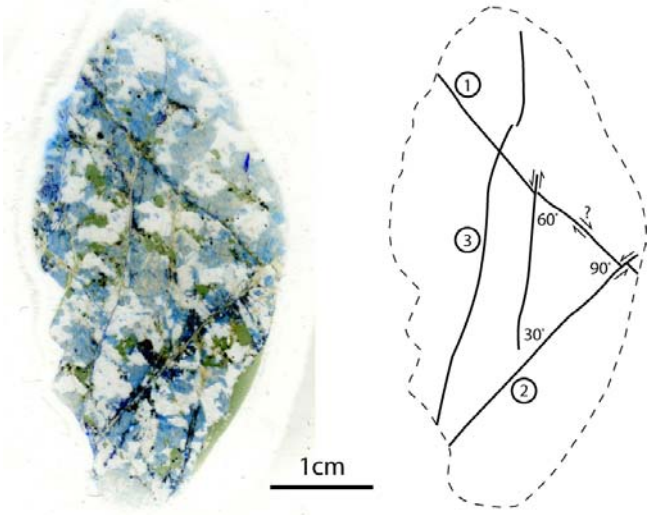

Figure 70. Scanned image of the oriented thin section of sample GPF2 (left) and sketch showing the geometry and sense of shear of the main fractures 1, 2, and 3 described in the text.

The main brittle fractures truncate vein-like structures up to 5mm thick that contain recrystallised material. The recrystallised material is composed of grains and subgrains of quartz and feldspars 10 to 250μm long, as well as some small (<50μm) epidote crystals between the subgrains. There is no grain shape fabric developed in the recrystallised material. The vein-like structures have sharp edges, and sometimes contain fragments of altered host rock that are broken up by smaller fractures that are filled with the same recrystallised material as the main parts of the vein (Figure 71). Massive aggregates of radial arrangements of pale green chlorite (PPL) with low interference colours fill some parts of the vein-like structures, and also veins that branch off from the recrystallised material into the host rock.

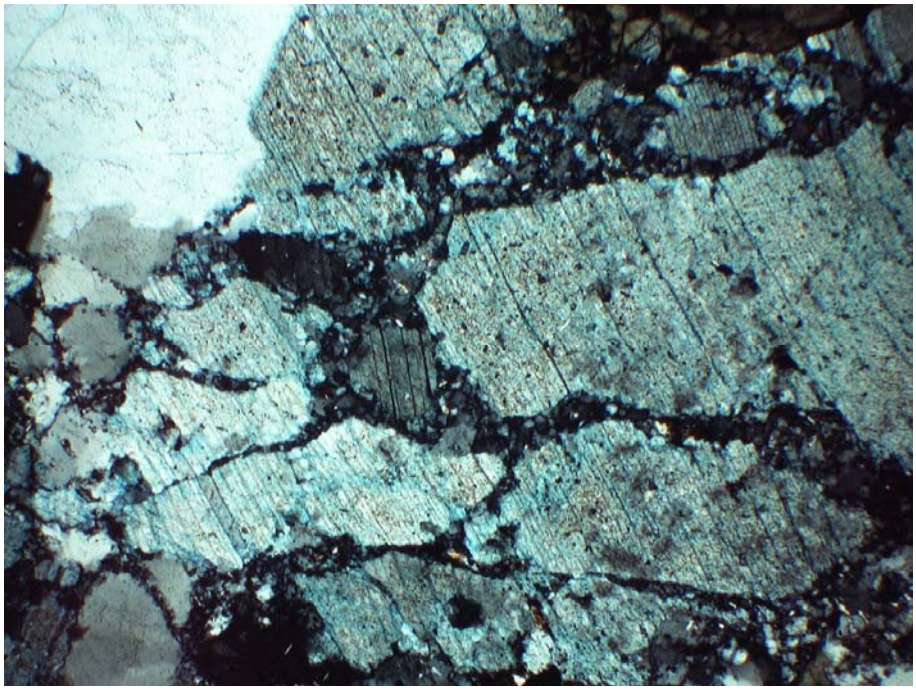

Figure 71. Photomicrograph showing fractures that break up a fragment of altered host rock (plagioclase feldspar in this image) contained within a vein-like structure. The recrystallised material that fills the main part of the vein-like structures is also present in the smaller fractures in the fragment. A small part of the plagioclase crystal is completely bounded by the small fractures, and has undergone some rotation with respect to the original crystal orientation (XPL, field of view 1,6mm).

4.4.4.1 GPF 2: summary

The host rock in sample GPF2 has been extensively altered; biotite and hornblende are chloritized, and plagioclase is extensively sericitized. Numerous fluid inclusion trails and intra- and inter-granular fractures cross-cut the sample that are filled with epidote and chlorite.

4.5 Skeeter fault

Skeeter fault is well exposed at locality 1 where it is composed of three fault core strands and numerous secondary structures. As described in section 3.5.3 the northern fault core strand at this locality varies significantly in thickness, with the deformation element that comprises the strand changing as the thickness changes (Figure 72). Three samples were collected from the northern fault core strand so that the relationships between adjacent cataclasites and pseudotachylytes could be studied; sample SK8 is from the cataclasite dominated section of the strand, SK9 is from a portion of the pseudotachylyte-bearing section, and SK10 is taken from the portion of the strand where the pseudotachylyte appears to pinch-out into cataclasites in the outcrop.

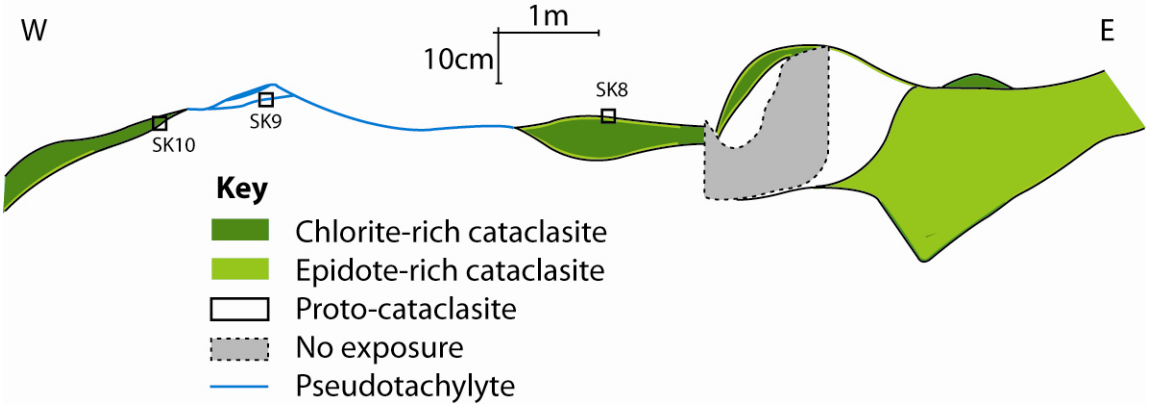

Figure 72. Baseline map of northern strand of Skeeter with the localities of the samples marked on. The map is reproduced from Figure 41, Ch. 3 for reference.

Sample SK8 contains a green, epidote- and chlorite-rich, foliated cataclasite, juxtaposed against wall rock (Figure 43). In thin section three distinct fabric domains can be recognised within the cataclasite. Immediately adjacent to the wall rock is a narrow (0.1-1mm) domain of extremely fine-grained, unfoliated cataclasite consisting of ~80% matrix material and ~20% clasts. The matrix material is dark to medium brown (PPL), and contains epidote and quartz crystals up to 30µm in diameter. Clasts are ≤0.5mm and are composed of predominantly plagioclase, with some epidote aggregates also present as clasts. The clasts do not have a preferred shape orientation, and are rounded. Within this domain, a zone of increased porosity defined by abundant blue resin trends parallel to the wall rock contact, and truncates some porphyroclasts. The wall rock edge is rough due to irregular pits where fragments of grains have been plucked and the intersections of wall rock fractures with the fault rock. However, the fine-grained cataclasite approximates the wall rock edge but does not closely follow the wall rock irregularities.

The extremely fine-grained cataclasite separates a domain of foliated cataclasite from the wall rock. The transition to the foliated cataclasite is sharp but irregular, and is marked by a significant decrease in the proportion of matrix material. The foliated cataclasite domain is defined by the presence of two foliations, and is 10-13mm wide (Figure 73). Within the domain, the cataclasite contains rounded clasts ≤1mm in a matrix of extremely finely grained material that comprises 70-90% of the domain. Larger clasts are composed of feldspars, epidote aggregates, and chloritized hornblende fragments.

Two foliations are evident within the foliated cataclasite that correspond to the R and P Riedel shear orientations (see Figure 43). In thin section the R-foliations are defined by straight, narrow (≤0.1mm) seams of extremely fine grained (≤15μm size) cataclasites that lack porphyroclasts. These shear bands generally cut across the P-foliations, but the P-foliations also bend in to parallelism with the R-foliations locally. The P-foliations are defined by fabric elements that are either compositional and/or grain size banding. P-foliations are wavy in both hand specimen and in thin section, and are less distinct than the R-shears. Compositional fabric elements are defined by bands of feldspar-rich, epidote-rich, and apparently undeformed epidote (vein fill). Commonly, feldspar-rich bands are made up of extremely fine grains (≤50μm) that form tails to porphyroclasts and strings inter-mingled with similar grain size epidote bands (Figure 73).

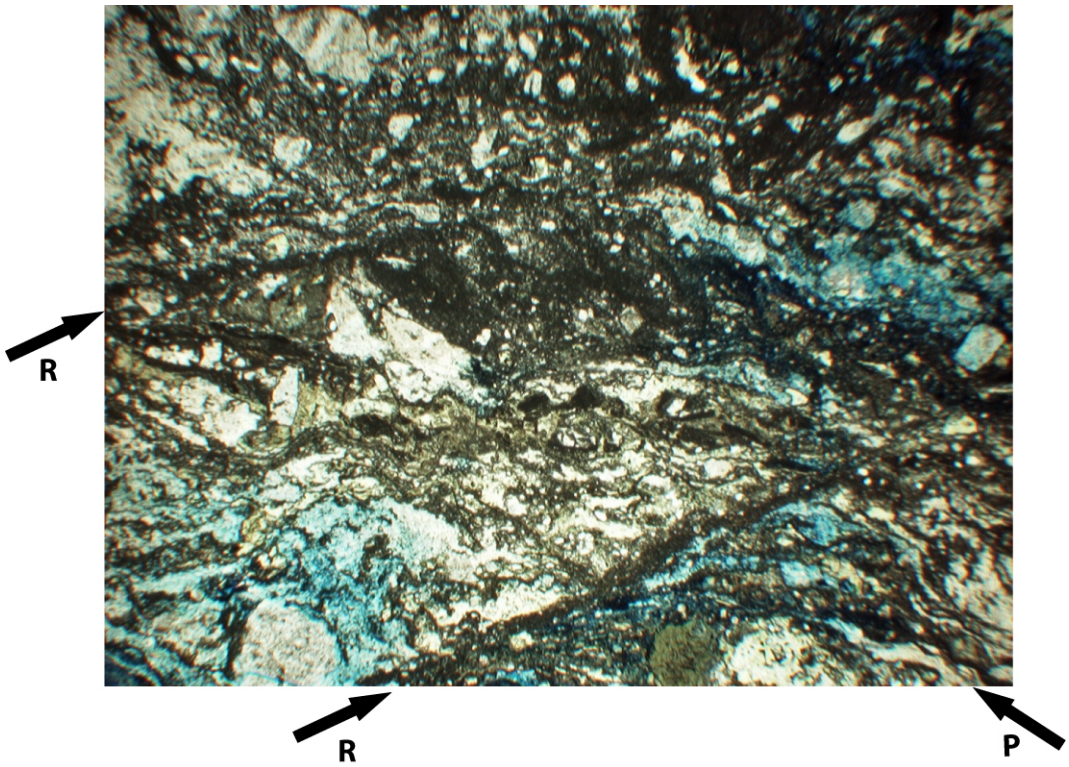

Figure 73. The foliated cataclasite domain showing the orientation of R and P foliations. P foliations are frequently defined by alternating feldspar-rich and epidote-rich bands in which the grain size is ≤50μm (arrows; XPL, field of view 3.1mm).

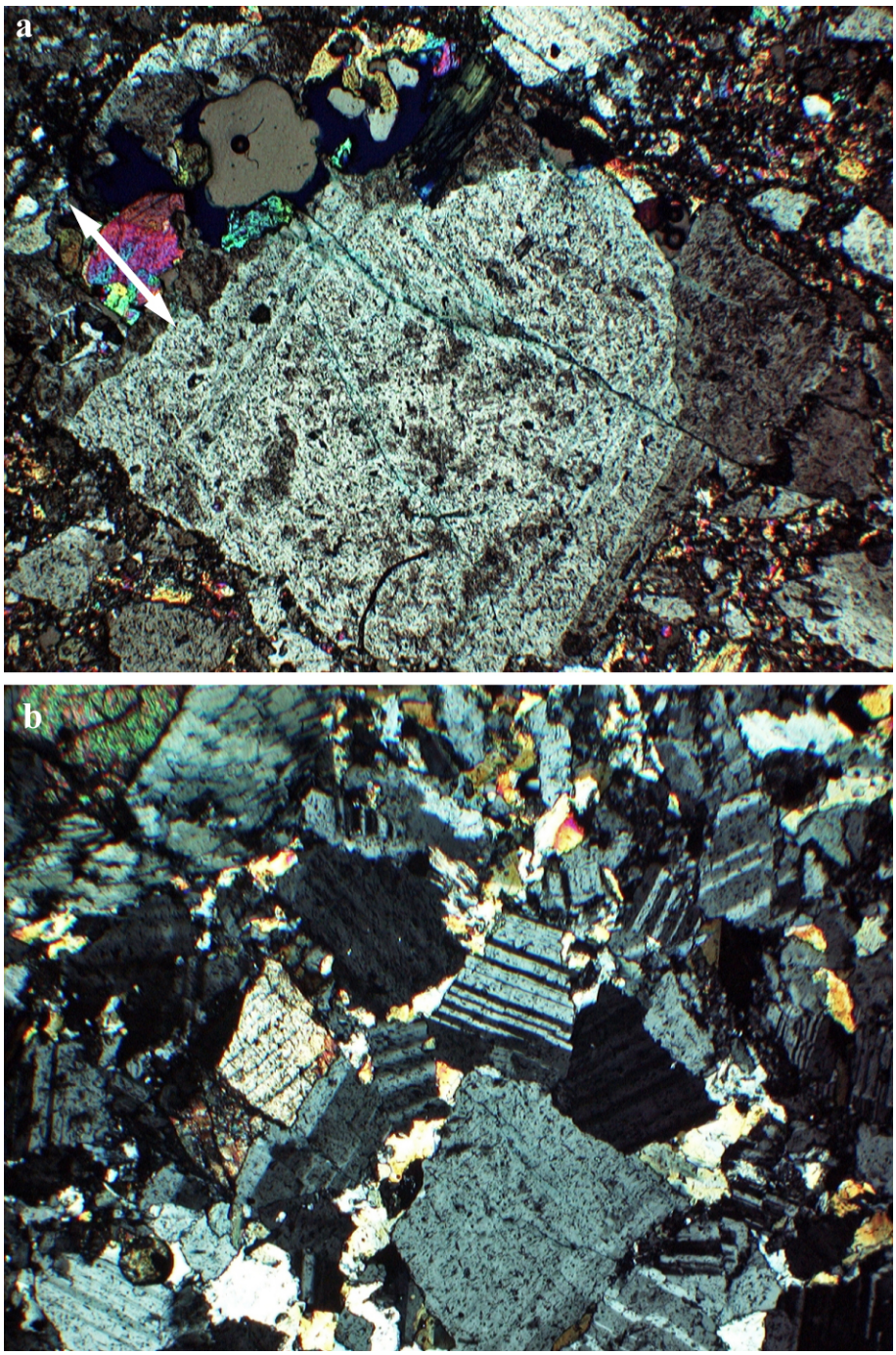

Figure 74 The unfoliated cataclasite in SK8. a. A plagioclase feldspar clast containing an epidote-filled, fracture (white arrow, top left, partly filled with blue resin) as well as a narrow, branching fracture similar to those developed in the wall rock (see Figure 75, XPL, field of view 3.1mm). b. Undeformed epidote (bright yellow interference colours) in the matrix of the unfoliated cataclasite (XPL, field of view 1.6mm).

The domain furthest from the wall rock is an unfoliated, coarse-grained cataclasite. Clasts 0.25-5mm in size comprise ~60% of the domain, between which a fine grained matrix (0.01-0.25mm) is present. The clasts are mostly composed of plagioclase and alkali feldspar fragments, some of which contain subgrains developed along grain boundaries. Multi-crystalline clasts are common, and chlorite, chloritized biotite and hornblende, and epidote fragments are also present. Quartz only forms small clasts and is also found within

the matrix. The clasts are sub-angular to rounded and frequently contain veins that are truncated at the edge of the clast, indicating that they formed before the cataclasite (Figure 74). Matrix material comprises ~40% of the unfoliated domain, and contains clasts that are ≤0.25mm, though the grain size grades through the transition from clasts to matrix. Epidote, chlorite and quartz are the principal constituents of the matrix. The extremely fine grain size of the matrix means that fracture surfaces and crystal faces are difficult to distinguish. However, in some places interstitial epidote has developed between clasts, and has not been subsequently fractured.

The portion of wall rock that is present within sample SK8 contains numerous products of fault-related processes. Fractures in the wall rock appear to splay from the cataclasite-wall rock contact, or in some cases from within the extremely fine-grained cataclasite (Figure 75). The fractures are commonly up to a centimetre long, though the lengths are difficult to estimate as they approach the edge of the section. They form angles of 35-60º to the wall rock edge in the plane perpendicular to the fault containing the slip vector. These fractures tend to be present within plagioclase feldspar crystals, are often filled with epidote, and have a branching morphology. One fracture that splays from the cataclasite-wall rock contact at an angle of ~40º bends so that it becomes approximately parallel to the trend of the contact, and can be traced for a further 3cm in this orientation. Between this long, low-angle fracture and the cataclasite, the wall rock exhibits greater damage than the wall rock further from the cataclasite, and epidote is more abundant (see Figure 75).

Clasts in the unfoliated domain occasionally contain fragments of dark brown, aphanitic material with few rounded clasts (<10%). This material is similar to the fine-grained cataclasite adjacent to the wall rock, and in some cases looks similar to pseudotachylyte. However, SEM imaging shows that the material is composed of small (<10μm), granular epidote crystals, with occasional plagioclase, alkali feldspar and quartz clasts (Figure 76). The dark brown aphanitic material may represent portions of relic slip surfaces, but there is no evidence to suggest that it is pseudotachylyte.

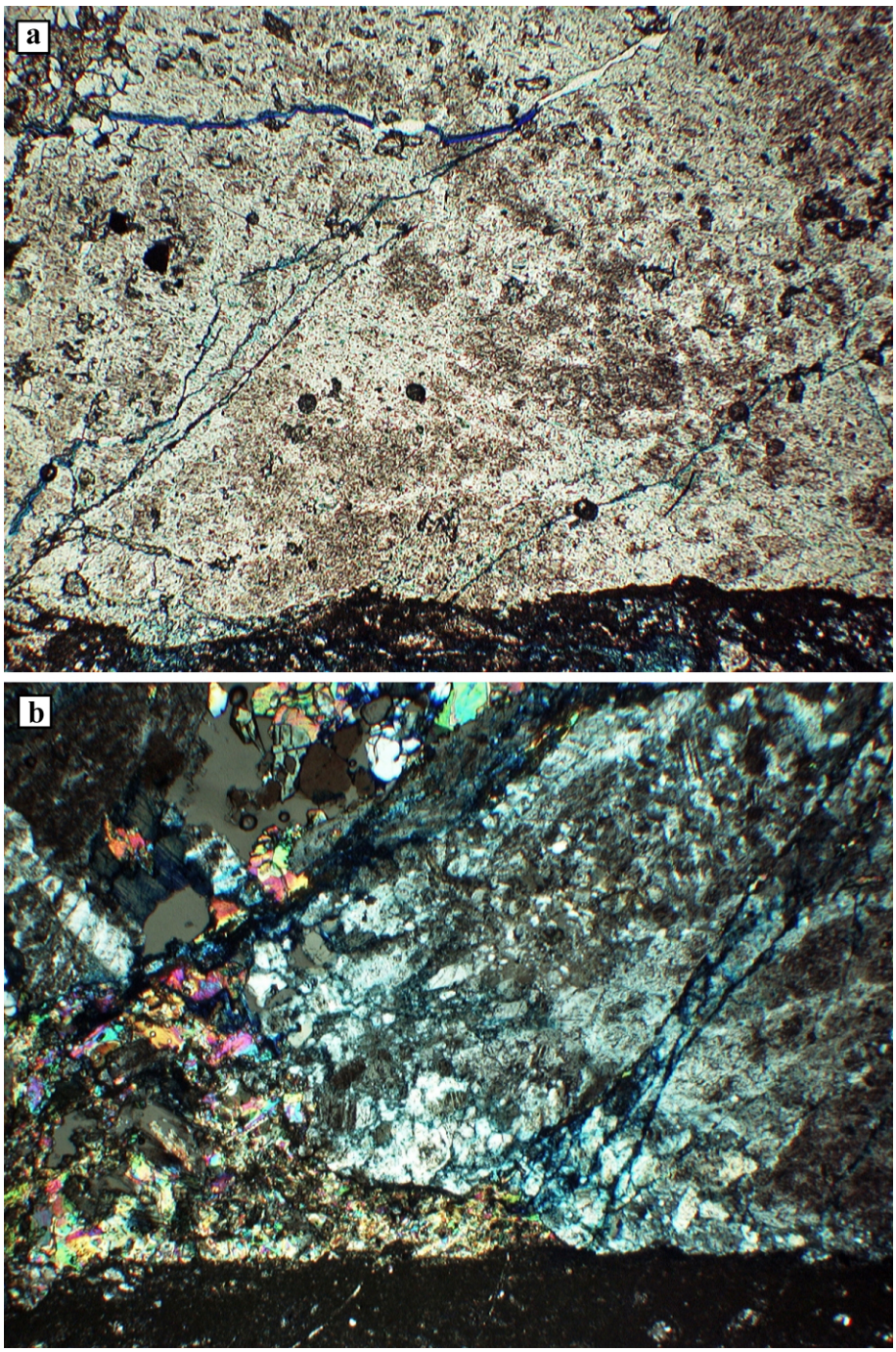

Figure 75. Photomicrographs illustrating wall rock fractures in sample SK8. a. Fractures in the wall rock that splay from the cataclasite-wall rock contact form angles of 35-60º to the wall rock edge (PPL, field of view 3.1mm). b. A triangle shaped wedge of epidote (lower left) within the fragment of wall rock bounded by the cataclasite (bottom) and the long, low-angle fracture described in the text. The upper edge of the epidote wedge has an angle that is similar to the angles formed by other fractures in the wall rock that splay from the cataclasite (XPL, field of view 3.1mm).

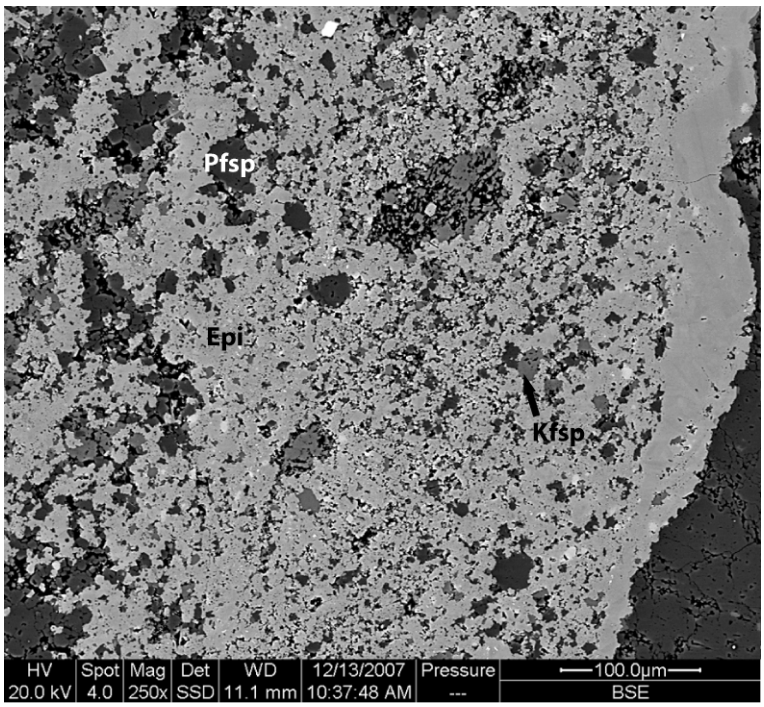

Figure 76. BSE image of a fragment of dark brown, aphanitic material in the unfoliated cataclasite. SEM analyses shows that the material is primarily granular epidote, but does not show any evidence for pseudotachylyte (Epi = epidote, Pfsp = plagioclase, Kfsp = alkali feldspar).

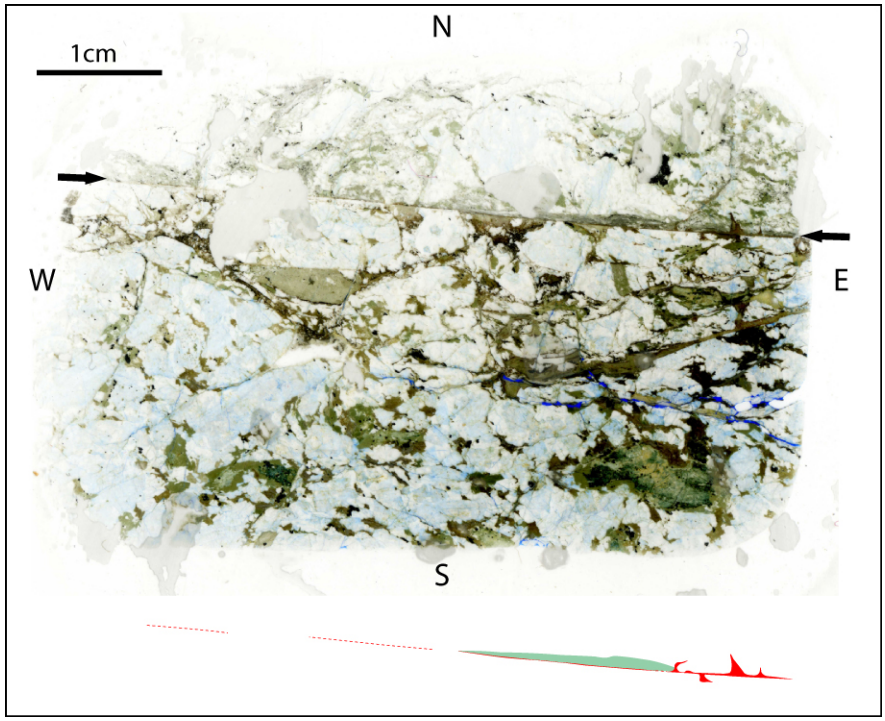

Figure 77. Scanned image of thin section SK9 with an interpretive map of the central slip surface geometry (red = pseudotachylyte, green = foliated cataclasite). Note juxtaposed wall rock textures.

Sample SK9 contains one through-going slip surface that separates two distinctly different wall rock types; the southern wall rock contains abundant pseudotachylytes, and the northern is massively fractured but lacks pseudotachylytes (Figure 77). The slip surface is straight, and is defined in parts by a pseudotachylyte generation surface. The central slip

surface pseudotachylyte is intermittent as a single vein cannot be traced for the entire length of the thin section. However, a continuous slip surface can be defined by the juxtaposed wall rock types, which cross-cuts all minerals, fabrics and possible pseudotachylytes developed in the wall rocks on both sides. The central slip surface is also cross-cut in by small (<<1mm) displacement shear fractures. Where pseudotachylyte is not developed, the slip surface either forms one edge of a zone of foliated, extremely finely-grained cataclasite, or no slip surface can be identified.

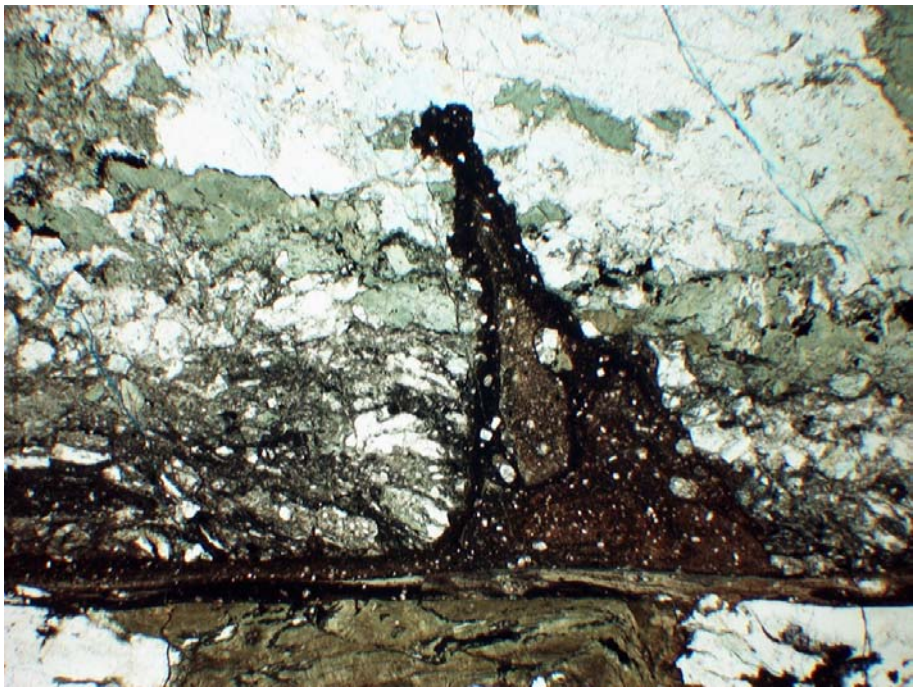

Figure 78. The central slip surface in SK9 is partly defined by a pseudotachylyte generation surface. Photomicrograph showing an injection vein from the central pseudotachylyte that cross-cuts the cataclasite to the north (top). In this image, the central slip surface trends left to right (PPL, field of view 3.1mm).

The pseudotachylyte vein along the central slip surface is straight, brown or black (PPL), with yellow-orange interference colours (Figure 78). Flow banding and injection veins up to 1.6mm long are frequently developed in and around the vein. Rounded lithic clasts up to 0.15mm long comprise <5 to ~15% of the pseudotachylyte. The clasts are composed of cataclased minerals including quartz, plagioclase and alkali feldspars, which often have a matrix that contains chlorite. Microcrystallites and vesicles cannot be identified with an optical microscope. The central pseudotachylyte cross-cuts pseudotachylyte veins in the southern wall rock, but appears to be related to the foliated cataclasite in the northern wall rock. Where the pseudotachylyte vein is well-developed (in the eastern part of the thin section) it has sharp edges and a maximum thickness of 0.25mm, but the vein pinches out where the foliated cataclasite ends (see Figure 77). Further to the west in the section the central slip surface is defined by juxtaposed wall rock. Some pseudotachylyte ≤50μm

thick is intermittently developed along this part of the slip surface, but is difficult to distinguish. Sections of the slip surface that are not defined by pseudotachylytes are mostly defined by an exceptionally sharp contact between wall rock types, which is commonly filled with opaque minerals.

To the north of the central slip surface the wall rock is composed of ductiley deformed rock that has subsequently been extensively cataclased. Throughout the cataclasite quartz displays sweeping undulose extinction and has recrystallised by subgrain rotation recrystallisation. Plagioclase and alkali feldspar are not altered and have subgrains developed along crystal boundaries, but core-mantle structures are not well-developed. Hornblende and biotite are both completely replaced with chlorite, which is cataclased. The northern cataclasite contains disordered domains of varying degrees of comminution that become progressively finer-grained towards the central slip surface. Domains are up to ~10mm across and are separated by narrow (<0.1mm) slip surfaces of intensely comminuted material. The largest domains predominantly contain plagioclase feldspar

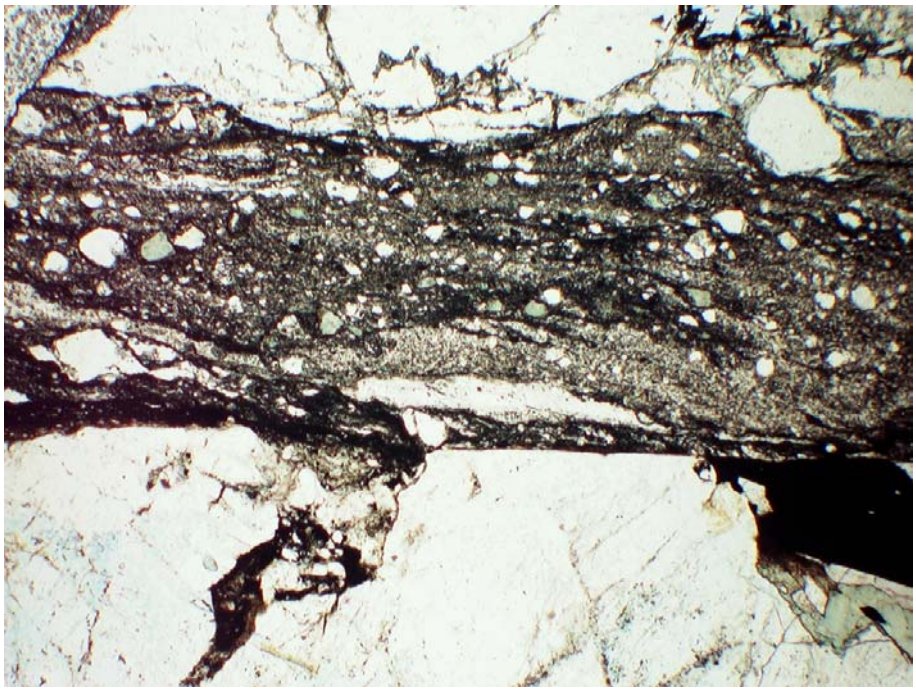

Figure 79. A photomicrograph showing the foliated cataclasite to the north of the central slip surface. The foliation is defined by compositional and grain size domains that are oriented ~15º to the trend of the central slip surface (PPL, field of view 3.1mm).

crystals, which are fractured. Offset twins in plagioclase illustrate that the fractures have small amounts of shear (≤50μm), but the crystals have undergone little cumulative shear strain. Immediately adjacent to the central slip surface, a domain of cataclasite 0.2 to 1mm thick is composed of clasts 0.01 to 0.7mm long in an aphanitic groundmass (Figure 79).

The clasts are rounded aggregates of recrystallised quartz, fragments of feldspars with fracture surfaces and occasional recrystallisation structures, chlorite fragments and opaques. A foliation defined by bands of aphanitic material and opaques within the cataclasite oriented 15º clockwise from the central slip surface is developed in this domain. Numerous high angle fractures cut large (>0.1mm) plagioclase crystals at ~90º to the central slip surface splay from the foliated cataclasite. Some of these fractures appear to branch away from the central slip surface.

The wall rock to the south of the central slip surface in SK9 contains numerous pseudotachylyte veins in host rock that shows variable amounts of deformation; for the most part the wall rock in the slide is fractured but not extensively sheared, but the pseudotachylyte veins encompass lenses of cataclasite and cross-cut cataclasites localised in shear fractures. The shear fractures containing cataclasites cross-cut the wall rock, apparently linking biotite and amphibole phases, which are invariably also cross-cut by pseudotachylytes, suggesting that these minerals are preferentially broken as well as melted during pseudotachylyte generation. Pseudotachylytes form a complicated inter-connected network of veins that are rarely parallel to the central slip surface. The pseudotachylytes are mostly replaced and/or altered, but can be recognised from their vein geometries, flow textures, and lithic clast content, shape and composition.

Pseudotachylyte veins are brown to orangey green, and display a wide range of flow and mixing textures (Figure 80). Bright interference colours indicate that the pseudotachylyte groundmass has been completely replaced, likely with biotite and/or chlorite. Lithic clasts in the veins are rounded and embayed, and are generally 0.01 to 0.6mm though occasionally reach >2mm where the pseudotachylytes are widest. Clasts are frequently composed of biotite and hornblende, as well as quartz, plagioclase, alkali feldspar, and fragments of cataclasites. Injection veins are common, branching from thicker pseudotachylytes at a wide range of angles. Overall, the frequency of pseudotachylytes and injection veins gives the wall rock a brecciated appearance, especially close to the central slip surface. Randomly oriented microcrystallites overgrowing lithic clasts are identifiable in some of the veins where the pseudotachylyte shows least evidence for replacement in thin section. Most of the microcrystallites are ≤10μm long and 3μm wide, and have a plagioclase-like composition, though some smaller (≤7μm long, 1μm wide) microcrystallites likely with a biotite composition are also developed.

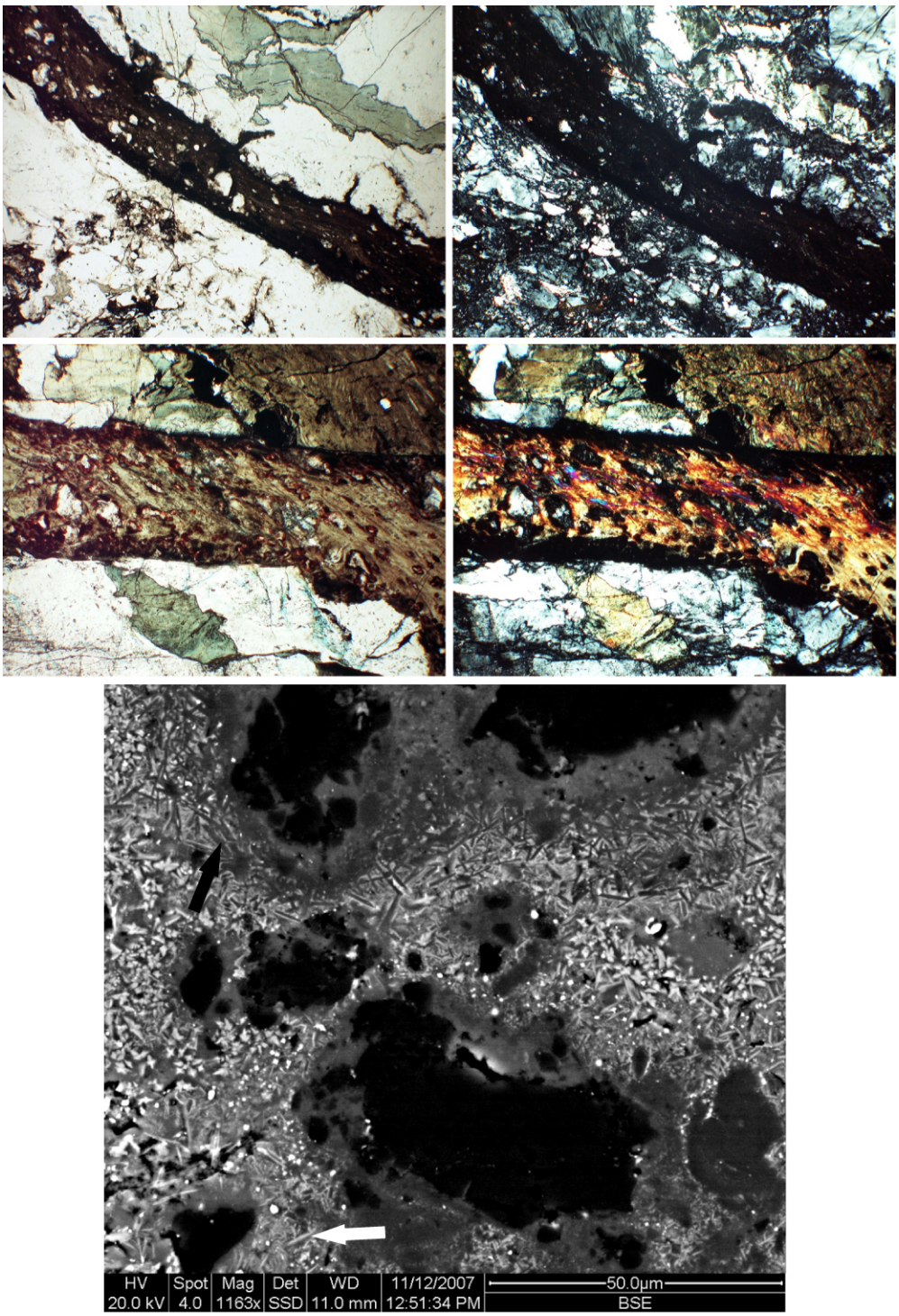

Figure 80. Photomicrographs and an SEM image of the pseudotachylytes in the southern wall rock of sample SK9. TOP; A narrow vein containing typical dark brown, aphanitic matrix that is isotropic. MIDDLE; A vein containing pseudotachylyte that has been replaced by greenish brown matrix material which has bright interference colours (left PPL, right XPL, field of view in all images 1.6mm). BOTTOM; a BSE image of another pseudotachylyte vein showing plagioclase (black arrow) and biotite (white arrow) composition microcrystallites.

In outcrop, the pseudotachylyte that defines the central slip surface within sample SK9 pinches out laterally into a thicker fault core composed of cataclasite (Figure 72). Sample SK10 is taken from the section of the fault strand where the pseudotachylyte and cataclasite are both present. The sample contains a localised fined grained cataclasite that

separates a northern chlorite-rich fault breccia from wall rock that is relatively undeformed in the south.

The localised cataclasite is 1 to 3.6mm thick in the sample, and is composed of clasts (20 to 40%) in a matrix (60 to 80%) of fine (≤7.5μm) chlorite, quartzo-feldspathic material and possibly epidote (Figure 81). The clasts are rounded to sub angular, 15μm to 600μm long, and are composed of plagioclase, alkali feldspar, quartz, chlorite, opaques, and some aggregates of recrystallised quartz and feldspars. Some clasts have tails of completely recrystallised quartz and possibly feldspar with a grain size of around 10 to 20μm. The tails define a compositional foliation in the localised cataclasite that is oriented sub-parallel to 10º to the trend of the cataclasite. The contact between the localised cataclasite and wall rock to the south is rough; several laterally adjacent triangle-shaped embayments have developed in response to shear fractures in the wall rock and give the wall rock edge a serrated appearance. Where the wall rock edge is approximately straight, portions of crystals have been plucked, resulting in an irregular wall rock edge. A narrow (≤0.25mm) seam of aphanitic ultracataclasite-like material in which clasts (≤5%) are rounded and ≤0.08mm defines the edge of the localised cataclasite, cross-cutting material in the embayments. The aphanitic seam is straight, and runs from point to point of the wedge-shaped protrusions between embayments. Cataclasites within the embayments are cross-cut by the edge of the localised cataclasite, which truncates compositional banding and some clasts.

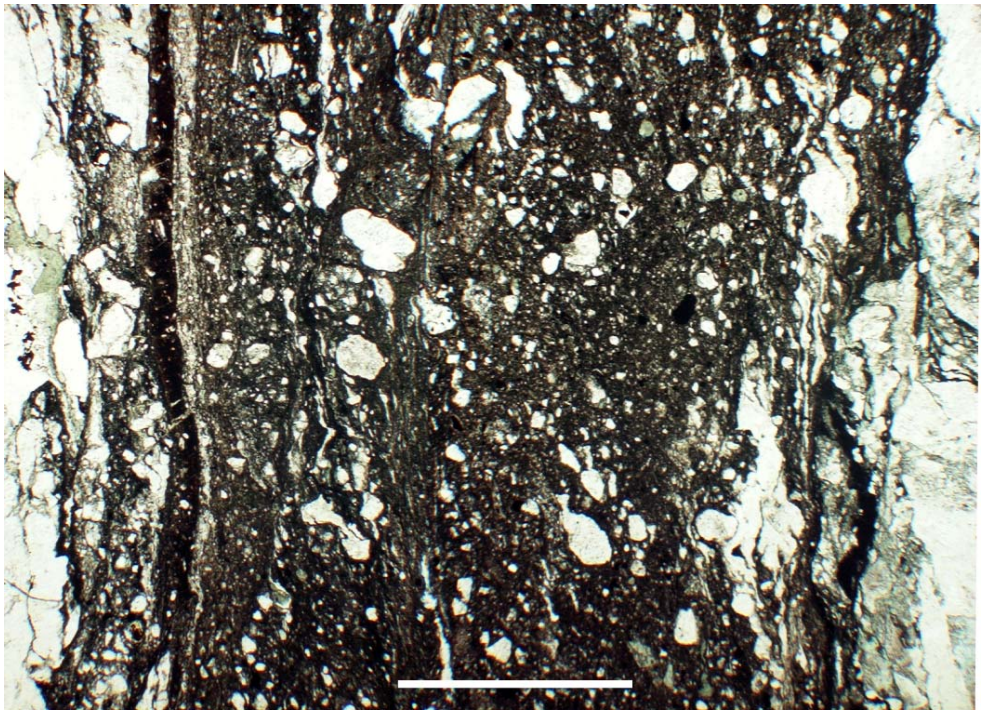

Figure 81. The localised cataclasite in SK10 is composed of 60 to 80% matrix in which clasts are rounded to sub-angular. Scale bar 1mm.

One irregularity in the wall rock contains material that might be pseudotachylyte; it is dark to pale brown, aphanitic, and contains ~15% rounded clasts (Figure 82). Additionally, compositional variations that potentially represent flow banding are defined by colour variations in the groundmass, opaque material localised at the wall rock edge is similar to a chilled margin and one small (~0.15mm long) injection vein intrudes a plagioclase in the wall rock. Microcrystallites are not evident in thin section, but the wall rock irregularity has a similar geometry to an injection vein. Results of SEM analyses to determine a melt origin for this pseudotachylyte are inconclusive (Figure 82). The groundmass between clasts does not contain microcrystallites, and appears to be comprised of amorphous material with an alkali feldspar composition containing numerous titanite droplets. Compositionally the pseudotachylyte is extremely similar to the localised cataclasite. However, texturally the pseudotachylyte is distinct in that it appears to be matrix-supported, whereas the localised cataclasite is clast-supported. There are very few small grains in the pseudotachylyte, with amorphous material comprising the majority of the matrix.

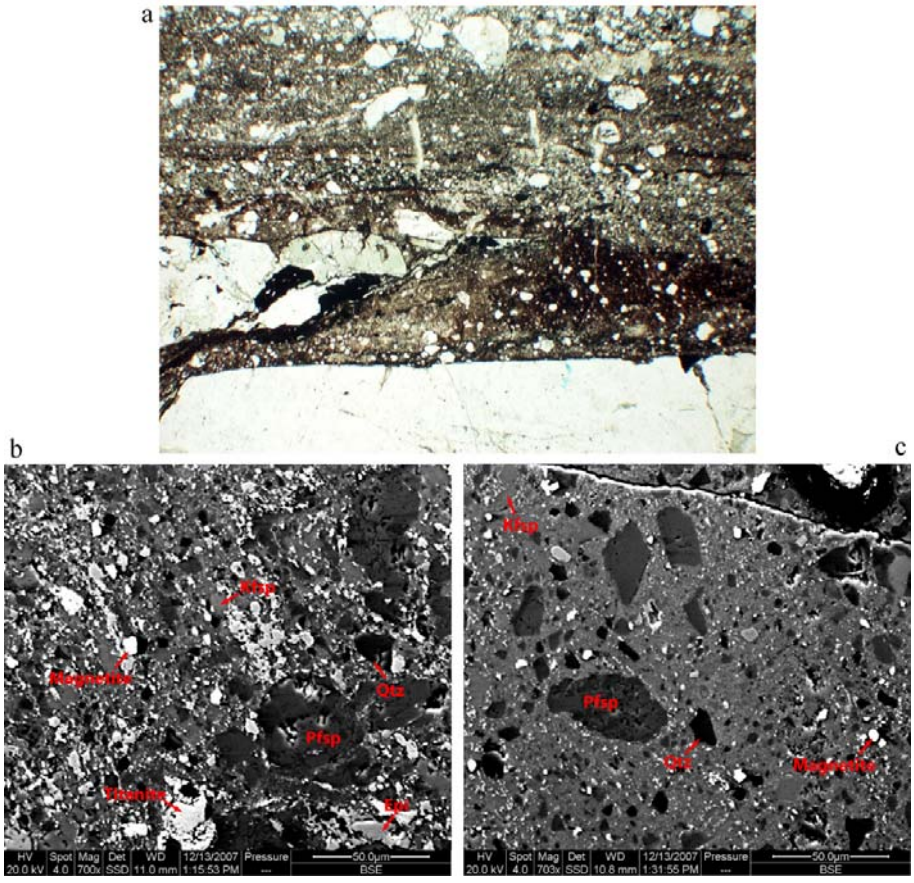

Figure 82. An irregularity in the wall rock – localised cataclasite possibly contains pseudotachylyte. a. Photomicrograph of the irregularity showing the pseudotachylyte, which contains compositional variations, and few rounded clasts (PPL, field of view 3.1mm). b. BSE image of the localised cataclasite showing a granular, clast-supported texture. c. BSE image of the pseudotachylyte which does not contain microcrystallites but is matrix-supported with an amorphous matrix of alkali feldspar and titanite (Epi = epidote, Pfsp = plagioclase, Kfsp = alkali feldspar, Qtz = quartz).

The southern wall rock in sample SK10 is composed of host rock that is pervasively fractured. Twinned plagioclase shows that the fractures are mostly shear fractures with tens of microns offset on twin planes that are as little as 20μm apart. Typically, the wall rock contains tens of fractures per millimetre. The fractures are inter-crystalline and are developed in plagioclase, alkali feldspar, quartz and hornblende. Micro-cataclasites (<10μm) are developed along fractures in all minerals. Deformation lamellae in quartz are cross-cut by the fractures. Though pervasive, and apparently mutually cross-cutting, two predominant orientations can be qualitatively recognised; one at ~40º clockwise from the localised cataclasite, and one sub-parallel (<10º) to the localised cataclasite. Wider (~0.1mm) fractures parallel to the low-angle set contain chlorite. The injection vein-like structure in the pseudotachylyte described above trends into a shear fracture 0.1 to 0.3mm wide containing cataclasite in which the wall rock minerals are comminuted, forming angular clasts ≤0.1mm long. This shear fracture curves back towards the localised cataclasite and encompasses a portion of wall rock in which the pervasive fractures are more frequently developed. The fractures are more closely spaced, and contain thicker (tens of microns) micro-cataclasites.

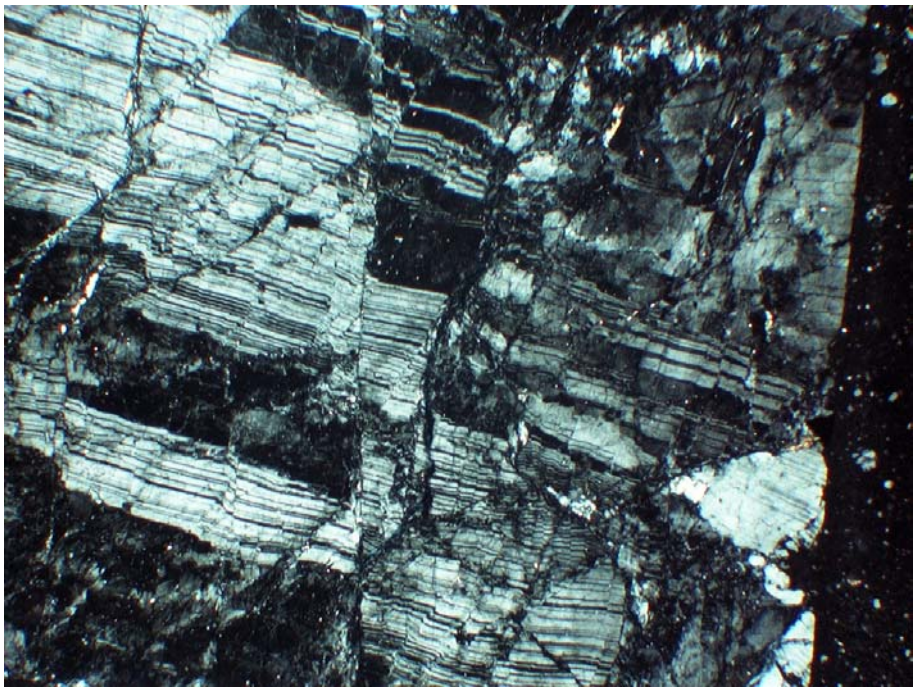

Figure 83. The southern wall rock in sample SK10 is pervasively fractured. Twinned plagioclase shows that many of the fractures are inter-crystalline shear fractures with up to tens of microns displacement (XPL, field of view 3.1mm).

To the north of the localised cataclasite, sample SK10 is composed of a fault breccia (Figure 84). The breccia has a complicated texture; randomly oriented, inter-connecting seams of cataclasite ~1 to 3mm wide separate fragments of less deformed rock that are

centimetres across. The breccia as a whole contains ~40% chlorite, most of which is euhedral and forms a matrix within the cataclasite seams where it can locally reach 80%. Clasts in the cataclasite seams are 0.02mm to several millimetres long, and are composed of angular fragments of quartz, plagioclase, alkali feldspar, chlorite that has replaced biotite which has lower interference colours than the matrix chlorite, and calcite. Calcite also forms euhedral crystals in the matrix of some of the cataclasite seams. Plagioclase and alkali feldspar are pervasively sericitized throughout the breccia, including within the less deformed fragments. The less deformed fragments retain the igneous texture and mineral assemblage of the host rock, with additional chloritization of biotite. Quartz consistently displays sweeping undulose extinction, and subgrain rotation recrystallisation has occurred in localised seams. However, the less deformed fragments are also heavily fractured; healed fractures in plagioclase and alkali feldspar are truncated by seams of cataclasite, and chlorite-filled inter-crystalline fractures appear to splay from the cataclasites. Truncated clasts show that the localised cataclasite cross-cuts both the seams of cataclasite and less deformed fragments of the breccia. Locally, material from the breccia spalls into the localised cataclasite, raising the proportion of clasts.

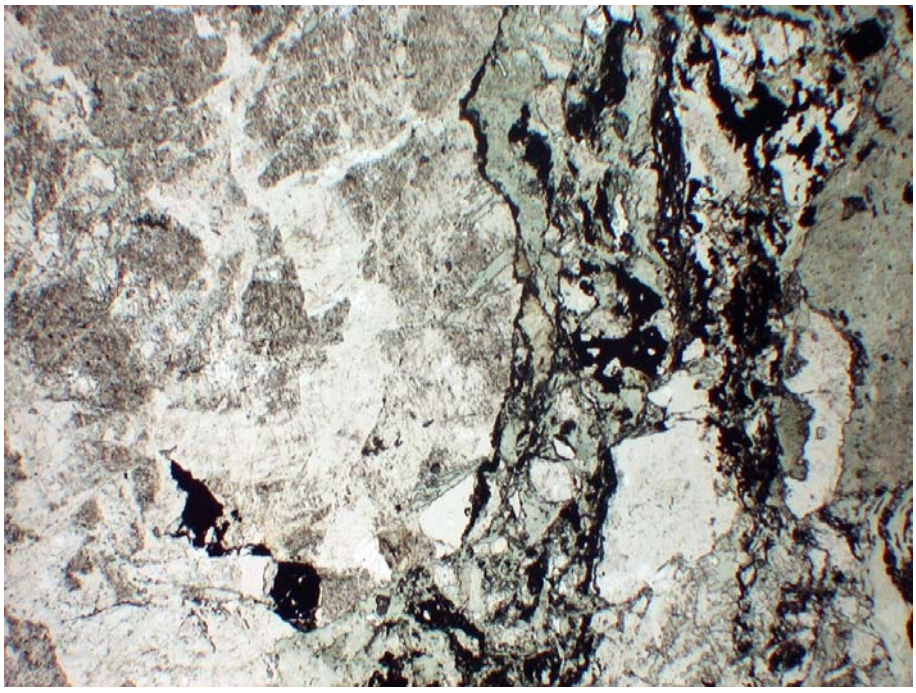

Figure 84. Immediately to the north of the localised cataclasite, a fault breccia is composed of seams of cataclasite that separate fragments of less deformed rock. This photomicrograph shows part of a seam of cataclasite (right), which is rich in chlorite (pale green) juxtaposed against less deformed rock (left) in which plagioclase and alkali feldspars are extensively altered (PPL, field of view 3.1mm).

4.5.1.1 SKF; summary

Samples from adjacent parts of a fault core strand of the SKF contain different deformation elements. Brittle foliated cataclasites, pseudotachylytes and cataclasites formed during the latest stages of deformation are laterally juxtaposed. Chlorite is abundant in some parts of the fault showing that fluid flow was likely heterogeneously distributed in the fault core. Brittle fault rocks cross-cut crystal-plastic deformation products, indicating that early slip was accommodated by localised ductile deformation.

4.6 The Glacier Lakes fault

The GLF is composed of a series of sub-parallel fault core strands that are composed primarily of cataclasites. Three oriented samples of fault core material from the fault zone were collected for detailed analysis (Table 2). Sample GLF5 is taken from the northern bounding fault core strand which forms the wall of the fault gulley at locality 2 (see Figure 31). The sample encompasses the entire thickness (≤15mm) of the fault core strand; the south edge of the sample is exposed as a fracture surface decorated with slickenlines, and the wall rock to the fault zone is present immediately to the north of the fault core (Figure 85). Pseudotachylytes were not identified in the GLF from field observations.

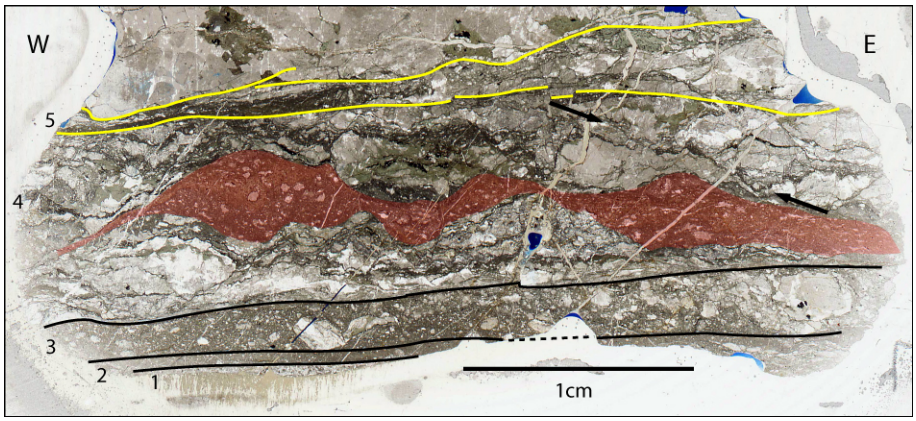

Figure 85. A photograph of part of the thin section of sample GLF5 showing the northern bounding fault core strand of the GLF. The fabric domains described in the text are indicated.

The fault core material within sample GLF5 is texturally complex, comprising domains of cataclasites, foliated cataclasites and a single pseudotachylyte strand. The domains are generally separated by slip surfaces that trend parallel to the edges of the fault core. A transect from south to north across the fault core material shows that the domain at the southern edge of the section (the exposed surface in the field, domain 1) is a narrow (~0.5 to 0.75mm) zone containing abundant euhedral, tabular quartz and chlorite. Quartz

(≤0.1mm) and chlorite (≤0.25mm) are inter-grown and form a cement that accounts for ~50% of the zone between fragments of cataclasite (Figure 86). The cataclasite fragments are angular to sub-rounded, 0.015 to 0.5mm long, and are consistently the same composition as the adjacent cataclasite. Subtle changes in the adjacent cataclasite matrix to clast ratio are reflected in the composition of the fragments in the southern quartz and chlorite rich zone, suggesting that they are locally derived. The contact between the southern zone and the adjacent cataclasite (domain 2, Figure 85) is sharp and irregular. Numerous fractures filled with the same composition as the quartz and chlorite cement appear to splay from this contact, and are ≤3mm long, cross-cutting all of the other fabric domains in the fault core material. The fractures generally have a common orientation, oriented up to 60º counter-clockwise from the trend of the contact.

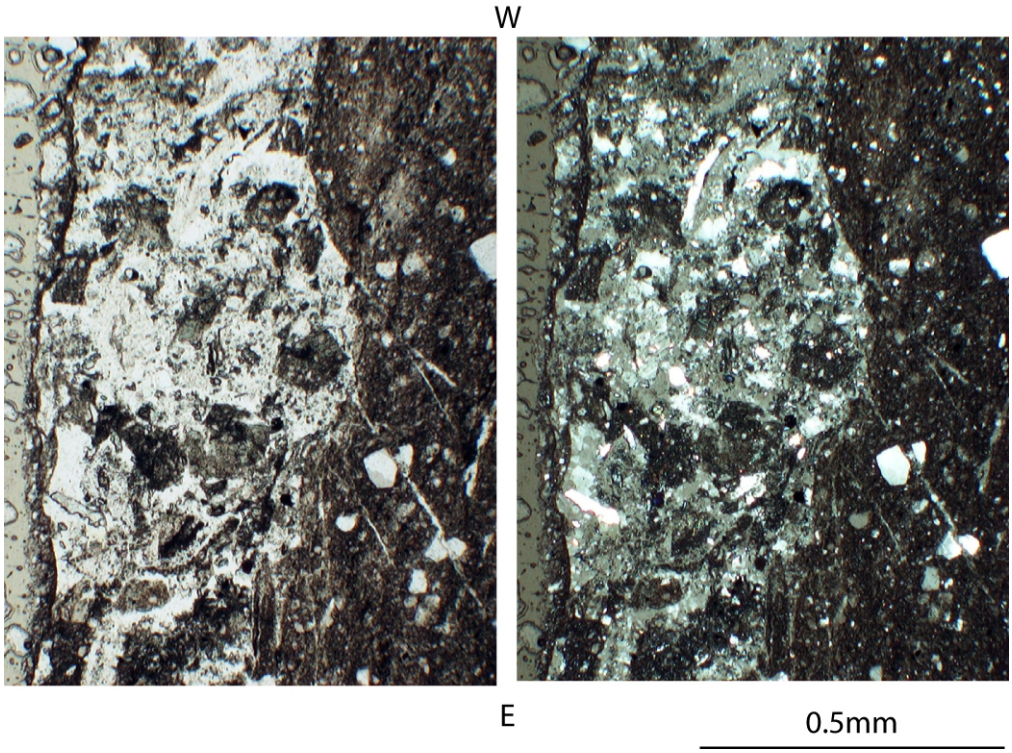

Figure 86. Photomicrographs of fabric domain 1 in sample GLF5 (left PPL, right XPL). The domain is composed of fragments of cataclasite that are cemented with euhedral quartz and chlorite.

A thin (≤1mm) cataclasite (domain 2) is present adjacent to the southern quartz- and chlorite-cemented domain. This cataclasite is pale to medium brown and contains rounded or sub-rounded clasts up to 0.2mm long. Clasts are randomly oriented and are composed of fragments of quartz and feldspar that do not exhibit recrystallisation textures or other early deformation features. The clasts are present in an aphanitic matrix that forms 80% of the cataclasite. The northern edge of this fine-grained cataclasite is sharp and generally planar, except for where it wraps around protruding clasts from the coarser cataclasite to the north. There is no distinct edge material that might comprise a slip surface between the

two cataclasites, the transition is apparent only because of a significant change in the clast to matrix ratio.

The coarser cataclasite (domain 3) to the north of the fine-grained cataclasite contains clasts 0.05 to 2.5mm long which comprise ~50% of the domain. The clasts are rounded to sub-angular and are composed of plagioclase and alkali feldspar that are often sericitized (in some cases completely sericitized), quartz, some of which shows evidence of extensive bulging recrystallisation, clasts of earlier-formed cataclasite (with chlorite in the matrix), chlorite, and opaque minerals. In general, the feldspars in this cataclasite do not show evidence for dynamic recrystallisation, though it is possible that some aggregates of very fine subgrains may contain feldspar. The matrix of the coarse cataclasite is a brown, opaque material that has a green tint in places suggesting chlorite is a significant constituent.

A foliated cataclasite (domain 4) is present to the north of the coarser grained cataclasite (Figure 87). The transition from unfoliated to foliated cataclasite is delimited by a narrow (≤0.25mm) seam of chlorite- and quartz-rich material that appears to cross-cut the foliation in places. This seam is extremely fine grained (~5μm) and contains very few clasts. The seam does not truncate clasts in the coarse unfoliated cataclasite, but its edge is distinct due to an abundance of tiny (<5μm) opaques. In places this seam has a similar colour and aphanitic texture to a pseudotachylyte. The foliation in the foliated cataclasite is defined primarily by fabric elements that contain differing grain sizes, which are associated with compositional changes. Extremely fine-grained (~10μm) quartz and epidote-rich elements are dark orange-brown, ≤0.3mm thick and give the cataclasite a crenulated appearance as they are irregularly shaped. Between these extremely fine elements, are coarser (mostly ≤0.3mm, with exceptional grains that are up to 1.5mm) quartz and feldspar rich elements. The quartz in the coarser elements has undergone extensive bulging recrystallisation. Feldspars display undulose extinction and minor subgrain development and are often sericitized. Shear fractures cross-cut the foliated cataclasite, adding a secondary foliation oriented ≤50º clockwise from the trend of the edge of the fault core. These shear fractures are generally contained within the foliated cataclasite, cross-cutting several fabric elements, or are truncated by the adjacent pseudotachylyte.

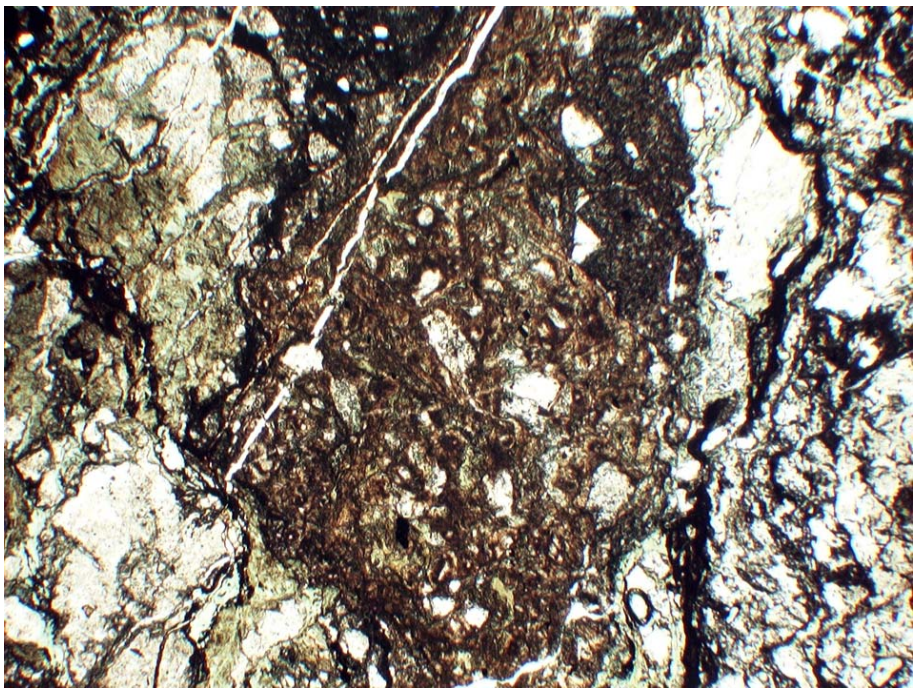

Figure 87. The foliated cataclasite is cross-cut by a pseudotachylyte vein (centre) that truncates the foliation (PPL, field of view 3.1mm).

A single pseudotachylyte strand is present within the GLF fault core that cross-cuts the foliated cataclasite. The pseudotachylyte vein ranges in thickness from 0.5 to 3mm with an irregular, wavy morphology. At the scale of the thin section, injection veins are absent, though the orientation of the vein sub-parallel to the trend of the cataclasite seam suggests it may be a fragment of generation surface (see Figure 85). The vein is composed of an orange-brown or brown groundmass which often forms halos around clasts and defines faint flow fabrics. Chlorite is also present in the groundmass between the brown material. Clasts are rounded, ≤0.5mm long, and are composed of feldspar, sericitized feldspar, sericite, quartz and fragments of cataclasite containing all of these minerals and also chlorite. Microcrystallites are difficult to identify within the pseudotachylyte with an optical microscope, but SEM analysis shows that randomly oriented, lath-shaped microcrystallites characteristic of chilled melt are present (Figure 88). The observed microcrystallites are up to ~20µm long, ~5µm wide, and have a feldspar composition, with fine (~1µm) laminations probably of biotite or titanite. There are also tiny (<10µm long), acicular crystals between the feldspar microcrystallites that are too small for their composition to be reliably defined, but are likely similar to biotite. The arrangement of microcrystallites into spherulites or bow-tie morphologies is rarely evident as the groundmass is extensively disrupted by chlorite development.

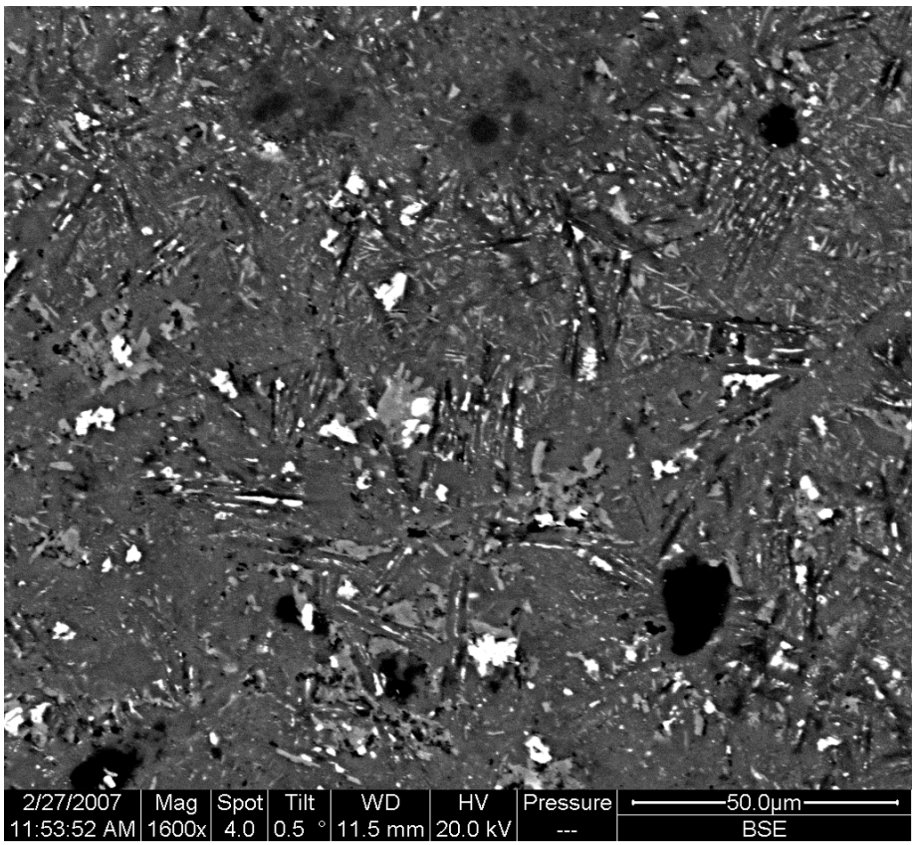

Figure 88. BSE image of the GLF pseudotachylyte showing feldspar composition microcrystallites in a groundmass of chlorite (pale grey).

A wedge-shaped domain containing a fault breccia (domain 5, Figure 85) is juxtaposed between the foliated cataclasite and the wall rock in sample GLF5. The transition from foliated cataclasite to fault breccia is marked by an approximately straight seam of extremely comminuted cataclasite 0.05 to 0.8mm thick that cross-cuts the foliation in the foliated cataclasite. This seam of material is composed of >90% dark brown, aphanitic material in which clasts are rounded fragments of feldspar or aggregates of crystals derived from the foliated cataclasite. Within domain 5, clasts (>80%) are angular and 0.02 to 4mm or more long. The clasts are mostly mono-crystalline fragments of plagioclase, alkali feldspar, quartz and hornblende, reflecting the host rock composition. The matrix in the breccia is similar to the cataclasite at the boundary with the foliated cataclasite; it is dark brown, aphanitic and contains some fragments of feldspar and quartz crystals ≤25µm. The wall rock edge of the fault breccia is at an angle of around 5º to the boundary with the foliated cataclasite giving domain 5 a wedge shape. The wall rock edge is defined by a series of inter-linked fractures (Figure 89). Brittle shear fractures are developed in plagioclase and alkali feldspar, which offset twins in plagioclase by <25µm in a left-lateral sense. Where the fractures trend into quartz, subgrains are developed indicating that the shear offset is accommodated by localised crystal-plastic deformation. These fractures are

connected longitudinally in a series of non-coplanar segments that give the edge of the fault core a diffuse appearance.

Figure 89. The wall rock edge in GLF5 is defined by a series of inter-connected fractures. In plagioclase and alkali feldspar, brittle shear fractures that offset twins in plagioclase by <25µm. Shear fractures in feldspars trend into quartz where the shear offset is accommodated by localised crystal-plastic deformation (XPL, field of view 3.1mm).

Alteration of the wall rock in GLF5 has caused pervasive sericitization of plagioclase and alkali feldspars. Biotite is chloritized, but hornblende is unaltered. Fractures in the wall rock have a dominant orientation at 30 to 40º counter-clockwise to the overall trend of the domain boundaries within the fault core. These fractures are opening mode (containing minor chlorite and sericite) or shear fractures with <25µm offset. Shear fractures defined by localised cataclasites up to 0.1mm thick cross-cut the entire thin section and are centimetres in length that are. Longer fractures form angles of ~25º with the domain boundaries in both clockwise and counter-clockwise orientations.

Samples GLF3 and GLF4 are taken from the fault core strand within the fault trough at locality 23 (see Figure 28, Ch. 3), and contain a wide variety of deformation products including pseudotachylytes, ultracataclasites, cataclasites, fault breccias and mylonitic rocks. These deformation elements are disordered by a late stage brecciation event that has fragmented and mixed all of their textures. Pseudotachylyte veins are difficult to identify confidently as microcrystallites are not discernable in thin section. However, orange-brown veins up to 1.2mm wide that contain flow banding have sharp edges that cross-cut the adjacent cataclasites and ultracataclasites. These veins contain rounded and embayed

clasts (<10%) in a groundmass of extremely fine epidote (≤10μm) and chlorite, as well as some aphanitic, isotropic material. Injection veins are not present in the samples, and the veins are extremely fragmented. Ultracataclasites are homogeneous dark brown to black (PPL) layers in which clasts (~15%) are angular to rounded. The matrix is predominantly epidote and chlorite (≤15μm) with some quartz and feldspar. In both pseudotachylytes and ultracataclasites the clasts are composed of quartz, aggregates of recrystallised quartz and feldspars, cataclasites with epidote as a component of the matrix, and clusters of epidote crystals.

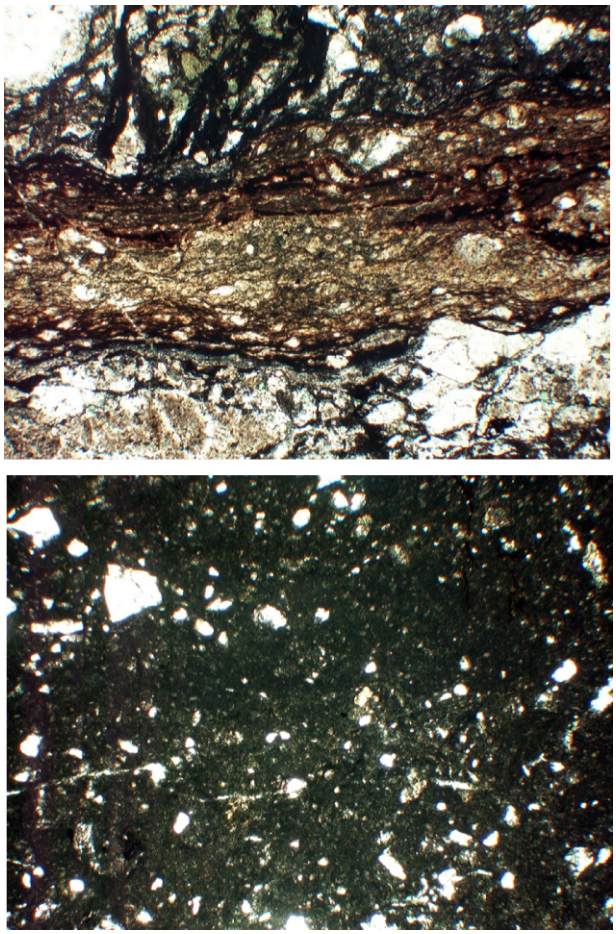

Figure 90. Photomicrographs of pseudotachylytes and ultracataclasites in the GLF. Top: an orange-brown pseudotachylyte vein (centre) in which flow banding is evident cross-cuts the adjacent cataclasites. Bottom: a typical ultracataclasite texture in which sub-angular to rounded clasts are present in a homogenous black, aphanitic matrix (both images PPL, field of view for both is 3.2mm).

Fault breccias are common in both GLF3 and GLF4, laterally grading into coarse-grained cataclasites. Plagioclase is pervasively sericitized in the fault breccias and in the clasts in cataclasites. Fault breccias show that the degraded feldspars may also have subgrains developed along grain boundaries by bulging recrystallisation, though it is difficult to distinguish in the most altered grains. Quartz contains sweeping undulose extinction and significant subgrain development likely by bulging recrystallisation. Biotite and

hornblende are chloritized, and in places recrystallised. This mineral assemblage is cut by numerous fractures in a wide variety of orientations, which are mutually cross-cutting with shear displacements of on the order of millimetres to tens of millimetres. The fractures are filled with aphanitic epidote and chlorite, and have slightly curved traces. Cataclasites have grain size distributions that range from similar to fault breccias to ultracataclasites. The clasts in the cataclasites include altered feldspars, aggregates of recrystallised quartz, hornblende, and fragments of cataclasites. The matrix material is commonly similar to the matrix of the ultracataclasites, comprising fine grained (≤15μm) epidote and chlorite, as well as some quartz and feldspars.

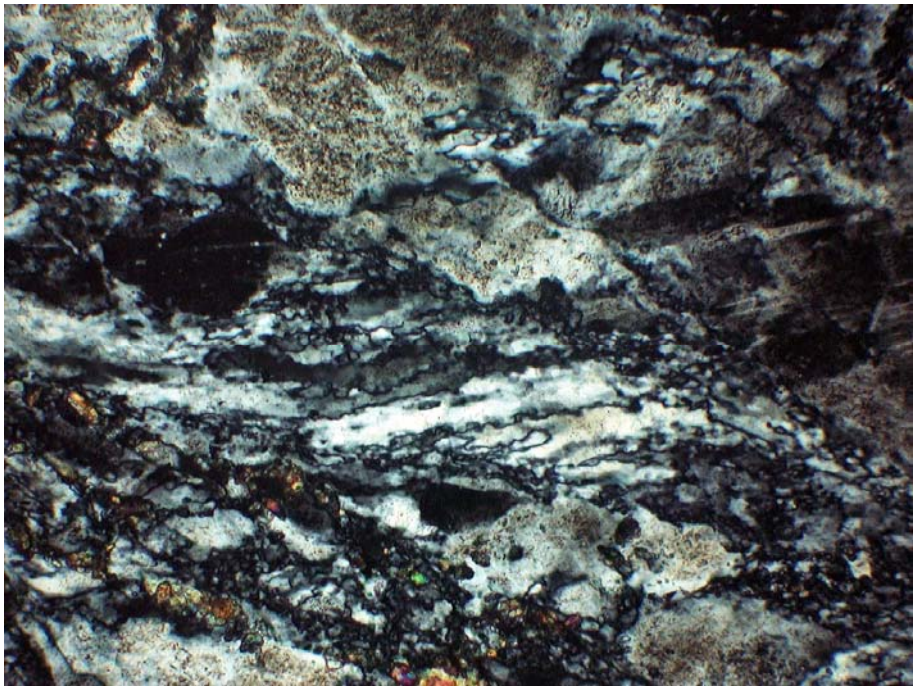

Figure 91. Recrystallised quartz and feldspar in the GLF. A layer of quartz subgrains developed through bulging recrystallisation has a grain size of around 10μm. Plagioclase and alkali feldspar (top) display a core-mantle texture derived from incipient recrystallisation (XPL, field of view 0.8mm).

Extensively recrystallised quartz and feldspar aggregates are locally developed in sample GLF3, which have a mylonitic fabric (Figure 91). Quartz is completely recrystallised by bulging recrystallisation and possibly subgrain rotation, and consistently has a grain size of ~10μm. Plagioclase and alkali feldspar have some subgrain development along grain boundaries, and frequent survivor clasts show patchy undulose extinction and are fractured, indicative of a core-mantle texture. Biotite and hornblende are absent from this ductiley deformed portion of the sample, which is likely because in hand specimen the sample contains a fragment of aplite dyke. All of the deformation products in the two samples are brecciated and cross cut by numerous, chaotic fractures containing chlorite, quartz, and some alkali feldspar. The brecciation has caused a massive disordering of the

textures in the sample so that no single pseudotachylyte, ultracataclasite or slip surface can be traced for more than several centimetres in the samples.

4.6.1.1 GLF; summary

The GLF fault core contains predominantly cataclasites and ultracataclasites as well as occasional pseudotachylytes. Crystal plastic deformation is predominantly restricted to quartz bulging recrystallisation, with feldspars deforming by fracturing and cataclasite flow. Pseudotachylytes in GLF5 cross-cut all other fabric domains, but are fragmented in GLF3 and GLF4 suggesting that more than one generation event occurred along the fault.

4.7 Interpretation

4.7.1 The GPF

The GPF fault rocks demonstrate a long and complex history of deformation; cross-cutting relations are evident between mylonites, cataclasites, ultracataclasites and slip surfaces in outcrop and also in thin section.

The GPF deformation history is characterised by early localised ductile deformation. Dynamic recrystallisation of quartz and feldspars (with some fracturing of feldspar survivor grains) is pervasive throughout the fault core deformation elements, and is much more developed than in the host rock. Quartz shows evidence for both bulging recrystallisation and subgrain rotation recrystallisation, suggesting deformation occurred at temperatures of around 200 to >400ºC (see section 1.2.2 for a discussion of recrystallisation mechanisms as temperature gauges in natural faults). Core-mantle textures with diffuse boundaries are indicative of bulging recrystallisation of feldspar, suggesting deformation occurred at higher temperatures (450 to >600ºC). Feldspar recrystallisation products therefore indicate that peak temperatures observed in the fault core rocks of the GPF are 600ºC or more. Subsequent lower-temperature deformation should be expected to over-print early high temperature textures. Equigranular, polygonal crystals of quartz in sample GPF6 suggest some static annealing has occurred, though this is evidently spatially heterogeneous (Heilbronner and Tullis, 2002). Despite the significant ductile deformation of the GPF fault cores, foliations are not observed in thin section in any of the GPF samples. Foliations are observed to develop in shear zones where quartz and biotite subgrains coalesce into elongate ribbons (e.g. Tullis *et al.*, 2000). The absence of a foliation may indicate that diffusive mass transfer, grain boundary sliding and possibly

superplasticity were important during deformation, though further work to analyse the presence or absence of a lattice-preferred orientation is required to infer these processes (e.g. Rutter *et al.*, 1994; Stunitz and Fitz Gerald, 1993).

Ductile deformation textures in the GPF are consistently cross-cut by the products of cataclasis, brecciation and frictional sliding. Progressive deformation therefore involved primarily brittle mechanisms and induced multiple slip events. Sample GPF10 contains several different deformation phases (Figure 56, 56, 57) that are distinguished primarily by cross-cutting relations. The latest deformation in the slide is the localised brittle comminution of the central aphanitic zone. Two fractures splay from within this zone, suggesting that they represent either syn- or post-slip secondary structures associated with the aphanitic zone. These fractures are filled with quartz and chlorite and are not deformed. The central aphanitic zone itself cross-cuts a fault breccia that formed during a brittle deformation event, likely a high strain rate slip event. The matrix to the fault breccia is composed of chlorite, typical of greenschist facies pressure and temperature conditions (e.g. Bruhn *et al.*, 1994). The fault breccia contains clasts of pseudotachylyte material, implying that a pseudotachylyte-generating slip event occurred before the brecciation slip event. The fault breccia intrudes the wall rock cataclasite in sample GPF10, and truncates quartz and chlorite veins present in the wall rock cataclasite. The wall rock cataclasite deformation features were therefore developed prior to the production of the fault breccia. Within the wall rock cataclasite, early fractures in feldspar survivor grains (the earliest brittle deformation in the slide) are healed and overprinted by dynamic recrystallisation textures. Dynamic recrystallisation products in quartz and feldspars are cut by brittle fractures, giving the cataclastic texture, and are in turn cross-cut by quartz and chlorite filled veins.

Ultracataclasites in samples GPF5, GPF6 and GPF7 are brittle deformation products that also cross-cut ductile deformation prevalent in the wall rock, and have involved localised fluid flow. The ultracataclasites show abundant evidence for localised fluid influx during deformation; the matrix of the ultracataclasites contains an extremely large proportion of hydrothermal chlorite and epidote, and quartz and alkali feldspar veins are common. Accurately determining the proportion of chlorite and epidote from microstructural observations is difficult as the matrix is so fine-grained. However, it is clear that precipitation of these minerals occurred continuously during progressive deformation as fragments of re-worked ultracataclasite that contain epidote can be identified in the ultracataclasites. It is therefore likely that a substantial proportion of the ultracataclasite

volume is composed of a hydrothermal mineral assemblage that is the product of fluid flow rather than comminuted host rock minerals. Cross-cutting relations in the ultracataclasite matrix indicate that chlorite superseded epidote as the predominant hydrothermal product. Quartz and alkali feldspar veins cross-cut the ultracataclasites. A large proportion of clasts in the ultracataclasite are composed of quartz and alkali feldspar; the clasts that show least evidence for recrystallisation are angular quartz clasts. Quartz in the wall rock to the ultracataclasites is intensely recrystallised, suggesting that the quartz veins have been re-worked by the ultracataclasite.

4.7.2 The SKF

Fault-related deformation in the SKF shows a similar pattern of early ductile deformation over-printed by later brittle deformation to the GPF, but is characterised by spatially heterogeneous deformation products.

Crystal plastic deformation is most pronounced in sample SK9, where recrystallised quartz and subgrains around feldspars are brecciated, and worked into cataclasites in the northern wall rock. Feldspar subgrains are distinct from survivor grains, which have sharp edges. The combination of crystal-plastic deformation of quartz and feldspar indicates temperatures of 450 to ≤600ºC during deformation. Foliations that might have developed in the deformed rock are not evident in the recrystallised material, but if so would probably have been destroyed by later brecciation. In all three SKF samples, the wall rock to the fault core (Figure 72) does not contain evidence for crystal-plastic deformation, suggesting that the recrystallisation observed in some of the fault rocks must have been extremely localised.

Brecciation and cataclasis characterise the majority of the SKF deformation, implying temperatures less than around 300ºC for a large proportion of the deformation. The products of the latest slip event in each sample can be identified from cross-cutting relations in thin section. In SK8, distributed cataclasite flow likely produced the foliated cataclasite which is subsequently deformed. The foliated cataclasite has a similar mineral assemblage to the unfoliated cataclasite but is more comminuted, suggesting that slip was progressively localised onto this zone. If distributed cataclastic flow occurred across the foliated cataclasite, the thickness of the slip surface would have been 10 to 13mm. It is also possible that the narrow, extremely fine-grained material localised at the cataclasite edge could represent the final deformation product as this appears to cross-cut the foliated cataclasite in places. The thickness of the narrow comminuted cataclasite is 0.1 to 1mm.

A single, straight slip surface cross-cuts all fabrics in SK9, and is defined in part by pseudotachylytes. This pseudotachylyte thickness is up to 0.25mm. However, if the foliated cataclasite adjacent to the pseudotachylyte was coeval with the pseudotachylyte, with incipient melting occurring at the foliated cataclasite edge, then the slip surface thickness would have been negligible to 1mm. In sample SK10, the localised cataclasite cross-cuts all other deformation fabrics, suggesting that it formed latest in the slide. Although pseudotachylyte might be present in wall rock irregularities, it is cross-cut by the localised cataclasite. The localised cataclasite thickness is 1 to 3.6mm.

The pseudotachylyte along the central slip surface in SK9 suggests that the last slip event on the north strand of the SKF was an earthquake rupture event. The three samples taken from the fault core show that the earthquake produced different fault rock types and textures with a lateral distance of as little as a metre along strike (the approximate distance between SK9 and SK10). The thickness of the slip surface therefore seems to control the product of brittle deformation.

Mineral phases that were precipitated from hydrothermal fluids are heterogeneously distributed in the three SKF samples. SK8 contains a significant proportion of epidote in the matrix of the cataclasite and foliated cataclasite, as well as in wall rock fractures. SK10 also contains extremely comminuted epidote and chlorite in the localised cataclasite. The fault breccia to the north of the localised cataclasite is dominated by chlorite, and also contains calcite. However, SK9 contains much less chlorite and epidote, particularly in the cataclasite to the north of the central slip surface. The wider parts of the fault core therefore seem to have accommodated more hydrothermal mineralisation than the narrow pseudotachylyte-bearing section. This might suggest that the localisation of slip in the narrow fault core inhibits permeability creation in some way, perhaps by inducing a finer-grained fault rock assemblage, or effectively seals the fault by generation of pseudotachylytes. Lower fluid volumes are thought to promote pseudotachylyte generation by inhibiting competing slip weakening mechanisms such as thermal pressurization (Sibson, 1973). However, the wider parts of the fault core may be wider because they hosted more fluid. In either case, the inter-relation between slip and fluid flow has caused contrasting deformation products to be laterally juxtaposed. Further slip would presumably change the geometry of the fault core, suggesting that the arrangement of slip products observable today is not steady-state and that the fault architecture would change as displacement increased.

4.7.3 The GLF

Samples of fault core from the GLF show that GLF fault rocks have undergone intense deformation involving some intra-crystalline mechanisms, but the majority of textures relate to brittle fracturing.

Ductile deformation is evidenced by the intense recrystallisation of quartz by bulging recrystallisation along with weakly recrystallised feldspars in sample GLF3 (see Figure 91). In this portion of the sample, a foliation is developed by trails of subgrains between feldspar survivor grains with core-mantle structures. Such a texture is indicative of moderate strain at mid-greenschist facies conditions; feldspar has deformed primarily by brittle fracture, with limited recrystallisation (Passchier and Trouw, 2005; Tullis *et al.*, 2000). Peak temperatures during deformation from combined quartz and feldspar textures are therefore interpreted to have been of the order of 400 to ≤500ºC. Quartz subgrains produced by bulging recrystallisation are also common in clasts in the cataclasites and ultracataclasites, indicating that ductiley deformed rocks have subsequently been cataclased.

Cataclasis and progressive comminution of fault rocks in the semi-brittle to brittle regime characterises the majority of deformation in the GLF samples. Most GLF deformation is therefore inferred to have occurred at temperatures less than 300ºC. Cataclasites contain fragmented recrystallised quartz, but the deformation of feldspars is dependent on composition; plagioclase is sericitized throughout the GLF fault rocks and deformed almost exclusively by brittle fracture, whereas microcline tends to be less altered and frequently shows sweeping undulose extinction and subgrains with vague boundaries. Sericitization of plagioclase has occurred without preferred orientation of new sericite crystals, but is pervasive throughout the samples. The compositional change involved in sericitization is thought be a reaction-weakening process as micas (sericite) are weaker than feldspar (e.g. Evans, 1990; Wintsch *et al.*, 1995). However, cataclastic flow in plagioclase has not occurred, and the reaction to sericite has apparently not affected the rheological response of plagioclase to deformation. Alteration of the feldspars may therefore be interpreted to have occurred due to post-deformation fluids, but there is no difference in the plagioclase texture according to whether fragments are within cataclasites, foliated cataclasites, ultracataclasites or mylonites. Fluid flow must have been uniform throughout the fault cores to achieve penetrative alteration in fault rocks with presumably segregated permeabilities.

The last deformation on the GLF was brittle and involved pseudotachylyte generation and brecciation of the fault rocks accompanied by fluid migration that precipitated quartz and chlorite in newly-created fractures. Pseudotachylytes were apparently repeatedly generated along the GLF utilising spatially discrete slip surfaces associated with different fault cores, though uncertainty remains as to the precise nature of the internal architecture of the fault (see section 3.7.2.1). Slip inferred from slickenlines on the exposed edges of fault cores likely occurred late in the GLF deformation history; analysis of fabric domain 1 of sample GLF5 shows that the slickenside is composed of cataclasite fragments cemented by a similar quartz and chlorite assemblage to that in associated with the latest brecciation event. Temperatures were likely less than ~300ºC to induce brittle failure of the fault cores (e.g. Stipp *et al.*, 2002). The composition of hydrothermally precipitated quartz and chlorite is difficult to interpret given the number of factors that control the composition of hydrothermal mineral phases. However, chlorite generally precipitates at temperatures in excess of 300ºC indicating that the migrating fluids were hotter than the ambient temperatures associated with the brittle failure of the GLF.

4.8 Discussion

4.8.1 Comparing fault systems; the GPF and GLF

Microstructural observations show that the differences between the GPF and GLF are subtle; both faults display evidence for early ductile deformation that is over-printed by brittle cataclasis and pseudotachylyte generation. All inferences as to the deformation history for the faults must be qualified in the context of the small number of samples analysed. Further sampling and microstructural analysis will inevitably lead to better constrained models for the deformation histories of the two faults.

Crystal-plastic dynamic recrystallisation mechanisms have been used to estimate the temperatures at which the two faults deformed. The GPF contains more certain evidence for recrystallisation of feldspar (see Figure 57) than the GLF, indicating that early GPF deformation occurred at higher temperatures than early GLF deformation. In general the intensity of recrystallisation is greater in GPF samples than in GLF samples, consistent with field observations that suggest macro-scale mylonitic fabrics are more pronounced in the GPF than the GLF. Mylonitic fabrics in GLF3 are developed in what appears to be a fragment of dyke in hand specimen. Dykes are observed to localise crystal plastic deformation in other parts of the Sierra Nevada (e.g. Christiansen and Pollard, 1997), so

the dyke-hosted deformation may not be related to the GLF if it is a fragment of previously deformed wall rock that has been worked into the fault.

Brittle and semi-brittle deformation textures predominate in both faults showing that the environmental conditions during deformation were similar, and therefore that the period of activity for the GPF and GLF likely overlapped significantly (Figure 92). It is notable that neither fault contains brittle textures that have subsequently been overprinted by crystal-plastic deformation. The transition from crystal-plastic to brittle may have been sharp for the study area faults, or the faults may have accommodated little deformation during the transitional conditions. In either case, the faults do not show evidence for oscillating crystal-plastic – brittle deformation mechanisms. Pseudotachylytes in both faults also indicate that although the time-averaged strain rates for the faults may have differed, the slip accumulation occurred in large slip events on both faults.

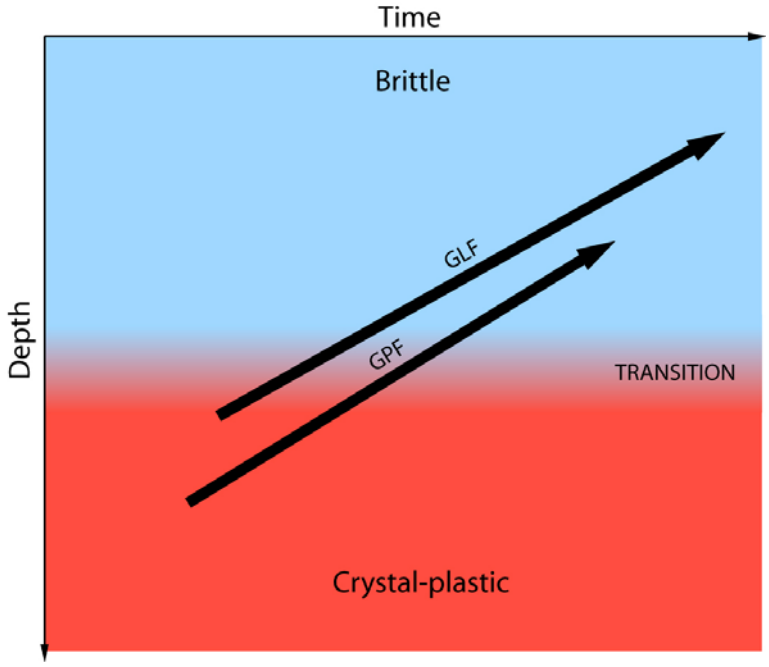

Figure 92. A schematic representation of the duration of fault activity in the crystal plastic and brittle regimes for the GPF and GLF. The GPF likely localised deformation at higher temperatures than the GLF, which seems to cross-cut the GPF from field observations.

The architectures for the GPF and GLF presented in section 3.6.3 are significantly different, but microstructural observations and reactivation analysis suggest that the two faults were potentially coeval for a significant period of their deformation histories (Figure 93). The greater predominance of crystal-plastic deformation in the GPF implies that the GPF predates the GLF, deforming at higher temperatures and pressures. However, the

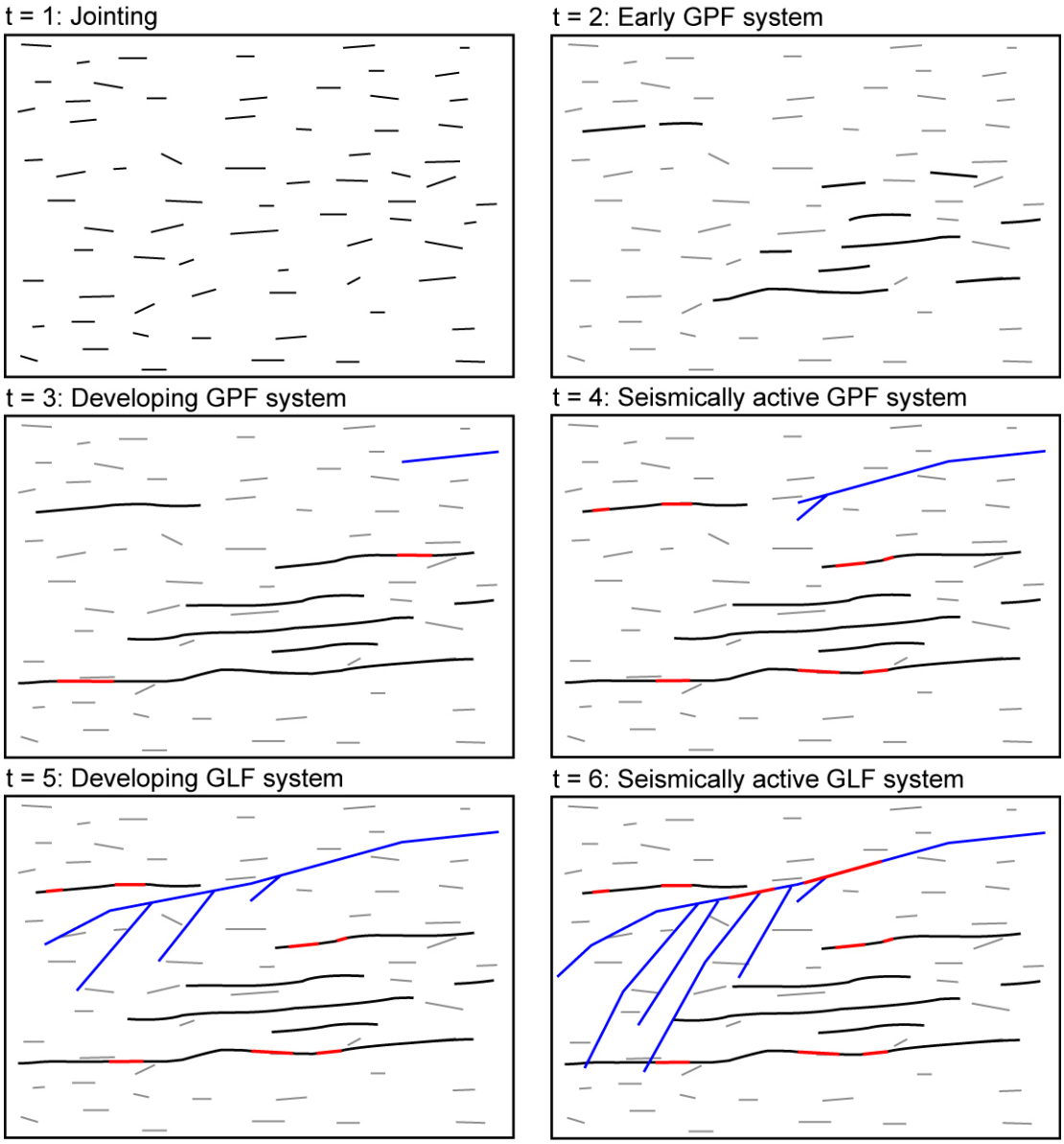

Figure 93. Cartoon illustrating the inferred relative of development of the GPF and GLF systems of faults, and the likely timing of pseudotachylyte generation. The time steps are relative, and no scale is implied.

t = 1: Jointing. Opening mode fractures form in response to pluton cooling, accompanied by hydrothermal fluid flow, precipitation of epidote-chlorite-quartz mineral assemblage, and small amounts (<1m) shear displacement across some fractures. The cartoon does not imply orientation or separation properties for the joint populations.
t = 2: Early GPF system. Joints act as planes of weakness localising shear displacement. The early GPF faults (black lines) deform by crystal-plastic deformation mechanisms, linking end-to-end in some cases.
t = 3: Developing GPF system. GPF faults continue to accumulated displacement by semi-brittle deformation mechanisms, achieving total lengths by continued end to end linkage. Some pseudotachylyte generation possible. An incipient GLF structure (blue line) nucleates.
t = 4: Seismically active GPF system. The latest stages of deformation in the GPF system are brittle, including repeated earthquakes, generating pseudotachylytes in patches along the faults; early pseudotachylytes are brecciated and altered. The GLF continues to develop by brittle deformation.
t = 5: Developing GLF system. The GPF system deformation slows, possibly to a stop, preserving structures that formed late in the deformation history. The GLF is the predominant active system, continuing to propagate.
t = 6: Seismically active GLF system. The GPF system is no longer active, but the GLF continues to develop to its final geometry. Displacement is accumulated on the GLF by earthquake rupture. The splay faults are fully developed and accumulate displacement accommodating off-fault strain.

deformation mechanisms are similar in the faults for a period of activity in both systems, suggesting the systems were coeval for a period. Cross-cutting relations defined in the field and show that the final stages of GLF deformation probably occurred after the GPF system had become inactive. The architectures of the faults are therefore sensitive to subtle differences in the extrinsic controls on fault architecture. Figure 93 shows a model for the development of the Granite Pass area structures based on these observations. However, further work is required to accurately determine either the temperatures during brittle deformation, or the absolute timing of faulting in each fault system to more confidently asses the differences in the deformation histories.

4.8.2 Identifying pseudotachylytes

Pseudotachylytes are often considered to be rare fault rocks as they are relatively infrequently reported in descriptions of faults (Magloughlin and Spray, 1992; Sibson, 2003), despite theoretical studies suggesting that they should be common (Jeffreys, 1942; McKenzie and Brune, 1972). Sibson and Toy (2006) suggest that this apparent scarcity is either because pseudotachylyte is in fact rarely generated, or because it is rarely preserved in recognisable form. The Sierra Nevada is cited as an area where pseudotachylytes are not developed (e.g. Di Toro and Pennacchioni, 2004) based on the lack of reported occurrences. Differentiating between these two explanations is important because melt generation has fundamental implications for the interpretation of faults as seismogenic, determining the slip-weakening mechanism for seismogenic faults, and understanding the partitioning of stored elastic strain energy released during a rupture event.

Pseudotachylytes have been confidently identified based on the criteria proposed by Magloughlin and Spray (1992) in each of the faults described in this chapter, as well as in the LLF from field observations and un-reported thin section analysis (Table 3). Pseudotachylytes have also been identified in the Mount Abbot Quadrangle (see Chapter 5), and multiple pseudotachylyte generations can be distinguished in the GPF, SKF, and LLF. These observations suggest that pseudotachylytes were commonly generated in the Sierra Nevada, and are likely not limited to the faults analysed in this study.

Pseudotachylytes have only been reported once from the Sierra Nevada (McNulty, 1995), despite the area having been the focus of numerous studies of fault initiation and development (e.g. d'Alessio and Martel, 2004; Martel, 1990; Martel *et al.*, 1988; Pachell and Evans, 2002; Segall and Pollard, 1983b). Several properties are common to many of the pseudotachylytes that make them difficult to identify confidently, and may explain the

lack of reported occurrences. In outcrop, pseudotachylytes are limited to narrow (≤20mm) veins that have limited lengths due to relatively short (several metres) along-strike exposures. The longest pseudotachylyte generation surface identified in the field could be traced for around 4m. Pseudotachylytes were not identified at all in outcrop in the GLF as they are entirely contained within fault cores of cataclasites, and are re-worked.

Fault characteristics	**GPF**	**LLF**	**SKF**	**GLF**
Mapped trace length (km)	6.7	2.3	1.4	8.2
Max. observed offset (m)	80	36	22	125
Field criteria				
Generation surface/injection vein geometry	×	×	×	
Sharp edges	×	×	×	
Quenched margins	×	×	×	
Aphanitic matrix	×	×	×	
Glassy lustre/conchoidal fracture surface	×	×	×	
Thin section/SEM criteria				
Quenched vein margins	×		×	
Variation in microcrystallite textures and/or size with respect to the vein margin			×	×
Vesicles and amygdales				
Newly recrystallised high-temperature mineral phases in a vein				
Dendritic microcrystallite habits				
Presence of abundant sulphide droplets	×	×	×	×
Spherulites			×	
Melting effects in clasts within the pseudotachylyte	×	×	×	×
Certain recrystallisation features				
Systematic chemical relations between pseudotachylyte and host rock	n/a	n/a	n/a	n/a

Table 3. Summary of the identification criteria for pseudotachylytes and the observed criteria for the Granite Pass fault pseudotachylytes. Thin section/SEM criteria are taken from Magloughlin and Spray (1992).

Thin section observations of pseudotachylytes reported in this chapter show that pseudotachylytes are difficult to identify due to a number of factors. Veins may be as narrow as 10μm (e.g. Figure 63) and fragments of pseudotachylytes in breccias and cataclasites show that they are re-worked by subsequent brittle deformation (e.g. Figure 68). Microcrystallites, with or without dendritic habits, are though to be the best indicator of a melt origin for a melt rock (Maddock, 1983). However, microcrystallites have only been distinguished in the SKF (Figure 80; see also section 6.3.3) and the GLF (Figure 88), and only SKF pseudotachylyte veins contain microcrystallites that can be distinguished optically. The rarity of microcrystallites is due in part to alteration of the groundmass of many veins by chlorite, biotite and epidote (e.g. Figure 80). In some cases, pseudotachylyte veins are completely replaced by granular epidote- and chlorite-rich mineral assemblages, whilst still retaining the characteristic pseudotachylyte generation surface and injection vein geometry. Microcrystallites are also absent from some pseudotachylytes in which the groundmass is completely amorphous (e.g. Figure 67).

Traditionally accepted identification criteria are therefore difficult to apply to some pseudotachylyte veins.

Observations of pseudotachylytes presented in this study suggest that pseudotachylytes are under-reported in fault-related literature, rather than being rarely generated for two reasons; they are difficult to identify and are often poorly preserved. These observations therefore suggest that by analogy with the Sierra Nevada, pseudotachylytes in general are likely under-reported rather than rarely generated. The conclusion that pseudotachylytes are likely under-reported due to unusual or poor preservation is in contrast to that of Sibson and Toy (2006), who suggested that melt-generation is a rare phenomenon in the context of global tectonic activity. Significantly this study shows that pseudotachylytes are susceptible to alteration so fault zones, which are commonly assumed to be fluid-saturated, are generally unlikely to contain well-preserved glasses or microcrystallites. Re-worked pseudotachylytes show that mature faults that have undergone kilometres of displacement, and perhaps thousands of earthquakes, could have generated pseudotachylytes many times but they would likely be cannibalised by the progressive deformation. Re-worked and altered pseudotachylytes are likely given the evidence presented in this chapter. Fragments of pseudotachylyte where the groundmass was completely replaced with chlorite or epidote prior to brecciation would be essentially impossible to distinguish from cataclasites and ultracataclasites in which the matrix is often also composed of chlorite or epidote.

Pseudotachylyte generation requires energy input in the form of heat energy to raise the temperature of the slip surface, to overcome the latent heat of fusion and to raise the temperature of a melt beyond its melting temperature (Fialko and Khazan, 2005; Nielsen *et al.*, 2008). The source of heat energy during coseismic slip is frictional heating across the slip surface (pre-melt lubrication) or shearing of a viscous layer of melt (post-melt lubrication), which are thought to be components of E_H in the slip weakening model of an earthquake rupture (see Section 1.4). The dissipation of energy released by an earthquake is difficult to constrain (e.g. Chester *et al.*, 2005; Kanamori and Rivera, 2006); McGarr (1999) showed that the radiated energy probably accounts for less than 6% of the total energy released, but E_H and E_G cannot be directly measured. Recent studies (e.g. Shipton *et al.*, 2006) have sought to provide geologic insight into the earthquake energy balance by discussing coseismic processes that might consume energy. However, the importance of energy consumed by pseudotachylyte generation is currently overlooked due to reports suggesting pseudotachylytes are rarely generated. This study shows that pseudotachylytes

are likely more commonly generated than is accepted, suggesting melting of fault rocks could account for a significant proportion of E_H.

4.8.3 The slipping zone

Slip surfaces associated with discrete brittle slip events can be identified in thin section from the products of frictional heating and localised cataclasis. Pseudotachylytes attest to frictional heating within a zone sufficiently narrow for the heat generated to cause melting of the rock (e.g. Kanamori and Heaton, 2000). Coseismic slip is an inherent requirement of pseudotachylyte formation, and so pseudotachylyte generation surfaces must reflect the geometry of the slipping zone (Sibson, 1975). Cataclasis, in which crystal structures remain undeformed but grains fracture, rotate and slide past one and other, causes grain size reduction and shape change, and results in random-fabric cataclasites (Rutter, 1986; Sibson, 1977). Crystal plastic and diffusive mass transfer products may also localise slip, but will not be discussed in this section as they are associated with macro-scale ductility, and do not relate to seismic or high strain rate slip events (Rutter, 1986).

Pseudotachylytes in the GPF, SKF and GLF define generation surfaces that are straight and narrow (observed thicknesses range from ~10μm to 3mm). Pseudotachylytes documented in this chapter cross-cut cataclasites (GPF11) and essentially undeformed host rock (GPF11), and are developed entirely within relatively homogeneously deformed fault core cataclasites (GLF5), as well as at fault rock - wall rock contacts and interfaces between different fault rock types (SK9). Thin sections of GPF pseudotachylytes shows that generation surfaces branch in a direction normal to the slip vector in the slipping plane. This supports field observations showing that generation surfaces branch in a direction along strike of the slipping plane (see Figure 38). Some pseudotachylyte generation surfaces in these faults are therefore an inter-connected network of surfaces with slightly different orientations.

Shear fractures in the samples analysed in this chapter include discrete fractures ~10μm thick with tens of microns displacement, shear fractures with centimetres offset, and discrete zones of localised cataclasis, all of which cross-cut other deformation elements. Small shear fractures tend to be straight to curvi-planar and contain fragments locally derived from the adjacent wall rock, as well as hydrothermal minerals, which may or may not be cataclased. Localised cataclasites never offset markers by magnitudes of displacement that can be measured in thin section, but are consistently defined by more extremely comminuted material, implying extra cataclasis. The central aphanitic zone in

GPF10 is an example of a localised cataclasite (Figure 56). This zone cross-cuts the adjacent fault breccia, is 0.2 to 1.5mm thick and contains characteristically fine grained (aphanitic) layers of matrix material with slightly differing colours in which clasts 25 to 500μm long are composed of recrystallised quartz and feldspar. The layering is sub-parallel to the zone margins, and may give rise to anisotropic elastic and permeability properties. Similar localised cataclasites are developed at the fault rock – wall rock interface in samples SK8 and SK10, and between fabric domains in GLF5. These zones approximate the wall rock edge, but are straight rather than following the wall rock topography exactly.

Cataclastic flow involves non-localised brittle fracturing that induces dilation, and may result in apparent macro-scale ductile fabrics (Rutter, 1986; Tullis and Yund, 1987). At the scale of the thin section, non-localised cataclasis can be inferred for a number of deformation elements. Ultracataclasites in samples GPF5, GPF6, GPF7 and GLF4 are composed of a large (>90%) proportion of extremely fine-grained matrix material (typically ≤5μm), and display macro-scale ductile fabrics (e.g. see Figure 27). Though the ultracataclasites are cross-cut by brittle shear fractures, high-angle fractures and fractures with a sidewall ripout geometry splay from the ultracataclasite edge in sample GPF6. This suggests that all or some of the ultracataclasite was undergoing cataclastic flow and therefore the slipping zone was up to 5.5cm thick. Foliated cataclasites in GPF11, SK9 and GLF5 closely associated with pseudotachylytes. In each case, the foliations in the cataclasites are consistent with the sense of shear defined for the fault (left-lateral in all three faults), and the GPF11 seems to be coeval with the adjacent pseudotachylyte. At the thin section scale, these units are straight, and are 0.01 to 9mm thick. Unfoliated cataclasites, or cataclasites with weakly defined foliation are also likely the product of cataclasite flow; the localised cataclasite in sample SK10 is up to 3.6mm thick and cross-cuts an adjacent fault breccia.

The narrow fault core in sample GLF5 and the ‘slipped zone’ in GPF11 both demonstrate that slip surfaces are re-used, re-worked and therefore must be re-developed in a zone of fault rocks only centimetres thick. Pseudotachylytes in both samples cross-cut foliated cataclasites that are inferred to result from cataclastic flow, implying that the pseudotachylyte generation surfaces have locally cross-cut older slip surfaces. In GPF11, brecciated pseudotachylytes attest to slip surfaces (generation surfaces) that have been re-worked and cannibalised by progressive deformation. Fragments of broken pseudotachylyte are incorporated into cataclasites and foliated cataclasites that probably

accommodated cataclastic flow showing that a new slip surface has developed by brecciation and comminution of the fault rock assemblage. However, the super-position of multiple generations of pseudotachylytes and cataclasites indicates that the localised zones of deformation are repeatedly re-utilised during progressive deformation.

4.9 Summary

Microstructural analyses of the GPF, SKF and GLF show that the faults are all composed of a suite of deformation elements that includes fault breccias, cataclasites, foliated cataclasites, pseudotachylytes, ultracataclasites, and mylonites formed by crystal-plastic deformation. In the GPF, SKF, and to a lesser extent GLF, early deformation was accommodated by crystal-plastic deformation mechanisms in both quartz and feldspar. As deformation progressed the mechanisms switched to brittle cataclasis, brecciation and pseudotachylyte generation. Hydrothermal fluids were localised in each of the faults, altering biotite, hornblende and plagioclase and precipitating significant volumes of chlorite and epidote, though the products of fluid flow are heterogeneously distributed. The GPF and SKF in particular are composed of fault cores in which deformation elements are heterogeneously distributed, emphasizing the along-strike variability observed in these faults in outcrop. Pseudotachylytes identified in the GPF suite of faults show microstructures typical of a melt origin, as well as extensive replacement and alteration by hydrothermal fluids. Slip surfaces defined by pseudotachylytes have complex geometries in which branching occurs in along strike and up-dip directions. The thickness of fault cores and slip surfaces appears to control the deformation product, and by inference active deformation processes, during coseismic slip; pseudotachylytes are generated where slip surfaces are thin (≤1mm). The GLF fault cores are composed of cataclasites, foliated cataclasites, ultracataclasites and pseudotachylytes. Pseudotachylytes are contained within the fault core strands and cross-cut the other deformation elements. Crystal-plastic deformation is observed in the GLF fault cores, but inferred temperatures of feldspar recrystallisation are lower than for the GPF suite of faults. Temperature estimates during deformation from crystal-plastic deformation products suggest that the GPF was active at higher temperature, and likely depth, than the GLF. This suggests that the GPF was active earlier than the GLF, which is consistent with cross-cutting relations defined in the field.

5

Small Faults in the Mount Abbot Quadrangle

5.1 Introduction

Faults and joints in the Mount Abbot Quadrangle have been the focus of numerous previous studies (Christiansen and Pollard, 1997; d'Alessio and Martel, 2004; Davies and Pollard, 1986; Martel, 1990; Martel and Pollard, 1989; Martel *et al.*, 1988; Segall *et al.*, 1990; Segall and Pollard, 1983a; Segall and Pollard, 1983b; Segall and Simpson, 1986). The results of previous work show that small faults have simple, straight geometries inherited from pre-existing cooling joints. Pseudotachylytes have been observed in the Sierra Nevada in the Bench Canyon shear zone (McNulty, 1995) and the Kern Canyon fault (R. Sibson, *pers. comm.*), but not from exposures of faults in the Mount Abbot Quadrangle. A model for fault growth from the linkage of pre-existing structures (cooling joints in the Sierra Nevada) proposed by Martel *et al.* (1988) and Martel (1990) is widely used as a generic model for fault growth from a population of pre-existing discontinuities. In the absence of pseudotachylytes quasi-static processes are assumed to predominate in the Sierra Nevada faults. Modelling by various authors has shown that the geometries of faults recorded in the Mount Abbot Quadrangle in particular can be adequately described by quasi-static fault growth (e.g. Cooke, 1997; Martel, 1997).

The purpose of this chapter is to analyse the geometry, composition and deformation histories of small faults (slip ≤1m) from the Sierra Nevada. Field results are presented in the form of detailed, outcrop-scale maps of several faults from the Mount Abbot Quadrangle. Thin section and SEM observations of samples taken from these faults are used to describe the fault rock assemblages and to infer the deformation histories of the faults. The results will be used to assess how faults in granitic rocks develop during the earliest stages of slip.

5.2 Geologic setting

The Mount Abbot Quadrangle is in the central Sierra Nevada, California, approximately 55km to the north of the Kings Canyon study area (see Figure 5). Fieldwork results presented in this chapter are from the Bear Creek drainage (Figure 94). All of the study localities are within the Lake Edison granodiorite (Bateman, 1992; Lockwood and Lydon, 1975), a fine- to medium-grained, equigranular, hornblende-biotite-granodiorite. Radiometric dating of the Lake Edison granodiorite has yielded a range of ages that are consistent with a Late Cretaceous age of emplacement for the granodiorite. One U-Pb zircon age was is reported as 89.8 ± 1.8 Ma (Stern *et al.*, 1981), K-Ar dating of biotite indicates the rock cooled through the biotite closure temperature (~300ºC) at 77Ma (Kistler *et al.*, 1965) or 82Ma (Evernden and Kistler, 1970), and one $^{40}Ar/^{39}Ar$ hornblende age was reported as 86.8Ma (Tobisch *et al.*, 1995). East-northeast striking, steeply dipping joints are ubiquitous throughout the Lake Edison granodiorite (e.g. Lockwood and Lydon, 1975). The joints are thought to have formed as propagating mode I cracks in response to intrinsic thermal stresses of the magnitude 60-123MPa brought about by pluton cooling (Bergbauer and Martel, 1999). Though the absolute timing of jointing cannot be established from field observations, Segall *et al.* (1990) showed that they likely formed within a few million years of pluton emplacement. Segall and Pollard (1983b) showed that many of the cooling joints in the Bear Creek drainage were re-activated as left-lateral strike slip faults. Fault-related sericite dated with the $^{40}Ar/^{39}Ar$ technique has constrained the time at which the Bear Creek faults were active; Segall *et al.* (1990) obtained an age of 78.9 ± 0.4Ma, and Pachell *et al.* (2003) calculated an age of 79.7 ± 0.16Ma for the same material but from a different fault. These consistent ages strongly indicate that the joints formed and were reactivated as faults with several millions of years of pluton crystallisation and cooling.

5.3 Methods

Excellent exposures are numerous in the Bear Creek drainage area where extensive ice-scoured pavements have developed on the valley floor. Often these exposures are flat, resulting in exposure of steeply dipping faults and joints in a plane approximately perpendicular to the structures, and containing the slip vectors of strike-slip faults. The flat surfaces also mean that the geometries of the structures in the maps are not distorted by an irregular topography in the surface exposure and therefore that angular relations are accurately represented. Maps of small faults were constructed in the field using a baseline mapping technique; a string was stretched in a straight line approximating as best as

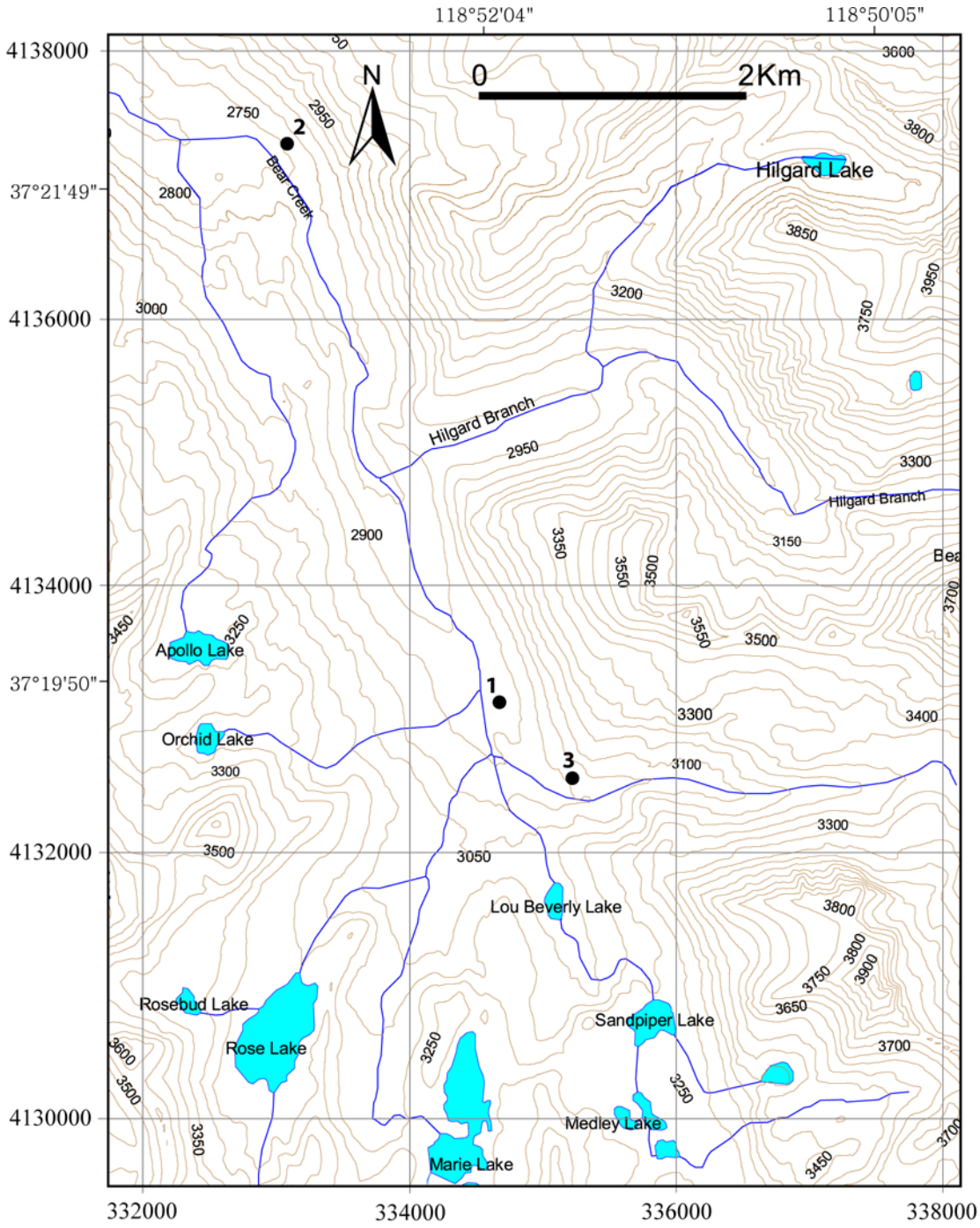

Figure 94. A map of part of the Mount Abbot Quadrangle showing the location of the studied faults. Contours are in intervals of 50m, datum refers to the NAD83 UTM coordinate system, latitudes and longitudes are shown for reference.

possible the trend of a fault trace. The orientation of the surface of the exposure, and the trend of the string was recorded, and structures mapped by measuring distances at which the features of interest were from the string at regular intervals along strike. All features in a strip 1m wide were recorded in the construction of the maps. Apparent offsets were measured on markers such as aplite dykes and mafic enclaves. However, the flat exposures provide few opportunities to record slickenline orientations, and make measuring strikes and dips of steeply dipping structures difficult. Sampling the faults was

also made extremely difficult by the nature of the exposure; a drilling permit was requested from the Sierra National Forest, but was denied. Samples of faults could only be collected where altered host rock surrounding a fault trace caused the trace to be slightly proud of an exposure surface.

5.4 Fieldwork results

Joints and faults are ubiquitous throughout the Mount Abbot Quadrangle. The results presented in this section focus on detailed outcrop-scale data collected from three localities in the area (Figure 94). The observed faults have displacements ranging from 0.12 to 0.85m, and lengths up to 54.5m (Table 4). The faults all have one of two distinct geometries; straight traces and subsidiary structures, or branching traces and wavy subsidiary structures.

Name	Measured Length (m)	D_{MAX} (mm)	Locality	Geometry
P9F	21#	120	1	Straight
P12F	45#	85	2	Straight
AB9F1	54.5#	130	1	Branched
AB9F2	6.5*	Unknown	1	Branched
DBF	45#	70	3	Branched

Table 4. Summary of the faults described in this chapter. Measured length is a minimum estimate of the trace length of the fault (# indicates faults where neither tip was exposed, * indicates faults where one tip was exposed), D_{MAX} is the maximum observed apparent offset (all left lateral strike-slip), localities refer to those shown in Figure 94.

5.4.1 Straight faults

5.4.1.1 Fault P9F

Fault P9F is a left lateral strike-slip fault with 120mm maximum apparent offset. The fault is exposed at locality 1, and is composed of two segments that are linked by a series of subsidiary structures in a left step geometry (Figure 96). The main fault segments are 0.5 to 7mm thick, and are filled with an epidote and chlorite mineral assemblage. An alteration halo surrounds the traces of the segments, in which feldspars are bleached and dark biotite and hornblende crystals are replaced with paler chlorite. The alteration halo around fault P9F is 24 to 68mm wide.

The northern segment of the fault is oriented 056/90 and is straight, except for a bend approximately 3m from its western tip, beyond which the fault trace is rotated 5º counter-

clockwise from the trend of the main segment. Offset dykes show that the slip along the fault ranges between 70 and 120mm, and appears to be relatively consistent. An adjacent fracture trace runs parallel to the main fault segment in the plane of the exposure. The adjacent trace is 4cm to the south of the main segment and is 5.25m long. This parallel fracture has a maximum observed left lateral apparent offset of 110mm, and is linked to the main fault segment by numerous subsidiary structures that are mostly at acute angles counter-clockwise to the trend of the parallel fracture.

The southern fault segment is only exposed for 5.15m of its length. The segment has a straight trace that trends approximately parallel to the northern segment. A slight kink is present in the southern fault trace near the western edge of the exposure. The southern segment does not cross any displacement indicators so the magnitude of slip on this segment is unknown. The southern segment is 0.5 to 3.5mm thick and is filled with the same epidote and chlorite rich mineral assemblage as the northern trace.

The two fault segments are linked by a series of subsidiary structures in a left-step geometry. The stepover region is 0.9m wide and the segments overlap by 5.85m (overlap to separation ratio ~6.5). The subsidiary structures are fractures with a similar appearance to the main fault segments; they are filled with an epidote and chlorite mineral assemblage and are also surrounded by alteration halos up to 50mm wide, though in general the halos are 10 to 30mm wide. The east edge of the stepover is defined by a fracture that splays from the N segment forming an angle of 25º with the segment trace (position i, Figure 96a). This bounding fracture links to the southern fault segment through a smaller fracture in an en-echelon, right-step geometry. Within the stepover, fractures link directly from the northern to southern fault segments, forming angles of 49 to 58º with both the northern and southern fault segments. The subsidiary fractures generally have simple traces, forming either single fractures, or fractures that branch once. Fractures that branch consistently do so towards the south (position ii). Two fracture traces die-out within the stepover, splaying from the northern trace but terminating before connecting with the southern trace (position iii). One fracture has a right-step approximately 0.35m from the northern fault segment (position iv). The western edge of the stepover is defined in the exposure by two sub-parallel fractures that form angles of ~10º with the northern fault segment (position v). Although not completely exposed, these fractures link with the southern fault segment, and appear to have slightly more complex geometries than the other subsidiary fractures as they branch more frequently. No fractures splay from the northern fault segment beyond the bend in its trace.

5.4.1.2 Fault P12F

Fault P12F is exposed at locality 2 and has a similar geometry to fault P9F in that there are two main fault segments separated by a left-step (Figure 96). The northern segment is ~25.5m long and dies out to the northeast, around 20m beyond the mapped extent of the fault. This segment is <1 to 7mm thick. It is predominantly filled with epidote, except where the trace is significantly less than 1mm thick and is too fine to contain any distinguishable crystals. Alteration halos are absent from both fault segments and all subsidiary structures.

The southern segment is ~28m long, though it may be longer as the termination of the fault in the southwest is poorly exposed, and there are indications that the southern segment may link to another segment through another left step. The southern segment is up to 4mm thick, which tapers to zero towards its termination in the east. However, the southern segment is complicated to the west of the stepover due to the presence of several sub-parallel fractures. One of the fractures can be traced through the entire length of the fault segment, from which several fractures splay at low angles and bend towards parallelism with the continuous fracture within several centimetres (position i, Figure 96b). The splay fractures have traces of tens of centimetres up to 2.25m. Quartz mineralisation is also confined to the southern fault segment, occurring in splay junctions and in one pocket between the sub-parallel fractures.

The stepover between the two fault segments is up to 0.4m wide, and the segments overlap by 5.6m (overlap: separation ~14). In general the traces of the two fault segments are straight and approximately parallel, though complexities in this arrangement are evident. The trace of the northern fault segment is straight until 3.5m from the western tip where a counter-clockwise bend of 5º occurs (position ii). Beyond the bend, within the stepover region, the trace of the northern fault segment is irregular and contains two discontinuities; a join between two traces with different orientations (position iii), and a small left step (2cm wide; position iv). The southern fault trace is straight until a bend at 2.65m from the eastern tip which rotates the trace 10º counter clockwise.

Subsidiary fractures are abundant within the stepover region. The western edge of the stepover is defined by a splay fracture that branches once to the north (position v). The fracture splays from a fracture that is sub-parallel to the southern segment at an angle of 20º, but does not connect to the northern segment. In this part of the stepover, where the northern segment terminates, the two fault segments are close together (~17cm apart). The

eastern edge of the stepover occurs just before the bend in the southern fault segment, and is marked by a fracture that splays from the southern fault segment at an angle of 30º. This fracture dies out in less than half of the stepover width. The most easterly fracture to connect the two fault segments also splays from the southern strand at 30º, but branches once in a northerly direction close to the northern segment. The rest of the subsidiary fractures are mostly straight, although some branch once or twice to the north or south. These fractures form angles of 25º to the southern fault segment in the western part of the stepover where it is narrow, with the splay angle becoming progressively larger as the stepover becomes wider to the east (55º maximum).

Fault P12F cross-cuts a series of interconnected dykes that allow the magnitude of apparent slip to be measured for the fault segments, and for shear and opening mode subsidiary fractures to be identified (Figure 95). The northern fault segment has a maximum apparent left-lateral slip of 0.41m near the eastern edge of the map extent. The slip magnitude decreases with a gradient of 0.09 until it drops sharply in the middle of the stepover and then increases once more before the fault terminates. A prominent slip minimum in the profile may suggest that the northern fault is itself composed of two smaller segments that have linked and are accumulating slip as a single fault. Apparent slip on the southern fault segment decreases gradually into the stepover region with a gradient of 0.06. However, a noticeable increase in the gradient to ~0.17 occurs which coincides spatially with the occurrence of the first subsidiary fractures with shear offset. Beyond the zone of subsidiary fractures, slip on the southern fault segment diminishes to zero at a very low gradient (0.01).

One of the subsidiary fractures (labelled S_4 in Figure 95) is prominent in the profile as the measured slip is an order of magnitude greater than all of the other subsidiary fractures (profiles are constructed assuming slip tapers to zero at a fracture tip or intersection with a fault segment). Fracture S4 has 0.15m maximum slip close to where slip on the northern fault segment becomes less than slip on the southern segment. The rest of the subsidiary fracture slip magnitudes are all small (≤0.02m) with limited data yielding triangular profiles. A cumulative slip profile shows that slip decreases in the stepover region from a peak near the western edge of the stepover. However, the amount of cumulative slip in the stepover is similar to the slip on the northern fault segment before it enters the stepover.

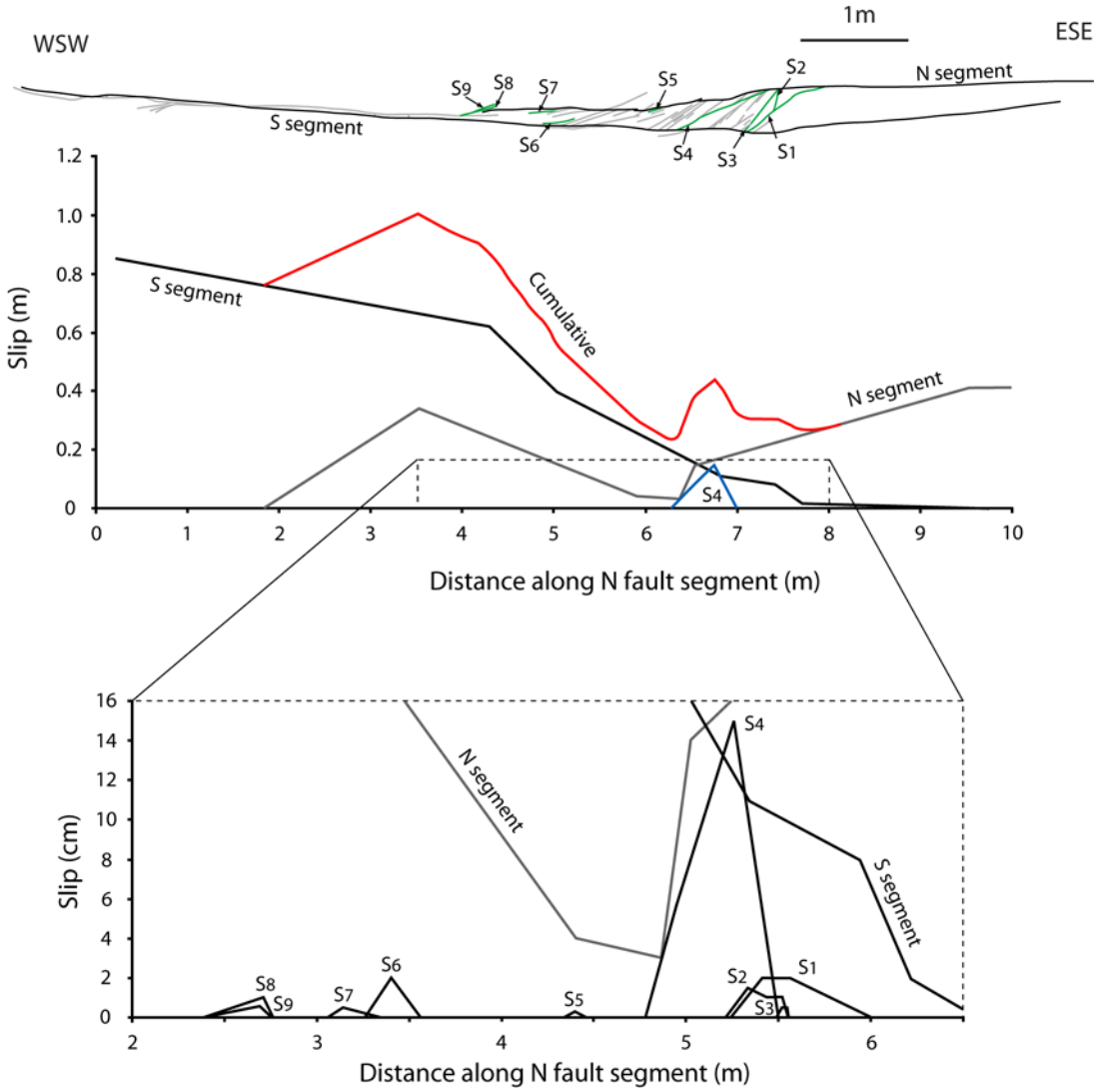

Figure 95. Slip profiles (apparent left-lateral strike slip) measured for the two fault segments and the subsidiary fractures that comprise fault P12F from offset dykes. Note that only fractures with shear displacement are included in the slip profiles (top, green); all other fractures are opening mode. Profiles are constructed assuming linear slip gradients between measured slip magnitudes and that slip diminishes to zero at fracture tips. Distances are measured along the trace of the northern fault segment, where slip measurements are projected onto the trace in a direction orthogonal to the trace.

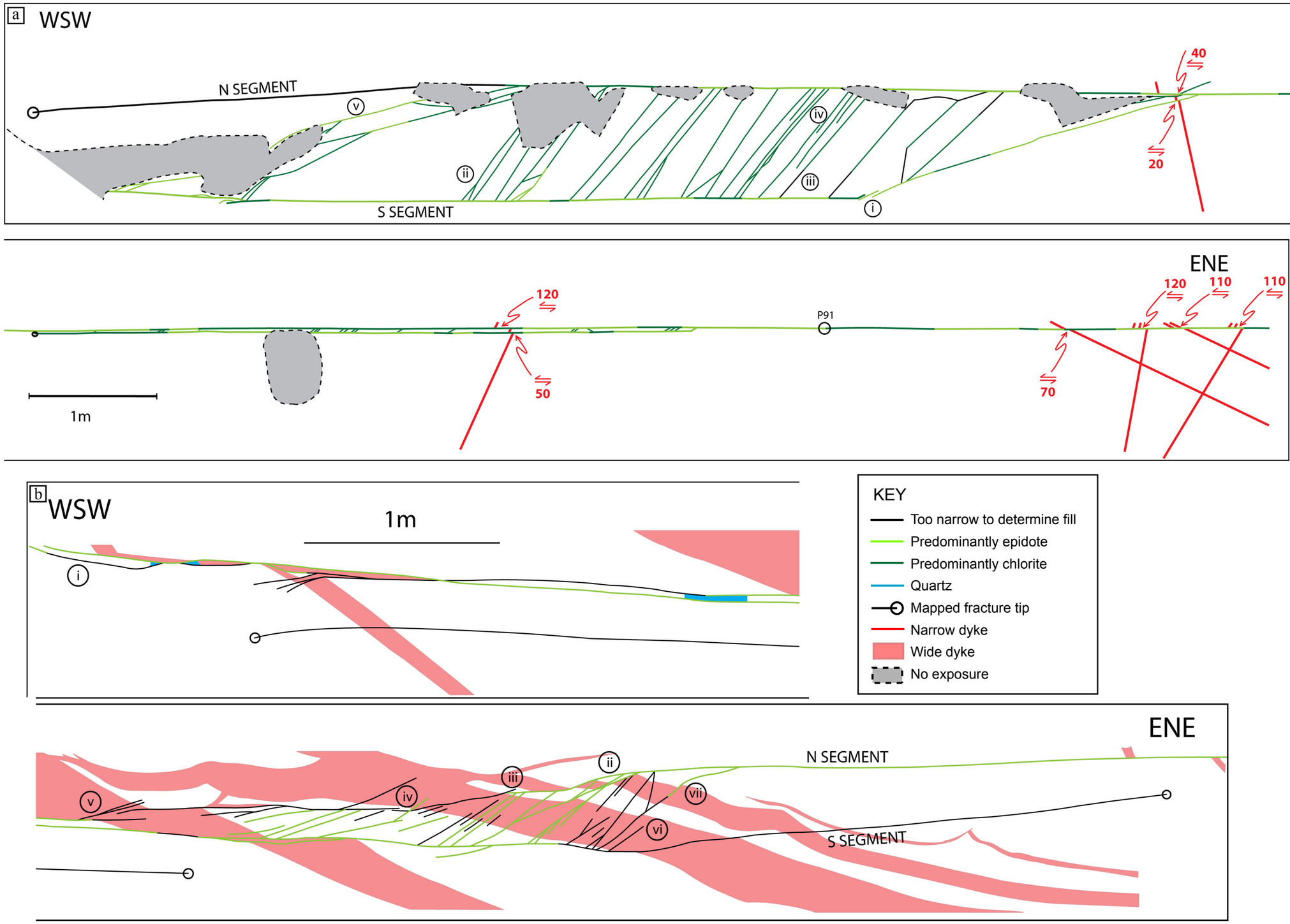

Figure 96. Maps showing the geometry of the straight faults a. P9F and b. P12F at localities 1 and 2. P91 marks the site from which a sample of P9F was collected. Fault traces are coloured according to their predominant fill. Each map is split into two separate pieces from an original continuous map (box outlines). Labelled offsets are in millimetres and roman numerals mark positions referred to in the text.

5.4.2 Branching faults

5.4.2.1 AB9F1 and AB9F2

Two faults are exposed at locality 1 that have traces with significantly different geometries to fault P9F (Figure 97). Fault AB9F1 is at least 54.5m long, and has a maximum apparent left-lateral offset of 110mm. The fault trace is up to 10mm wide and is mostly filled with chlorite, in which angular clasts of quartz and feldspars ≤4mm are present. In one place, the trace is composed of a network of chlorite-filled, inter-connected fractures that are ≤2mm, giving a total trace width of 13mm. Alteration accompanies much of the fault trace, with halos ≤30mm thick. Portions of the fault trace are predominantly filled with epidote instead of chlorite, which are ≤4mm wide in the exposure.

Fault AB9F1 has a complex trace from which numerous subsidiary structures branch. A single fracture trace can be traced for the entire length of the mapped extent of the fault, which forms the main fault trace. The eastern part of this fault trace is straight for 2.25m, beyond which it becomes irregular. The irregularity is due to several bends (both clockwise and counter-clockwise) of ~10º in the trend of the trace. Additionally there are two places to the east of the large central patch of no exposure and one to the west, where the trace branches into two or more strands that subsequently rejoin to make a single trace. Where multiple strands are present, they curve away from the trend of the main trace, reaching a maximum separation of 0.15m, and curve back again (e.g. position i, Figure 97a). To the west of the central area of no exposure is a complex network of fractures; the main trace takes a small right-step (5cm wide) which is accompanied by fractures that branch off on either side.

Numerous subsidiary fractures branch from the main fault trace. The fractures are 5cm to several metres long and nearly always form acute angles counter-clockwise to the trend of the main trace. Subsidiary fractures are filled with epidote or chlorite, and some have alteration halos ≤30mm wide. Shorter fractures tend to be straight, whereas longer fractures often have slightly wavy or curved traces. Some longer fractures (>1m) also branch away from the main fault trace (e.g. position ii). Portions of subsidiary fractures are composed of en-echelon arrangements of smaller fractures. The segments within en-echelon arrays form acute angles counter-clockwise to the trend of the fracture, consistent with left-lateral slip, and are ≤0.45m long. A fracture that is partly composed of en-echelon segments cross-cuts the dyke with 40mm offset on the main fault trace with no apparent offset in the plane of the exposure (at position iii).

Fault AB9F2 is also exposed at locality 1, and has a similar geometry to fault AB9F1 (Figure 97). The fault is at least 6.5m long, though is poorly exposed at both terminations so the total length cannot be determined. The fault does not cross-cut any offset markers, so the amount of shear offset is unknown. However, AB9F2 is inferred to have some shear offset based on the similarity in the geometry of the fault trace and subsidiary structures to fault AB9F1. Opening mode fractures are never observed with similar branching geometries. Fault AB9F2 has a maximum thickness of 12mm and is filled with either epidote or chlorite, along with ubiquitous sub-angular to sub-rounded clasts ≤4mm that are composed of quartz or feldspars. Two forms of alteration of the host rock are associated with the fault trace; a white alteration halo in which feldspars are bleached accompanies some of the subsidiary structures, and zones in which feldspars are altered to pink are developed in the central discontinuity (see below) and the adjacent fault strands. Quartz is present in one lens 7mm wide and 0.6m long within the main fault trace, as well as in some adjacent subsidiary structures in the western part of the exposure.

The trace of fault AB9F2 shows two fault segments separated by a structural discontinuity (left step) in the middle of the mapped portion of the fault. Two fault segments overlap by 1.5m and are connected as the segments terminate against each other. The maximum width of the overlap is 0.2m (overlap: separation ~7.5), and the segment traces define a rhomb-shaped block of host rock that is pervasively altered so that feldspars are pink. Both segments have wavy traces with clockwise and counter-clockwise bends of 5 to 12º producing deviations from a straight trend with amplitudes of up to 0.1m. The most significant bend is associated with the overlap region where the western fault segment bends 30º counter-clockwise to the overall trend of the segment at the eastern edge of the overlap.

Subsidiary fractures branch from both fault segments, and are present within the overlap region. The fractures are 1 to 4mm wide and are filled with chlorite and/or epidote. Fractures are distributed asymmetrically about the fault segments. To the north of the fault trace, fractures form acute angles counter-clockwise to the trend of the trace. These fractures are 0.04 to >1.7m long and have branching angles that are commonly ~30º. The fractures are often form curving traces that bend back towards the fault trace or away from the fault trace. Some fractures to the north of the fault trace branch once or twice in a direction away from the trace. To the south of the fault segments, several subsidiary fracture traces trend sub-parallel to the fault segments (e.g. position i, Figure 97). Sub-parallel fractures branch from the fault trace at angles of up to 25º and all have bends

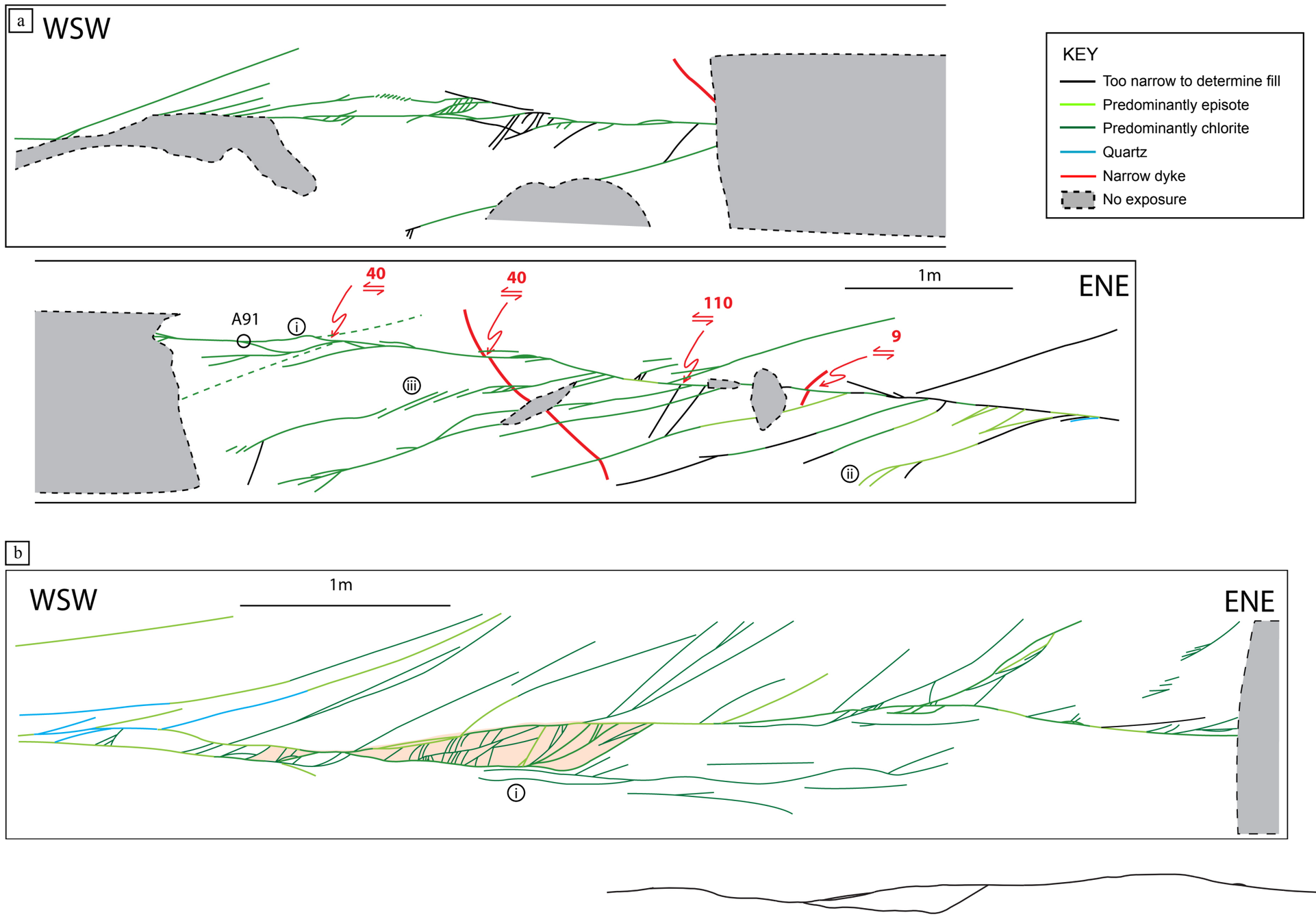

Figure 97. Maps of branched faults a. AB9F1 and b. AB9F2 exposed at locality 1. A91 is the site from which a sample of fault AB9F1 was collected. Fault traces are coloured according to their predominant fill, labelled offsets are in millimetres and roman numerals mark positions referred to in the text. a. Map is split into two sections. Sketch (lower right) shows the interpreted geometry of the main fault strands.

within several tens of centimetres resulting in a sub-parallel arrangement. Smaller linking fractures are present between the fault segment and sub-parallel subsidiary fracture traces that also form counter-clockwise angles of up to 30º with the main trace. Some linking fractures also branch once. Within the overlap zone, two orientations of subsidiary structures are present; one at low (≤20º) to the fault trace, and one at higher (30 to 60º) to the trace. The higher angle fractures branch either towards the north or south.

5.4.2.2 The DBF

The DBF is exposed at locality 3 (Figure 94) and is at least 45m long with a maximum apparent left-lateral offset of 70mm (Figure 99). The fault forms a single fault trace in the exposure, indicating that it does not incorporate any significant structural discontinuities. However, within the exposure the fault is composed of two distinct sections; the western part of the fault has a similar branching trace to faults AB9F1 and AB9F2, and the eastern section has a straight trace similar to faults P9F and P12F.

Approximately 4.5m of the western section of the DBF is exposed. The trace in this part of the fault is composed of a network of inter-connected fractures with an overall width of 25mm. At the west end of the exposure, the fault trace comprises two main strands. The northern strand bifurcates several times within 1.5m so that multiple fractures are present, beyond which the fractures re-join one another to form a single strand (at position i, Figure 99). The southern strand bifurcates twice in around 0.6m and the fractures subsequently re-join, but the strand terminates 1.5m from the edge of the exposure (position ii). At the termination of the southern strand, a series of short, high angle (~50º) fractures are present between the northern and southern strands. The fracture to the south of the southern strand has a trend that is ~5º more southwesterly than the DBF trace. This fracture seems to link to the DBF through a series of subsidiary structures (position iii), but it is unclear how significant the structure is within the DBF structure due to the lack of exposure (i.e. it is impossible to tell if the fracture links to the DBF at its western end as well).

Individual fractures within the network in the western section of the DBF are straight or slightly wavy and are 0.18 to 1.28mm thick. The fractures are mostly filled pseudotachylyte that is purple-black, crystalline, and frequently displays conchoidal fractures. Sub-millimeter laminations and rare feldspar clasts <<1mm diameter are contained within the pseudotachylytes. Portions (≤0.2m long) of some of the fractures are filled with aphanitic epidote. All of the fractures have sharp edges and cross-cut apparently undeformed protolith that is not altered. However, the host rock between

fractures within the network is often cut by small (<<1mm thick) cross-cutting fractures that give the rock a brecciated appearance, and in some places pseudotachylytes appear to cross-cut cataclasites. Subsidiary fractures are associated with the western section of the DBF that are mostly developed between the strands of the fault trace, but are also occasionally present to the north of the trace. All of the fractures are either filled with chlorite, or are too narrow to contain any distinguishable crystals. Between the fault strands subsidiary fractures have various orientations, but to the north the fractures form acute counter-clockwise angles with the trend of the fault (≤60º).

The fault trace becomes poorly exposed in a narrow gulley (~10cm wide) beyond the west end of the mapped section of the fault in Figure 99. However, the rock to the north of the trace is well exposed and contains numerous fractures. Though these fractures are not present where the fault was mapped in detail, their abundance and proximity to the trace of the DBF suggests that they are fault-related; areas more than several metres away from faults do not contain such closely spaced structures. Fault-related subsidiary structures are therefore heterogeneously distributed along strike. The fractures are in two principal orientations defined in relation to the edge of the fault trace gulley (Figure 98). High angle fractures form angles of 55 to 65º to the DBF trace in the plane of the exposure and are up to approximately 1m long. Some of the high angle fractures branch once away from the fault trace. Lower angle fractures at 10 to 35º to the fault are several metres long, and curve back to re-join the main fault trace. The low angle fractures are mostly cross-cut by the higher angle fractures, though high angle fractures splay from one of the low angle fractures.

The eastern section of the DBF comprises ~10m of the fault trace in the exposure. This section of the fault is composed of a single straight fracture trace that is 1 to 11mm thick. The trace is predominantly filled with epidote, as well as one chlorite-rich patch that is ~1m long. An alteration halo 20 to 70mm thick in which feldspars are bleached white surrounds the fracture trace. Two quartz lenses within the fracture trace are ~10 and ~20mm long, and both are 7 to 10mm wide. Four subsidiary structures are developed along the 10m eastern section. These fractures are 0.2 to 0.7m long and form acute angles counter-clockwise to the trend of the main fault trace of up to 20º. The subsidiary fractures all curve slightly back towards the main trace. A series of north-south trending opening-mode fractures cross cut the DBF that are 0.5 to 1mm thick with similar alteration halos to the DBF that are 10 to 25mm thick.

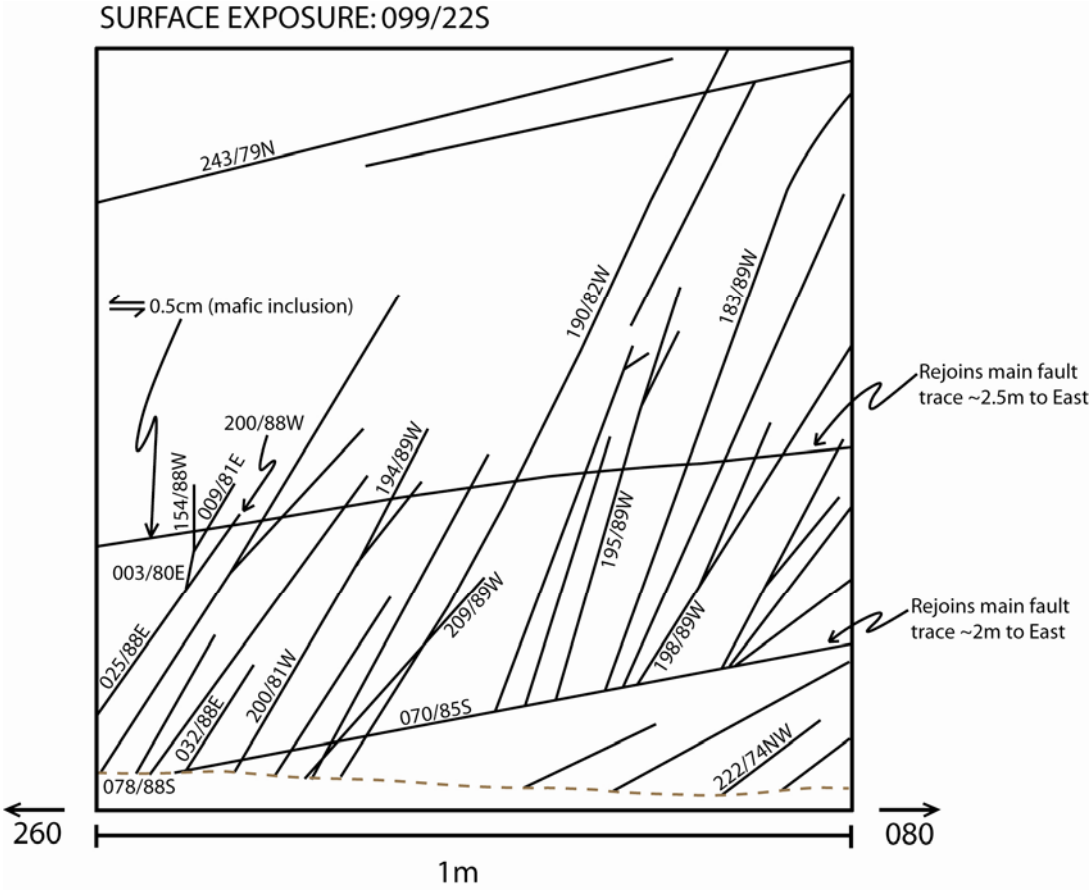

Figure 98. A metre square transect taken at 12.5m west of the west end of the mapped fault trace in Figure 99 placed with the base of the square approximately parallel to the northern edge of the DBF fault trace (brown dashed line). The transect shows fractures are developed adjacent to the fault in two principal orientations. Fractures that branch consistently do so away from the fault.

The two sections of the DBF join within the exposure at locality 3. Where the sections join, the trace of the eastern section thickens to a maximum of 50mm. Two fractures of the western section coalesce into this thicker eastern fracture trace, trending onto the edges of the thick section. The portion of host rock between the two western fractures that coalesce with the thick section is altered so that chlorite has replaced hornblende and biotite and there are chlorite crystals between feldspar and quartz. The host rock is also fractured with the fractures becoming more closely spaced towards the thick fracture trace, grading into a cataclasite. A series of arcuate fractures are localised around the join in the two sections of the DBF. These fractures splay from the outer edges of the fault trace and curve away from the fault trace, before re-joining ≤2m further along strike. Some of the fractures do not splay from the main fault trace, but are sub-parallel to the adjacent arcuate fractures. The fractures are all filled with chlorite, or are too fine to contain any identifiable material, and do not have associated alteration halos.

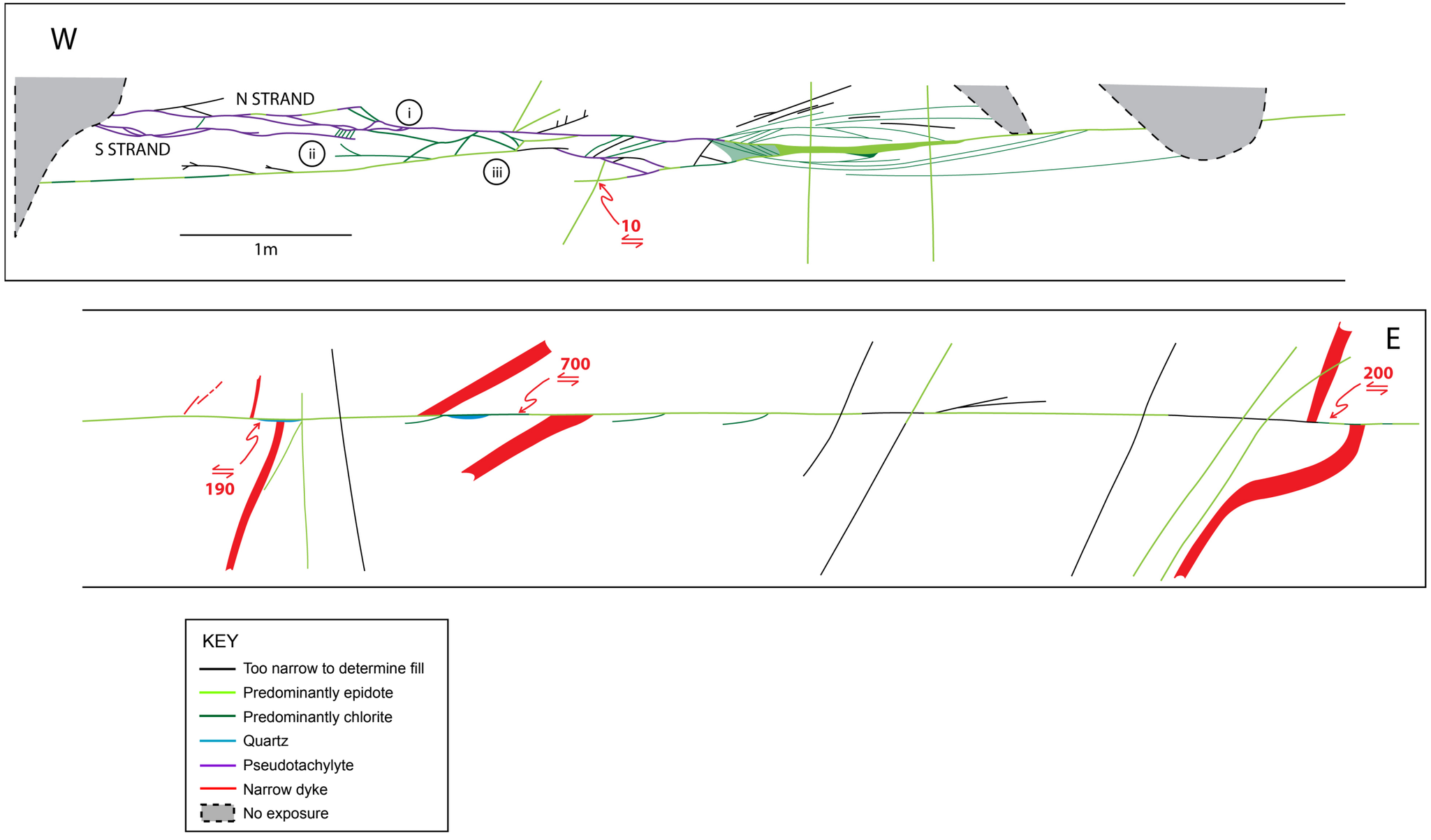

Figure 99. Map of the DBF exposed at locality 3 showing two differing styles of fault geometry. The western section contains pseudotachylytes and is branched, and the eastern section is predominantly filled with epidote and is straight. Fault traces are coloured according to their predominant fill, labelled offsets are in millimetres and roman numerals mark positions referred to in the text.

5.5 Microstructural analysis

5.5.1 Straight faults

One sample was collected from fault P9F that contains the trace of the fault (see Figure 96 for the location of the sample). The thin section prepared from the sample approximately horizontal, which is therefore close to perpendicular to the vertical fault. Within the section, the fault forms a straight trace that is 1.5 to 2.2mm thick. The fault fill is texturally complex, comprising fabric domains with various mineral assemblages that are cut by numerous veins.

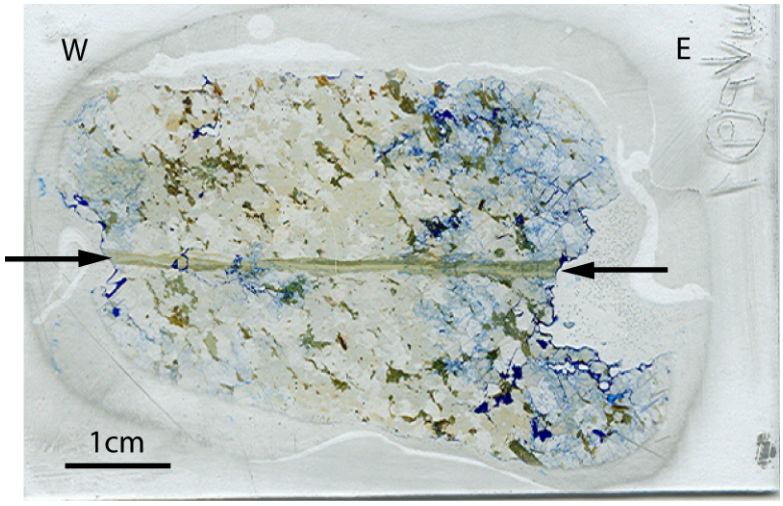

Figure 100. Scanned image of the thin section made from a sample of P9F. The fault trace (between arrows) is straight and varies in thickness from 1.5 to 2.2mm.

One prominent slip surface can be traced through the length of the thin section (Figure 101). The slip surface is defined by a seam of aphanitic, dark orangey-brown material that ranges from 0.15mm to negligible thickness where two distinct fabric domains are juxtaposed immediately against one another. The slip surface is straight, except for one small left step (0.5mm wide) and cross-cuts fabric domains, but wraps around rather than truncates clasts in adjacent domains. A secondary slip surface splays from the main slip surface at an angle of ~12º. The secondary slip surface is ≤0.5mm thick and trends into a quartz vein with the same orientation. SEM imaging shows that the main slip surface in P9F truncates clasts in the fault trace, has irregular edges, and is compositionally similar to adjacent epidote-rich domains (Figure 102). However, the grain size is much reduced in the slipping zone compared to the epidote-rich domain due to comminution of the material.

The main slip surface is intimately associated with veins. A parallel trending vein contains euhedral, tabular epidote crystals ≤0.2mm in length in a groundmass of smaller ≤50µm granular epidote crystals. The large crystals are limited to the widest part of the vein (~0.9mm) but the groundmass fills fractures in the adjacent fabric domain giving the domain a brecciated appearance. Numerous veins form counter-clockwise angles of 50-60º to the central slip surface in the plane of the section. Some of these fractures are truncated by the slip surface, and some cross-cut the slip surface, but they are consistently filled with massive epidote and cross-cut the wall rock.

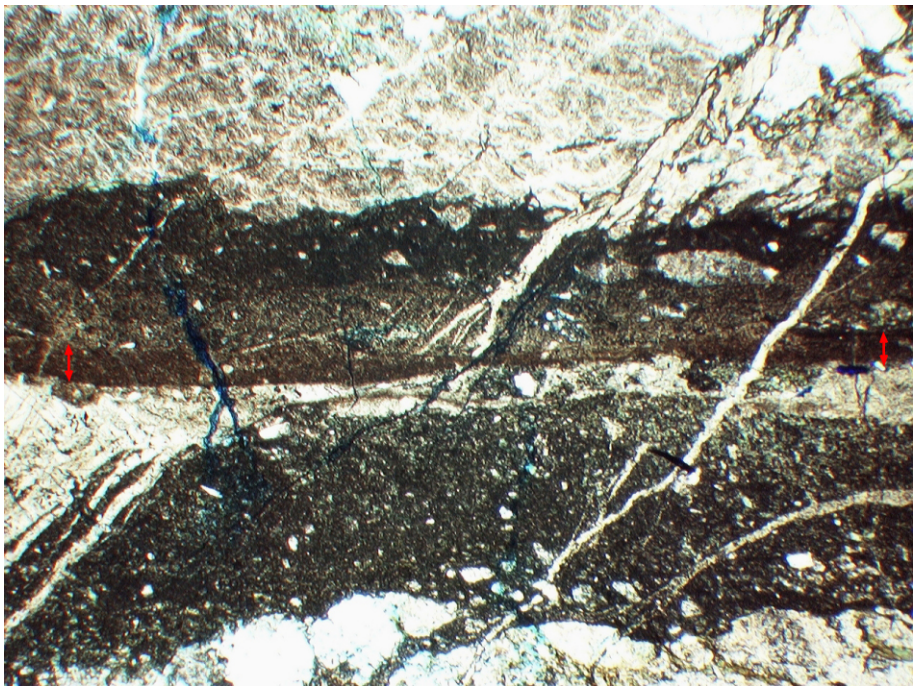

Figure 101. A photomicrograph of the central slip surface (red arrows) within the sample from fault P9F (PPL, field of view 3.1mm).

In general the material within the fault is epidote- and chlorite-rich. However, domains of varying composition are present within the fault. The domains are 0.3 to 0.8mm thick and up to several centimetres long, and trend parallel to the strike of the fault. Domains are cross-cut by the central slip surface, but otherwise domain boundaries are marked only by sharp changes in composition. Epidote dominated domains are prevalent in the centre of the fault trace, close to the main slip surface. The epidote within these domains is mostly comprised of angular crystals ≤20µm long that are likely fragments of crystals, though some large euhedral crystals (see above), and occasional angular fragments of epidote ≤0.15mm long are present. Clasts of rounded quartz and feldspars ≤0.16mm in diameter are occasionally present in the central epidote domains. Chlorite-rich domains are often found at the edges of the fault trace flanking the epidote domains. The chlorite domains are composed of a fine-grained (≤35µmm) matrix of chlorite and quartz. Clasts are much

more common in the chlorite domains, comprising up to 10% of the domain in some places. The clasts are rounded, 0.05 to 0.5mm, and are composed of quartz and feldspars (some of which are sericitized), and which both occasionally contain undulose extinction and subgrain recrystallisation.

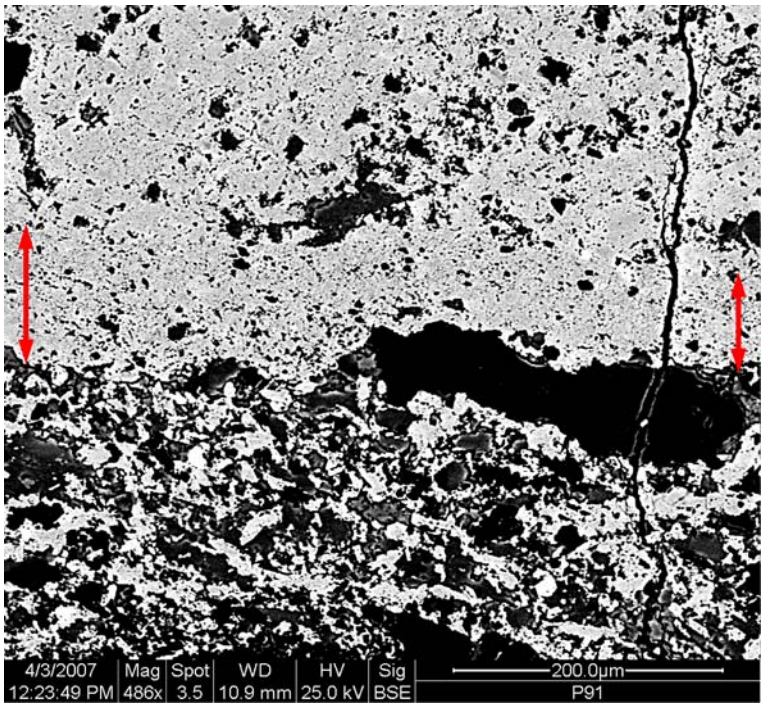

Figure 102. SEM back-scattered electron image of the central slip surface in P9F (indicated by arrows). The slip surface is defined by finer-grained (comminuted) epidote compared to the adjacent epidote rich domain (top). The lower domain contains a smaller proportion of epidote, as well as quartz and alkali feldspar.

Slivers of material that are ductiley deformed within the fault trace are adjacent to the wall rock in some parts of the section. The material in these slivers is composed of quartz and feldspar that are 0.05 to 0.3mm in size, and has a recrystallised fabric in which small equant grains are prevalent. Quartz crystals often have sweeping undulose extinction and have undergone significant bulging and subgrain rotation recrystallisation. Feldspars also show undulose extinction, and some have undergone intracrystalline deformation and exhibit core and mantle arrangements of subgrains. Some plagioclase feldspars are fractured, with small intracrystalline shear fractures offsetting twin planes. Slip surfaces cross-cut the slivers of ductiley deformed material that are sub-parallel to the trend of the central slip surface and that appear to splay from the edge of the fault trace. The slivers are also often separated from the wall rock by slip surfaces, though there are some places where intracrystalline deformation mechanisms look to have been active locally within narrow zones in the wall rock adjacent to the fault.

The edges of the fault trace in the sample from fault P9F are rough. Fractures that splay into the wall rock for a short distance then bend back towards the fault trace are common. The distance from the splay junction of these fractures, to the place where the fractures rejoin the fault trace is commonly several millimetres along strike, and the fractures extend up to 0.8mm into the wall rock. The fractures are filled with a similar material to the fabric domain immediately adjacent to the fracture. Embayments in the wall rock are also present along the fault-wall rock contact, which have a similar geometry to the fractures that splay and rejoin the fault trace. These embayments are often filled with cataclasite that is composed of fragments of quartz and feldspars that show similar intracrystalline deformation textures to those described above. Some clasts are also apparently locally derived from the wall rock.

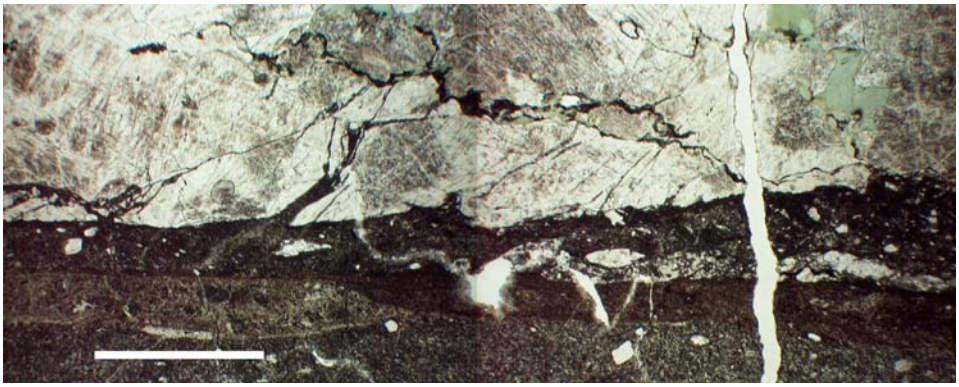

Figure 103. A sidewall ripout geometry fracture from P9F, scale bar 1mm.

The host rock surrounding the trace of fault P9F is pervasively altered; plagioclase feldspar has undergone extensive saussuritization and biotite and hornblende is replaced completely by chlorite. Alkali feldspars have undulose extinction and some display weakly developed deformation lamellae. Quartz crystals have undergone some recrystallisation. The most striking aspect of the wall rock is the development of closely spaced (several tens per millimetre) fluid inclusion trails in quartz. The trails are consistently oriented 30 to 40º counter-clockwise to the trend of the central slip surface on both sides of the fault trace. Where quartz crystals are adjacent to alkali feldspars, the inclusion trails trend into, and are parallel to, dusty-looking straight features (Figure 104). Detailed examination of the streaks in alkali feldspars shows that their orientation is independent of crystallographic orientation. Individual fluid inclusions are too small to distinguish with a microscope within the streaks, but the alkali feldspar within the streaks goes into extinction in a slightly different orientation to the host crystals indicative of a healed fracture. The same alkali feldspar seems to fill fractures where the streaks trend into healed fractures in plagioclase, which are also partly filled with epidote. Larger fractures oriented parallel to

the inclusion trails and streaks in feldspars are ≤0.12mm wide and are filled with epidote. The streaks in alkali feldspars are truncated where chlorite has replaced an adjacent hornblende or biotite.

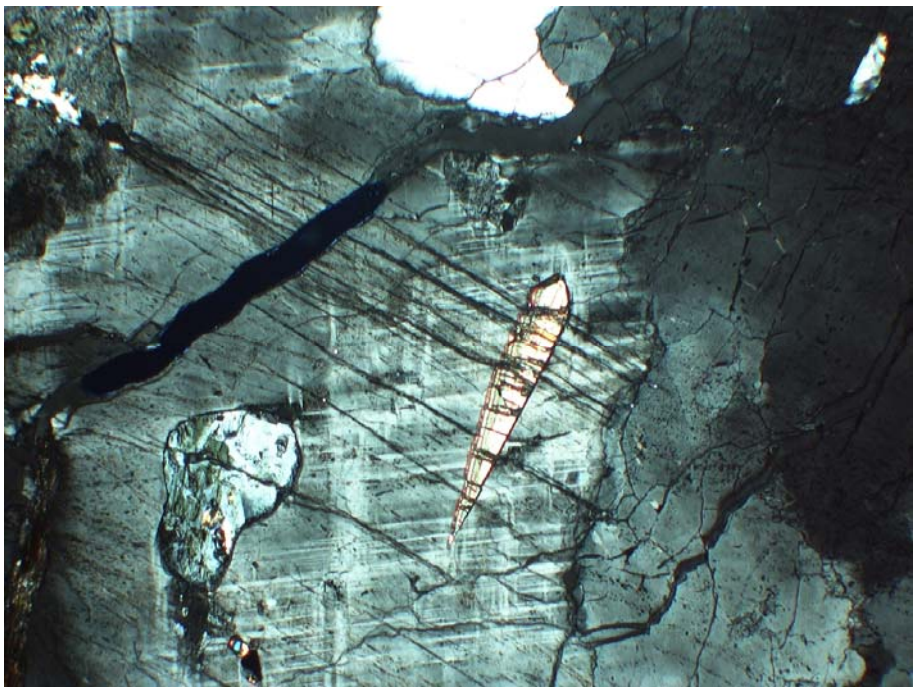

Figure 104. Fluid inclusion trails in quartz (lower right, indicated by the white arrow) are parallel to dusty-looking streaks in alkali feldspars that may be healed fractures (black arrow). In this photomicrograph the trails trend top left to lower right and are kinked slightly at the boundary of an inclusion in the microcline (XPL, field of view 1.6mm).

5.5.2 Branching faults

5.5.2.1 Fault AB9F1

One sample was collected from fault AB9F1 (Figure 105). Though the fault trace has a complex geometry in outcrop, the sample was extracted from immediately adjacent to a branch in the trace and contains two closely spaced fault strands (see Figure 97 for the sampling site). However, the thin section produced from the sample contains only one of the strands as the sample broke along the southern strand, so the overall thickness of the fault is impossible to evaluate. The fracture trace within the hand specimen is 10 to 16mm wide. The thin section comprises a northern fault strand with a chlorite-rich brecciated zone to the south.

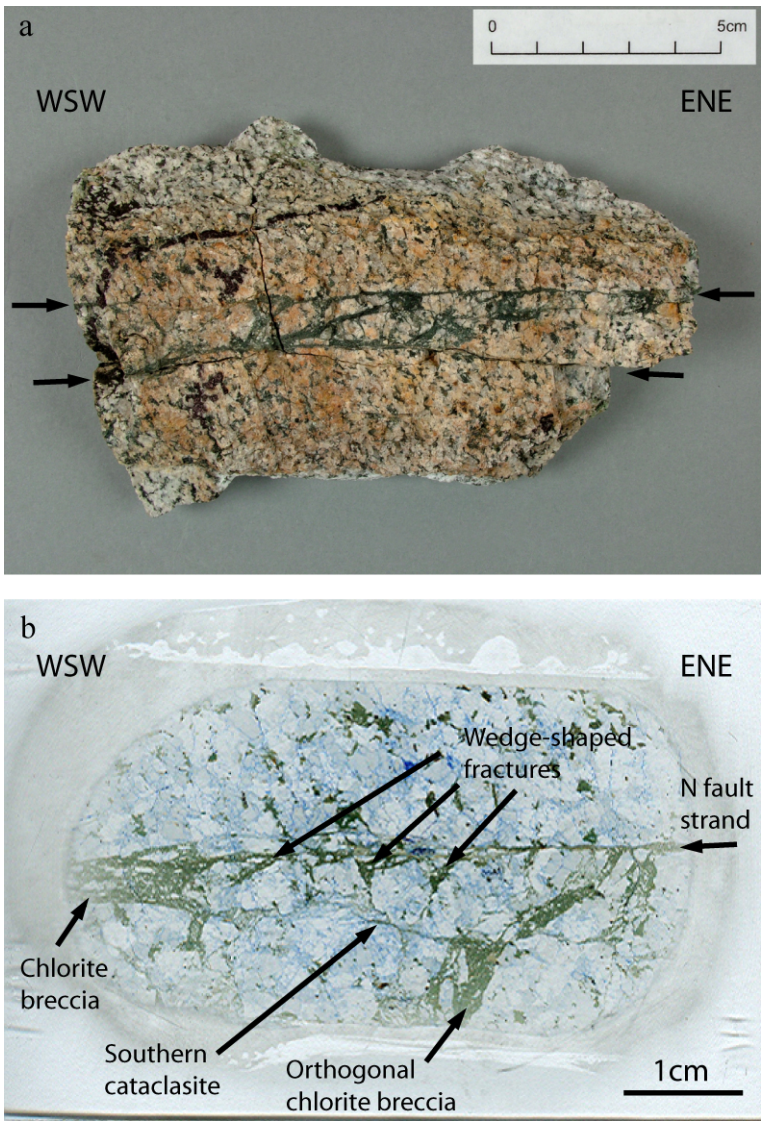

Figure 105. a. Photograph of the reassembled pieces of the sample of fault AB9F1 showing that the trace at the sampling site was composed of two closely spaced fault strands that bound brecciated host rock. b. Scanned image of the thin section constructed from the sample showing the main components of the fault rock.

Part of the northern edge of the fault within the thin section is defined by a wavy, 50 to 450μm thick seam of cataclasite that represents the northern fault strand (Figure 106). The cataclasite contains ~30% clasts that are ≤150μm, sub-angular to rounded and composed of feldspar, quartz and calcite. In general, the clasts do not exhibit intracrystalline deformation textures. The matrix (70%) of the cataclasite is ≤5μm, and is composed of cataclased epidote, chlorite and some quartz and feldspar fragments. This localised cataclasite trends laterally into a wider fracture that contains elongate fragments of quartz and feldspar that are ≤2.5mm long (Figure 106). The elongate clasts are aligned parallel to the trend of the localised cataclasite, which cross-cuts the surrounding matrix. This matrix is ≤40μm primarily composed of euhedral chlorite and epidote, as well as fragments of muscovite, quartz and feldspars. The chlorite has dark brown interference colours and

forms circular aggregates 20 to 70µm in diameter of radial, euhedral crystals. Occasional (30µm wide) epidote-filled veins that form 30º counter-clockwise angles with the trend of the localised cataclasite cross cuts the wall rock, localised cataclasite and chlorite-rich matrix.

Figure 106. The localised cataclasite (dark, aphanitic material left-centre) cross-cuts the chlorite breccia and trends into a wider section of the fracture (PPL, field of view 3.1mm).

The localised cataclasite dies-out within the thickest (~6mm) part of the fault in the section. A fault breccia fills the wide part of the fault trace (Figure 107). The breccia is composed of clasts 0.05 to 4mm long that are angular to sub-rounded. Some of the clasts are fragments of undeformed quartz and feldspars. However, the majority of clasts display undulose extinction (quartz and feldspars), and some have extensive subgrain development including core-mantle textures in feldspars, and completely recrystallised quartz and feldspars. Some feldspars have also developed subgrains that are extremely localised in narrow zones that trend into fractures filled partly with epidote. Approximately 60% of the fault breccia is chlorite that forms circular to tabular aggregates of radially arranged crystals that are consistently 20 to 70µm in diameter. The chlorite comprises ~90% of the matrix of the breccia, which also contains quartz and feldspar fragments. The chlorite consistently impinges on the edges of fragments in the fault breccia, as well as the wall rock, giving the fragment edges an irregular, indented form.

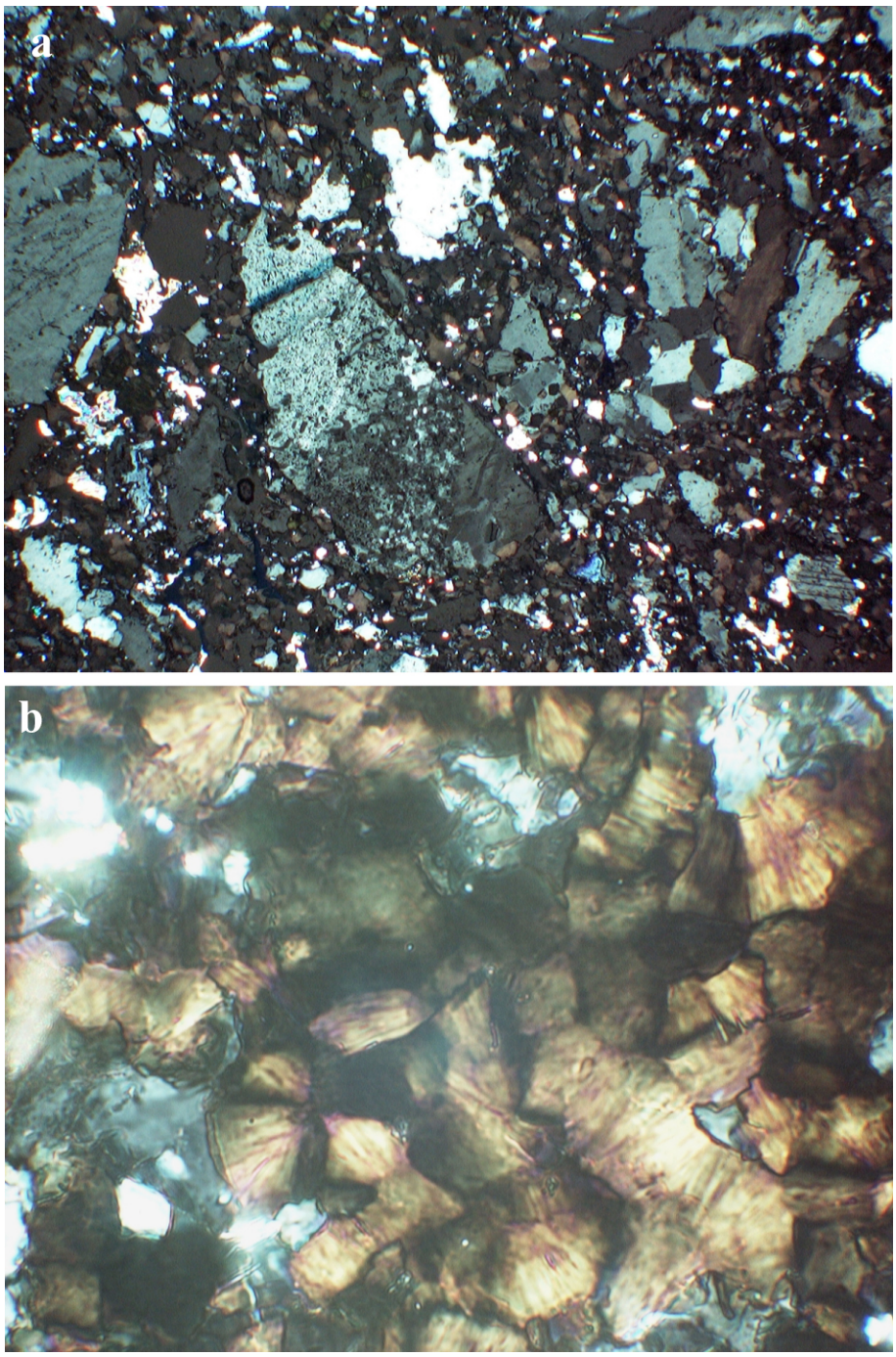

Figure 107. The chlorite breccia that fills the widest part of the fault trace in the thin section of AB9F1. a. Note the uniform size of the chlorite aggregates (brown) and the impinged edges to the fragments (XPL, field of view 1.6mm). b. Detail of the chlorite aggregates showing radial arrangement of euhedral crystals (XPL, field of view 0.2mm).

A series of fractures branch south from the narrower parts of the northern fault strand at high angles (40 to 80º). The fractures are wedge shaped; they are widest (1.5 to 4.2mm) adjacent to the northern strand and taper to the south with lengths up to around 5mm. Each fracture is filled with a very similar breccia to the widest part of the fault, and the wider sections of the northern fault strand. The fill is characterised by clasts 0.05 to 1.1mm long of feldspars, quartz and some muscovite in a matrix dominated by tabular aggregates of

euhedral chlorite (Figure 108). The high angle fractures are truncated by the localised cataclasite within the northern fault strand, and taper into narrow fractures that mostly branch at least once before connecting with a localised zone of cataclastic deformation to the south. This cataclasite is 0.05 to 1mm thick, is wavy on the sub millimetre scale, and had one sharp bend of around 30º. Where narrower, the cataclasite is composed of clasts of quartz and feldspars 0.05 to 150μm in an epidote and chlorite matrix with a grain size of ≤30μm. The feldspars are all heavily altered, and the clasts have blurred edges. Wider parts of the cataclasite have clasts up to 1.1mm long of quartz and feldspars with straight edges. Epidote and chlorite are scarce in the matrix in wider parts of the cataclasite, which is composed of small quartz and feldspar fragments that have undulose extinction and subgrain development.

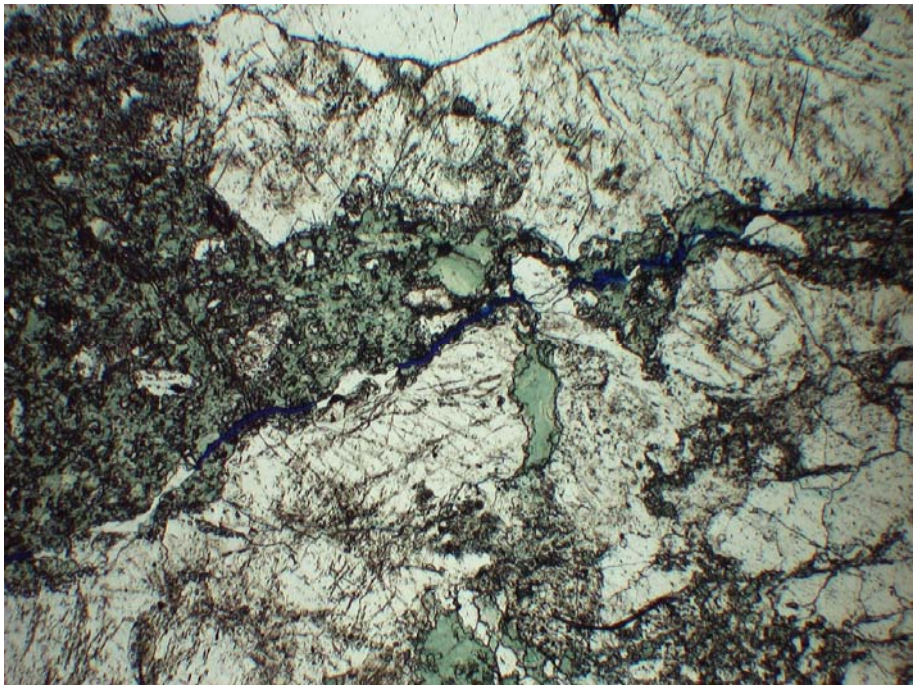

Figure 108. A wedge-shaped fracture that branches from the chlorite breccia and is filled with the same material as the chlorite breccia. The fracture tapers away from the fracture (towards the right in the image; PPL, field of view 3.1mm).

The chlorite-breccia that fills the majority of the fractures within the fault trace is also contained within wide (~5mm) zones that are approximately orthogonal to the trend of the fault and which pass out of the section. These zones are also connected to the cataclasite described above and along with the high angle fractures bound fragments of the host rock that are up to 20mm long. The fragments contain some internal deformation features that are truncated by both the northern fault strand and the seam of cataclasite to the south. Some alkali feldspars contain irregular-shaped healed fractures that branch and are partly filled with chlorite. The healed fractures cross-cut fluid inclusion trails in quartz and dusty

streaks in alkali feldspar that are similar to those developed in the wall rock to P91. Recrystallisation of feldspar and quartz occurs in localised seams that sometimes trend into chlorite-filled fractures (Figure 109). Chlorite is also present between subgrains developed in these localised zones.

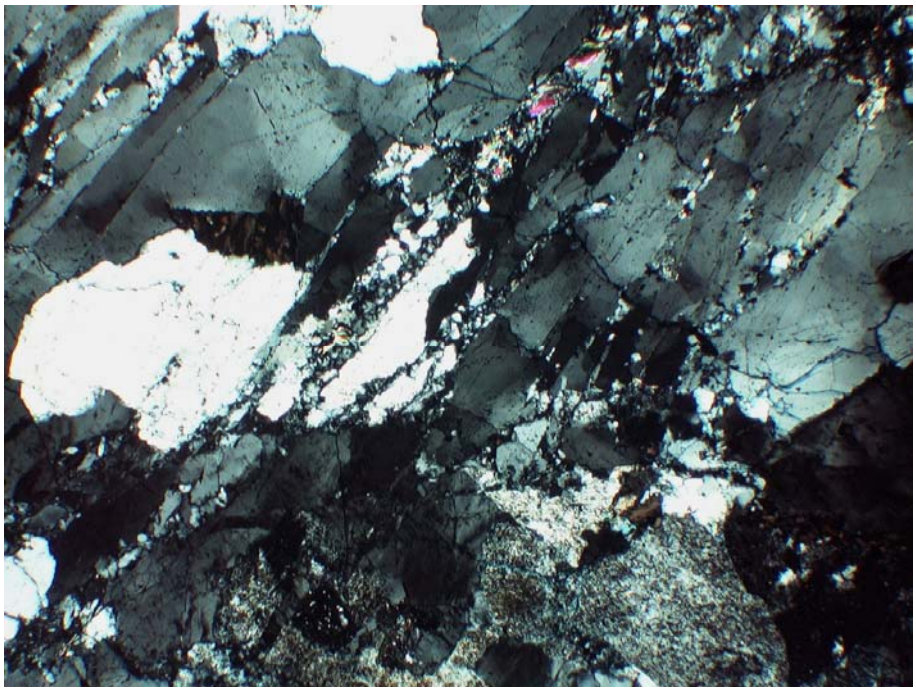

Figure 109. Internal deformation within the fracture bounded fragments. The localised cataclasite in the northern fault strand is approximately parallel to the base of the image. Recrystallisation of feldspars is extremely localised (XPL, field of view 3.1mm).

The wall rock margin at the northern edge of the fault is often difficult to define. Adjacent to the narrowest parts of the north fault strand, the wall rock edge is rough; small (sub tenths of a millimetre scale) irregularities are filled with cataclasite. Where the chlorite breccia is adjacent to the wall rock, the chlorite impinges on quartz and feldspars giving the edge a slightly diffuse appearance. Several slivers of quartz in which subgrains are developed are present between the fault rock and the wall rock, and one quartz crystal shows a chequer-board extinction pattern characteristic of high temperature (>500ºC) grain boundary migration recrystallisation. Quartz crystals and quartz subgrains are often easily defined in plane polarised light as they have extremely narrow fractures around their edges filled with epidote. Feldspars in the wall rock adjacent to the fault trace have also undergone recrystallisation in places, but these are consistently localised into zones of deformation in which subgrains are developed and epidote is present between the crystals. The localised zones occasionally branch, and trend into the zones of quartz recrystallisation. One prominent zone of feldspar recrystallisation splays from the fault trace, and bends back in 15mm further along strike.

Fluid inclusion trails in quartz, dusty streaks in alkali feldspars and fractures in plagioclase feldspars that are filled with epidote, chlorite or calcite are all similarly oriented in the wall rock in one of two predominant orientations (around 25º or 45º to the northern fault strand). Plagioclase in the wall rock is also extensively sericitized.

5.5.2.2 The DBF

One sample was collected from the pseudotachylyte-bearing part of the DBF immediately to the west of the extent of the baseline map (Figure 99) where the fault is poorly exposed. The sample could not be fully oriented, so the section is cut approximately perpendicular to the fault and parallel to the inferred slip vector (assumed to be horizontal for a strike-slip fault). The fault comprises a single, straight trace 11 to 15mm wide between two portions of wall rock (Figure 110).

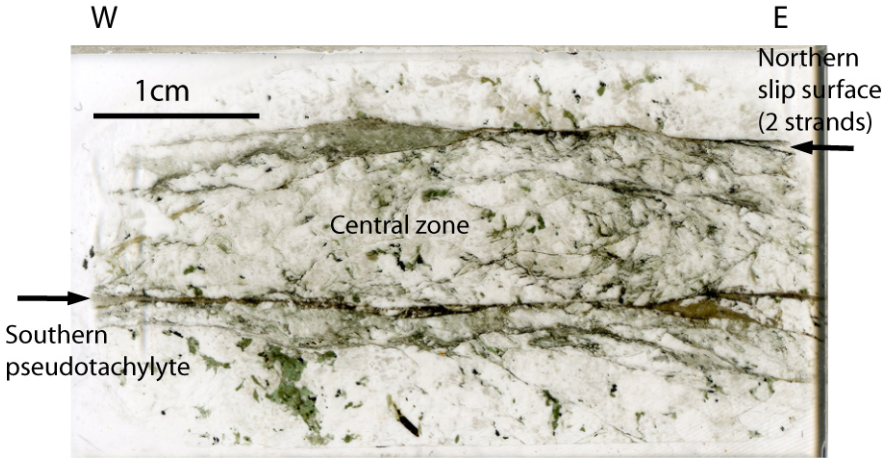

Figure 110. Scanned image of the thin section of the DBF showing the geometry of the fault trace and the main components of the fault rock.

Two slip surfaces are prominent towards the edges of the fault trace. The southern slip surface is defined by a pseudotachylyte vein that is 0.15 to 0.9mm thick (Figure 111). The vein is straight but appears to bifurcate around a large fragment of fault rock at one end of the thin section. The vein edges are sharp and straight, except for narrower parts of the vein where clasts from the adjacent fault breccia protrude into the pseudotachylyte. Injection veins ≤0.5mm long branch from the main vein at high angles. The pseudotachylyte is pale yellowish brown to brown (PPL) or green where the groundmass is replaced with chlorite. In crossed nicols, the pseudotachylyte material is low order yellow or grey interference colours, and appears striped in places where alternating strips go into extinction at the same time. Flow banding is developed in wider sections of the vein, but is not apparent in XPL. Lithic clasts 0.01 to 0.45mm long are rounded or sub-angular in narrower parts of the vein. The clasts are predominantly composed of recrystallised quartz

and feldspars, with occasional fragments of undeformed single quartz or feldspars. Microcrystallites are not distinguishable in the pseudotachylyte groundmass, which is completely aphanitic. Some small circular features (<5μm radius) might be vesicles, spherulitic structures or devitrification products.

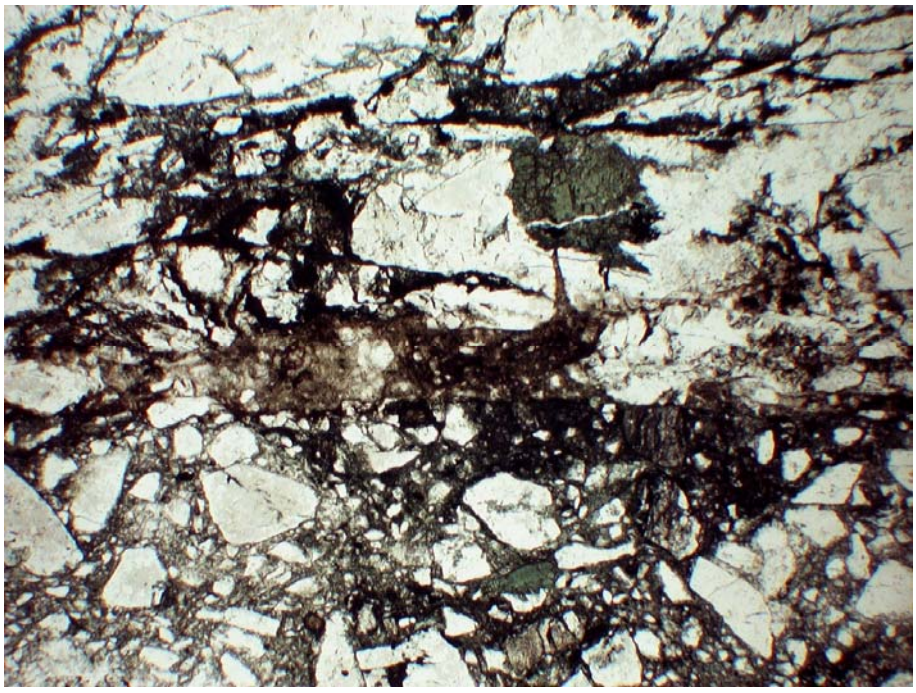

Figure 111. The northern pseudotachylyte in the DBF (brown vein running left to right in the image) cross-cuts a chlorite breccia (bottom). Note the injection vein in the centre of the image (PPL, field of view 3.1mm).

A melt origin for the pseudotachylyte is confirmed by the presence of spherulitic textures developed in an amorphous groundmass where the small circular features were observed in thin section. SEM imaging shows that lithic clasts (predominantly composed of quartz) within the pseudotachylyte are frequently surrounded by fringes of dendritic microcrystallites probably of plagioclase (Figure 112). The spherulitic fringes appear to grow into, and overprint, a biotite-like composition groundmass containing numerous titanite droplets. The groundmass contains compositional variations including domains in which titanite droplets are absent as well as subtle variations in the iron, magnesium and aluminium content, which mix and define flow banding at the micron scale. Compositionally the bulk melt (represented by the groundmass which is more abundant than the spherulites and/or clasts) is anomalous in the context of the DBF and the fault wall rock; there is little biotite in the rock. In particular, the calcium, silica and sodium content of the melt is low, whereas plagioclase is abundant in the wall rock. Bulk rock melting along a slip surface should produce a melt in which more closely matches a plagioclase composition. The small amount of total slip on the DBF (0.7m) shows that the slip increment that generated the pseudotachylyte must also have been small. The relative

displacement of the opposing wall rocks was small so the wall rock cannot have moved far from the point at which the melt was generated, suggesting extremely localised melting. The origin of the biotitic composition of the melt is therefore incompatible with bulk rock melting.

The striped areas identified under cross-polarised light are defined by domains of slightly different composition in the pseudotachylyte groundmass (Figure 112). The stripes have a flame-like appearance, but are mostly straight and approximately parallel. Individual stripes cannot be traced for more than ~100μm across the pseudotachylyte as the stripes are disrupted by lithic clasts. In general, larger stripes are located towards the middle of the pseudotachylyte. Within the striped areas, the overall composition of the pseudotachylyte is similar to the biotite composition of the groundmass away from striped areas, but the stripes are slightly more or less enriched in iron and magnesium (paler stripes in Figure 112 are brighter as they are more iron and magnesium rich giving a higher mean atomic number). Texturally, the striped compositional domains appear to have formed early in the cooling history of the pseudotachylyte melt; they are overprinted by the spherulitic fringes and contain some evidence of interaction with the flow structures that are prominent away from striped areas. However, the mechanism by which the apparent un-mixing of the melt into such a geometric texture is achieved remains unclear. If fractional crystallisation of the spherulitic fringes enriched the melt in iron and/or magnesium then flow-like structures would be expected from the mixing of two fluids with different compositions. The stripes require a static environment or mechanism of un-mixing.

The southern pseudotachylyte juxtaposes a chlorite breccia, which is between the pseudotachylyte and the wall rock, and a central recrystallised zone. The chlorite breccia is composed of 40-60% clasts 0.025 to 1.6mm long that are angular to sub-rounded. The clasts are composed of fragments of extensively recrystallised quartz and feldspar, as well as some fragments of undeformed quartz, feldspar, chlorite and biotite. The largest clasts always contain aggregates of multi-crystalline material. The matrix within the breccia contains crystals of chlorite and quartzo-feldspathic material ≤10μm in length. The wall rock edge adjacent to the chlorite breccia is wavy on the centimetre scale (with an amplitude of ~1mm), and minor irregularities are common where fractures in the wall rock intersect with the fault trace. Lenses of calcite crystals ≤5μm are mixed with quartzo-feldspathic material similar to that in the breccia matrix in a narrow zone that is immediately adjacent to the wall rock but inconsistent along strike.

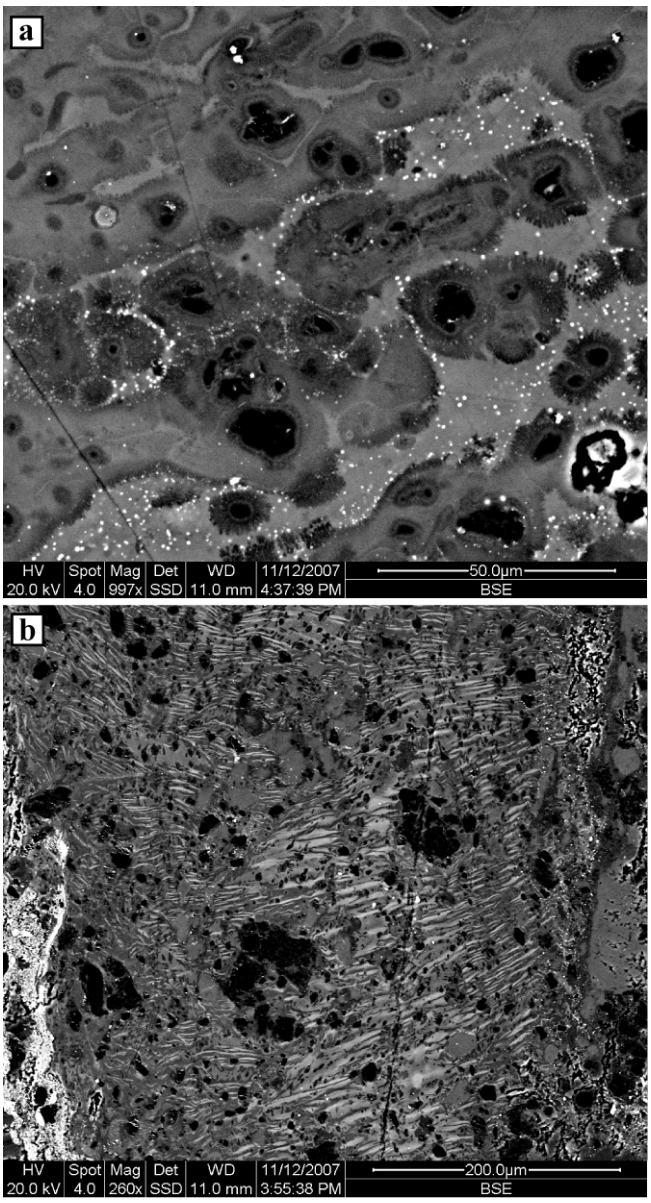

Figure 112. SEM back-scattered electron (BSE) image of the northern pseudotachylyte strand in the DBF. a. Lithic clasts are surrounded by fringes of dendritic plagioclase microcrystallites. b. BSE image of the stripes of compositional variation developed in parts of the pseudotachylyte groundmass. The stripes are defined by subtle differences in the iron and magnesium content.

The second prominent slip surface is at the northern edge of the fault trace. The slip surface is mostly defined by aphanitic material that is often opaque and is decorated with strings of calcite crystals (≤8µm) in places. The geometry of the slip surface is complicated; at the eastern edge of the thin section two strands are present that are 25µm and 10µm thick. These two strands coalesce to form a single slip surface 20 to 60µm thick and ~15mm long. The slip surface bifurcates into two strands which surround a cataclasite. Towards the edge of the section, the strand adjacent to the wall rock becomes exceptionally narrow (≤10µm), and small orange-brown injection vein type structures

≤70μm branch off at high angles, suggesting pseudotachylyte may be present. The other strand of the slip surface dies out within ~15mm in the central recrystallised zone.

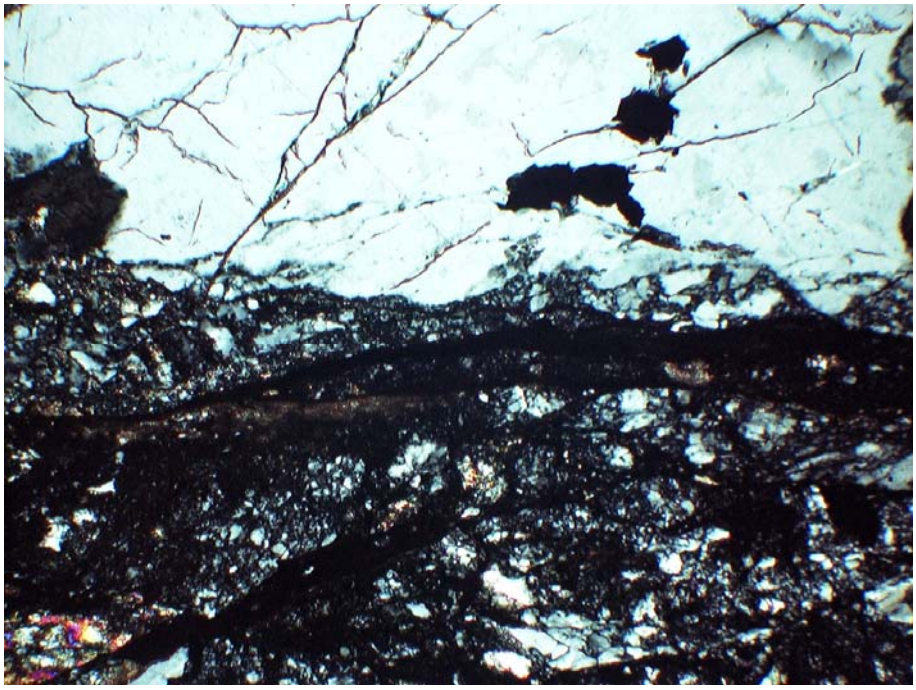

Figure 113. The southern slip surface is defined by a wavy, aphanitic band of comminuted material that cross-cuts extensively recrystallised material. A lens of ductiley deformed material is present between the wall rock (top) and the slip surface (XPL, field of view 1.6mm).

The aphanitic material in the northern slip surface may contain some pseudotachylyte (Figure 114). The slip surface defined in thin section contains predominantly granular cataclastic material composed of angular quartz, feldspars and metal oxides that are ≤8μm long. However, a thin (~20μm) band in which there is an amorphous groundmass containing flow banding-like compositional variations and small fringes surrounding lithic clasts is present between the cataclasite and the wall rock. This material shares many of the characteristics of the pseudotachylyte in the northern slip surface, though the band is so thin the diagnostic properties of a pseudotachylyte cannot be confidently identified. Further analyses including EBSD or TEM work may help to constrain whether the material is glassy, and therefore of melt origin.

The northern slip surface defines the fault rock – wall rock contact, which is smooth and slightly wavy on the centimetre scale. However, some lenses of recrystallised material ≤5mm long and ≤0.5mm thick are present between the southern slip surface and the wall rock. Within these lenses, quartz is recrystallised to a consistently small grain size (≤10μm) and feldspar frequently displays core-mantle structures. Calcite is also present in the lenses, replacing some of the smallest fraction of the recrystallised quartz.

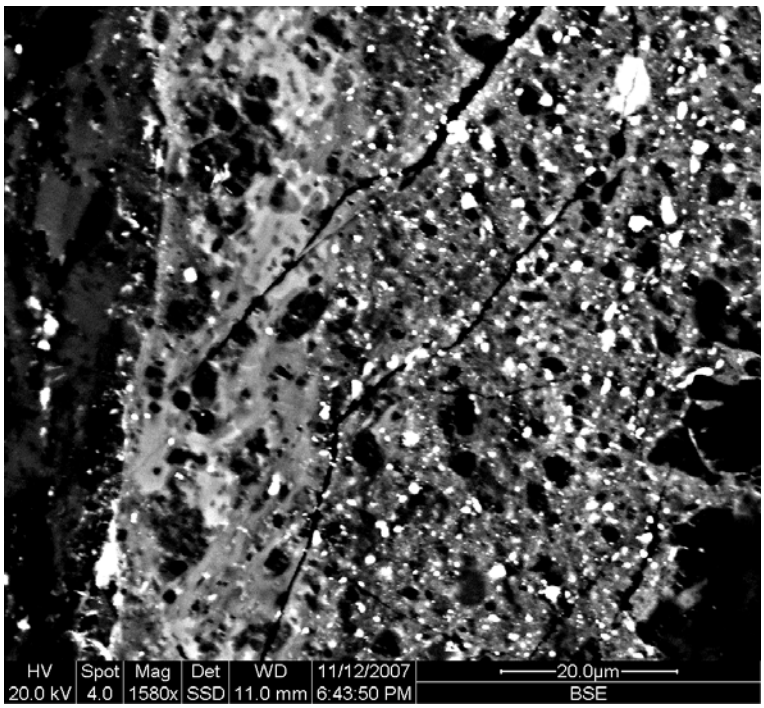

Figure 114. SEM back-scattered electron image of one of the strands of the southern slip surface close to where the two strands that comprise the slip surface join. The strand is composed of granular-looking quartz, feldspars and metal oxides (right), and possibly some pseudotachylyte (left). The pseudotachylyte seems to contain a similar texture to the pseudotachylyte described in the northern strand.

The two principal slip surfaces encompass a central zone of deformed rock that accounts for the majority of the fault thickness. The central zone is composed of host rock that has undergone varying amounts of intra-crystalline deformation (Figure 115). Quartz crystals (~10 to 450µm) have undergone extensive bulging and subgrain rotation recrystallisation, but do not define a grain shape fabric. Feldspars have also been recrystallised by bulging recrystallisation and form core-mantle structures. Hornblende is uncommon in the intensely recrystallised parts, and displays undulose extinction and is broken down into hornblende and quartz inter-growths around the edges of crystals. Some domains within the central zone are much less deformed; deformation lamellae and undulose extinction in quartz are overprinted by incipient bulging recrystallisation, occasional myrmekites and some localised recrystallisation along healed fractures are developed in feldspar, and hornblende is fractured. These domains are generally bounded by fractures or cataclasites. Fractures pervasively cross-cut the central zone, many of which appear to splay from the northern pseudotachylyte vein but do not cross-cut the entire zone. The fractures that splay from the pseudotachylyte have two predominant orientations; one set forms high angles with the vein (~60º), and another set form low angles and often have sidewall ripout geometries (Figure 116). One isolated pseudotachylyte vein extends into the central zone.

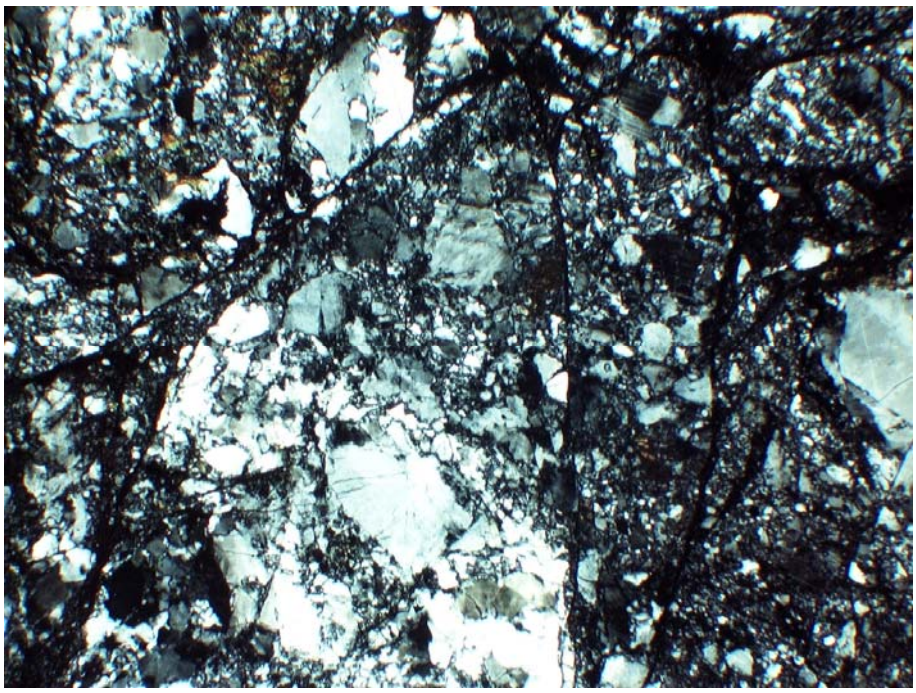

Figure 115. The central portion of the DBF is extensively recrystallised in places and is cross-cut by numerous brittle fractures. The northern pseudotachylyte is parallel to the base of the image (XPL, field of view 3.1mm).

The wall rock on either side of the DBF is much less deformed than the fault rock. Quartz crystals consistently contain deformation lamellae in two conjugate orientations, one at ~20º counter-clockwise to the fault trace and one at ~15º clockwise, and minor recrystallisation by subgrain rotation along grain boundaries. The lower angle deformation lamellae occasionally contain fluid inclusion trails. Feldspar often has myrmekite developed around crystals edges. Fluid inclusion trails at high angles (~70º) to the fault trace cross-cut quartz and feldspar crystals, and are undeflected by deformation lamellae and subgrain development. The wall rock contains many opening mode fractures at counter-clockwise angles of 25 to 35º to the fault trace. These fractures are up to 5mm long, and are much more frequently developed in quartz than in feldspar. One vein that appears to splay from the main fault trace is filled with small (≤0.6mm) feldspar and quartz crystals that quite angular, but which have recrystallised along grain boundaries. This vein is truncated by one of the lenses of recrystallised material between the northern slip surface and the wall rock in the fracture trace.

Figure 116. Sidewall ripout fracture splaying from the northern pseudotachylyte vein (PPL, scale bar 1mm).

5.6 Interpretation

5.6.1.1 P9F

The fault rock compositions and textures in P9F are indicative of brittle deformation occurring at low to medium temperatures (i.e. <300ºC). The latest stages of slip on P9F likely occurred on the central slip surface; the slip surface truncates veins that cross-cut the adjacent fabric domains. Coarse, euhedral epidote is undeformed and distributed along the central slip surface in a zone with a geometry that is similar to a pull-apart structure. The epidote probably crystallised in a void that opened in response to slip on the fault. If this was the case, the width of the euhedral epidote zone suggests a slip increment of ~3.2mm. The central slip surface therefore represents extreme localisation of slip onto a zone ≤0.15mm thick that is mostly straight, except for one small left step, and is composed of extremely fine grained, cataclased epidote. It is also evident that the central slip surface was well-developed after only 120mm total displacement on the fault. Pseudotachylyte is not present in the fault suggesting that slip events may not have reached seismic velocities. However, the low angle fractures that splay from the fault trace, and re-join some distance along strike have a geometry similar to sidewall ripout fractures described for pseudotachylyte-bearing faults elsewhere (Swanson, 1989). These structures are indicative of adhesive wear associated with slip events, rather than quasi-static fault processes.

The epidote- and chlorite-rich fabric domains that are cross-cut by the central slip surface are also dominated by brittle deformation textures. All of these domains are filled with minerals that are not derived from the host rock, and wall-rock derived clasts are rare. Most crystals are fragments that have fractured edges, and the fabric domains have characteristic random fabrics. Cross-cutting relations show that the domains did not form at the same time. Hydrothermal fluids were therefore flushing the fault episodically,

depositing material that filled any spaces, or perhaps replacing pre-existing material in the fault, which was then cataclased. The similar composition of the hydrothermally deposited material suggests that deformation of the material within the domains and the latest stages of slip occurred at similar temperatures. Though hydrothermal chlorite and epidote are difficult to use as temperature gauges (Decaritat *et al.*, 1993), previous analyses of fluid inclusions in normal fault zones suggests that hydrothermal chlorite-epidote assemblages were deposited at temperatures of 300ºC or more (Bruhn *et al.*, 1994).

Slivers of ductiley deformed rock containing quartz and feldspars that have deformed by intra-crystalline deformation mechanisms are juxtaposed against the predominantly brittle fault rock assemblage. Temperatures in excess of ~450ºC are required to achieve feldspar recrystallisation (see section 1.2.2 for a review of recrystallisation temperature regimes). As the adjacent epidote-chlorite domains have not undergone high temperature alteration, the ductiley deformed rock must pre-date the brittle cataclasites. Where the ductiley deformed material is immediately adjacent to the wall rock (and not separated by a slip surface), the wall rock is significantly less deformed. Bend-in fabrics and a gradual strain gradient defined by sheared minerals are not present in outcrop or thin section. The strain gradient from the ductile slivers into the wall rock is therefore extremely steep. It seems likely that the ductile slivers nucleated on a pre-existing discontinuity in the rock such as a vein or small dyke, allowing a significant increment of strain increase to occur in an extremely localised zone. However, the assemblage of feldspars and quartz are not typical vein or dyke fill. The general scarcity of fragments of recrystallised material within the cataclasites suggests that material has been lost from the system, possibly as a result of fluid migration, so elucidating the earliest stages of deformation is difficult.

The wall rock to P9F has been altered and intensely fractured; fluid inclusion trails in quartz and the dusty streaks in feldspars likely represent healed opening mode fractures. The trails are undisturbed by recrystallisation of quartz crystals in the wall rock, and are parallel to chlorite-filled veins in the wall rock that cross-cut the wall rock – fault rock boundary, suggesting that they formed at relatively low temperatures. As the trails have a consistent orientation, they may be related to the stress acting on the fault during brittle deformation. The orientation of the healed fractures (forming acute counter-clockwise angles with the slip surface on both sides of the slip surface) matches the expected orientation of micro-fractures in the dilational quadrant of the process zone of a propagating mode II left-lateral fault, but not the orientation of micro-fractures produced during mode I crack propagation (Vermilye and Scholz, 1998).

If the healed fractures do represent a relic process zone for the fault, P9F is likely to have propagated as a shear crack rather than nucleating on a pre-existing opening mode crack. However, the location of the sample site near to the middle of the fault strand indicates that if the fault had propagated as a mode II crack, it must have propagated a relatively long distance (more than 5m in either direction from the sample site). There is also abundant evidence for high temperature deformation within the fault rock assemblage, showing that early ductile slip accumulated at elevated temperatures compared to the temperatures at which the healed fractures are inferred to have formed. The timing of generation of the healed fractures in relation to fault slip could be established by evaluating the temperatures at which the fractures formed through fluid inclusion analysis. This would show whether the fractures were coeval with the earlier stages of slip. The mode of fault nucleation and propagation could also be investigated further by analysing the micro-fracture orientation and distribution along the fault trace and with distance away from the fault trace.

5.6.1.2 Fault AB9F1

Fault AB9F1 is dominated by the chlorite breccia that comprises the majority of the fault rock. The last slip on the fault is associated with the brecciation of previously deformed rock, as well as undeformed wall rock as a significant proportion of the clasts in the breccia are composed of undeformed wall rock crystals. Some late-stage minor slip localisation also appears to have occurred where cataclasites are present along the northern fault strand. However, the cataclasites are not continuous at the thin section scale. The fault breccia is extensively chloritized, but is generally not disrupted by later slip accumulation. Chlorite crystals in the matrix of the breccia are fine and euhedral, and have not been deformed sine they grew in the matrix of the breccia. The breccia is a brittle fault rock that has an unusual grain size distribution compared to cataclasites. The chlorite is uniform in size, and the fragments comprise a small proportion of the fault rock, implying that there are many small grains and few large grains for a rock that has undergone little comminution. As the chlorites are euhedral and not cataclased the cumulative fracture surface area in the rock is small.

The euhedral chlorite likely formed in one of two ways; the chlorite was precipitated from hydrothermal fluids after the fault breccia formed, replacing some of the groundmass in the breccia matrix, or the chlorite was deposited from hydrothermal fluids present during the last increment of slip on the fault and the chlorite filled new space formed by dilation. Microstructural observations of the texture of the chlorite alone are insufficient to distinguish between these two scenarios. However, the presence of injection vein-like

structures that are filled with the chlorite breccia suggests that the fault fill may have been fluidized during the brecciation event. The presence of a free fluid phase during a slip event would increase the effective pressure acting across the fault, and volume expansion of the fluid by thermal pressurization could cause brecciation. The injection vein structures, and the inferred dilation from the volume of chlorite suggests fluid was present during the last slip event on this fault.

Lenses of ductiley deformed material are developed locally between brittle fault rock and the wall rock. Similarly to P9F, the ductile deformation predates the brecciation event as the fault rock assemblage is not recrystallised at high temperatures (i.e. temperatures greater than ~450ºC which are required for feldspar intra-crystalline deformation). The juxtaposition of the recrystallised material in the lenses and the less deformed wall rock indicates a steep strain gradient is present between the two. Foliations indicative of a macro-scale ductile shear zone are absent in outcrop and in the wall rock in thin section. These textural characteristics suggest the ductile deformation nucleated on a material discontinuity.

Evidence for high temperature deformation of the wall rock is shown by chessboard extinction patterns in quartz that are produced by grain boundary migration recrystallisation and indicate temperatures >500ºC during deformation. Wall rock alteration of plagioclase and alkali feldspar is ubiquitous, and hornblende is chloritized. However, fractures and healed fractures are less well-developed in the wall rock of AB9F1 than P9F. Fractures that are present are filled with calcite or muscovite as well as epidote. The fracture-hosted mineral assemblage indicates greenschist facies conditions with temperatures of >300ºC (Bruhn *et al.*, 1994). Fractures along quartz grain and subgrain boundaries are common, and imply dilation of the wall rock in deformation that has occurred at temperatures less than ~280ºC (Stipp *et al.*, 2002) assuming that the intra-crystalline deformation that had already induced quartz subgrain growth would have continued at higher temperatures than this. Low temperature dilation in the wall rock is consistent with the inferred low temperature brecciation of the fault rock from the chlorite breccia, but a direct correlation is impossible as cross-cutting relations are absent from thin section.

5.6.1.3 The DBF

The DBF fault rock assemblage comprises intensely recrystallised quartz and feldspars that are overprinted by brittle slip surfaces. Pseudotachylytes in the DBF attest to slip

occurring at seismic velocities. The southern pseudotachylyte defines a generation surface that is straight, that bifurcates in one place, but which is not disturbed by later deformation. However, there are no cross-cutting textures between the southern pseudotachylyte and the northern slip surface. The pseudotachylyte generation surface may have been abandoned after the pseudotachylyte solidified, and slip transferred laterally to the northern slip surface so the absolute order of slip events is unclear. If melt is present decorating the narrow parts of the northern slip surface then the volume of melt generated during a slip event on that surface is small. Numerous other brittle textures are present in the fault; fractures branch from the southern pseudotachylyte in two orientations, cataclasites are developed adjacent to the northern slip surface, and the central recrystallised zone is pervasively cut by small slip surfaces. These fractures cut quartz and feldspars, indicating that the temperatures during brittle deformation were ≤300ºC (Stipp *et al.*, 2002). The cumulative effect of these brittle features is to give the rock a brecciated appearance.

The striped areas in the southern pseudotachylyte of the DBF are interesting in that similar textures are not reported in the literature. Foliations are developed in mylonitized pseudotachylytes (Lin *et al.*, 2005; Passchier, 1982); if the DBF pseudotachylyte had been ductiley deformed a shear zone would localise on the fine-grained groundmass and impose a foliation at low angles to the margin edges. The stripes form at approximately 90º to the margin edges, so mylonitization cannot account for this fabric.

Brittle fractures are common in the fault rock of the DBF, but are rarely associated with precipitation of hydrothermal minerals. Chlorite decorates some of the shear fractures in the central zone, and calcite is present at the northern and southern edges of the fault rock. Chlorite also forms the matrix of the breccia cross cut by the southern pseudotachylyte. However, a qualitative comparison to P9F and fault AB9F1 shows that the proportion of material precipitated from hydrothermal minerals is small. The wall rock to the DBF is less altered than the wall rock to the other two faults. Alteration halos are absent from the pseudotachylyte-bearing portion of the fault in outcrop, and thin section analysis shows that hornblende is unaltered and that feldspar is not sericitized. Fluid flow along this part of the fault was therefore limited through the deformation history of the fault. The presence of fluids is thought to inhibit melt generation (e.g. Sibson, 1973), so the absence of fluids might explain why pseudotachylytes were generated along the DBF.

Much of the fault rock in the DBF is composed of intensively recrystallised quartz and feldspar that deformed at high temperatures (>450ºC). Though many of the original

crystals have been completely recrystallised, there are no grain shape fabrics or foliations developed in the ductiley deformed zones. The relation between the ductiley deformed material and its wall rock is unclear as brittle slip surfaces are present at both edges of the ductiley deformed zone. However, the assemblage of minerals within the ductiley deformed zone includes hornblende, and is the same as the host rock assemblage. It therefore seems unlikely that the ductile deformation localised on a pre-existing material discontinuity such as a vein or dyke. As with P9F and AB9F1 there is no field or thin section evidence for a macro-scale shear zone centred on the DBF.

The DBF wall rock contains little alteration of feldspar or hornblende, indicating that fluid migration through the rock was minimal compared to the other two faults described. The wall rock does show evidence for diffuse high temperature deformation in the recrystallisation of quartz by both subgrain rotation and grain boundary migration mechanisms. However, feldspars in general have not deformed ductiley, indicating temperatures may have reached a maximum of around 400-450ºC. The deformation lamellae in quartz and fractures at 25-30º to the slipping zone are formed at lower temperatures (<200ºC to ~300ºC; Passchier and Trouw, 2005) and so may be genetically related to the slip surfaces within the fault trace; the angles between the fractures and the slip surfaces are consistent with the fractures forming during left-lateral slip on the DBF.

5.7 Discussion

5.7.1 Why are the faults different?

The three faults studied in thin section share many similar characteristics; they all have apparent left-lateral displacements of tens of centimetres, they all cut the same granodiorite host rock, and they broadly have similar propylitic mineral assemblages. However, the faults are significantly different at field and thin section scales. The most important characteristics that make each fault distinctive are the geometry of the fault traces in outcrop and thin section, the inferred width of the slipping zone, the amount of material precipitated from hydrothermal fluids and degree of alteration to the wall rock, and the presence or absence of pseudotachylyte (see Table 5).

Fault	Trace morphology	Fault rock type	Width of slipping zone (mm)	Relative proportion of hydrothermal minerals	Wall rock alteration
P9F	Straight	Cataclasite	0-0.15	High	Pervasive
AB9F1	Branched	Breccia	≤16	High	Pervasive
DBF	Branched	Pseudotachylyte	0.2-1	Low	Limited

Table 5. Summary of the key characteristics of the three faults studied in thin section.

Propylitic mineral assemblages and wall rock alteration attest to fluids flowing through or near the faults. In the case of P9F the euhedral epidote crystals adjacent to the slipping zone and comminuted epidote and chlorite crystals that comprise the fabric domains within the fault trace indicate that the most significant volumes of fluid flow are associated with fault slip. Minerals precipitated from fluids in P91 are either comminuted or euhedral. However, in AB9F1 all of the chlorite in the matrix of the chlorite breccia is euhedral, and seems to be associated with the brecciation of the fault rock and the wall rock. Though both faults have hosted hydrothermal fluids, the final increment of slip on AB9F1 apparently occurred when the pore fluid pressure (P_f) was high, perhaps due to the presence of a free fluid phase during slip. Elevated P_f to values approaching, or greater than, σ_n (normal stress acting on the fault) would cause hydro-fracturing (Sibson, 1986), and could explain the irregular geometry of the chlorite breccia in thin section. In contrast, fault P9F accumulated slip in discrete increments, but maintained P_f levels that were insufficient to cause brecciation.

The DBF fault trace also has a branching geometry in the western section, but is a pseudotachylyte-bearing fault in which the evidence for fluid flow is minimal compared to the other two faults; the wall rock is relatively un-altered, and the proportion of the fault rock assemblage that is composed of minerals deposited from hydrothermal fluids is small. The branching geometry is therefore unlikely to be due to elevated P_f, in the way inferred for AB9F1. Sibson (1973) suggested that melt generation is likely limited to incipient structures in which fault permeability is low, thereby restricting the potential for fault-hosted fluids to decrease the effective normal stress across the slipping zone. The DBF seems to be an example that supports this theory. The branching geometry of the DBF must have been imposed on the fault prior to pseudotachylyte generation, or is the product of the pseudotachylyte generating slip event. As all of the fractures in the branching network are filled with pseudotachylyte (as identified in outcrop), and pseudotachylytes are absent from the eastern section of the fault which is not branching, the pseudotachylyte generating process is likely associated with the branching geometry. Various authors (e.g. Fliss *et al.*, 2005; Lawn, 1993; Rosakis, 2002; Segall, 1984) have shown that a branching

morphology can be associated with a dynamically propagating crack. Earthquake rupture fronts are observed to propagate at inter-sonic velocities, and so the branching geometry of the DBF pseudotachylyte fault could reflect the processes associated with the breakdown of material strength at the front of an earthquake rupture.

One striking characteristic of the DBF is the difference in the geometry of the fault trace between the western branching section and the eastern straight section. If the geometry of the trace is an indicator of slip processes, then the two sections of the fault could be inferred to have deformed in different ways. The western branching section may the product of earthquake rupture processes, but the eastern section lacks the outcrop scale evidence for having experienced an earthquake rupture. The eastern section of the fault is in fact very similar in appearance to P9F. As described above P9F is intimately associated with fluid flow. By comparison with P9F, the eastern section of the DBF likely has hosted greater volumes of fluid flow than the western section. Compartmentalisation of the fault with respect to fluid flow, resulting in a 'dry' western section, and a 'fluid-hosting' eastern section, could explain the along-strike differences in the fault trace geometry; the dry section maintained extremely low P_f resulting in pseudotachylyte generation, but P_f in the western section was high enough to inhibit melting but also so low that brecciation did not occur, in the same way as P9F.

Spatially variable fluid-fault interactions through the deformation history of the DBF could explain the differences in the fault trace geometry, but require the fault permeability to become compartmentalised, and remain so, as slip accumulated. Structural controls on permeability are observed to cause anisotropic fluid-flow at large scales (e.g. Caine and Tomusiak, 2003; Rowland and Sibson, 2004), but the DBF fault trace implies compartmentalisation over tens of metres or less. Fault-induced permeability is maintained by cataclasis causing local dilation (e.g. Barton *et al.*, 1995). The DBF eastern section may therefore be inferred to have undergone a more prolonged, continuous brittle phase of deformation than the western (pseudotachylyte) section. It is unclear if the eastern section has a greater magnitude of slip than the western section, and the relative timing of activity on each section is unknown. However, pseudotachylytes in other areas have been inferred to display 'lock-up' behaviour, representing the final slip increment on a fault (e.g. Di Toro and Pennacchioni, 2005). The pseudotachylyte effectively welds the opposing wall rocks. A similar effect might have occurred in the DBF along the western section, but not the eastern section. The eastern section could therefore have continued to deform, or propagate towards the western section if the sections were not linked, after the

pseudotachylyte generation event promoting fluid flow and hydrothermal mineral deposition.

The field and thin section observations describing faults P9F, AB9F1 and the DBF highlight several important characteristics of small faults:

1. The deformation history of the fault has a significant influence on fault geometry, permeability and fault rock assemblage, even after small amounts of slip.

2. Fluid-fault rock interaction is critical to the slip mechanism during any increment of slip, and appears to control the resulting fault geometry.

3. Lateral structural heterogeneity is established after small finite displacements (<1m), and may be expected in other small displacement faults.

The mineral assemblage and brittle textures that characterise the Bear Creek faults are similar to those observed in faults with much larger displacements; in particular localised zones of comminuted cataclasite or ultracataclasite that cross-cut coarser cataclastic fault rocks are present in faults such as the Punchbowl (Chester and Chester, 1998) and San Gabriel faults (Evans and Chester, 1995), California. Both of these faults have accommodated tens of kilometres of displacement. Faults P9F and AB9F contain slip surfaces that are similar to the Punchbowl and San Gabriel faults at the thin section scale. This suggests that slip surfaces that develop early in the deformation history of a fault might be re-used consistently as displacement is accumulated. If this is the case, the grain size distribution of the comminuted slip surfaces is established after small amounts of slip. Previous studies have used the grain size distribution of fault rocks to determine the cumulative fracture energy required to generate mature fault zones (Chester *et al.*, 2005; Wilson *et al.*, 2005). The observations of the small faults in this chapter demonstrate that relating the fracture energy of fault rocks from mature fault zones requires the deformation history of a fault to be accounted for; if the grain size distribution of a slip surface or particular cataclasite is established early in the deformation history, the only fracture energy consumed by continued deformation will be to maintain that distribution should healing occur. Continued deformation in the form of seismic slip events will expend a smaller and smaller proportion of the total energy released during larger and larger ruptures. Estimating fracture energy from fault rocks is likely more complex than is currently appreciated, and current estimates based on fault rock analysis are likely too great.

5.7.2 Comparison with previous work

Based on field observations of joints and small faults in the Mount Abbot Quadrangle, Segall and Pollard (1983b) proposed that faults in the area nucleated on pre-existing cooling joints. They cite several pieces of evidence in support of this theory: slipped and un-slipped joints coexist in the same outcrops, fractures without shear offset have undeformed mineral fillings, but fractures that are offset have deformed fillings, and some joints occur without joints, but faults always occur in association with joints. Martel *et al.* (1988) and Martel (1990) extended the joint reactivation theory by analysing the geometries of faults hundreds of metres to kilometres in length. These two studies showed that reactivated joints develop splay fractures in the dilational quadrants at their terminations in response to the stress intensification induced at the crack tips. They proposed that with increasing displacement, splay fractures link reactivated joints side to side and end to end to form simple fault zones, where slip is localised onto boundary faults that inherit their morphology from the initial joints. Further slip accumulation may lead to the development of compound fault zones where more than one simple fault zone links to form a larger structure (Figure 117). This conceptual model is hereafter referred to as the fracture linkage model.

All of the outcrop-scale maps of fault geometries presented by Segall and Pollard (1983b), Martel *et al.* (1988) and Martel (1990) show that reactivated joints (or small faults) have straight or slightly kinked traces with straight geometries. The straight faults described in this chapter (P9F and P12F) have comparable outcrop-scale geometries to those described by these authors. In particular the simple, straight geometries of the fault traces and the stepover geometries are very similar.

Faults P9F and P12F may therefore be examples of the reactivated joints described previously, and might be expected to develop through a series of linkages to that proposed by the fracture linkage model. However, this study provides additional data concerning the slip distribution in the stepover in fault P12F (Figure 95). The slip profiles show that one splay has accumulated much more slip than any of the others (S_4). Studies that focus specifically on fault slip profiles in normal faults have interpreted this pattern of slip distribution as being an intermediate stage between faults propagating toward one another and the linkage of two fault strands into a single fault with a bend (e.g. Cartwright *et al.*, 1995; Gupta and Scholz, 2000; McLeod *et al.*, 2000). The fracture linkage model requires faults with stepovers to localise slip onto the boundary faults, with the tabular region in

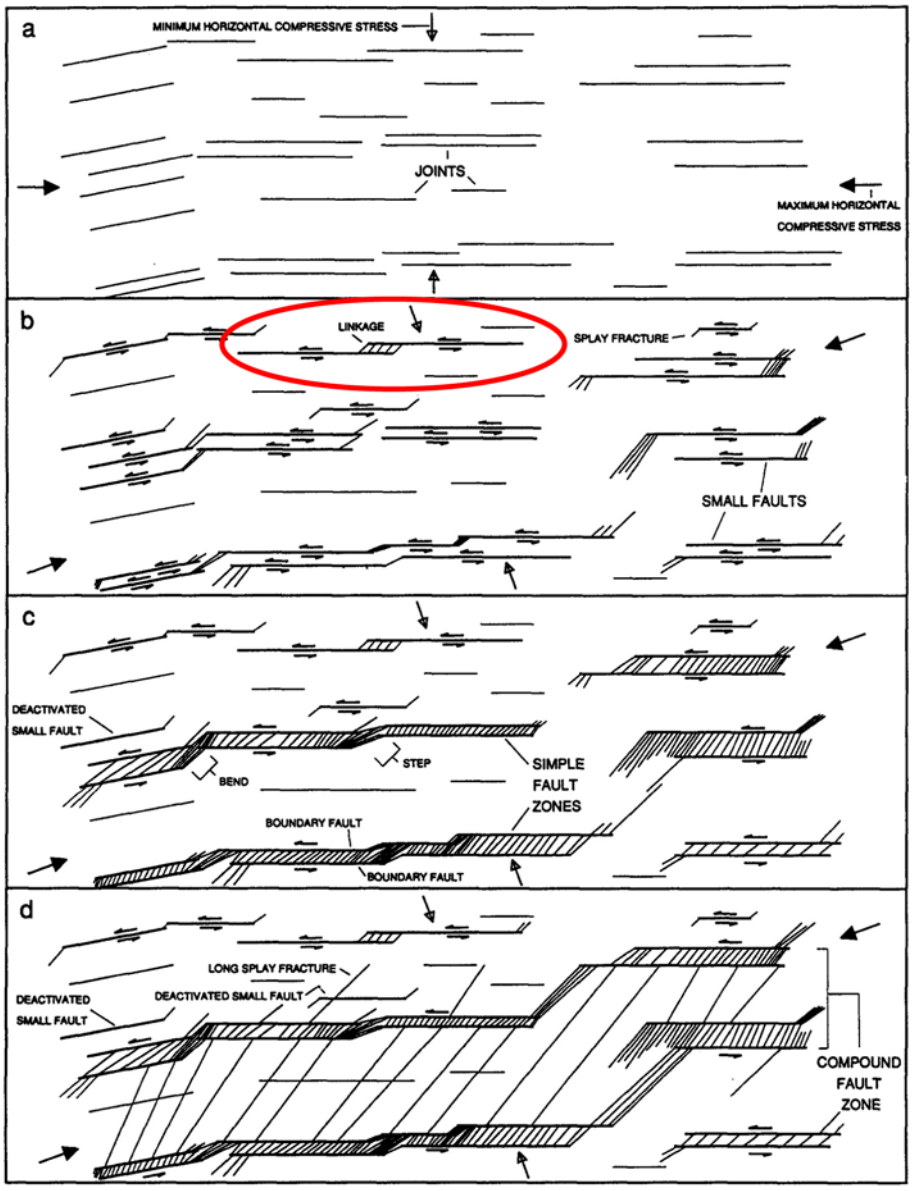

Figure 117. A conceptual model describing the development of fault zones in the Sierra Nevada, adapted from Martel (1990). a. Opening mode fractures (joints) form in response to pluton cooling. b. Some joints are reactivated when the regional stress field rotates and accumulate small (≤2m) amounts of slip. Splay fractures develop near reactivated joint tips. Note that the circled geometry is similar to that of the stepover in P12F. c. Simple fault zones form where reactivated joints link side to side and end to end. d. Compound fault zones may form where simple fault zones link.

between subsequently becoming heavily fractured but accommodating little shear strain. The slip profiles for fault P12F therefore seem to be at odds with the fracture linkage model, suggesting that the model may not be appropriate to all faults in the study area. It is also possible that the stepover in P12F is an example of the geometry of fractures circled in Figure 117b. In the absence of nearby joints to link side to side or end to end with, a single fault trace with a bend in the position of S4 may be expected to develop from P12F. If this is the case, the fracture linkage model should have an additional evolutionary path where faults link end to end but do not develop a tabular zone of fractured rock between boundary

faults. Further fieldwork to identify more structures with intermediate stages of evolution would help to demonstrate that this is the case.

Microstructural observations of faults from the Mount Abbot Quadrangle are presented by Segall and Pollard (1983b) and Martel *et al.* (1988). Both of these studies show that small faults are dominated by ductile fabrics that result from intra-crystalline deformation of primarily quartz. They show that meso-scale fabrics identified in the fault rocks in outcrop reflect foliations developed by grain shape fabrics defined by recrystallised quartz crystals. Feldspars are present in the fault rocks as larger, undeformed porphyroclasts. These observations are not consistent with the thin section analysis of P9F; epidote and chlorite are absent in their descriptions, and cataclastic fabrics are restricted to fractures that cross-cut the ductile features. Martel *et al.* (1988) conclude that cataclastic textures are only developed in the boundary faults in simple and compound fault zones They inferred that longer structures cause 'stress shadows' to develop in the adjacent rock leading to localisation of strain onto the longer faults. The required time-averaged increase in strain rate that accompanies the localization is thought to cause cataclasis rather than ductile deformation. Cataclasites in P9F suggest that brittle fault rock assemblages are not restricted to relatively mature fault zones. However, the early stage of ductile deformation represented by the slivers of recrystallised quartz and feldspars in P9F may be directly analogous to the fabrics described by Martel *et al.* (1988), though in the case of P9F these fabrics have been overprinted by fluid flow and cataclasis.

Faults with branching geometries such as AB9F1 and the DBF have no analogous examples in the literature describing the structures in the Mount Abbot Quadrangle. The branching fault traces and numerous splay fractures with curved traces are newly identified geometries. Pseudotachylytes have also not been previously reported in faults in the area, and the central Sierra Nevada is cited as an example of a well-studied area where pseudotachylytes are absent (e.g. Di Toro and Pennacchioni, 2004). As well as the DBF, pseudotachylytes were identified in several other faults in the Mount Abbot Quadrangle during fieldwork for this project (Figure 118), suggesting that pseudotachylytes should not be considered as absent in the area. This is of significant importance to understanding the mechanics of faulting in the central Sierra Nevada; pseudotachylytes imply dynamic rupture process, whereas faults in the area have previously been described exclusively in terms of quasi-static processes (e.g. Martel, 1997; Martel and Boger, 1998; Martel and Pollard, 1989).

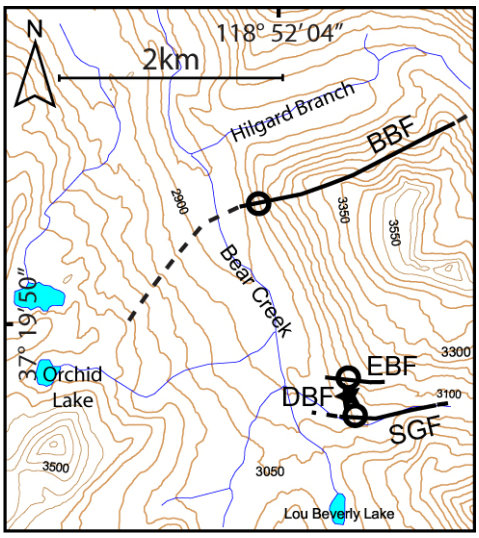

Figure 118. Map of part of the Mount Abbot Quadrangle showing localities where pseudotachylytes were identified during fieldwork (circles). The DBF locality is shown for reference. BBF is Big Bear fault, EBF is East Branch fault, SGF is Seven Gables Trail fault.

5.7.3 Inferring earthquake source parameters for a DBF rupture event

5.7.3.1 Magnitude (M_w)

Pseudotachylytes in the DBF are the strongest possible indicators that the fault experienced seismic slip events, rather than aseismic creep (e.g. Cowan, 1999). Generally, pseudotachylytes are thought only to be generated in moderate to large seismic events that involve significant amounts of coseismic slip (e.g. Kanamori and Heaton, 2000); the DBF has a small apparent cumulative displacement so provides an opportunity to derive earthquake source parameters from an earthquake with a small inferred magnitude. Empirically derived scaling relations (Hanks and Bakun, 2002; Wells and Coppersmith, 1994) show that the relation between subsurface rupture length, l, and magnitude can be expressed as:

$$Mw = 4.38 + 1.49.\log l \,.$$

Equation 3

If the exposed length of the DBF had slipped (45m) in a rupture event, and assuming that this is equal to the maximum subsurface rupture length, the magnitude of the earthquake rupture would have been approximately 2.4. Similarly, the maximum slip, D, is related to the magnitude by:

$$Mw = 6.69 + 0.74 \log D \,.$$

Equation 4

The maximum observed displacement on the DBF is 0.7m; an earthquake with a maximum slip of 0.7m would be predicted to have a magnitude of ~6.6. However, microstructural observations show that a significant proportion of the shear displacement on the fault was accumulated by both ductile and brittle deformation mechanisms prior to the pseudotachylyte-generating slip event. The maximum slip for the pseudotachylyte generating event must therefore be less than 0.7m. Scaling relations (Scholz *et al.*, 1986) show that the subsurface rupture length is ~10^4 times greater than the maximum slip. Thus, the exposed length of the DBF suggests the co-seismic slip was on the order of 0.0045m.

5.7.3.2 Frictional shear resistance

The frictional shear resistance during coseismic slip reduces in response to some slip-weakening mechanism. However, the absolute value of coseismic shear resistance cannot be directly measured by seismological methods (Kanamori and Brodsky, 2004). The heat energy generated per metre squared by the frictional resistance on a sliding interface can be approximated by (Sibson, 2003):

$$Q = \tau_f . u ,$$ **Equation 5**

where τ_f is the average shear resistance (MPa) during slip u (m). Assuming all of the frictional energy is released as heat, pseudotachylytes can be used to constrain τ_f as the energy required to melt the rock can be evaluated (Barker, 2005; Di Toro *et al.*, 2005b; Sibson, 2003). Following the method of Barker (2005) and Sibson (2003) and assuming uniform adiabatic shearing within a slipping zone of thickness t_s (m), the heat energy required to generate a pseudotachylyte vein is given by:

$$Q = \Delta T . c_p . \rho . t_s ,$$ **Equation 6**

where ΔT is the temperature rise (ºC), c_p is the heat capacity (J ºC^{-1} kg^{-1}), ρ is the density of the host rock (kg m^{-3}). Combining equations 3 and 4 shows that τ_f is given by:

$$\tau_f = \frac{\Delta T . c_p . \rho . t_s}{u} .$$ **Equation 7**

Field and thin sections can be used to determine t_s (0.2 to 1mm for the DBF). Evaluating the melting temperature of the host rock is not straight forward as the pseudotachylyte generation is a non-equilibrium melting process. The composition of the DBF melt is also

unusual, so an accurate melting temperature is impossible to gauge. However, Wenk *et al.* (2000) and Sibson (2003) argue that using a value of 1000 ºC for ΔT is sufficient to account for the latent heat of fusion, and would induce partial melting in the majority of crustal rock types under a range of ambient temperatures. Using equation 5, with values of 1000 ºC for ΔT, 1000 J ºC^{-1} kg^{-1} for c_p for silicate rocks (Sibson, 2003), 2700 kg m^{-3} for the density of the granodiorite host rock, and 0.0045m coseismic slip (u), τ_f is 600MPa for t_s = 1mm and 120Mpa for t_s = 0.2mm. The greatest uncertainty in this calculation is the magnitude of coseismic slip as the absolute length of the DBF cannot be measured. As a means of testing the sensitivity of τ_f to the magnitude of slip, the same calculation was performed for 100m and 500m long faults. The value for u scales with fault length, giving u = 0.01m for a 100m long fault and u = 0.05m for a 500m long fault. Accordingly, for a 100m long fault, τ_f is 270MPa for t_s = 1mm and 54MPa for t_s = 0.2mm. For a 500m long fault, τ_f is 54MPa for t_s = 1mm and 11MPa for t_s = 0.2mm.

The results show that τ_f calculated with the above method is most sensitive to the thickness of the melt layer; for a given fault length τ_f can vary by an order of magnitude with a small (<1mm) change in melt thickness. Using the length of the exposed part of the DBF and a thickness of melt of 1mm results in significantly higher τ_f than the values of 100 to 250MPa calculated by Barker (2005) for shallowly dipping pseudotachylytes up to 200m long and 5cm thick. This suggests that the true thickness of the DBF slipping zone was much thinner than 1mm (which represents a likely maximum thickness of the melt layer) and emphasises that slip may be extremely localised during an earthquake rupture event.

Di Toro *et al.* (2005b) discuss a similar method for evaluating τ_f to the above formulation. They show that there are several additional complexities in the pseudotachylyte generation process that must be accounted for; extra heat energy is consumed by the latent heat of fusion, energy is also consumed by further heating of the melt, and lithic clasts within a pseudotachylyte have not melted and so the clasts have not consumed latent heat of fusion. Di Toro *et al.* (2005b) also show that determining the thickness of the slipping zone from pseudotachylytes is complicated by the irregular geometries of the generation surfaces and injection veins, and that measuring the coseismic slip is also difficult if precursory cataclasites are present in the fault. Their analysis of 63 pseudotachylyte bearing faults showed that τ_f was less than 42.4MPa in all cases.

The DBF pseudotachylyte has relatively simple deformation history compared to the examples studied by Di Toro *et al.* (2005b) and Barker (2005) due to the small finite

displacement on the fault. However, the additional energy sinks identified by Di Toro have not been assessed in this study. Assuming that prediction of coseismic slip from the scaling relations is appropriate, the results presented here are likely minimum estimates for τ_f as the latent heat of fusion of the melt would increase the magnitude of Q in equation 4, and therefore increase τ_f. Further analysis to constrain a value for the thickness of the slipping zone, the proportion of clasts in the DBF pseudotachylyte, and to estimate the melting temperatures of the melt and the maximum temperature the melt was heated to would provide a more accurate estimate of τ_f.

5.7.3.3 Slip weakening distance

Estimates of the slip weakening distance (D_c) for earthquakes from seismological data generally yield values of tens of centimetres (e.g. ~1m, Bouchon *et al.*, 1998; ~0.4m, Ide, 2002; ~1m, Ide and Takeo, 1997; 0.4 - 0.9m, Mikumo *et al.*, 2003). Hirose and Shimamoto (2005b) used the results of high velocity rock friction experiments to show that D_c and melt thickness are both exponential functions of slip, producing curves with similar characteristic distances. They compared their experimental results with field data describing the thickness to displacement ratio of pseudotachylyte veins in the Outer Hebrides (Sibson, 1975). They concluded that D_c for the Outer Hebrides faults was 0.39±0.15m. Hirose and Shimamoto (2003) showed that during experimental pseudotachylyte generation the fractal dimension of the melting surface topography increases from 1.0 to 1.1 once a continuous film of melt is generated along the surface, and steady state dynamic friction is reached (i.e. the amount of slip is greater than the slip weakening distance). Di Toro *et al.* (2005b) measured the fractal dimension of the melt-decorated surfaces in the pseudotachylyte-bearing faults, and used the results to compare their natural examples to the experimentally produced melts of Hirose and Shimamoto (2003). Di Toro *et al.* (2005b) inferred a slip weakening distance of 1.17m for their pseudotachylyte-bearing faults.

All of the estimates of D_c from seismologic and field and experimental data are at least of the order of tens of centimetres. Some of these estimates specifically assess D_c for pseudotachylyte-bearing faults. If melt lubrication was the active slip weakening mechanism during the DBF rupture event, then the coseismic slip associated with the event is two orders of magnitude less than all of the estimates of D_c. This suggests that the DBF rupture event did not reach D_c and therefore that the melt was generated prior to catastrophic failure of the fault. Hirose and Shimamoto (2005a) show that the dynamic shear resistance during high velocity rock friction experiments undergoes two stages of

weakening; initial weakening is followed by a significant strengthening phase before weakening to a steady state value is achieved. The strengthening phase during the experiments occurs immediately prior to the creation of a complete melt layer. Patches of melt decorate the sliding surface, but not enough melt has been generated to form a through-going layer. While patches of melt are present, the shear resistance increases with slip. The DBF pseudotachylytes do not decorate the entire fault length, suggesting that the DBF rupture event may have arrested in a slip-strengthening phase prior to the creation of a melt layer. However, Fialko and Kahzan (2005) showed that the strengthening phase observed in the experiments are likely to diminish with increasing normal stress, and therefore depth in the crust. They suggest that strengthening in response to be melting is unlikely, except for earthquakes in quartz-rich rocks at <5 to 7km depth. The geometry of the melt patches in the DBF could be explained by rupture arrest in response to dynamic strengthening, but this interpretation requires further work to constrain the depth at which the pseudotachylytes were generated.

6

Using Thermochronology to Constrain Deformation Conditions

6.1 Introduction

The mechanisms by which rocks deform at the grain scale are dependent on a number of characteristics of the deformation environment. Temperature, lithostatic pressure, differential stress and strain rate all control to an extent whether crystals deform by crystal plastic mechanisms or by brittle fracture. For a given mineral phase, the intra-crystalline deformation mechanisms that are active during deformation are also controlled by these parameters. Different grain-scale deformation mechanisms are observed to result in differing fault architectures; an extreme example is the contrast between a ductile shear zone exhumed from great depths in the crust and a brittle faults observed in many shallow sedimentary rocks. The characteristics of the deformation environment therefore control the grain scale deformation and fault architecture. Defining these characteristics, and how they vary through the deformation history of a fault, should demonstrate the influence of such extrinsic controls on fault architecture.

Classically, syn-kinematic equilibrium mineral assemblages associated either with contact metamorphic aureoles (Stipp *et al.*, 2002), or hydrothermal minerals (e.g. Di Toro *et al.*, 2004; Di Toro and Pennacchioni, 2004; Toyoshima, 1990) have been utilised to constrain the ambient temperatures and pressures during deformation. The Pyramid pluton granodiorite has not undergone contact metamorphism, and sedimentary rocks are absent from the vicinity of the pluton. Hydrothermal mineral assemblages place approximate constraints on ambient temperatures and can only be used to infer lithostatic pressures as they rely on cross-cutting relations.

A plutonic setting for the Granite Pass area provides an opportunity to directly estimate changes in ambient temperature since pluton crystallisation by using a suite of

thermochronometers that are sensitive to different temperatures. Exhumation of the pluton from its crystallisation depth can also be estimated from thermochronometric analyses. Combining these data provides a method for accurately determining changes in the deformation environment during the period in time that deformation occurred.

Estimating the timing and duration of fault activity is critical to an analysis of the variation in temperature and lithostatic pressure by thermochronometric methods; the results of the analyses are absolute ages. Pseudotachylytes are cooled, friction-induced melts formed during slip events that occur at seismic velocities (Sibson, 1975). As the direct products of earthquake ruptures, pseudotachylytes provide an opportunity to date the rupture events that caused the formation of melt in a fault zone. Pseudotachylytes are present in the faults of the Granite Pass suite of faults. The high potassium content of the host granodiorite suggests that the cooled melt products that make up the pseudotachylytes will also have a high potassium content. The pseudotachylytes are therefore likely to be particularly suitable for geochronological analysis by the K-Ar method of dating. A cooling history for the host pluton may be determined by dating a variety of minerals that have a range of closure temperatures. Comparison of the calculated ages for the pseudotachylytes with the cooling history will allow the temperature and pressure conditions prevalent during deformation to be constrained. Other fault rock textures that can also be directly related to temperature and pressure include intra-crystalline deformation mechanisms in quartz and feldspar, which have been experimentally determined and correlated with natural faults in other tectonic settings (Hirth and Tullis, 1992; Stipp *et al.*, 2002; Tullis and Yund, 1985).

The purpose of this chapter is to present the results of a K-Ar thermochronological analyses of the Pyramid pluton (see Appendix 1). These data comprise the first reported ages of crystallisation of minerals from the Pyramid pluton. The results of K-Ar analyses of several pseudotachylyte samples from the SKF are also presented, and in combination with microstructural analyses of the fault rock assemblage, allow the environmental conditions prevalent during deformation to be inferred.

6.2 Structure of this chapter

This chapter will summarise the methods utilised in the thermochronological analyses, including a summary of the experimental design, the theoretical basis for the K-Ar technique, descriptions of the samples analysed and the technical procedures used for each technique. The results of the analyses will be presented and the geological significance of the results discussed.

6.3 Methodology

6.3.1 Experimental design

Pseudotachylytes are formed during slip events at seismic velocities and so offer a chance to date past earthquake ruptures. The host granodiorite in the study area contains abundant biotite and hornblende, mineral phases that are expected to have high potassium contents. Biotite and amphiboles have been observed to melt preferentially during the non-equilibrium melting of fault rock during slip events (Maddock, 1992) and so the potassium contained in these phases is likely to have been passed on to the pseudotachylyte during melting and subsequent re-crystallisation. The likely presence of potassium in the cooled melt means that a dating technique based on the decay of radioactive parent ^{40}K to stable daughter ^{40}Ar would be suitable. Two techniques may therefore be utilised; the K-Ar isotopic method and the $^{40}Ar/^{39}Ar$ dating method. Any radiometric age determination requires the mobility of the parent and daughter isotopes (see below) to be closed with respect to the system, or mineral, being dated. Fault zones are often cited as acting as conduits for fluid migration (e.g. Caine *et al.*, 1996), suggesting that potassium and argon might be mobile in fault rocks. The analyses of pseudotachylyte have therefore been carried out using the K-Ar method in this investigation as this is a quicker, less expensive technique that will determine whether the K-Ar system is suitable for dating the pseudotachylytes.

Three samples of pseudotachylyte were collected from a particularly well exposed section of Skeeter fault (locality 35, see Appendix 1 for location). At this locality pseudotachylytes were abundant in the outcrop, and more than one type of pseudotachylyte could be distinguished on the basis of varying colour, clast content and vein thickness. Cross-cutting relations between the differing pseudotachylyte veins indicated that more than one earthquake rupture had propagated along the exposed segment of the fault zone at this outcrop. The three samples that were analysed were from separate localities within the outcrop, and were chosen to represent the variety of veins present. Two samples of the host granodiorite were collected from fresh exposures near the centre of the pluton and far from any mapped faults so that the cooling history of the pluton could be inferred. Biotites and hornblendes were separated from the host rock samples for analysis by the K-Ar method. The closure temperatures of the two types of minerals with respect to radiogenic argon are different (see Table 1), allowing the rate of cooling of the ambient temperature to be determined when the calculated ages are discordant.

Sample Name	Sample Type	Composition	Analytical Technique	Closure T (ºC)
SKL	Fault rock	Pseudotachylyte	K-Ar	150*
SKR	Fault rock	Pseudotachylyte	K-Ar	150*
SKZS	Fault rock	Pseudotachylyte	K-Ar	150*
GPP1b	Host rock	Biotite	K-Ar	350#
GPP1h	Host rock	Hornblende	K-Ar	550†
GPP3b	Host rock	Biotite	K-Ar	350#
GPP3h	Host rock	Hornblende	K-Ar	550†

Table 6. Summary of sample types and thermochronometer used to analyse the samples in this study. References for closure temperatures are *Reimold *et al.* (1990) #Berger and York (1981), †Harrison (1981).

6.3.2 Theoretical background: the K-Ar method

The K-Ar method is based upon the radioactive decay of naturally occurring ^{40}K to stable ^{40}Ar. ^{40}K undergoes branched decay so that 11% of ^{40}K atoms decay to an excited state of ^{40}Ar by electron capture, a further 0.16% decay directly to the ground state of ^{40}Ar by electron capture, and ~88.8% of ^{40}K atoms decay to stable ^{40}Ca by β decay (Faure, 1986). The accumulation of radiogenic ^{40}Ar in a K-bearing system closed to potassium and argon can be defined using the branching ratio for the decay of ^{40}K as:

$$^{40}Ar^{*} = \frac{\lambda_e}{\lambda} {}^{40}K\left(e^{\lambda t} - 1\right) \qquad \textbf{Equation 8}$$

where λ_e refers to the radioactive decay constant of ^{40}K to ^{40}Ar, and λ is the total decay constant of ^{40}K. By calculating the number of ^{40}Ar and K atoms in a system, the age of a K-bearing material to be calculated by solving the above K-Ar equation for *t*:

$$t = \frac{1}{\lambda} \ln\left[\frac{^{40}Ar^{*}}{^{40}K}\left(\frac{\lambda}{\lambda_e}\right) + 1\right] \qquad \textbf{Equation 9}$$

The following conditions must be satisfied for a K-Ar age to be confidently interpreted: (i) the system (mineral) being dated is closed with respect to Ar (i.e. below the closure temperature of the mineral), (ii) the mineral being dated must have cooled rapidly so that it became closed to ^{40}Ar over a small time interval, (iii) no ^{40}Ar has been incorporated into the mineral other than from decay of ^{40}K, i.e. no excess Ar is present in the system, (iv) the mineral is closed to K, (vi) $^{40}K/K$ is constant in nature, (vii) the decay constants of ^{40}K are accurately determined, and are not affected by environmental conditions such as pressure and temperature (Faure, 1986). The analytical procedure must accurately measure the

concentrations of ^{40}Ar and ^{40}K, and suitable corrections should be made for atmospheric ^{40}Ar.

6.3.3 Sample description

This section will provide detailed hand specimen, thin section and SEM scale observations of each of the samples so that geologic factors can be considered during interpretation of the dating results. The methodology follows that of Chapter 4.

6.3.3.1 SKL – pseudotachylyte

Sample SKL is an un-oriented sample of pseudotachylyte collected from the Skeeter fault at locality 1 (see Appendix 2). Pseudotachylyte is readily identified in outcrop and hand specimen as dark-coloured crystalline material that cross-cuts the host rock (Figure 119). The sample contains two principal veins, hereafter vein SKLa and vein SKLb (Figure 119), which are approximately planar and have a variety of associated secondary veins. The geometry of the primary veins is consistent with that of generation surfaces, and therefore that the secondary veins are injection structures formed by volume expansion during melting (Sibson, 1975). The two generation surfaces have different appearances in hand specimen, suggesting that they may represent two separate slip events. Pseudotachylyte material was extracted from the vein SKLa for dating by the K-Ar method, and so is described in detail below.

Generation surface SKLa ranges in thickness from 20mm to 1mm within the sample, and has a relatively simple 3D geometry. Vein margins are sharp and generally planar except where high angle secondary fractures splay from the main vein. Material within the vein has bands of differing colour developed on weathered surfaces, though the vein is homogeneous dark grey to black when freshly exposed. In hand specimen, it is apparent that vein SKLa and associated injection veins are amongst the latest deformation features developed; they are rarely cross-cut and are observed to overprint both the cataclasites, as well as other pseudotachylyte veins. Lithic clasts are visible within veins in the hand specimen that are ≤3mm, rounded and are clearly multi-crystalline aggregates in some cases.

Figure 119. Photograph of a cut face through sample SKL showing pseudotachylyte veins SKLa and SKLb that have geometries indicative of generation surfaces (dark-coloured bands running left to right through sample) and an obvious injection vein structure (circled). The upper vein in this image was dated by the K-Ar method, scale bar is in centimetres.

The pseudotachylyte veins in sample SKL represent parts of a complex deformation history. As well as veins SKLa and SKLb, areas of comminuted host rock are developed on either side of the two generation surfaces, and some of the smaller pseudotachylyte veins are clearly cross-cut and offset by later shear fractures. Fractured crystals and minor epidote and chlorite mineralization present immediately above the vein SKLa attest to a degree of cataclasis having occurred at some stage prior to melt generation (Figure 119). Dark-coloured hornblende crystals around vein SKLa have elongate forms with wavy edges and are aligned to form a weak foliation at an angle to the pseudotachylyte vein, suggesting ductile deformation also occurred before pseudotachylyte generation. However, none of the deformation fabrics present in the sample are penetrative, and there are some areas of essentially undeformed host rock.

In thin section the pseudotachylyte forms massive, dark-coloured veins. Microcrystallites are readily discernable in thin section in both plane-polarized and cross-polarized light (Figure 120) as acicular crystals contained within an aphanitic groundmass. Microcrystallites are ≤100μm long, are up to 20μm wide, and form domains of differing crystal size within the vein. Close to the vein margins, all crystals are poorly developed and the vein fill is dominated by cryptocrystalline, glassy material. Within ~0.5mm of the margin, microcrystallites become abundant, comprising ~80% of the vein fill, and predominate over a cryptocrystalline groundmass (~10%), and lithic clasts (~10%). Clasts range in size from 10-600μm, are composed of quartz, K-feldspar, plagioclase feldspar,

and are distributed throughout the vein. Spherulitic textures defined by radial arrangements of microcrystallites overgrowing clasts are observed immediately adjacent to the cryptocrystalline vein margins. Fabrics are extensively developed within the domains of varying microcrystallite size where the long-axes of the crystals are aligned and appear to wrap-around clasts (see Figure 120) indicating flow in the melt phase. Devitrification and alteration textures are absent from vein SKLa.

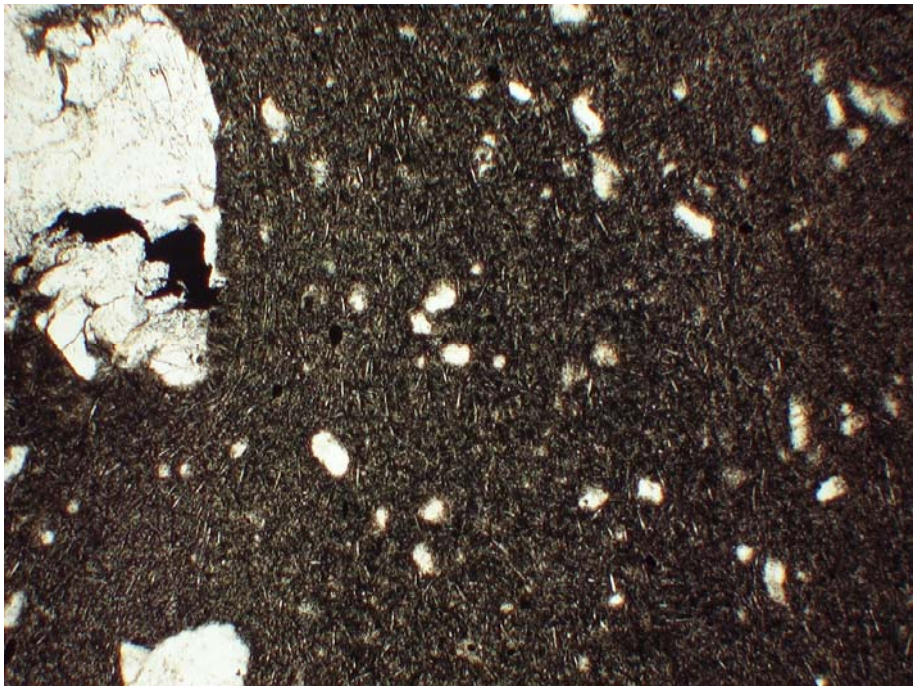

Figure 120. Photomicrograph of pseudotachylyte from sample SKL showing abundant microcrystallites developed in the vein with aligned long axes that wrap around a large clast indicating flow in the melt phase (plane polarised light, field of view 1.6mm).

Microcrystallites are most frequently randomly oriented within the pseudotachylyte veins. SEM analysis shows that all the microcrystallites have approximately similar compositions; larger (≤100μm) microcrystallites of plagioclase feldspar predominate, between which smaller (≤25μm) microcrystallites of plagioclase feldspar containing some anomalous Fe and Mg are developed (Figure 121). The microcrystallites form a mass of delicate, interlocking, acicular crystals that comprise nearly the entire vein fill. Consequently the proportion of the material that is groundmass, which has a composition similar to plagioclase feldspar along with iron and abundant titanite droplets, is small.

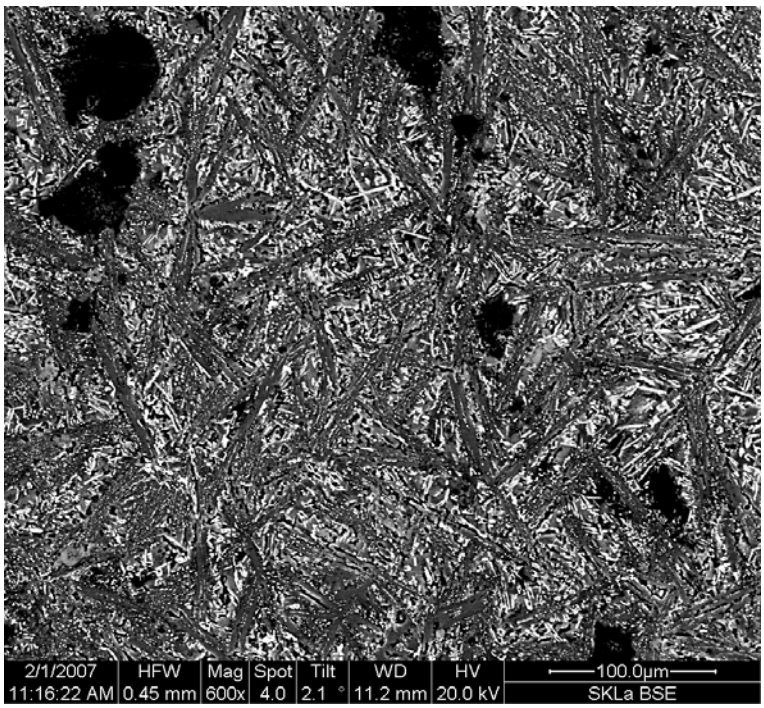

Figure 121. SEM back scattered electron (BSE) image of microcrystallites in pseudotachylyte vein SKLa showing large plagioclase crystals with smaller crystals of plagioclase enriched with Fe and Mg in between. The groundmass is negligible.

6.3.3.2 SKR – pseudotachylyte

SKR is an unoriented sample of Skeeter fault from locality 1. Pseudotachylyte is present within the sample in an intricate network of inter-connected veins that likely represent a pseudotachylyte breccia. Identifying generation surfaces and injection veins is generally impossible in both hand specimen and thin section as the specimen is small compared to SKL and SKZS. Sample SKR also contains extensively developed cataclasites that are developed in association with the pseudotachylytes, and in some cases are difficult to distinguish from pseudotachylytes.

The pseudotachylytes within SKR are homogenous, dark grey or black veins with sharp edges. The veins are wavy at the centimetre scale with erratic geometries giving rise to irregular thickness changes. In general veins are 0.25 to 5mm thick, with order of magnitude thickness changes occurring within tens of millimetres. Locally, thicknesses reach 8mm at intersections that might represent dilational jogs during pseudotachylyte generation. Rounded lithic clasts are ≤1mm long and are scarce, especially in narrower veins. Pseudotachylytes generally overprint cataclasites and in some cases juxtapose cataclasites and undeformed host rock. Cataclased pseudotachylytes cannot be identified in hand specimen. The cataclasites are grey or grey-green but are distinguishable from the pseudotachylytes as they are consistently paler. The cataclasites range from lightly

fractured host rock to extremely comminuted material. The most comminuted material is localised in seams ≤5mm thick that tend to grade into coarser, less deformed material on at least one side. Epidote is present within some cataclasites forming aphanitic laminations and decorating some fracture faces.

The irregular geometry of the pseudotachylytes evident in hand specimen is reflected in thin section where the veins are extremely disordered. Thick veins trend into extremely narrow (<<1mm) slip surfaces along which pseudotachylytes are difficult to identify. Thicker veins are ≤8mm with sharp edges that frequently have a cryptocrystalline zone ≤0.3mm wide adjacent to the wall rock. The central portions of the veins are filled with pseudotachylyte that displays a pseudo-spherulitic texture; lithic clasts are surrounded by a halo of orange-brown aphanitic material which is compositionally different to the groundmass (Figure 122). The groundmass is composed of euhedral, tabular epidote and chlorite ≤20μm which is not the original groundmass composition. Microcrystallites cannot be distinguished in any of the pseudotachylyte veins with an optical microscope. Amygdales are developed in the groundmass and are filled with epidote. Lithic clasts (~10%) are ≤0.3mm, mostly embayed or rounded but some are angular. The clasts are composed of recrystallised quartz and/or feldspars that sometimes have calcite either in a matrix or filling in fractures. Some clasts are composed entirely of calcite. Fractures with small amounts of shear offset cross cut some of the pseudotachylyte veins that are decorated with chlorite.

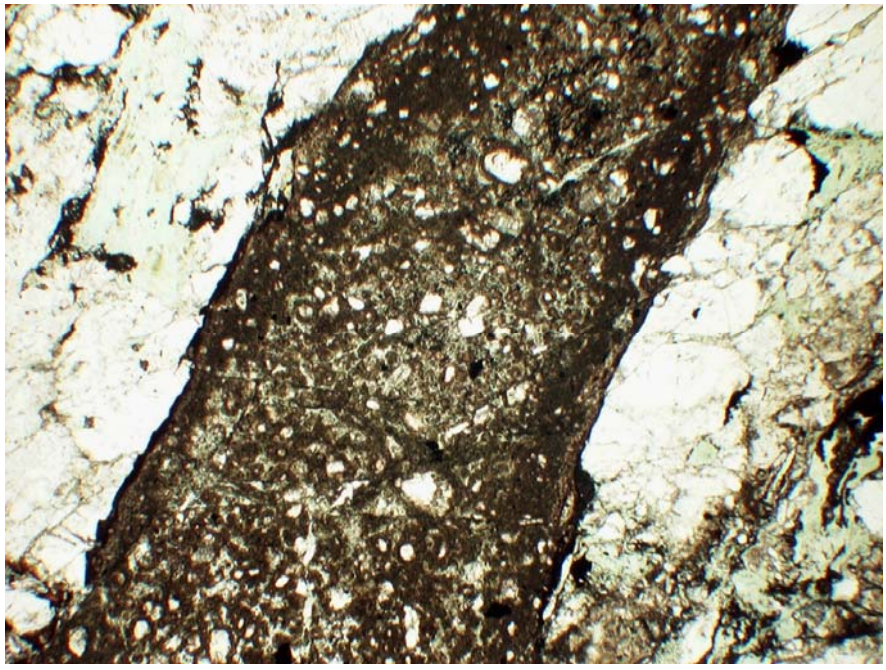

Figure 122. Photomicrograph of pseudotachylyte vein from SKR showing pseudo-spherulitic texture. Lithic clasts are surrounded by a halo of aphanitic material in a groundmass of epidote and chlorite (PPL, field of view 3.1mm).

The pseudotachylytes cross-cut intensely deformed rock that corresponds to the cataclasites visible in hand specimen. Brittle slip surfaces composed of dark brown to black, aphanitic material, ≤0.4mm thick cross-cut rock that has undergone extensive intracrystalline deformation. The slip surfaces are wavy, bifurcate in the section and contain occasional lithic clasts ≤0.2mm long. These strands of ultracataclasite material trend parallel to a zone of deformation composed of fragmented strings of recrystallised quartz and feldspars, which occasionally have calcite as a matrix. Pseudotachylytes cross-cut both the brittle slip surfaces and recrystallisation textures, but inter-finger with the fragmented material along some fractures.

Microcrystallites can be distinguished by SEM analysis of the pseudotachylyte veins in SKR (Figure 123). The microcrystallites are ≤20μm long and have a composition of plagioclase feldspar, between which smaller crystals that are more Ca and Mg rich are present. The pseudotachylyte texture is disrupted by alteration that seems to be replacement of the groundmass predominantly by alkali feldspar.

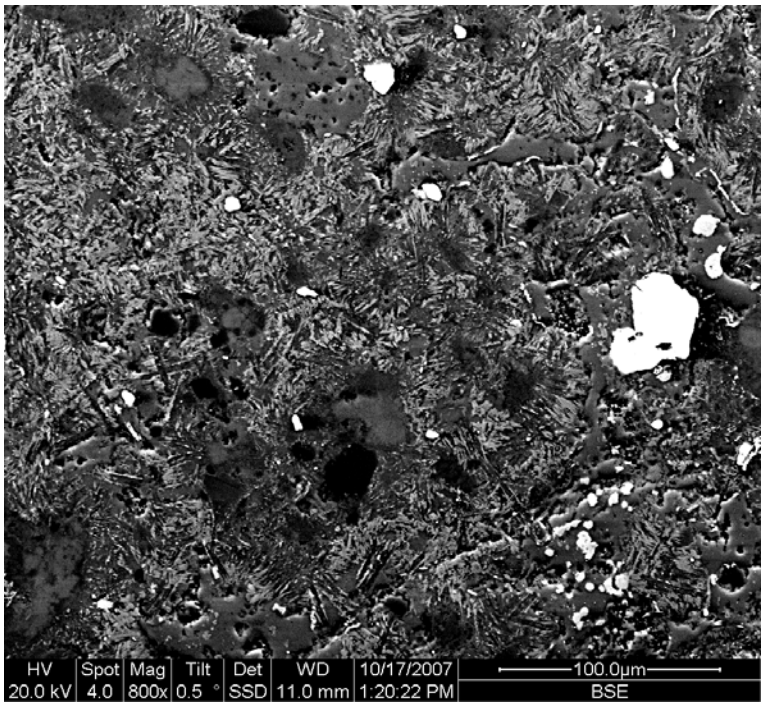

Figure 123. SEM back scattered electron (BSE) image of pseudotachylyte from SKR showing (≤20μm) microcrystallites between which smaller microcrystallites are more Ca and Mg rich. The texture is disrupted by alkali feldspar replacement of the groundmass.

6.3.3.3 SKZS – pseudotachylyte

Sample SKZS is an unoriented sample from Skeeter fault at locality 1 that contains abundant pseudotachylytes (Figure 124). Several different types of pseudotachylytes can be distinguished on the basis of colour and distribution within the sample. Homogenous,

black pseudotachylytes are arranged into two generation surfaces along with numerous other veins with irregular geometries in the upper part of the sample (Figure 124). At least one grey-green pseudotachylyte is also present. The grey-green pseudotachylytes are much less voluminous, are associated with cataclasites and epidote mineralisation, and are cross-cut by the black pseudotachylytes.

Figure 124. Photograph of a polished slice through sample SKZS.

The homogeneous, black pseudotachylytes were selected for dating due to their greater abundance and minimal evidence for alteration in hand specimen. The black pseudotachylytes form veins ≤20mm thick that have sharp edges which are mostly straight, except at branches or where thickness changes occur. Lithic clasts are rare in the black veins, ≤3mm long, and are consistently rounded. Two planar veins can be traced across the sample that are likely fragments of generation surfaces. Injection veins have a chaotic distribution, and appear to bound some large fragments of host rock. The black pseudotachylytes cross-cut host rock that has undergone grain size reduction in places, and has a weak foliation defined by aligned black minerals in one corner.

Thin section analysis shows that the pseudotachylyte in the black homogeneous veins is either microcrystallite rich, spherulitic, or aphanitic. Microcrystallites predominate in some of the pseudotachylytes comprising close to 100% of the vein fill in these veins (Figure 125). The microcrystallites are mostly colourless (PPL), or pale grey (XPL),

≤180µm long, ~5µm wide, and often form radial arrays around lithic clasts. Away from vein edges, brown microcrystallites are also present. The brown microcrystallites appear to be composed of sheaf-like bundles of exceptionally fine crystals that are ≤200µm long and fan-out to ≤100µm wide. Often the edges of the bundles are difficult to define as they are diffuse and closely spaced in regions between clasts. Spherulitic parts of veins are filled with orange-brown (PPL) microcrystallites ≤50µm long radially overgrowing lithic clasts. Some clasts have fringes of dark brown immediately adjacent to the clast edge, which is surrounded by orange-brown coloured crystals. Occasional bow-tie microcrystallites are present between the spherulites that are ≤50µm long. Aphanitic parts of veins have an aphanitic groundmass where the other types of vein fill have microcrystallites or spherulites, with the same morphology and clast composition as the other types. The aphanitic groundmass grades into microcrystallite-rich domains as the size and frequency of microcrystallites gradually increases.

Figure 125. Microcrystallites in SKZS have two compositions. Colourless acicular crystals radially overgrow lithic clasts (black arrow), and sheaf-like bundles of fine brown crystals (yellow arrow) are also present away from vein edges (PPL, field of view 1.6mm).

Though cryptocrystalline margins accompany many of the microcrystallite and spherulite veins, banding of the veins into ordered microcrystallite and spherulite domains does not occur within SKZS. All veins have rounded or embayed lithic clasts that are 0.01 to 0.85mm long that generally comprise ~20% of the vein fill. Most clasts are composed of fragments of recrystallised quartz (and possibly feldspars) with occasional calcite cements, but some are fragments of quartz, plagioclase feldspar, alkali feldspar or chlorite. Vesicles

are not developed in any of the veins. Vein margins are consistently sharp, but are irregularly shaped and are often embayed where the wall rock is composed of chlorite. Where adjacent to chlorite in the wall rock, the pseudotachylyte tends to have a slightly more red-brown colour (PPL) than where chlorite is not present.

SEM analysis of the pseudotachylyte veins in SKZS shows that two types of microcrystallite identified in thin section have different compositions (Figure 126a). Euhedral, acicular microcrystallites have a plagioclase feldspar composition similar to labradorite. These microcrystallites tend to overgrow plagioclase feldspar lithic clasts forming radial arrangements, and are also randomly oriented in spaces between clasts. The sheaf-like bundles of microcrystallites are also compositionally plagioclase feldspar, but are inter-leaved with layers of glass or cryptocrystalline material that contains iron and potassium. Microcrystallites in the spherulitic parts of veins mostly have a similar plagioclase composition to the sheaf-like bundles (Figure 126b). These microcrystallites are bow-tie shaped or form feather-shaped aggregates of tiny (~3μm) acicular crystals. Some euhedral plagioclase feldspar microcrystallites are also present around plagioclase clasts in the spherulitic domain. Aphanitic veins in thin section are filled with homogeneous masses of microcrystallites that are ≤5μm long (Figure 126c).

The pseudotachylytes in SKZS cross-cut host rock that is relatively undeformed. Feldspars are often fractured by both intra- and inter-crystalline fractures, which are mostly healed but with traces of chlorite along the fractures. Though the fractures often have small (<millimetres) of shear offset, the original feldspar crystal shape is usually recognisable indicating that the shear strain is small. Quartz generally displays undulose extinction and in some cases minor bulging recrystallisation along grain boundaries. Biotites and hornblendes are replaced with chlorite. Some localised zones of cataclasis are also cross-cut by the pseudotachylytes in which feldspars and quartz form angular fragments ≤250μm with a matrix of chlorite or calcite. However, the abundance of pseudotachylytes with various orientations means that the pseudotachylytes cross-cut the cataclasites in all cases, and no common orientation is present within the sample.

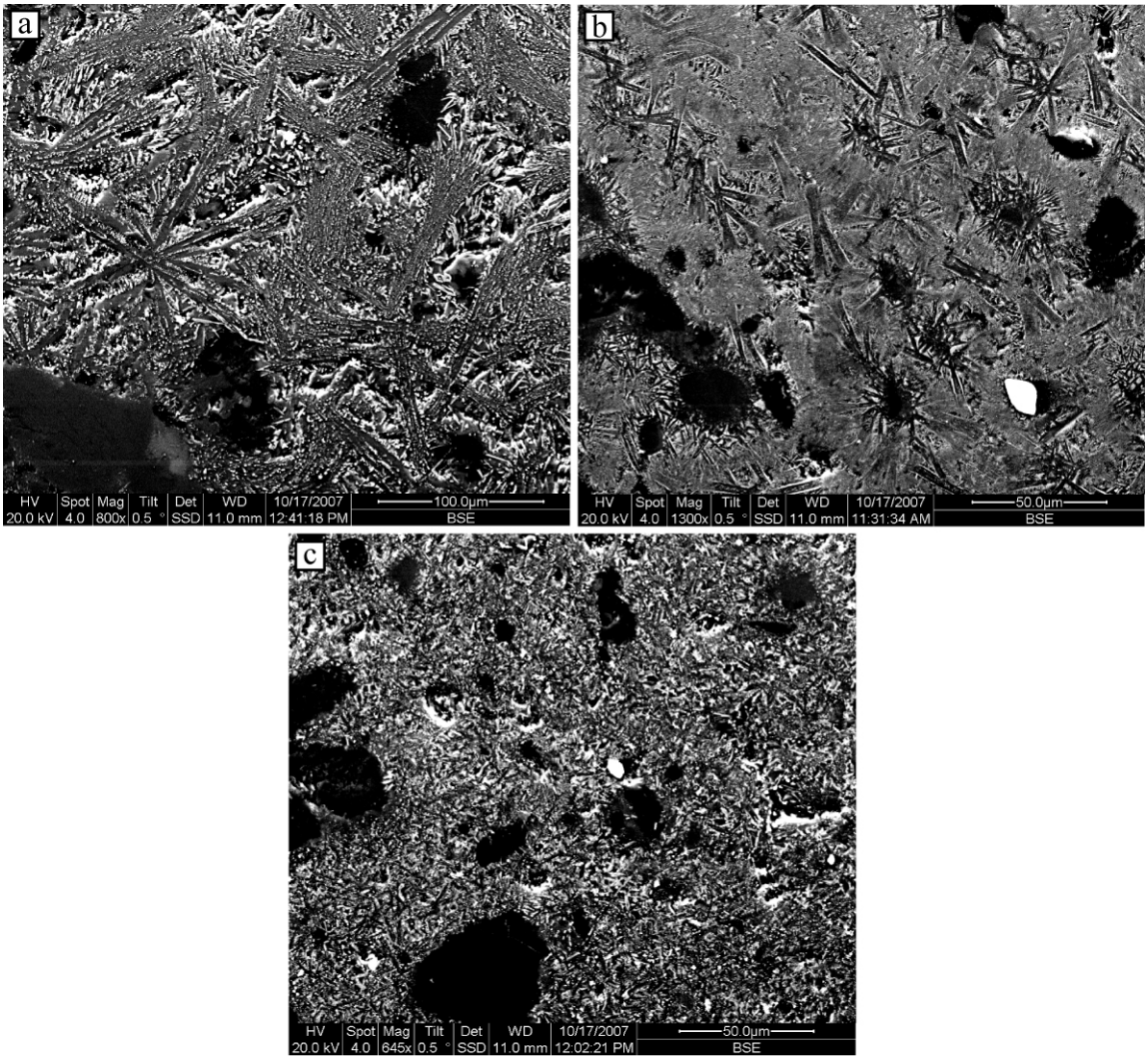

Figure 126. SEM back scattered electron (BSE) images of SKZS. a. Radial arrangements of plagioclase feldspar microcrystallites and sheaf-like bundles of plagioclase composition in the microcrystallite rich parts of the pseudotachylyte. b. BSE image of part of a spherulitic domain showing small bundles of plagioclase feldspar microcrystallites around plagioclase lithic fragments and bow-tie and microcrystallites. c. Veins that are aphanitic in thin section are composed of masses of microcrystallites ≤5µm long.

6.3.3.4 GPP1 and GPP3 – host rocks

GPP1 and GPP3 are samples of undeformed host rock collected from locality 35. The host rock is the Pyramid Pluton, a medium grained granodiorite. A full description of the host rock is provided in section 4.4. Both samples are unoriented and were collected from a locality where recent trail maintenance had created fresh exposure, minimising the effects of surface weathering.

Biotites separated from the hand specimen (see section *6.3.4.1* for method) were euhedral, black crystals 2 to 10mm in length. Most crystals were formed of stacks of biotite sheets with an approximately hexagonal shape. Some crystals were slightly folded or kinked, but

otherwise were undeformed. In thin section some of the biotites have fringes where they are replaced with chlorite, and apatite and zircon inclusions are common.

Hornblendes separated from samples GPP1 and GPP3 were small (0.4 to 1mm long) crystals that had irregular shapes due to fracturing, likely incurred during the sample preparation. The crystals were dark grey, and tended to be tabular or prismatic. Thin section analysis of the host rock shows that hornblendes are ≤5mm long, and contain inclusions of euhedral zircons and opaque minerals. Pyroxene is present towards the centre of some hornblende crystals, and the hornblende is replaced with biotite and chlorite around some crystal edges.

The composition of the hornblendes is particularly important to the K-Ar analysis as the relatively low concentration of potassium within hornblende makes the analysis sensitive to variations in the K wt% estimate. SEM back scattered electron images of hornblendes picked from the separated crystals show that some compositional variation is present in the crystals, which will likely affect the potassium content (Figure 127). However, the compositional domains are not systematically related to crystal size, shape, cleavage orientation or the geometry of fractures in the crystals.

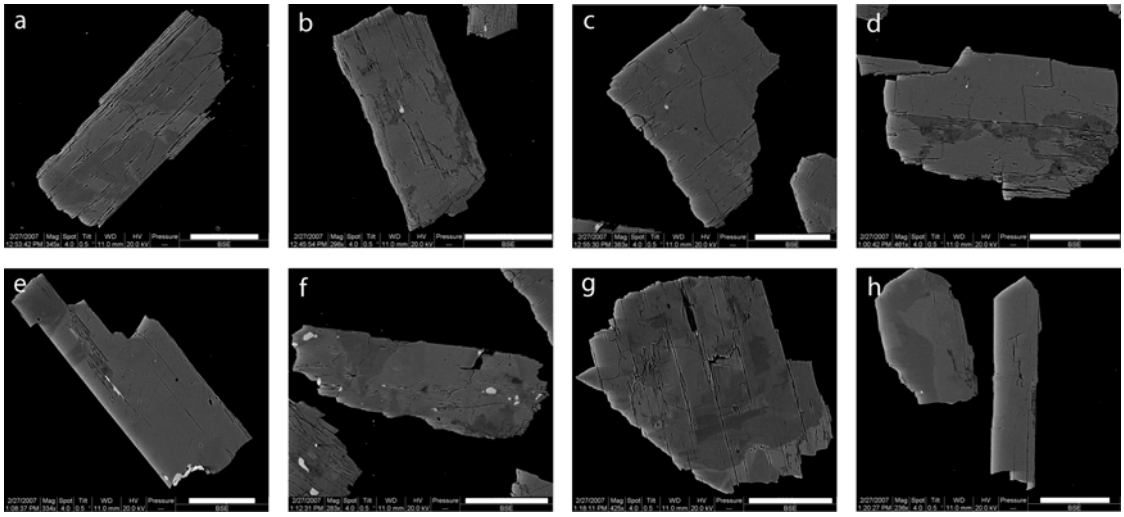

Figure 127. SEM electron back scatter (BSE) images of typical hornblende crystals that were analysed for K content with an electron probe microanalyser. Shades of grey represent differing chemical composition, but show no systematic correlation with crystal size or shape (scale bars in white are 200µm for a, c, d, e, g, and 300µm for b, f and h).

6.3.4 Analytical procedure

Pseudotachylyte material was separated from samples SKR and SKZS by crushing the bulk samples into fragments 1-5mm in size. Particles of pseudotachylyte were then hand-picked so that fragments containing one or more visible clasts, or with host rock material

still attached, were discarded. Sample SKL contained a single pseudotachylyte vein that was thick enough to enable material to be cut from the sample using a small rock saw. All of the separated pseudotachylyte samples were ground up and sieved. The 63-105μm fraction was selected for analysis as this is the most suitable size range to ensure individual grains derived from the extremely fine-grained pseudotachylyte would be compositionally homogeneous.

Biotite and hornblende crystals were separated from samples GPP1 and GPP3 by crushing the samples and picking under a binocular microscope. Only large, euhedral and undeformed crystals that lacked inclusions and attached fragments of crystals of different compositions were selected. The samples were then washed in de-ionized water and acetone and placed in an ultrasonic bath for 30 minutes.

The samples were analysed in the NERC Argon Isotope Facility (AIF) at the Scottish Universities Environmental Research Centre, East Kilbride, UK. The ^{40}Ar abundance was determined using the isotope dilution method, with ^{38}Ar as a tracer. Argon isotopic ratios were measured with a modified MAP 215-50 mass spectrometer. Each of the pseudotachylytes provided three duplicate aliquots for argon analysis that were weighed and wrapped in copper foil. Biotite analyses comprise three aliquots from GPP1, and 6 from sample GPP3. Hornblendes were analysed with 4 aliquots from GPP1 and two from GPP3.

The samples were analysed in two batches at the AIF. In each case, all packets were loaded into a glass tree along with packets containing standards HDB1, Bern 4m, GL-0 and BS133 which were used for instrument calibration. Individual packets were heated in a double-vacuum resistance furnace to ~1530°C for 10 minutes to achieve total melting. Gas released by fusion of each sample was purified using a combination of a CapaciTorr B200 getter at ~250°C to remove chemically active gases (CO_2, O_2, N_2, etc.), and a finger containing zeolite cooled to -78°C with an acetone-dry ice slush trap to remove water and hydrocarbons. The ^{38}Ar spike was introduced by a calibrated pipette system enabling a known amount of ^{38}Ar to mix with the sample gas. Further sample purification was achieved through a combination of two Zr-Al GP50 getters at room temperature and one at 250-300°C, removing any remaining chemically active gases. After cleaning, the sample gas was expanded into an MAP-215 mass spectrometer in static mode and the argon isotope ratios were measured.

Instrumental mass discrimination was checked by analysis of air samples immediately following each sample to date. Background levels of argon and spike composition and sensitivity were monitored by concurrent analyses of blanks of the mass spectrometer and the extraction line and isolated spikes. Ages were calculated, after correcting for machine mass discrimination and system blanks, using the decay constants of Steiger and Jager (1977). Analytical errors based on uncertainties in Ar, K and mass measurements were then estimated for each individual age using the K-Ar Age Program for USGS Digital Data Systems, written by G. B. Dalrymple, 1988, following the method of Cox and Dalrymple (1967) and Dalrymple and Lanphere (1969). The standard deviation of analytical precision (σ) is calculated by:

$$\sigma \cong \left[(\sigma_k)^2 + (\sigma_x)^2 + (\sigma^{40/38})^2 \left(\frac{1}{r}\right)^2 + (\sigma^{36/38})^2 \left(\frac{1-r}{r}\right)^2 \right]^{1/2} \qquad \textbf{Equation 10}$$

where σ_k is the standard deviation of the potassium analyses, σ_x is the standard deviation of the tracer calibration, $\sigma^{40/38}$ standard deviation of the mass-spectrometer measured ratio $^{40}Ar/^{38}Ar$, $\sigma^{36/38}$ is the standard deviation of the measured $^{36}Ar/^{38}Ar$ and r is the fraction of ^{40}Ar that is radiogenic. Values of 0.5% for σ_k, 0.3% for σ_x are derived from repeated measurements of standards in the XRF facility (see below) and on international standard biotites respectively (Dalrymple and Lanphere, 1969). Argon isotope ratio errors are calculated from a least squares regression of the mass spectrometer measurements assuming error only in the intensity of the measurements, and calibrated by concurrent analyses of blanks and isolated spikes.

The potassium content of the biotite and pseudotachylyte samples was measured from 1g packets at the University of Edinburgh using X-ray fluorescence (XRF). Hornblende potassium contents were established by analysing crystals with a Cameca SX100 electron probe microanalyser at the University of Strathclyde. More than 30 hornblende crystals were selected from samples GPP1 and GPP3 by picking under a binocular microscope in the same way as for the argon analyses. The two groups of crystals were mounted for the probe and at least 100 compositional analyses were carried out at random spatial positions within each crystal population to provide a statistically significant data set.

6.4 Results

6.4.1 K-Ar results

In total twenty four aliquots were analysed by the isotope dilution method yielding nine biotite K-Ar ages, six hornblende ages and three ages for each of the three pseudotachylytes (Table 7). Analytical errors are given as absolute values and as percentages of the calculated ages, and 1σ determined from the duplicate aliquots is used as an overall uncertainty on the ages. The full results of XRF analyses of the pseudotachylyte and biotite samples are included in Appendix 4.

Sample	$^{40}Ar_{AIR}$ (%)	K_2O (wt%)	Mass (g)	^{40}Ar (mol/g), x10^{-10}	$\sigma^{40/38}$ (%)	$\sigma^{38/36}$(%)	$^{40}Ar/^{40}K$, x10^{-3}	Age, Ma	Error, Ma
BIOITITE									
GPP1 (21)	2.358	8.84	0.01465	10.38	0.2828	40	4.738	79.76	1.030
GPP1 (20)	5.588	8.84	0.01712	11.78	0.2828	13.33	5.379	90.29	1.042
GPP1 (22)	1.896	8.84	0.03227	11.07	0.2828	33.33	5.054	84.96	0.898
GPP3c (18)	1.38	8.881	0.01272	11.54	0.2828	50	5.249	88.15	0.973
GPP3a (14)	1.36	8.625	0.01375	10.82	0.2828	50	5.064	85.11	0.934
GPP3c (17)	1.205	8.881	0.01467	11.33	0.2828	50	5.149	86.51	0.904
GPP3b (16)	2.662	8.782	0.01324	10.68	0.2828	33.33	4.907	82.54	1.031
GPP3a (13)	0.6575	8.625	0.01566	10.99	0.2828	66.67	5.142	86.41	0.826
GPP3b (15)	1.442	8.782	0.01258	11.13	0.2828	50	5.117	86.00	0.969
							Average age (Ma):	**85.5**	
							Standard Deviation:	**3.0**	
							%RSD	**3.6**	
HORNBLENDE									
GPP3h (22)	7.962	0.530	0.04964	0.8941	0.2828	33.33	6.803	113.4501	4.111
GPP1h (19)	6.387	0.497	0.05098	0.8435	0.2828	40	6.856	114.3085	4.012
GPP3h (23)	7.874	0.530	0.10031	0.884	0.2828	20	6.726	112.1967	3.045
GPP1h (20)	7.433	0.497	0.10115	0.8011	0.2828	22.22	6.511	108.724	3.021
GPP1h (21)	7.842	0.497	0.15098	0.793	0.2828	15.39	6.445	107.6543	2.680
GPP1h (24)	7.739	0.497	0.14952	0.8931	0.2828	14.29	7.259	120.8098	2.937
							Average age (Ma):	**112.9**	
							Standard Deviation:	**4.7**	
							%RSD	**4.2**	
MELT									
SKL (17)	3.794	3.87	0.01525	4.329	0.2828	50	4.513	76.05	1.670
SKL (18)	3.621	3.87	0.02973	4.208	0.2828	33.33	4.388	73.98	1.126
SKL (19)	4.352	3.87	0.04779	4.239	0.2828	16.67	4.42	74.51	0.844
							Average age (Ma):	**74.9**	
							Standard Deviation:	**1.1**	
							%RSD	**1.4**	
MELT									
SKR (14)	18.74	4.02	0.01561	4.796	0.2828	11.11	4.815	81.02	2.201
SKR (15)	21.72	4.02	0.03169	4.457	0.2828	5.132	4.474	75.40	1.257
SKR (16)	19.39	4.02	0.05130	4.631	0.2828	3.083	4.649	78.29	0.888
							Average age (Ma):	**78.2**	
							Standard Deviation:	**2.8**	
							%RSD	**3.6**	
MELT									
SKZS (11)	3.445	3.66	0.01615	4.64	0.2828	50	5.116	85.97	1.734
SKZS (12)	3.765	3.66	0.03158	4.547	0.2828	25	5.013	84.29	1.092
SKZS (13)	4.363	3.66	0.04939	4.491	0.2828	15.39	4.952	83.28	0.912
							Average age (Ma):	**84.5**	
							Standard Deviation:	**1.4**	
							%RSD	**1.6**	

Table 7. K-Ar results. Columns indicate measured values of atmospheric Ar ($^{40}Ar_{AIR}$), K concentration, aliquot mass and measured ^{40}Ar that were used to calculate the age of each sample. Values for $\sigma^{40/38}$ and $\sigma^{38/36}$ were used to calculate errors, as described in the text. Biotite and melt K contents were measured by XRF, with an associated analytical error of 0.5%.

Calculated host rock biotite ages range between 79.76 ± 1.03 and 90.29 ± 1.04Ma with a mean age of the nine analyses of 85.53 ± 3.05Ma (Figure 128). All analytical errors were less than ~1Ma, or 1.29% indicating consistent analytical conditions. K values for the biotites ranged from 8.625 to 8.881 wt% showing a degree of variation existed between aliquots. However, the range of calculated biotite ages does not correlate with the K variation; both the oldest and youngest calculated ages are from aliquot GPP1. Two data points are outside the 1σ deviation from the mean, both of which are from sample GPP1. Calculated hornblende ages range between 108 ± 2.68 and 121 ± 2.94Ma with an average of 113 ± 4.70Ma from the population of 6 aliquots. Analytical errors are ≤3.62%, a higher value than the biotites which reflects the smaller amounts of K and radiogenic Ar in the crystals. Two aliquot ages lie outside 1σ of the population, though one of these is within error of the minimum 1σ value.

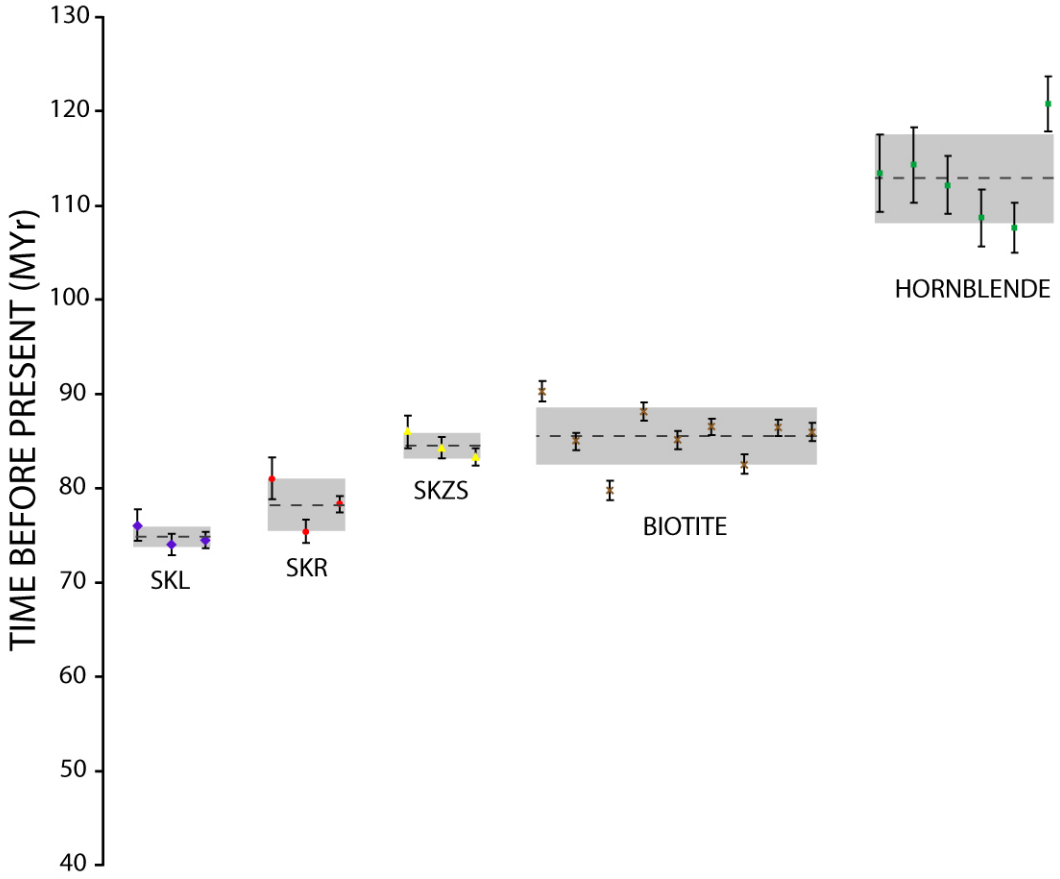

Figure 128. Box-plot of the calculated ages for each of the aliquots analysed. Data points are arranged into groups representing the sample from which the aliquots are derived. Error bars are the analytical error associated with the age calculation, grey boxes indicate 1σ derived from all ages from each sample.

The three pseudotachylyte samples each provided three duplicate aliquots that yielded mean ages of 74.9 ± 1.07Ma (SKL), 78.2 ± 2.81Ma (SKR), and 84.5 ± 1.36Ma (SKZS)

with 1σ encompassing the range in the three aliquot ages for each sample. Analytical errors were all less than 2.72% again suggesting consistency in the analytical conditions.

6.4.2 Hornblende K analysis results

In total 103 individual analyses of GPP1 and 117 analyses of GPP3 were undertaken with the electron probe microanalyser. The sampling pattern was random with respect to the compositional variation; points selected for the compositional analyses were taken from all parts of the grains (Figure 129a). As the compositional variations observed in the hornblendes do not correlate with crystallography, the sampling pattern should fully represent the population of potassium concentrations in the samples. Intra-grain variation is present within all of the analysed grains (Figure 129b); the maximum range in one grain with three or more spots is 0.435wt% and the minimum is 0.04wt%.

The distribution of potassium concentrations for the populations of grains from GPP1 and GPP3 are very similar; both show a slightly bimodal distribution of K wt% within the range of around 0.05 to 0.8 wt% (Figure 130). The mean, median and standard deviation of the two sets of data are also very similar suggesting that there is little difference in the potassium content between the two samples. Though the variability in the parent nuclide (in this case K) content has a significant influence on the age calculation for the K-Ar method (see Equation 9), the method requires a representative value of K content as the daughter (Ar*) is measured from aliquots containing a large number of grains. The Ar* measurements are not sensitive to the intra-crystalline K variation, which would also effect the Ar content. The aliquots analysed for Ar in this study contained tens of grains, so the measured Ar values are directly comparable to a K value determined from 30 grains from each of GPP1 and GPP3. The mean potassium concentrations were therefore used to calculate the ages of the hornblendes.

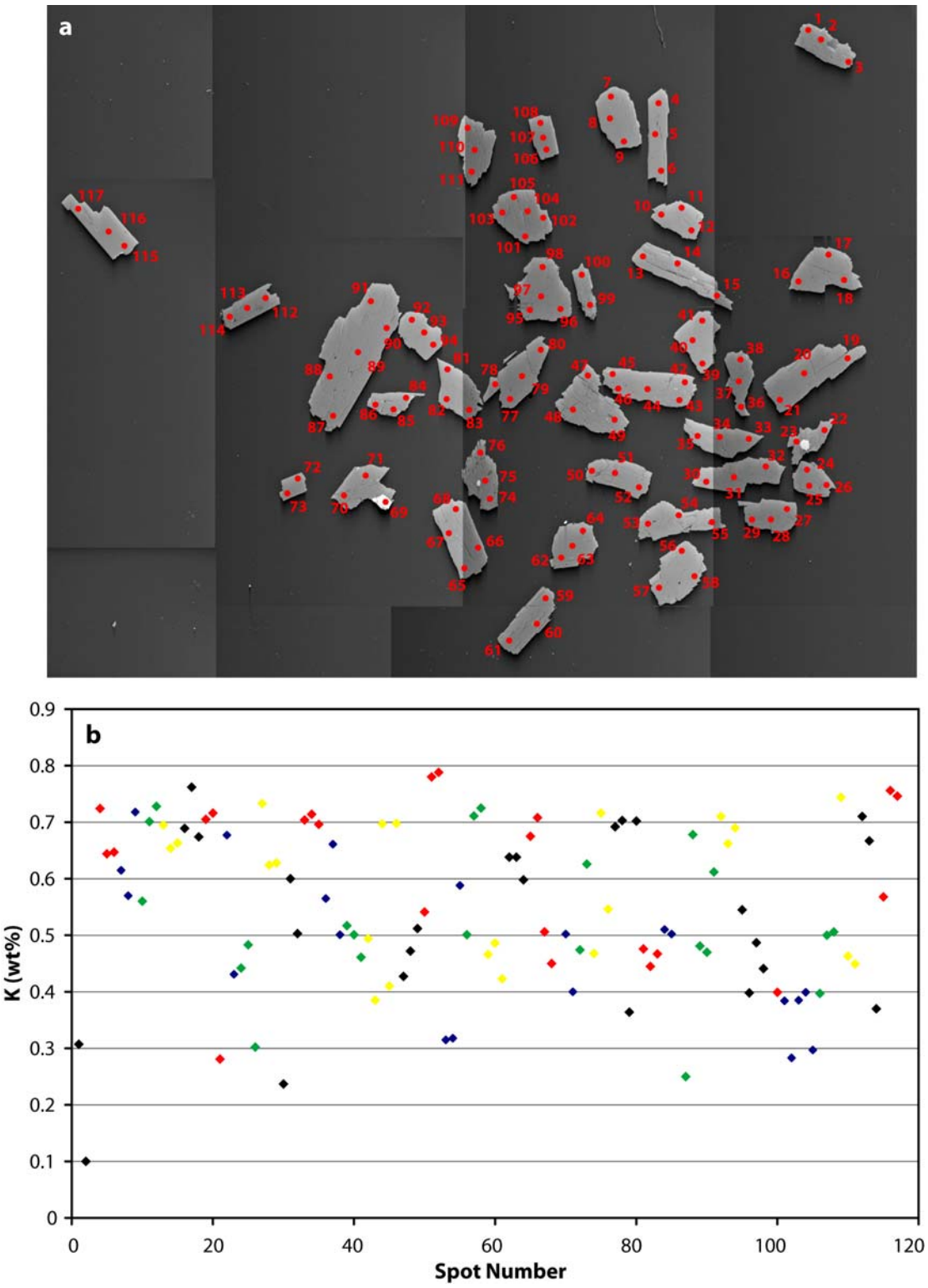

Figure 129. a. Back scattered electron (BSE) image of the hornblende grains analysed from sample GPP3 (field of view ~9mm). Red spots and corresponding number indicate the spots analysed with the electron probe analyser. b. Plot showing the intra-grain variability of the K content of the hornblende grains within sample GPP3. Data points from the same crystal are shown in the same colour (spot numbers correspond to those shown in a.), the colour for each grain alternates between black, red, blue, green, yellow.

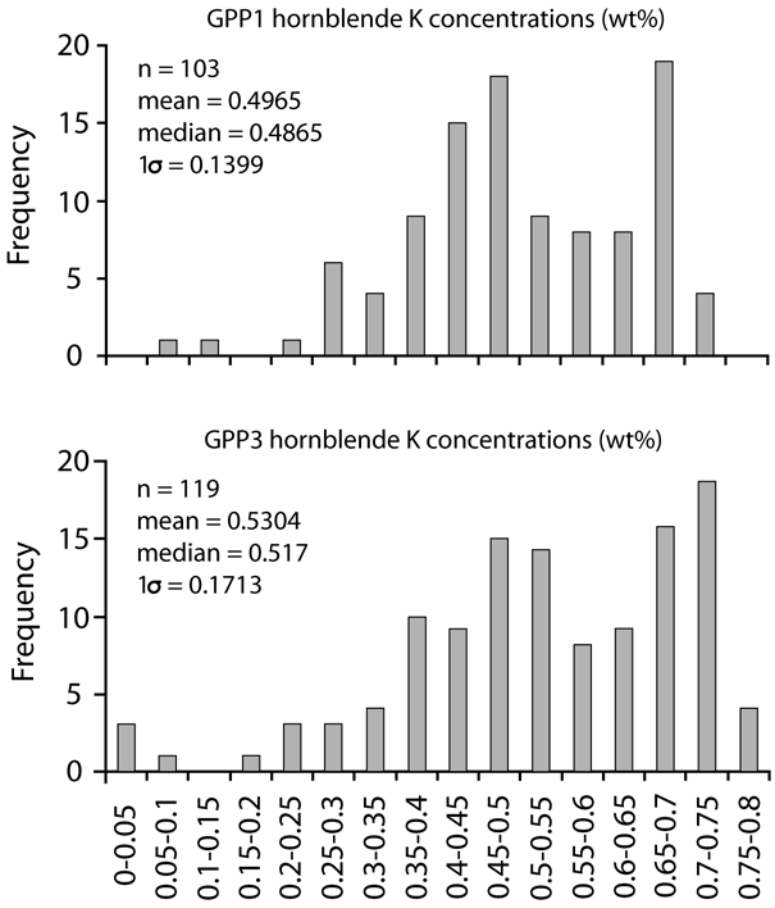

Figure 130. Histograms of hornblende K concentrations (wt%) for two populations derived from the host rock samples GPP1 and GPP3. Frequency distributions are similar for the two populations, which is reflected in the similarities in the mean, mode etc and 1σ. Concentration bins are of the form a < - ≤ b where a and b are concentrations (wt%).

6.5 Discussion

6.5.1 Pluton cooling

Samples GPP1 and GPP3 were taken from fresh exposures at locality 35, approximately 80m away from any mapped faults. As the macro-scale fault zone widths defined in Chapter 3 are generally ≤30m, the samples should not have been influenced by fault activity. Processes such as intra-crystalline deformation in quartz, fracturing, and fluid flow and alteration inferred from observations in Chapter 4 are therefore all inherent to the evolution of the Pyramid pluton, regardless of tectonic activity.

The calculated ages for the Pyramid pluton biotite and hornblende separates represent the times at which the crystals last cooled below the closure temperature of the minerals with respect to Ar (Figure 131). If the samples, and therefore the pluton, cooled from crystallisation temperatures to the modern low temperature without significant re-heating

by metamorphic events, then the discordant ages of the sample minerals can be used to construct a cooling history for the pluton (T-t diagram; Figure 131). Metamorphic rocks are present in the central Sierra Nevada. These rocks are mostly roof pendants that represent the remnants of country rock volcaniclastic during the Mesozoic Nevadan orogeny (Bateman, 1992). Some Cretaceous metavolcanic rocks, including tuffs and other pyroclastic strata, were also deposited during the orogeny. However, these rocks are only preserved as narrow seams between the plutons in the study area (Moore, 1978). The Pyramid pluton does not show any evidence for metamorphic recrystallisation, implying that the pluton has not undergone any significant regional metamorphism. Field relations show that the Pyramid pluton is not the youngest pluton in the study area (Moore, 1978). It is therefore possible that later intrusion of an adjacent pluton could have re-heated the Pyramid pluton. Locality 35 is ~900m from the nearest edge of the Pyramid pluton in map view, and is in fact close to the long-axis of the elongate pluton, minimising to as great an extent as possible the effects of re-heating by nearby pluton emplacement.

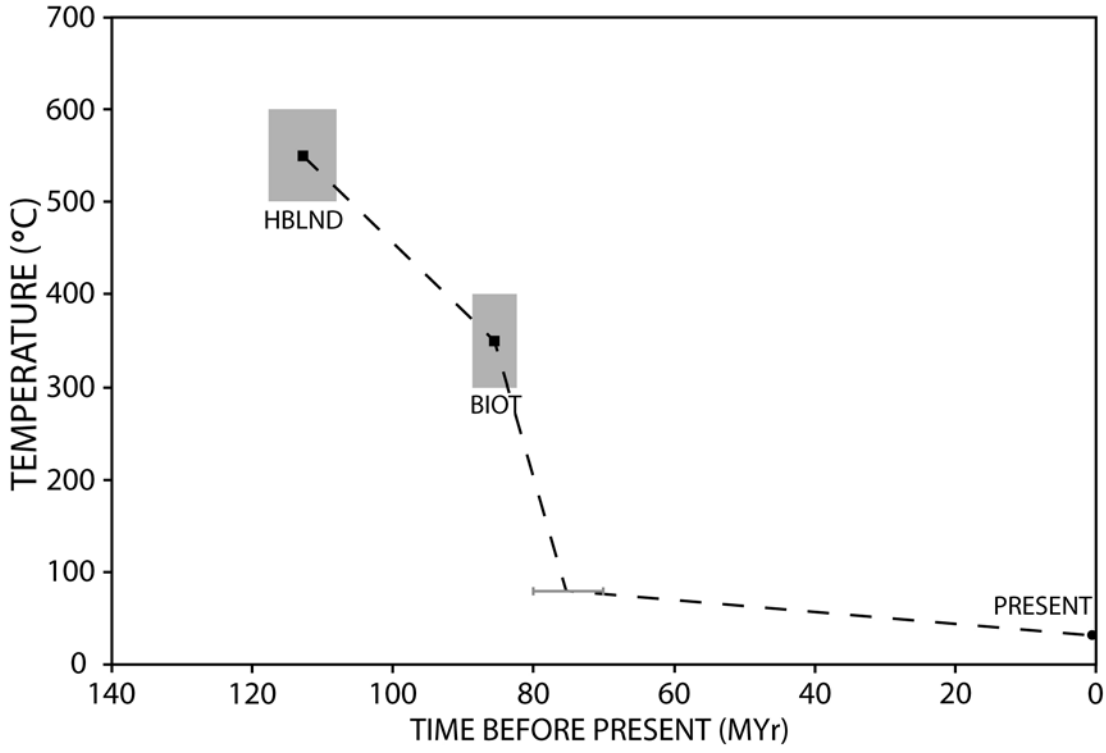

Figure 131. T-t cooling curve for the pyramid pluton defined by the discordant ages of hornblende and biotite. The approximate range of apatite (U-Th)/He ages calculated by House *et al.* (2001) and Clark *et al.* (2004) is shown by the horizontal bar; the closure temperature of apatite for the (U-Th)/He thermochronometer is around 80ºC.

The hornblende and biotite ages can be used as thermochronometers as long as the assumptions in the K-Ar method outlined in section *6.3.2.1* are evaluated. The reliability and accuracy of the analytic facility were consistent throughout the investigation. Analytical uncertainties were all of the order of a few percent, and duplicate aliquots

yielded ages that give 1σ of <4.2% for each of the samples. Contamination of the samples with atmospheric Ar was minimised by baking the aliquots at 100ºC for several days prior to fusion. Any sample or line contamination was corrected for by concurrent blank analyses. The decay constants of Steiger and Jager (1977) are international standards.

Closure temperatures are a function of the diffusivity of Ar within a particular mineral phase, and are dependent on a number of factors including grain size, cooling rate, pressure and to an extent composition (Dodson, 1973; Grove and Harrison, 1996; Harrison *et al.*, 1985; Hess *et al.*, 1993). Assigning a discrete closure temperature to mineral separates that cooled naturally is therefore problematic. However, experimental studies constrain closure temperatures for particular minerals by controlling the environmental parameters. Berger and York (1981) and Harrison *et al.* (1985) analysed biotites and showed that closure temperatures for Ar range from 280 to 400ºC, which is represented in Figure 131 by an uncertainty in the vertical axis (temperature). Similarly, Harrison (1981) showed that the closure temperature of hornblende with respect to Ar is 490 to 580ºC. The absolute closure temperatures for the minerals analysed in this study cannot be determined, especially as both biotites and hornblendes are affected by intra-crystalline alteration in the host rock, but the uncertainty that surrounds the closure temperatures is accounted for by assigning suitable errors in the temperatures to the T-t diagram.

The calculated ages of the hornblende and biotite separates indicate that the Pyramid pluton was emplaced in the mid Cretaceous. Two K-Ar ages of biotites from plutons near to the Pyramid pluton have been reported; the Cartridge Pass granodiorite cooled through the biotite closure temperature at 81 ± 3Ma (Dodge and Moore, 1968), and the LeConte Canyon alaskite biotites cooled at 80 ± 0.24Ma (Evernden and Kistler, 1970). The Pyramid pluton biotites are therefore several million years older than the biotites in these plutons, which agrees with the order of pluton emplacement defined by field relations (Moore, 1978). Additional constraints can be placed on the temperature evolution for the pluton after the temperature dropped below the biotite closure temperature by using different thermochronometers. House *et al.* (2001) and Clark *et al.* (2004) dated apatite crystals with the (U-Th)/He method, which has a closure temperature of around 80ºC. Their results show that apatites sampled at the same elevation as the Pyramid pluton in the study area are around ~72 ± 8 Ma and 80Ma respectively. These data indicate that the Pyramid pluton cooled rapidly from around 300ºC to less than 100ºC.

Pluton name	$^{206}Pb/^{238}U$ age in Ma (zircon)	K/Ar age in Ma (hornblende)	$^{40}Ar/^{39}Ar$ age in Ma (hornblende)	700–500 °C interval in m.y.	Cooling rate (°C Ma^{-1})	Source of data*
Gateway	116.7	103	N.D.†	14	14	(i)
Bass Lake	115§	109#	N.D.	6	33	(i)
Dinkey Creek	104.1	95	N.D.	9	22	(i), (ii)
Dinkey Creek	102 ± 1	N.D.	94	8	25	(iii), (iv)
Shuteye Peak	102	N.D.	98	~5	40	(i) and (v)
Illilouette Creek	99 ± 1	N.D.	94.5	~5	40	(v)
Jackass Lakes	98.1	95	N.D.	3	67	(i)
Red Devil Lake	97.7	87	N.D.	~11	18	(i)
Red Devil Lake	95 ± 1	N.D.	87	~8	25	(v)
Lake Edison	89.8 93.2	85	N.D.	~5 ~8	40 25	(i)
Lake Edison	88 ± 1	N.D.	86.8	1.2	167	(v)
Mount Givens	87.9 & 92.8**	88 & 89**	N.D.	~1 and ~3	~67	(i)
Mount Givens	90 ± 0.75	N.D.	89.7	~1	200	(iii), (iv)
Mount Givens	90 ± 1	N.D.	82.5	7.5	27	(v)
Lamarck	89.6	90 86	N.D.	~1 ~4	200 50	(i)
Cathedral Peak	86.2	86	N.D.	~1	200	(i)

Table 8. Compiled ages and cooling rates between 500 and 700ºC for various plutons in the central Sierra Nevada defined by zircon and hornblende ages, after Tobisch et al. (1995). *Sources are (i) Stern *et al.* (1981); (ii) Kistler *et al.* (1965); (iii) Tobisch *et al.* (1993); (iv) Renne *et al.* (1993) and (v) Tobisch *et al.* (1995). †N.D. = no data, § average of eight, # average of four, **not taken from same samples.

The closure temperatures and discordance in the calculated ages of the hornblende and biotite samples define the cooling rate of the pluton. The pluton cooled from ~550ºC to ~350ºC in around 28Ma, at a rate of ~7.1ºC Ma^{-1}, with maximum and minimum cooling rates predicted from the uncertainties in the ages and closure temperatures of 15.3ºC Ma^{-1} and 2.9ºC Ma^{-1} respectively. As a means of verifying the validity of this estimate, the decrease in temperature may be related to cooling due solely to exhumation. For a geothermal gradient of ~30°C/km, the temperature decrease would require exhumation of ~6-7km in ~28Ma at a rate of 240m/Ma (0.24mm yr^{-1}). This value is similar to erosion rates of 0.04 to 0.06mm yr^{-1} calculated for the Kern River canyon (Clark *et al.*, 2004), and is much less than 5km/Ma inferred from the Taiwan Central Range (Willett *et al.*, 2003)

suggesting that the estimated cooling rate for the Pyramid pluton is not unreasonable. Cooling rates have also been inferred for other plutons in the central Sierra Nevada. Using a closure temperature of 700±50°C for Pb* in zircon (Mattinson, 1978) and 500±50°C for Ar* in hornblende (Baldwin *et al.*, 1990) the time taken to cool from 700-500°C may be defined (Tobisch *et al.*, 1995). Table 8 shows the cooling rates in this temperature range are faster than the calculated rates for the Pyramid pluton, though faster rates should be expected at higher temperatures, and emphasises the need for thermochronometric constraints sensitive to lower temperatures.

6.5.2 Pseudotachylyte ages

6.5.2.1 Interpreting the calculated ages

The interpretation of the calculated ages for the three pseudotachylyte samples requires the assumptions inherent to the K-Ar isotopic method to be evaluated. Again, some of the conditions that must be met are dependent on the reliability and accuracy of the analytical facility. Contamination of the sample by atmospheric Ar was minimised by baking all of the aliquot packets for several days under high vacuum conditions before the analyses, and corrected for by concurrent blank analyses. Analytical uncertainties associated with the calculated ages are all low, suggesting consistent and accurate instrument measurements.

The application of the K-Ar isotopic method to dating pseudotachylytes is particularly complicated as the material that comprises each aliquot is composed of a mixture of melt-derived glass and lithic clasts of various compositions (Figure 132). Tectonic pseudotachylyte generation occurs during short duration, high temperature slip events that cause localised melting along a frictional surface. The composition of the melt is therefore a function of the host rock composition, which for a granodiorite has a relatively high potassium concentration. Pseudotachylytes should therefore be suitable for K-Ar analysis. However, the transient heat increase associated with pseudotachylyte generation, along with physical and chemical changes that can occur within both clasts and melt mean that the mobility of K and Ar within the pseudotachylyte system must be assessed.

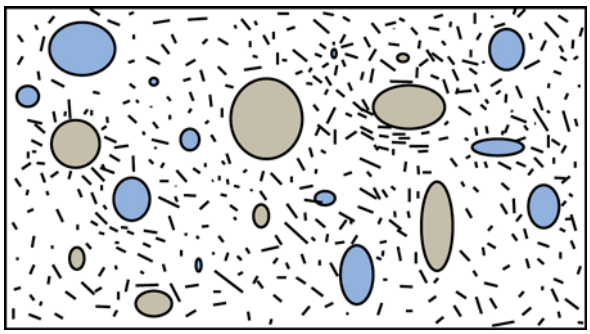

Figure 132. Schematic representation of a pseudotachylyte; lithic clasts of more than one composition are contained within a groundmass of melt-derived glass.

Pseudotachylyte glasses form when friction-induced melt is quenched, but are rarely composed of purely amorphous material. Instead the glasses contain aggregates of microcrystallites that are generally up to hundreds of microns in length. However, studies have shown that glassy rocks, in particular pillow basalts (e.g. Dalrymple and Moore, 1968; 1981; Seidemann, 1977), and also pseudotachylytes retain Ar (e.g. Di Vincenzo *et al.*, 2004; Magloughlin *et al.*, 2001; Sherlock and Hetzel, 2001; Warr *et al.*, 2007). The decay of ^{40}K to ^{40}Ar should therefore cause Ar* to accumulate in a pseudotachylyte. For pseudotachylyte to be useful as a geochronometer, the melt must not retain any Ar that formed prior to the slip event. As Ar is a noble gas, any existing Ar is likely to escape from host rock crystals into a volatile phase upon melting rather than be retained in the melt phase. The high temperatures and low viscosity of pseudotachylyte melts, and low pressures induced by slip-related dilation inhibit Ar solubility in the melts (Sherlock and Hetzel, 2001). Complete out-gassing of pre-existing Ar from the pseudotachylyte should therefore be achieved. Reimold *et al*. (1990) modelled the diffusion behaviour of Ar in glass and showed that Ar loss by diffusion is negligible below ~150ºC. As pseudotachylytes quench rapidly, the pseudotachylyte glass will quickly become a closed system to Ar and a calculated pseudotachylyte age could accurately reflect the age of a slip event as long as no subsequent re-heating events occur.

Post-solidification processes may also influence the mobility of both Ar and K in a pseudotachylyte glass. Devitrification of glass involves chemical rearrangement of the constituents of the glass into a crystalline form. As Ar is not chemically bonded to the glass, any physical disturbance is likely to cause Ar loss. Hydrothermal alteration of a glass usually results in the glass being replaced with chlorite, epidote, calcite or zeolites depending on the host rock mineralogy and/or composition of hydrothermal fluids. Hydrothermal alteration may cause either Ar loss (Sherlock and Hetzel, 2001) or Ar enrichment (Seidemann *et al.*, 1984) in a glass. It is also possible that K can be added to a

glass, though this requires a the presence of a K-rich fluid phase which is typically associated with sea water (e.g. Seidemann, 1977).

Lithic clasts contained within pseudotachylytes can have a variety of compositions as they are fragments of the host rock. Consequently, the K content of the lithic clasts may be more or less concentrated than in the pseudotachylyte glass. The rate of Ar* production is therefore likely to be different for different components of the pseudotachylyte system. When applied to pseudotachylytes, the K-Ar method is a bulk dating technique that determines a combined age for all of the components present in a pseudotachylyte. This poses a significant problem when minerals with high K concentrations comprise lithic clasts; in the case of the studied samples, alkali feldspars are present as clasts.

Pseudotachylyte clasts are likely sources of inherited Ar; they are fragments of wall rock that formed as the host pluton crystallised and so potentially contain Ar* produced prior to the pseudotachylyte generating event. A number of studies have suggested that the rapid heating and cooling associated with pseudotachylytes is insufficient to completely degas lithic clasts in a melt (Di Vincenzo *et al.*, 2004; Magloughlin *et al.*, 2001; Warr *et al.*, 2007). The clasts may therefore contain Ar* produced *in-situ* within the clast from before as well as after the slip event. Mantle-derived Ar incorporated into the crystals during pluton crystallisation may therefore also be retained in lithic clasts, especially in fluid inclusions in quartz or feldspars. Some clasts, especially hornblende or biotite fragments, will also be susceptible to the effects of hydrothermal alteration as outlined for glass above.

Given the numerous factors that complicate the interpretation of the pseudotachylyte ages, there are a large number of possible changes to the Ar and/or K isotopes that could cause the calculated ages to be either apparently too old, or apparently too young. However, the host rock lithology and tectonic setting suggest that there are several scenarios that are likely to be appropriate to the pseudotachylyte samples analysed in this study (Table 9). These scenarios differ according to the relative enrichment or depletion of either ^{40}K or Ar* in each of the pseudotachylyte system components, and whether each of the components is completely degassed (reset) at the time of pseudotachylyte generation. Note that even in the case where the both glass and clasts are completely reset by the melting event, the calculated age is older than the age of the slip event due to the presence of clasts with a higher K concentration than the glass. Evaluation of the likelihood of each of the

scenarios applying to the pseudotachylyte samples requires examination of the geologic properties of each sample.

	Matrix	Clasts	Likely Effect		
			K	Ar*	Overall
1	Reset	Reset	-	-	Old
2	Reset	Inherited Ar	-	Enriched	V. Old
3	Dissolved Ar	Inherited Ar	-	Enriched	V. Old
4	Devitrified	Inherited/reset	-	Depleted	Young
5	Altered/replaced	Altered	Either	Depleted	Young/Old

Table 9. A list of the most likely scenarios that could have caused the pseudotachylyte system to be enriched or depleted with K or Ar*, causing the calculated pseudotachylyte ages to be apparently too young or apparently too old.

6.5.2.2 The geologic evidence

Section 6.3.3 provides detailed descriptions of the three pseudotachylyte samples at hand specimen, thin section and SEM scales. The relative probability of the scenarios outlined in Table 9 based on the geologic observations are summarised in Table 10.

The pseudotachylyte glass in sample SKL is exceptionally well preserved; extremely fine microcrystallites of plagioclase feldspar (many ≤25μm) are abundant, and are undisturbed by devitrification or alteration products. The proportion of glass that is cryptocrystalline groundmass is very small, so alteration of the groundmass alone will have little effect on the composition of the glass. Sample SKZS contains microcrystallites that have differing habits, but which are compositionally similar. Plagioclase feldspar microcrystallites are arranged into microcrystallite-rich, spherulitic, and aphanitic domains. The domains show no evidence for significant alteration, and the preservation of exceptionally small (≤5μm) microcrystallites in the aphanitic domains suggests that devitrification effects are negligible. SKR is the only sample in which alteration and replacement of the groundmass with epidote, chlorite and alkali feldspar is widespread. The microcrystallites in this sample are distinguishable with SEM analysis, but the proportion of well preserved material is very small.

	Matrix	Clasts	Overall	SKL	SKR	SKZS
1	Reset	Reset	Old	Pos.	x	Pos.
2	Reset	Inherited Ar	V. Old	Likely	x	Likely
3	Dissolved Ar	Inherited Ar	V. Old	?	x	?
4	Devitrified	Inherited/reset	Young?	x	Likely	x
5	Altered/replaced	Altered	Young?	x	Pos.	x

Table 10. A qualitative assessment of the likely overall effects of the scenarios outlined in Table 9 on the three pseudotachylyte samples based on petrographic and SEM observations.

The three pseudotachylyte samples contain numerous lithic clasts, with proportions of clasts estimated as ~10% for SKL and SKR, and ~20% for SKZS. All of the samples contain clasts of feldspars, quartz, chlorite and calcite (sometimes as a matrix within the clasts). Clasts are frequently fragments of previously recrystallised or cataclased feldspars and quartz crystals. Deformation of the host rock minerals prior to the pseudotachylyte generating event could lead to Ar loss from K-bearing minerals, minimising the potential for inherited Ar in these pseudotachylyte clasts. The size of the crystals within the previously deformed aggregates is small, which might promote total degassing during transient heating. Qualitatively, there is little difference in the clast size and composition distributions between the samples.

6.5.2.3 Timing and duration of fault activity

Table 10 indicates that for each of the pseudotachylyte samples the most likely effect of the uncertainties surrounding the mobility of Ar and K throughout the lifetime of the pseudotachylytes is to make the calculated ages apparently older than the age of the pseudotachylyte generating event. In particular, the exceptional preservation in samples SKL and SKZS has minimised the effects of post-solidification processes that can cause K and/or Ar mobility. The ages calculated for SKZS and SKL therefore place probable upper bounds on the time at which the slip events that generated the pseudotachylytes took place (Figure 133). If SKL and SKZS have a similar clast size and composition distribution, then it is possible that they may be apparently too old by approximately the same amount of time. If this is the case, then although the absolute ages may be too old, the difference in ages between the three samples suggests that Skeeter fault was active for at least 10Ma. However, comparing the pluton cooling history (Figure 131) with the approximate closure temperature of glass (~150C; Reimold *et al.*, 1990) shows that at the time SKZS is calculated to have been generated, the ambient temperature was greater than 150ºC (Figure 133). The age for SKZS should be the same or younger than the time at which the ambient temperature decreased to less than 150ºC for Ar to be retained in the pseudotachylyte glass. That the calculated age is older than this time suggests that a bias has been introduced during the analytical procedure, and that the age for SKZS is relatively unreliable.

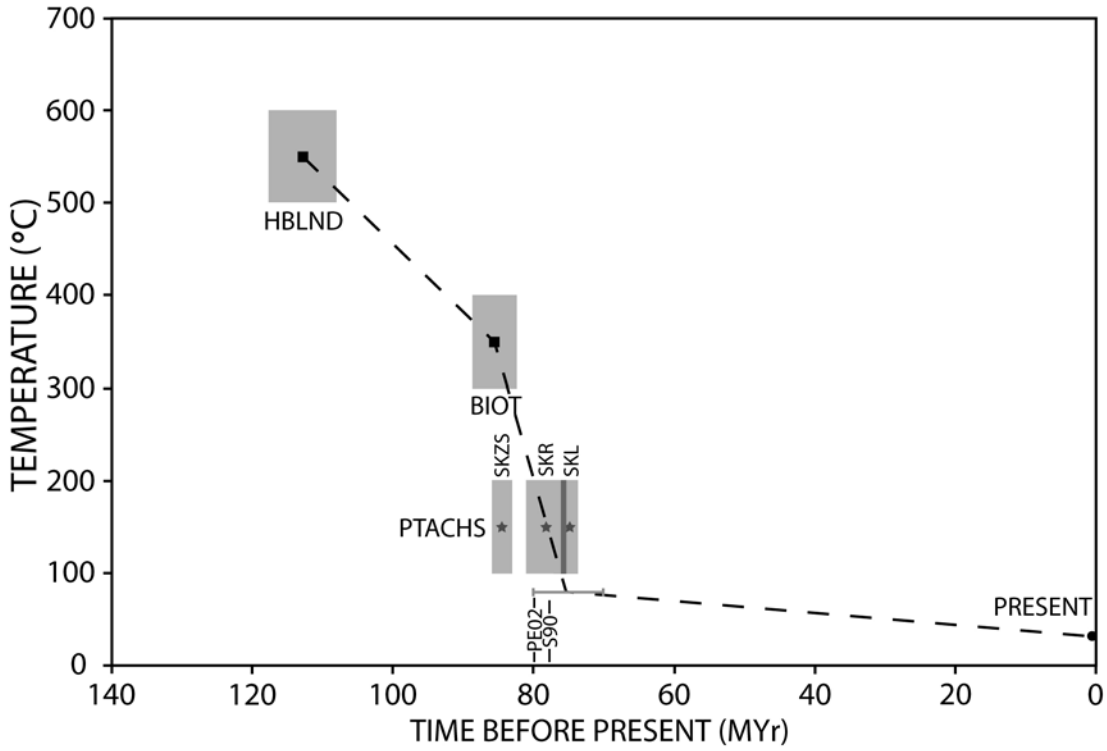

Figure 133. Cooling curve determined for the Pyramid pluton along with the ages of the three pseudotachylytes. Pseudotachylyte ages are plotted with a closure temperature of 150ºC (Reimold *et al.*, 1990), but the extensive number of uncertainties surrounding the application of the K-Ar method with respect to the pseudotachylyte system precludes their use as thermochronometers. The ages most likely place an upper bound on the timing of fault activity. Dates of fault activity in the nearby Mount Abbot Quadrangle are shown for comparison (PE02 = Pachell and Evans, 2002; S90 = Segall *et al.*, 1990)

Despite the many uncertainties in the application of the K-Ar isotopic dating technique to pseudotachylytes, the duplicate analyses of each pseudotachylyte sample in this investigation show a striking consistency. Sample SKR is particularly noticeable in this respect; the pseudotachylyte glass is extensively altered, and so microscopic observations of the sample might predict that the calculated ages of the SKR aliquots would be vastly different to the other two samples, and perhaps that the aliquots would not provide reproducible ages. The range of calculated ages for SKR is similar to the ranges of the other two samples, suggesting that the composition of SKR must be homogeneous at the scale of the aliquot size (as little as 0.015g). However, the effect of the compositional changes induced by alteration requires further analysis (by the $^{39}Ar/^{40}Ar$ method) to reconcile the similarity of the SKR ages with SKL and SKZS.

Pseudotachylytes ages directly record the timing of fault activity as pseudotachylytes are the product of slip events. The ages for the three pseudotachylyte samples are similar to estimates of the time of fault activity in the Mount About Quadrangle, ~55km to the north of the study area. Dates obtained from sericites (79.7±0.16Ma, Pachell and Evans, 2002), and from muscovite (78.9±0.4Ma, Segall *et al.*, 1990) from fault zones in the Mount Abbot

area are within the range of the three pseudotachylyte samples. Biotite K-Ar ages show that emplacement of the host plutons in the Mount Abbot quadrangle took place at around 80 to 90Ma (Evernden and Kistler, 1970; Kistler *et al.*, 1965), suggesting that the faults in the area were active a similar amount of time after pluton crystallisation.

6.5.3 Exhumation history

Lithostatic pressure is one of the extrinsic controls on fault zone architecture. The lithostatic pressure acting at a point on a fault at any time is a function of the depth at which the fault is buried and the density of the overburden:

$$P_v = \rho g h$$ **Equation 11**

where P_v is the lithostatic pressure, ρ is the density of the overburden, g is acceleration due to gravity, and h is the depth of burial. Determining the lithostatic pressure, and the variation of lithostatic pressure through time, therefore requires the rate of exhumation of a fault or its host rock to be established (Figure 134).

Using an empirically derived relation between the concentration of aluminium in hornblende and the pressure of crystallisation, Ague and Brimhall (1988) showed that the plutons in the central Sierra Nevada mostly crystallised at 2 to 3kb (8-11km) or 3 to 4kb (11-15km). Their study encompasses the whole Sierra Nevada batholith, so patterns in the crystallisation depth are generalised; according to their map the Pyramid pluton is located on the boundary between these two pressure ranges. The samples analysed by Ague and Brimhall were collected from the bottom of the Kings River canyon ~1500m below the altitude of the study area. It is therefore reasonable to estimate the depth of crystallisation of samples GPP1 and GPP3 as 7-14km. As the samples were collected at the modern surface, the depth at which they were buried has changed from 7-14km at ~113Ma (the age of the hornblendes) to 0km today.

Exposure of the Pyramid pluton implies that all of the overburden that was in place at the time of pluton crystallisation has been removed by erosion. The time and depth range of crystallisation of hornblendes in samples GPP1 and GPP3 imply a mean erosion rate from 0.062mm yr-1 to 0.12mm yr^{-1} since 113Ma depending on the crystallisation depth. House *et al.* (2001) inferred mean erosion rates of 0.04 to 0.05 mm yr^{-1} for the central Sierra Nevada during the Cenozoic from (U-Th)/He apatite ages, similar to denudation rates inferred from GPP1 and GPP3 if shallow crystallisation depths are assumed. However,

Yeend (1974) and Nilsen and Clarke (1975) report fluvial gravels of Eocene and/or Palaeocene age deposited in the Yuba and lower San Joaquin drainage. These gravels are sub-aerial and imply that the ~80Ma granites upon which they were deposited were at the surface of the Earth by the Eocene. The exhumation history for the central Sierra Nevada therefore appears to have an early rapid period of exhumation, followed by a prolonged period of slower exhumation rates.

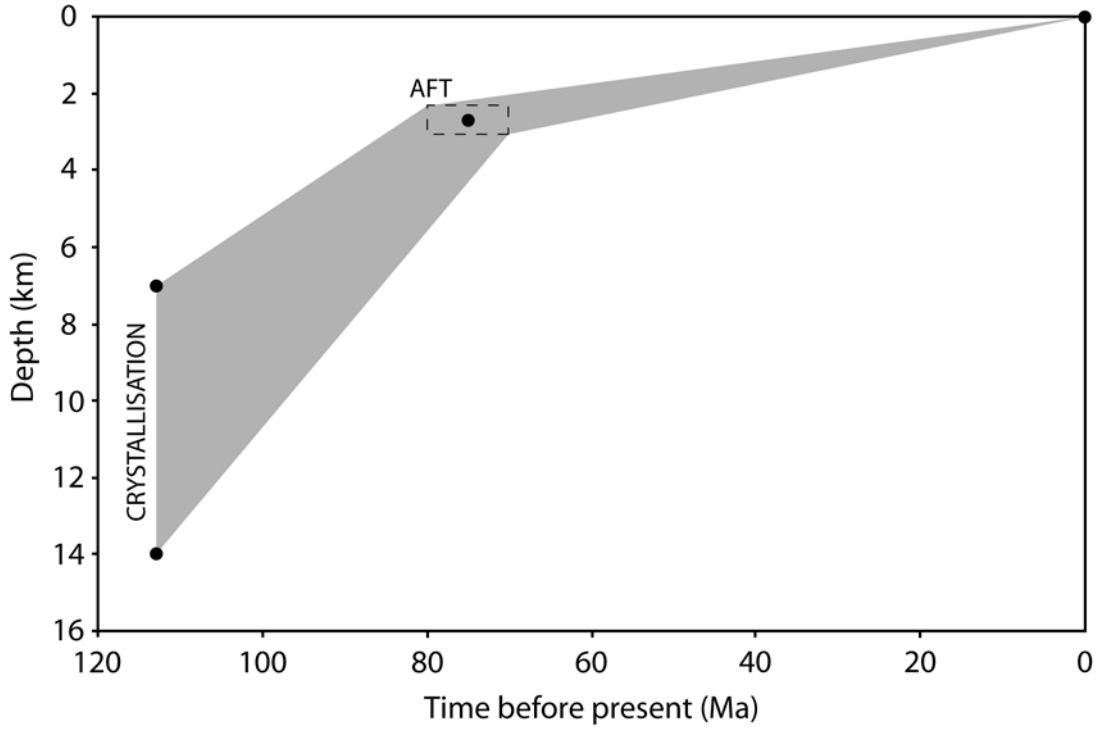

Figure 134. Range of potential exhumation paths for the Pyramid pluton estimated from samples GPP1 and GPP3 and assuming constant rates of erosion. The depth of crystallisation is derived from amphibole geobarometry (Ague and Brimhall, 1988), and apatite (U-Th)/He data constrain the time at which the pluton passed through ~3km depth (Clark *et al.*, 2004; House *et al.*, 1998; House *et al.*, 2001). The uncertainty in the time before present is due to errors reported for the published apatite (U-Th)/He data, and the depth uncertainty is derived from geothermal gradients of 25, 30 and 35ºC/Ma.

Clark *et al.* (2004) showed that the Sierra Nevada mountain range is characterised by a high elevation, low relief relict landscape that is cut by deep, steep-sided canyons. The study area is part of the relict landscape identified by Clark *et al.* (2004), who used (U-Th)/He dating to show that the apatites taken from samples at the relict surface have ages of ~80Ma. Apatite (U-Th)/He data from near the study area (<25km away) from House *et al.* (2001) show that apatites at the surface have ages of ~72 ± 8 Ma. As the closure temperature of apatite with respect to He is ~80ºC, the apatite ages can be used to infer the exhumation of the relict landscape; assuming a geothermal gradient of ~30ºC/km, the apatites were exhumed to less than 3km depth at around 75Ma. These data place a constraint on the exhumation history of the Pyramid pluton, assuming differential uplift is negligible at the scale of around 25km (the distance from the study area to the House *et al.*,

2001 sampling site), and indicate a non-linear exhumation rate since pluton crystallisation. Further evaluation of the exhumation rate requires apatite fission track analysis to determine how long the apatites associated with the relict surface remained in the partial annealing zone (e.g. Persano *et al.*, 2005a; Persano *et al.*, 2005b).

6.5.4 SKF deformation conditions

Combining the cooling history of the Pyramid pluton with an exhumation history derived from independent data allows a pressure – temperature – time path for the pluton to be constrained (Figure 135). The lithostatic pressure acting upon samples GPP1 and GPP3 (calculated from equation 9 assuming an overburden density of 2750kg m^{-3} for granitic rocks) varied from ~380MPa or ~190MPa depending on the depth of crystallisation, to a modern value of 0Mpa. Temperatures, defined by the closure temperatures of hornblende and biotite with respect to Ar, cooled from >550ºC to ~20ºC since 113Ma. Thus, the Pyramid pluton cooling and exhumation appear to impose a continuous, though non-linear, retrograde change in the lithostatic pressure and temperature on any progressed deformation in the pluton.

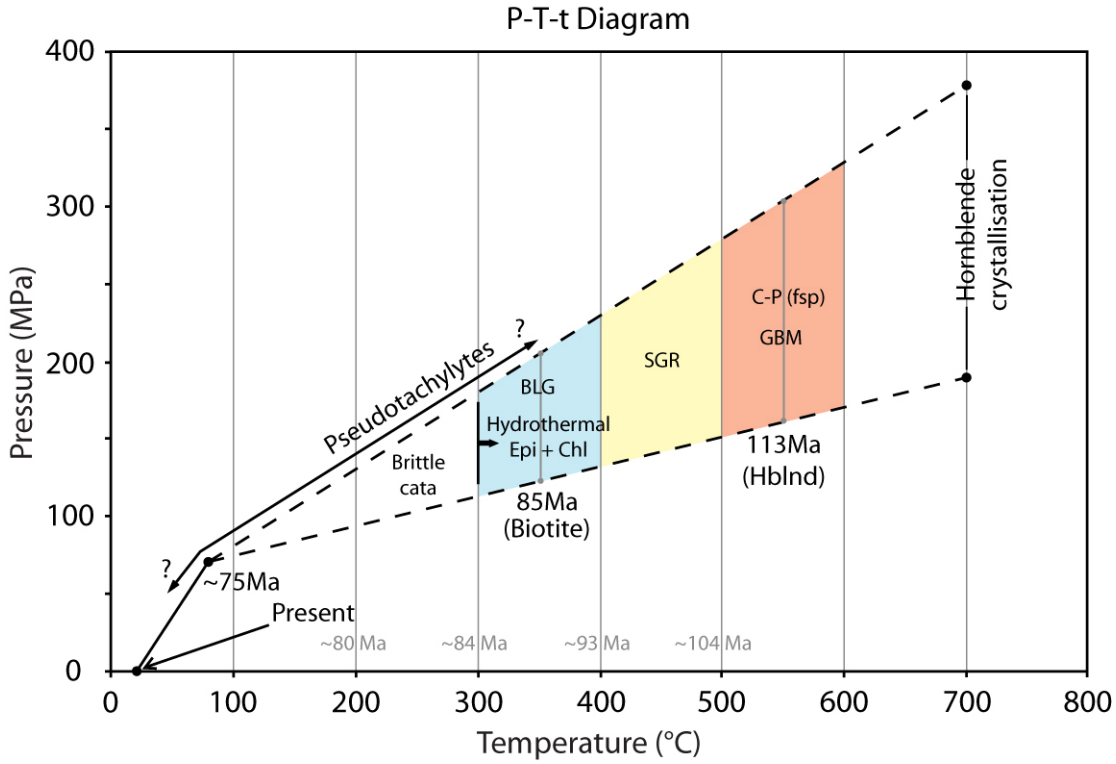

Figure 135. P-T-t diagram for the host rock samples GPP1 and GPP3 and the likely duration of pseudotachylyte generation by slip events on Skeeter fault. Vertical lines are labelled with the approximate time corresponding to the ambient temperature, extrapolated from Figure 131. The temperature ranges for the recrystallisation mechanisms in quartz calculated by Stipp *et al.* (2002) are shown (BLG = bulging recrystallisation, SGR = subgrain rotation recrystallisation, GBM = grain boundary migration recrystallisation, see section 1.2.2 for a discussion).

The estimates of the environmental conditions prevalent for the Pyramid pluton since crystallisation are based on analyses of undeformed samples. Correlating the conditions with faulting to evaluate the way in which the environmental controls dictate the style of deformation associated with faulting in the Pyramid pluton requires the time and duration of faulting to be known. Pseudotachylyte generation by slip events on Skeeter fault likely occurred over a period of ~10Ma at some time since ~85Ma. Though the absolute ages of the pseudotachylytes have not been reliably calculated in this study, it is likely that the pseudotachylytes were generated when the temperature was <350ºC, and when the lithostatic pressure was ≤150MPa (i.e. a depth of 5.5km).

Micro-scale observations (section 6.3.3, see also section 4.5) show that the SKF fault core samples contain a range of deformation products that allow a deformation history for the fault to be reconstructed. Recrystallisation of feldspars in samples of fault rock from Skeeter fault shows that early deformation occurred at temperatures 400 to ≤600ºC (see section 1.2.2 for a discussion of deformation mechanisms and temperatures). Fault displacement therefore accumulated initially by localised high temperature crystal-plastic deformation. Cataclasites, breccias and pseudotachylytes cross-cut the recrystallised portions of the rock, indicating that the deformation switched to brittle fracture as temperatures decreased to <300ºC. The T-t plot shows that the time taken for the temperature to decrease from >500 to 300ºC could have been as much as 40Ma. This represents a minimum duration for tectonic activity as the cessation of brittle deformation has not been constrained. The micro-structural observations show early high temperature deformation followed by later brittle, pseudotachylyte-generating slip events, consistent with the temperature and pressures changes estimated from the thermochronological analysis. The architecture of the fault is therefore a product of early crystal-plastic deformation followed by later brittle deformation, which were imposed by the deformation conditions.

Stipp *et al.* (2002) constrained the temperature ranges through which different dislocation creep crystal plastic mechanisms are active in quartz by analysing quartz veins formed in the contact metamorphic aureole of a syn-tectonic pluton. Their work shows that the predominant deformation mechanisms changed as the temperature decreased from >600ºC to <300ºC with distance away from the pluton contact. They define the transition from viscous (crystal-plastic) to frictional (brittle) deformation to occur at around 280 to 300ºC. The temperature ranges for bulging, subgrain rotation and grain boundary migration defined by Stipp *et al.* (2002) are plotted along with the SKF data in Figure 135, and show

that the quartz recrystallisation micro-textures observed in the SKF may correlate directly to their temperature ranges. However an anomaly occurs at the onset of brittle deformation in the SKF; pseudotachylytes, breccias and cataclasites all contain chlorite as a constituent of the matrix, and the chlorite is interpreted to be syn-kinematic in some of these deformation elements (see also section 4.6). Though using chlorite as a temperature gauge is not straight-forward (Decaritat *et al.*, 1993), hydrothermal chlorite in fault zones is generally accepted as indicating temperatures in excess of 300ºC (Bruhn *et al.*, 1994). Brittle deformation is therefore associated with temperatures greater than 300ºC, especially as some pseudotachylytes are brecciated by chlorite-bearing fluids.

The crystal-plastic to brittle transition in the SKF may therefore have occurred at higher temperatures than might be expected from previous studies. One explanation for this would be transiently elevated flow stresses and/or strain rates acting on the fault. Pseudotachylyte-generating rupture events indicate that the loading and relaxation of stress onto the SKF did occur rapidly. However, it is also possible that the hydrothermal fluid that deposited the chlorite was at higher temperatures than the ambient temperatures in the host rock. Further work to accurately determine timing of the pseudotachylyte generating events could resolve this issue.

6.6 Summary

Thermochronologic analyses of host rock minerals that are sensitive to different closure temperatures allows a cooling history for the Pyramid pluton to be determined, and constrains the temperature at various times since pluton crystallisation. Combining the cooling history for the pluton with the rate of exhumation inferred from independent data provides an estimate of the coupled temperature-lithostatic pressure that would have been acting on faults in the Pyramid pluton. K-Ar dating of pseudotachylytes is not a rigorous method for dating the timing of an earthquake rupture, but likely constrains the maximum age of the slip event. Information on the timing and duration of tectonic activity for the SKF derived from the pseudotachylyte data and also temperature ranges for intra-crystalline deformation mechanisms of quartz and feldspars shows that the inferred retrograde path of deformation conditions is consistent with the microstructural observations. The SKF architecture is therefore the product of the progressed deformation of the SKF initially by crystal-plastic, and later by brittle mechanisms.

7

Discussion and Conclusions

7.1 Fault architectures of seismogenic faults

7.1.1 Applying the three component conceptual model

The conceptual model proposed by Chester and Logan (1986) and Caine *et al.* (1996) for describing fault architecture divides fault zones into three different structural components; fault core, slip surfaces and damage zone. Fault cores are the most intensely deformed parts of a fault, and accommodate the majority of strain. Slip is frequently localised onto narrow (millimetres or centimetres) slip surfaces, which may be within a fault core. Fault-related subsidiary structures developed in the volume surrounding a fault core comprise the damage zone. The model does not imply that a fault must have undergone a particular magnitude of strain, that any of the components must be present in a fault zone, or that any pre-defined spatial relation exists between the components. The conceptual model may therefore be used as a basis for describing faults with extremely differing architectures.

Fault zone architecture is controlled by numerous factors that are either intrinsic properties of the fault or extrinsic properties of the deformation environment (Caine *et al.*, 1996). Intrinsic factors are characteristics of a fault that are either physical properties of a fault (3D geometry, displacement) or interactions between a fault and its environment that can only be brought about because of the existence of the fault (host rock lithology, fluid-fault rock interactions). Extrinsic factors are products of the deformation environment that are derived from 'far-field' tectonic processes; lithostatic pressure and temperature are dependent on depth of burial, and differential stress and time-averaged strain rate are imposed on a fault by plate tectonic forces.

However, the intrinsic properties of a fault are inherently dependent on the extrinsic factors, and *vice-versa* (e.g. the damage around a fault changes the local stress field, and

the shear strength of a fault determines both the instantaneous and time-averaged strain rate). The extrinsic factors that control fault architecture are variable during a period of prolonged fault activity. The inter-dependence of the intrinsic and extrinsic controls therefore means that the style of fault architecture for any given fault is the product of the unique deformation history of that fault. Defining a model of fault zone architecture in order to describe and predict the fluid-flow properties of a fault or to parameterise faults for modelling deformation processes must include an assessment of the deformation history of the fault. Additionally, understanding how transferrable any specific architectural model is to different faults requires an analysis of the sensitivity of fault zone architecture to each of the individual controlling factors.

The inter-dependent nature of the intrinsic and extrinsic controls on fault architecture leads to a potentially unlimited number of variations in the number of possible deformation histories for faults. Using models of fault architecture based on exhumed faults to predict the properties of faults at depth is therefore difficult as there should be a wide range of model architectures to match the variability in the deformation histories. A large number of parameters need to be constrained to compare and contrast fault architectures; for example the Punchbowl and Carboneras faults (see below) have similar magnitudes of displacement and were both active at relatively similar depths and yet the internal architectures of the faults are different. However, appropriate models for faults at depth could be identified if a large number of architectures were collated from case studies of exhumed faults with well-constrained deformation histories. A database of integrated model architectures would provide a means for predicting the architecture of a fault at depth by comparison with exhumed faults if some of the intrinsic and/or extrinsic controls could be established for that fault. Such a database would provide insight into which of the controls on fault architecture are most important in determining the architecture of faults, and should be the focus of future research.

7.1.2 The GPF fault architecture

A generalised model describing the spatial distribution and composition of the fault zone components for the GPF has been constructed from field data (Figure 136). The fault is heterogeneous along strike, and is composed of up to four fault core strands containing cataclasites and ultracataclasites that overprint mylonites. The fault core strands are tens of centimetres to several metres thick, with order of magnitude thickness changes occurring within tens of metres along strike. Fault core strands can be traced for hundreds of metres along strike and are sub-parallel to the overall fault zone orientation. However, the strands

are not continuous for more than hundreds of metres and are inferred to anastomose and bifurcate. Slip surfaces are defined by pseudotachylytes, polished surfaces with slickenlines and thin seams of extremely comminuted cataclasites. Slip surfaces are developed at the edges of fault core strands, within strands and between fault cores, and are shown to branch and be discontinuous at thin section as well as outcrop scales. A fault-related damage zone is defined by subsidiary opening mode and shear fractures that are developed between and outside of fault core strands. The damage zone contains an increased level of deformation compared to the background level of deformation represented by cooling joints that are inherent in the host rock.

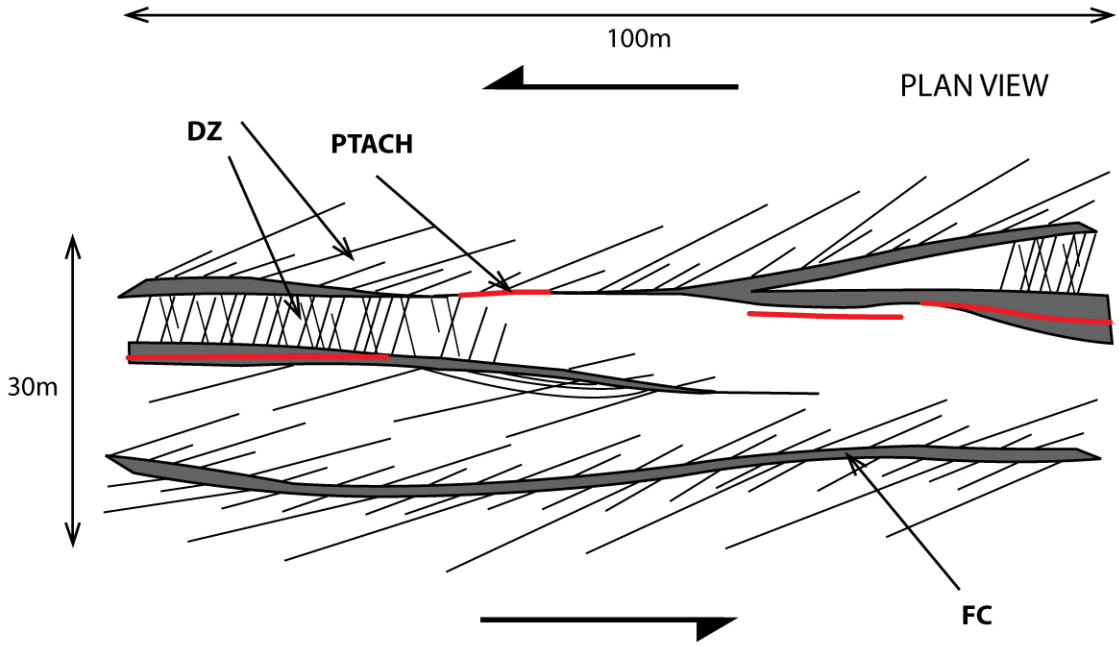

Figure 136. The model GPF architecture, reproduced from Figure 50, Ch 3. A plan view of the generalised fault zone architecture for the GPF showing multiple fault core strands (FC; grey) and abundant subsidiary structures (DZ; black lines) between and beyond the extent of the strands. Slip surfaces are represented by pseudotachylytes in this figure (red lines).

Field and microscope observations have constrained many of the intrinsic factors that control the GPF fault zone architecture. The GPF cuts crystalline granodiorite host rock, is at least 7km long and has a maximum observed displacement of around 80m. Offset dykes, ductile shear zone geometries and micro-scale fabrics are all consistent with left-lateral strike slip displacement. Fluid-fault rock interactions have occurred throughout the deformation history of the fault; chlorite, epidote and to a lesser extent calcite precipitated from hydrothermal fluids contemporaneously with crystal-plastic deformation and cataclasites, attesting to fluid migration through the fault zone from the earliest deformation onwards. Fluids have also chemically altered the host rock in the fault zone through sericitization of feldspars, and chloritization of biotites and hornblendes.

Some of the extrinsic controls on the GPF fault architecture, and their variation through time, can be evaluated by combining microstructural observations with the results of thermochronological analyses of the host rock in a similar way to the analysis of the SKF (Chapter 6). Isotopic K-Ar ages of hornblendes and biotites combined with an exhumation history inferred from apatite fission track ages define a P-T-t path for the Pyramid pluton. The changing environmental conditions can be related to the deformation of the GPF by identifying the deformation mechanisms that accommodated displacement through the history of fault activity (Figure 137). Crystal-plastic deformation of quartz and feldspars show that the earliest increments of displacement along the GPF occurred at high temperatures (~450 to 600ºC), and were accommodated by ductile deformation mechanisms. Ductile textures in GPF fault rocks are consistently cross-cut by fractures, brecciation and pseudotachylyte generation surfaces. As deformation progressed, it is evident that the brittle deformation mechanisms became predominant. The cooling and exhumation of the pluton has significantly influenced the mechanisms by which slip was accommodated on the GPF during its deformation history.

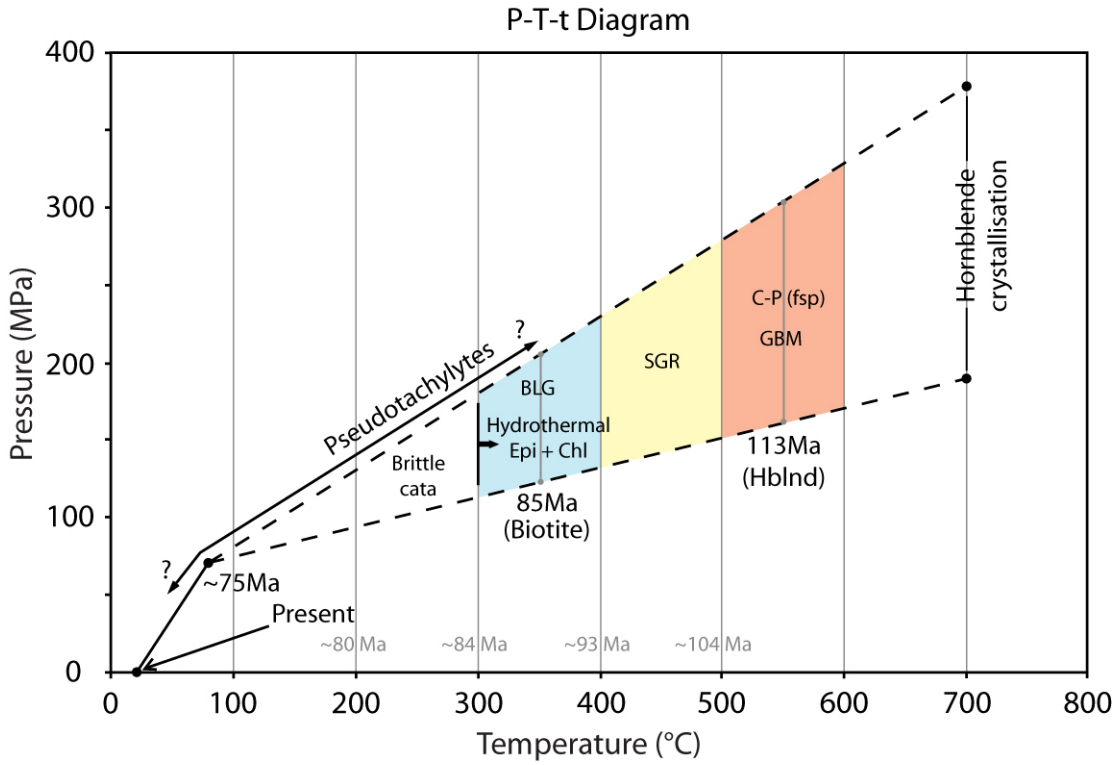

Figure 137. P-T-t diagram showing the inferred deformation history for the GPF, reproduced from Figure 135, Ch 6. Timing and duration of faulting can be constrained from the results of thermochronological analyses of the host rock, and by K-Ar ages of tectonic pseudotachylytes. BLG, SGR and GBM refer to the temperature ranges of bulging, subgrain rotation and grain boundary migration recrystallisation mechanisms in quartz as determined by Stipp *et al.* (2002).

The deformation history for the GPF interpreted from microstructures and cross-cutting relations is similar to that of the SKF (see section 6.5.4). The microstructural observations are therefore consistent with the interpretation of the GPF and GPF-parallel faults as sharing a common deformation history based on orientation data (section 3.8.2). Similar estimates of the timing and duration of GPF deformation should be expected for the GPF and the SKF. As the high temperature crystal-plastic deformation occurred close to the closure temperature of hornblende (~113Ma), and the GPF pseudotachylytes were generated at similar times to the SKF pseudotachylytes (likely at some time since 85Ma), the duration of faulting could be as great as 30Ma. The architecture of these two faults should be comparable as they have similar deformation histories. Further field analysis of the faults would indicate how similar they are, and by comparison indicate which of the intrinsic controls on fault architecture has caused any divergence in the architectures.

7.1.3 A fault growth model for the GPF

The ambient temperature and lithostatic pressure conditions during GPF fault activity are constrained by the temperatures at which crystal-plastic deformation mechanisms are active for quartz and feldspars, the cooling and exhumation of the host rock pluton, and the estimates of the age of the pseudotachylytes. However, developing a model for the deformation history of the fault also requires an understanding of the fault growth process. The fracture linkage model (FLM) proposed by Martel (1990) is based on field observations collected from the Sierra Nevada, and so may be applicable to the GPF (see sections 2.4 and 5.7.2 for a discussion of the details of the model). The FLM makes a detailed prediction regarding the architecture of compound fault zones, which represent the final stage of fault evolution. These fault zones are up to 10km long, a similar scale of structure to the GPF, and are composed of two planar boundary faults containing cataclasites that may have overprinted early ductile deformation. Subsidiary structures are restricted to within the tabular-shaped volume of rock between the planar boundary faults.

In contrast to the predicted architecture of a compound fault zone, the GPF is composed of several fault core strands that have variable thickness and are discontinuous at the km-scale. Subsidiary structures are also distributed throughout the fault zone and define the width of the fault zone where they are present beyond the limits of the fault core strands. These observations cannot be reconciled with the FLM, and suggest that the model does not apply to the GPF.

However, the GPF fault core and slip surface orientations match closely the distribution of the orientations of cooling joints measured in this study (Figure 49). Faults nucleate upon pre-existing cooling joints in the FLM, and the correlation between joint orientations and GPF orientations suggests that the GPF has re-utilised these pre-existing planes of weakness in the manner described by the FLM. The early stages of deformation in the GPF occurred at high temperatures and pressures. If cooling joints had formed and were reactivated during GPF deformation, then it is likely that ductile deformation was prevalent immediately after fault nucleation. Bűrgmann and Pollard (1992) showed that mylonites are developed at restraining bends between small faults from the same field area as the small faults that inspired the FLM. These mylonites develop fabrics in response to elevated mean stresses and contain foliations oriented 25 to 55º clockwise from the fault trace. Mylonitic fabrics are also reported by Christiansen and Pollard (1997), who showed that aplite dykes acted as nucleation sites for shear zones. The shear zones they describe develop forked or eye-shaped traces through longitudinal propagation by end to end linkage. If the GPF deformation took place at temperatures and pressures of sufficient magnitude, then mylonitic fabrics developed in and around early shear zones could produce the fault core strand geometry identified in the GPF. Curved foliations around the tips of small shear zones would also result in anisotropic mechanical heterogeneity that would likely be exploited by later brittle deformation.

The anastomosing nature of the GPF fault core strands can therefore also be explained if the early history of the fault was dominated by ductile deformation. Elastic stress changes associated with slip on the bounding faults of simple and compound fault zones result in damage zone structures are strictly limited to the region between boundary faults in the FLM, except near the ends of faults (Martel and Pollard, 1989). However, the coupled boundary fault architecture of compound fault zones never developed for the GPF, so the mechanical response to slip would be different to that modelled by Martel and Pollard (1989). Other processes that are quasi-static, dynamic or both, which cause off-fault damage are likely responsible for the GPF architecture.

7.1.4 Comparison of the GPF with published model architectures

The Punchbowl fault, southern California, is a former strand of the San Andreas fault system that accommodated 40 to 50km of right lateral strike-slip displacement, and has been exhumed from 2 to 4km depth (Chester and Chester, 1998; Chester *et al.*, 1993; Chester and Logan, 1986; Chester *et al.*, 2005). The Punchbowl fault juxtaposes two wall rock types; the Punchbowl formation (basal breccia overlain by interbedded pebbly and

arkosic sandstones and siltstones), and a basement terrane composed of biotite gneiss and quartzo-feldspathic gneiss. The fault trace is composed of two sinuous strands that are truncated at both ends by the San Andreas fault. The Punchbowl fault has been studied in great detail in two exposures of the northern strand of the fault trace in the Devil's Punchbowl Park (Chester and Chester, 1998; Chester *et al.*, 1993; Chester and Logan, 1986). The majority of displacement was accommodated by an ultracataclasite layer 0.15 to 0.55m thick. Within the ultracataclasite a prominent fracture surface is inferred to have accumulated the last few kilometres of displacement through localised co-seismic slip. A damage zone ~100m wide surrounds the ultracataclasite that contains microfractures and subsidiary faults (Chester and Logan, 1986; Schulz and Evans, 1998; Schulz and Evans, 2000; Wilson *et al.*, 2003). These observations provided the basis for a generalised model of fault architecture, the Punchbowl-type fault (Figure 138). The nearby San Gabriel fault is an example of a fault for which the Punchbowl-type model describes well the observed structure of the fault zone (Chester *et al.*, 1993; Evans and Chester, 1995).

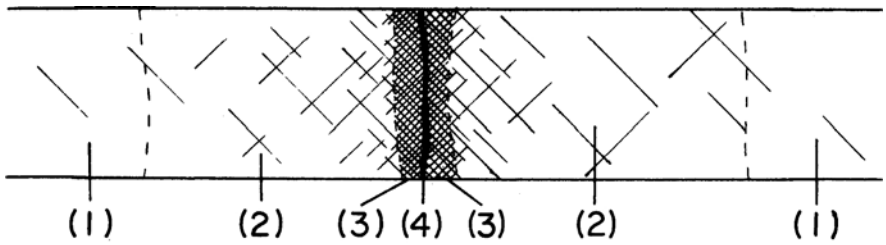

Figure 138. The model of fault zone architecture derived from the two exposures of the Punchbowl fault from Rice and Cocco, 2007; (1) undamaged host rock, (2) damage zone, 10s m to 100m wide, (3) gouge or foliated gouge, 1m to 10s m wide, (4) central ultracataclasite shear zone 10s to 100s mm wide, (5) prominent slip surface <1 to 5mm wide (based on Chester *et al.*, 1993).

Several significant differences are apparent between the Punchbowl and GPF fault architectures. Significantly, the GPF contains more than one fault core strand. Though ultracataclasites are described in the damage zone of the Punchbowl, they are not considered to have accommodated a large amount of displacement (Chester and Chester, 1998). Slip on the Punchbowl fault is extremely localised; kilometres of displacement have been accommodated on the central fracture surface that is millimetres thick. The GPF contains numerous slip surfaces distributed throughout the fault zone. Although the magnitude of slip on any of these surfaces has not been constrained, the small total displacement across the fault zone (<100m) suggests that all of the slip surfaces are likely to have small displacements compared to the total displacement.

The Carboneras fault, southeastern Spain, is an example of an exhumed, mature strike-slip fault zone for which the fault architecture is different to the Punchbowl-type model

(Faulkner *et al.*, 2003; Keller *et al.*, 1995). The Carboneras fault forms part of the Iberia-Africa plate boundary fault system, and has accommodated ~40km displacement (Faulkner *et al.*, 2003). As such it is directly comparable with the Punchbowl and San Gabriel faults. However, the generalised model for the architecture of the fault proposed by Faulkner *et al.* (2003) contains anastomosing strands of fault gouge, intercalated with blocks of host rock and dispersed fault planes. Faulkner *et al.* (2003) concluded that the strain-hardening behaviour of phyllosilicate-rich fault gouge inferred from experimental work would tend to diffuse strain across a zone, rather than localise strain (as must have been the case for the Punchbowl fault). The GPF architecture is similar to the Carboneras architecture in a number of respects; multiple strands of fault core material are present in the fault, slip surfaces are distributed throughout the fault zone, and subsidiary structures are developed surrounding the complex fault core geometry.

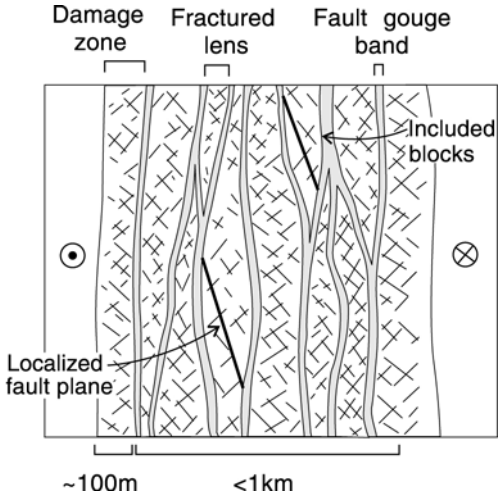

Figure 139. A generalised model for the architecture of the Carboneras fault, proposed by Faulkner *et al.* (2003), contains anastomosing strands of fault gouge, intercalated with blocks of host rock and dispersed fault planes (from Faulkner *et al.*, 2003).

The GPF is more similar to the Carboneras fault than the Punchbowl fault. The GPF has accumulated two orders of magnitude less displacement than the Carboneras and Punchbowl faults so the mechanical reasons that might explain this observation are difficult to assess. The most significant difference in the intrinsic controls on the Carboneras and Punchbowl faults is the host rock type. Faulkner *et al.* (2003) concluded that the most important factors controlling the architecture of the Carboneras fault were the phyllosilicate-rich host rock and the strain-hardening behaviour inferred for the phyllosilicate-rich fault gouge. The Punchbowl fault juxtaposes quartzo-feldspathic host rock types, though the ultracataclasite in both the Punchbowl and San Gabriel faults contain a high proportion of zeolites and clays derived from fluid-fault rock interaction (Chester *et al.*, 1993; Evans and Chester, 1995). In contrast the GPF cuts relatively

homogenous, isotropic crystalline granodiorite. However, inherited geometries in the form of pre-existing cooling joints are inferred to control the fault architecture in the growth model for the GPF. Host rock heterogeneity provided planes of weakness that were preferentially loaded to form fault core strands for both the GPF and Carboneras faults. The Punchbowl fault juxtaposes different host rock types so perhaps a material interface caused the extremely localised deformation. It seems likely that the host rock lithology and the earliest stages of fault evolution imposed structural controls on the architecture exposed today.

The similarity between the GPF and Carboneras faults emphasises the complex influence of the multiple controls on fault architecture; the faults have different displacements, and are developed in different lithologies and so might be expected to be distinct. Predicting the architectures of faults from information on only a few of the controlling parameters is therefore unlikely to be successful. The GPF model architecture has well constrained intrinsic and extrinsic controls and therefore should be transferrable to faults in similar lithologies with comparable deformation histories.

7.1.5 Implications for modelling earthquake ruptures

Recent studies that investigate earthquake ruptures by modelling the processes of rupture nucleation (Segall and Rice, 2006), slip-weakening (Rempel and Rice, 2006; Rice, 2006; Rice and Cocco, 2007) and rupture propagation (e.g. Poliakov *et al.*, 2002) have all defined a model architecture for a 'mature' fault zone that is based on the Punchbowl fault example. These studies often cite other faults such as the Median Tectonic Line (Wibberley and Shimamoto, 2003; Wibberley and Shimamoto, 2005), and Nojima fault (Lockner *et al.*, 2000) as examples of similarly structured, long-lived faults that have accommodated many tens of kilometres of displacement in support of a Punchbowl-based model. It is the case that these two other faults have localised deformation in a single distinct fault core, embedded in a damage zone. However, the GPF model architecture is much more complex than the Punchbowl-type model. Pseudotachylytes and pseudotachylyte-breccias in the GPF show that the fault has experienced multiple earthquake ruptures. The slip surfaces in the GPF defined by pseudotachylytes have complex geometries; branching occurs along strike and up/down dip. Slip surface thickness changes also occur in both directions. If earthquake rupture processes are generic to all slip events, rather than unique to individual ruptures, or fault zones, then any theories formulated to describe the earthquake rupture should apply to all seismogenic

faults. It is essential that models based on the Punchbowl fault architecture are transferrable to seismogenic faults that have different architectures.

7.2 The structure of strike-slip fault terminations at depth; the Glacier Lakes fault

7.2.1 Overview

The western termination of the GLF is defined by a gradual decrease in the slip on the main fault zone, accompanied by a broad (~1.4 km wide) zone of secondary faulting in the dilational quadrant of the left-lateral strike-slip GLF. Faults in this region splay from the main fault trace in a counter clockwise sense forming average dihedral angles of 39º with the main fault trace. The splay faults are up to 3 km long, with observed displacements generally decreasing away from the GLF. Similar scale structures are absent in the compressional quadrant of the fault, and also along the GLF further away from the termination.

The structures at the western extent of the GLF likely comprise a termination structure, rather than a step-over between two coeval strike-slip faults (i.e. the GLF and GPF). As described previously (sections 3.6.2 and 4.8), field and microscope observations of ultracataclasites and ductile deformation fabrics within the fault zone indicate that the GPF was active at higher pressures and temperatures than the GLF. The GPF and its associated suite of sub-parallel structures are consistently cross-cut by the splay faults from the GLF, but are never observed to cross-cut the splays or the GLF. This consistent relation between the two fault systems, together with the absence of ductile fabrics in the GLF boundary faults indicates that the GLF and related splays post-date the GPF to a large extent. However, the GPF was favourably oriented for reactivation by oblique-normal faulting during GLF deformation, showing that the faults likely interacted.

The GLF is an exhumed seismogenic fault, and therefore the data describing the composition and structure of the fault can be used to gain insight into the processes related to seismic slip at depth. The presence of pseudotachylyte within the fault core material of the GLF is the strongest possible evidence that the fault slipped at seismic velocities (Cowan, 1999; Magloughlin and Spray, 1992; Sibson, 1975). Assuming the mapped length of the GLF represents the sub-surface length of a single slip event, the GLF is a fault that could have experienced an earthquake rupture of up to magnitude Mw ~ 5.7 (using the scaling relations of Wells and Coppersmith (1994)). An earthquake of this

magnitude would be close to the transition between the different scaling regimes for small and large earthquakes (i.e. size regimes 1 and 2 of Scholz (2002)). Observations of the termination of the GLF are therefore significant as the data describe a fault that is at a stage of development either preceding or contemporaneous with this change in scaling relations. The total displacement on the fault is over 100 m, which could not have been accumulated in a single event. The following discussion considers the structure of the GLF termination to be the product of the cumulative displacement on the fault, which was likely accrued by some combination of seismic slip and aseismic creep (Sibson, 1989).

The overall geometry of the GLF and splay faults is similar to strike-slip fault terminations observed in many other tectonic settings. Small faults tens of metres long, with displacements up to tens of centimetres often display isolated splay fractures, or arrays of fractures in a horsetail geometry near their tips (Cruikshank *et al.*, 1991; Granier, 1985; Lim, 1998; Martel *et al.*, 1988; Segall and Pollard, 1983b). Such splay fractures develop in the extensional quadrant of small faults, and form similar angles with respect to the main fault trace as the GLF and splay faults. The Gemini fault zone, located in the central Sierra Nevada, is approximately 10 km long, with around 100 m displacement, and is composed of a zone of highly fractured and altered host rock bounded by sub-parallel faults (Pachell and Evans, 2002). The left-lateral Gemini fault zone is interpreted to have evolved from early, joint-nucleated faults and terminates in a series of subsidiary faults that splay counter-clockwise from the main fault trace in a similar way to the GLF (Martel, 1990; Pachell and Evans, 2002). Analogous structures are observed at the terminations of regional-scale faults tens of kilometres long with hundreds of metres to kilometres of displacement that likely cut the entire brittle crust (e.g. Deng *et al.*, 1986; Micklethwaite and Cox, 2006; Storti *et al.*, 2001). Mapped traces of earthquake surface ruptures and secondary structures at the terminations of active faults are often characterised by a similar geometry to the GLF termination (Bayasgalan *et al.*, 1999; DePolo *et al.*, 1991; Klinger *et al.*, 2005; Vauchez and Dasilva, 1992).

The GLF termination structure shows that structural complexity is present at the terminations of faults at depth, as well as around shallow exhumed faults and earthquake ruptures that cut the Earth's surface. Similar deformation should therefore be expected at depth at the end zones of other faults. Models of fault geometry that consider distributed surface complexity to focus onto a single fault surface at depth are likely to be oversimplified at fault terminations. Linkage zones and stepovers between faults, which

develop from the interaction of fault terminations (Martel, 1990), are therefore also likely to be characterised by distributed deformation at depth.

7.2.2 Comparison with model predictions of fault termination geometries

Several models have been proposed to explain the development of secondary structures at fault tips. Linear elastic fracture mechanics (LEFM) theory predicts that a single secondary fracture will grow at ~70º to the fault plane in response to stress intensification at the tips of a fault (e.g. Martel, 1997; Segall and Pollard, 1980). However, geological materials cannot sustain the infinite stresses predicted to occur at fault tips by the LEFM. It is also clear that the field observations of the splay faults at the termination of the GLF cannot be described by LEFM as there are multiple faults, which form angles of ~39º to the main fault.

Multiple secondary fractures forming angles of <50º with the main fault are predicted by models of quasi-static fault growth that incorporate a cohesive zone ahead of the fault tip in which shear stress is elevated (Cooke, 1997; Martel, 1997). Although at least some of the slip on the GLF was seismogenic, quasi-static processes may be prevalent early in the deformation history of the fault, and during inter-seismic periods (Sibson, 1989). Cooke (1997) showed that development of more than one splay fault is promoted by a spatial variation of frictional strength in the end zone of the fault, which would also result in a steep slip gradient as the displacement on the fault tends to zero. The slip gradient at the tip of the GLF is 0.015 (see Figure 9 and section 3.4.3), a similar order of magnitude to gradients observed at other fault tips (Shipton and Cowie, 2001). Bűrgmann *et al.* (1994) suggested that other factors that may control slip gradients include an inhomogeneous stress field due to fault interaction, inelastic deformation in the tip region of faults, and spatially variable host rock elastic modulus. Inelastic deformation is present at the GLF fault tip in the form of splay faults, which likely influenced the GLF slip profile, perhaps causing slip to remain low near the fault termination. The GLF and splays cut across several pre-existing fault zones (the GPF and sub-parallel faults) with distinct mechanical properties from the granitic host rock. Interaction with these faults, which will have distinct elastic properties from the host rock, may have influenced the development of multiple splays at the termination of the GLF.

Recent 2-D (Andrews, 2005; Poliakov *et al.*, 2002; Rice *et al.*, 2005; Yamashita, 2000) and 3-D (Aochi and Fukuyama, 2002; Dalguer *et al.*, 2003) models of dynamic rupture

propagation show that the stress changes induced by a dynamic shear rupture process are sufficient to generate secondary structures in a volume surrounding a fault plane (Figure 140). All of these models predict that the majority of the deformation develops in the dilational quadrant at the rupture tip. In the 2D models of Andrews (2005) the width of the zone of off-fault deformation increases as the dynamic rupture propagates, resulting in a triangular zone of off-fault deformation in the dilational quadrant. However in the 3D models of Dalguer *et al.* (2003) the width varies as a complex function of the primary fault geometry. Off-fault deformation is also dependent upon rupture speed, stress drop, static and dynamic friction coefficients, and other rupture properties (Poliakov *et al.*, 2002; Rice *et al.*, 2005).

The steeply-dipping GLF is exposed in a plane oriented approximately perpendicular to the fault which contains the slip vector (i.e. a horizontal plane of exposure for a pure strike-slip fault). Assuming that the plane of exposure cuts the fault mid-way through the fault width allows the mapped geometry of the GLF to be compared with results of dynamic rupture models. Comparisons between the field observations and the model predictions in this case are valid if an earthquake rupture had ruptured the entire length of the GLF (i.e. the rupture did not stop part-way along the fault). The geometry of the termination is an asymmetrical zone of damage emanating from the GLF into the dilational quadrant, similar to the models (Figure 140). Within the zone of damage the greatest intensity of strain (highest measured strike slip values on the splay faults) is located adjacent to the GLF fault plane (Figure 9), similar to the results of Andrews (2005). The ratio between the width of the zone of splays and the mapped fault length ($\leq$0.170) is also similar to the value of ~0.075 predicted by Andrews (2005), and would be the same if the GLF was 18.6 km long. The GLF splays are oriented at a counter-clockwise acute angle to the main fault as in the model of Dalguer *et al.* (2003). However, the wedge-shaped zone of off-fault deformation expected from several models is less well matched by the field observations (Figure 140). Two bends are present in the trace on the GLF, which may have influenced the distribution of the splay faults and could explain this discrepancy.

The geometry of the GLF termination structure seems to approximate the off-fault damage geometries predicted by both the quasi-static and dynamic models of fault growth. At the scale of the data presented in this study (metre- to kilometre-scale), there are no geometrical features predicted by either of the two sets of models that would allow the process of formation to be distinguished. Seismic activity has been inferred for the GLF on the basis of pseudotachylyte present in the fault rock, suggesting that dynamically

induced off-fault damage may be expected. Quasi-static processes are likely to have been prevalent during the early phases of fault activity, or during inter-seismic periods. It is therefore probable that the off-fault damage present around the GLF represents the superimposition of inter- and co-seismic processes. A future line of research could be to investigate the potential presence or absence of structures in the fault damage zone that are indicative of dynamic slip events; high angle secondary fractures (Di Toro *et al.*, 2005a), or fractures with a branching morphology (Kame and Yamashita, 2003; Sagy *et al.*, 2001) have been suggested to develop only under dynamic stress.

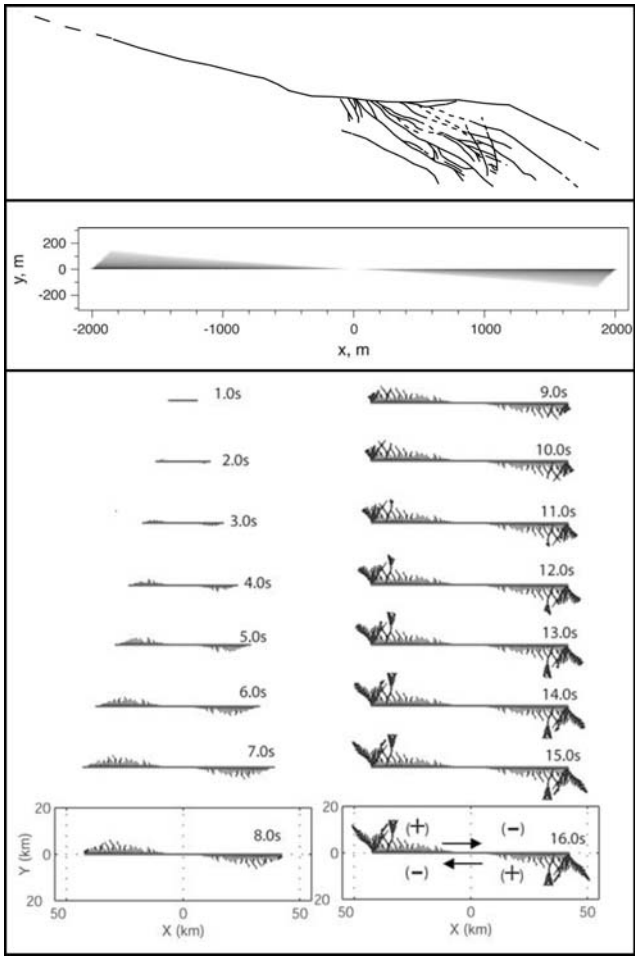

Figure 140. Comparison of the geometry of the GLF termination (top, map has been inverted to allow comparison of the left-lateral GLF with the right-lateral model faults) with the model predictions of Andrews (2005) (middle) and Dalguer *et al.* (2003; p. 5) (bottom). In each case off-fault damage is present in the dilational quadrant of the fault, with GLF splay fault orientations matching the orientations of new cracks developed under the model conditions of Dalguer *et al.* (2003).

7.2.3 Implications for rupture propagation

Models of rupture propagation (e.g. Harris and Day, 1999; Kase and Kuge, 2001) often assume that a slip patch or shear rupture propagates along a fault that is hosted in undeformed rock. However, the field data presented in this study indicate that fault

terminations at seismogenic depths are not contained within intact rock, and that the secondary structures associated with terminations take the form of macro-scale faulting, as well as likely micro-fracturing (Vermilye and Scholz, 1998). Fracturing of a host rock in this manner will change the bulk elastic properties of the rock (Ayling *et al.*, 1995; Ciccotti and Mulargia, 2004; Faulkner *et al.*, 2006; Nasseri *et al.*, 2007; O'Connell and Budiansky, 1974; Walsh, 1965), and lead to interaction between the secondary fractures and a dynamically propagating rupture front that will complicate the rupture growth (Andrews, 2005; Yamashita, 2000). The effects of pre-existing deformation on rupture processes must therefore be considered.

It is unlikely that the structures that comprise the end zone of the GLF were produced entirely by the most recent earthquake rupture as the individual splays have very large total displacements with respect to the magnitude of observed co-seismic slip. Slip on splay faults at the GLF termination was therefore accumulated over a significant fraction of the fault's history. This conclusion is reasonable as the majority of fault growth models that are derived from field observations (e.g. Chester and Logan, 1986; Mansfield and Cartwright, 1996; Martel, 1990; Seront *et al.*, 1998) predict that a zone of damaged rock evolves around a fault as a fault accumulates displacement. By the time a fault has grown to a size that would generate intermediate to large earthquakes, the rock surrounding the fault plane will contain numerous opening mode and shear fractures that will act as planes of preferential weakness. Successive earthquake ruptures occurring on the GLF must therefore have interacted with the pre-existing splay faults at the fault termination. Such subsidiary structures will also induce a heterogeneous spatial distribution of elastic properties. Willson *et al.* (2007) model cracks propagating through host rock with heterogeneous material properties and show that the locations and frequencies of evolving splay fractures are heavily influenced by the spatial distribution of such heterogeneities.

Models that examine the potential for ruptures to propagate beyond fault ends, or through stepovers between two faults (Harris and Day, 1999; Kase and Kuge, 2001) are directly investigating the zones where secondary structures are likely to be present. The effect of secondary macro- and micro-scale fracturing is to lower the elastic moduli of the medium in which they are contained (Walsh, 1965). The presence of pre-existing structures at fault terminations will therefore reduce the elastic moduli in those regions. Rice and Cocco (2007) suggest that understanding the high strain-rate constitutive response of the damage zone to dynamic slip is crucial to understanding the interaction between slip on a fault and its off-fault damage zone. They add that a non-linear response off the fault plane may alter

the normal stress on the fault itself (see also Faulkner *et al.* (2006)), and affect the energy balance of an earthquake rupture. A similar distribution of subsidiary structures would also be predicted at other discontinuities such as stepovers. Defining the extent and nature of the secondary structures around faults is therefore crucial to allow the effects of the damaged rock to be accounted for in models of rupture propagation.

7.2.4 Structural controls on aftershock distribution

The splay faults present in the end zone of the GLF are up to 3 km long and so could have experienced earthquakes up to magnitude Mw ~5.1 if the entire mapped length of the faults had slipped (Wells and Coppersmith, 1994). This magnitude is a similar size to observed aftershocks following magnitude Mw ~5.7 mainshocks, the maximum magnitude of an earthquake that would rupture the entire length of the GLF (e.g. Scholz, 2002). Areas of positive changes in Coulomb failure stress have been shown to correlate with the distribution of aftershocks around mainshock ruptures (Freed, 2005; King *et al.*, 1994; Toda *et al.*, 1998). Stress transfer modelling by Steven Micklethwaite of a GLF slip event shows that the distribution of splay faults correlates well with areas of positive Coulomb failure stress developed in response to slip on the GLF (Figure 141). This suggests that shear displacement on the splays could have accumulated during aftershock activity associated with a rupture on the main GLF fault plane. The splay faults at the GLF termination are approximately planar structures with a narrow range of orientations (see Figure 17), so aftershocks nucleating on the splays would have a limited range of possible focal mechanisms. Slip vectors measured from slickenlines exposed on the splay faults show more oblique rakes than the main fault (Figure 10), consistent with slip vectors calculated from static stress transfer modelling (Figure 141). The field data and model results therefore predict that any aftershocks should also have oblique slip vectors. These results suggest a strong structural control on the distribution and focal mechanism of aftershocks when a rupture end coincides with a fault termination.

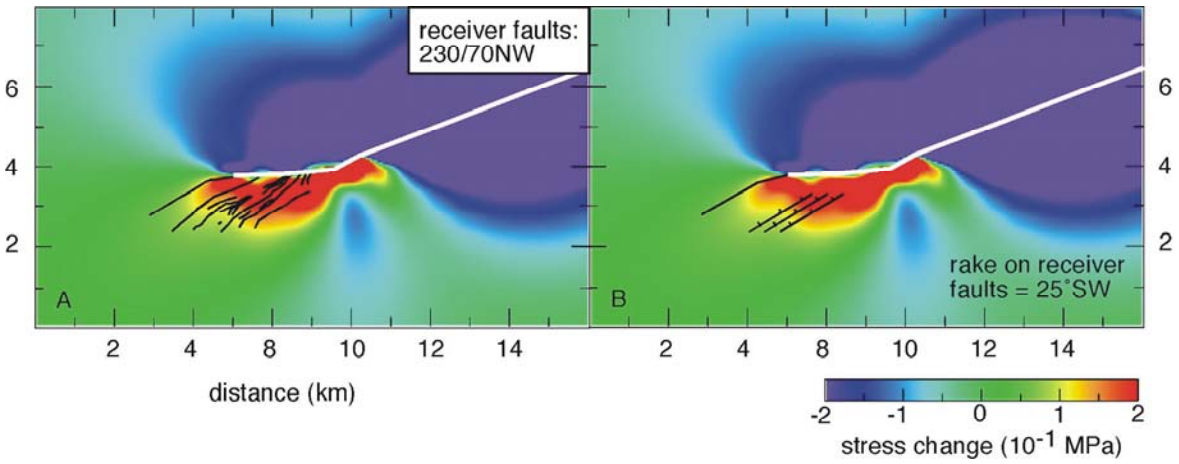

Figure 141. Coulomb failure stress change comparing stress change due to fault slip on the GLF to the distribution of the splay faults; model results produced by Steven Micklethwaite for Kirkpatrick *et al.* (in press).

Hardebeck (2006) showed that the focal mechanisms of closely spaced aftershocks of the 1989 Loma Prieta earthquake were very similar on scales of 0.5-5 km. At larger scales the aftershock focal mechanisms became increasingly heterogeneous, leading to the conclusion that that the homogeneity of the small-scale aftershock focal mechanisms was due to faults of similar orientations slipping in each aftershock. Collettini and Trippetta (2007) suggest that in typical continental crust there is a wide range of fault orientations that could slip during an earthquake, but that only the faults optimally oriented for slip will be triggered to form aftershocks. However, if a systematic distribution of secondary structures is present around the main fault, as is the case for the GLF, then it seems likely that the orientations of the secondary structures would control the aftershock focal mechanisms, rather than the orientation of the regional stress field. A narrow range of aftershock focal mechanisms determined by pre-existing fault termination structures should therefore be expected for currently active faults.

7.3 Slip weakening mechanisms in Sierra Nevada seismogenic faults

7.3.1 Identification criteria for slip weakening mechanisms in natural faults

Fault-related slip weakening mechanisms have been extensively investigated using theoretical models that utilise field and lab measurements of some of the important physical parameters in the models (see section 1.5 for a review of slip weakening mechanisms). Many of the theoretical models make assumptions regarding the nature of co-seismic slip that are inferred from geologic evidence, for example that in a fault zone

shear is localised within a fault core of fault gouge or ultracataclasite, and that fault zones are fluid-saturated. All of the proposed slip weakening mechanisms are shown to achieve a slip- or velocity-dependent reduction in shear strength. Some models have predicted well other earthquake parameters, such as the fracture energy or strong motion spectra, which can be independently measured in a rupture event. However, whether any particular slip weakening mechanism is predominant during a rupture event or within a fault zone remains unknown. This is fundamentally due to the difficulty in analysing tectonically active faults; the majority of earthquake slip occurs at depth in the crust and is localised onto structures that are too small-scale to be investigated using geophysical methods.

Geologic observations of exhumed seismogenic faults should provide direct insight into earthquake rupture processes, including the slip weakening mechanisms active in a fault zone, because fault zones are the product of accumulated slip. However, little unequivocal evidence has been reported in support of any of the mechanisms, and few of the theoretical models make predictions regarding the microstructures or textures that slip weakening mechanisms would produce in fault rocks so recognising the products of the various mechanisms is difficult. The lack of positively identified slip weakening mechanisms is also in part because there are significant problems in relating co-seismic slip products to field and micro-scale observations of faults; definitive indicators of seismic activity are lacking to the extent that only pseudotachylytes are accepted as explicitly recording earthquake ruptures, and the products of co-seismic slip are likely to be re-worked or altered by fluid flow during progressive deformation or exhumation of a fault.

The rest of this section will be used to review the reported structural evidence for active slip weakening mechanisms, and to highlight those textures and microstructures that might be expected to be associated with some mechanisms that have yet to be positively identified in natural faults. This will enable the slip weakening mechanisms in the Sierra Nevada faults to be analysed fully in the next section.

Melt lubrication is an effective slip weakening mechanism if a continuous layer of melt forms during slip (Di Toro *et al.*, 2006; Hirose and Shimamoto, 2005a), and is the best described slip weakening mechanism in natural faults. The structural organisation of pseudotachylyte veins within faults shows that pseudotachylytes are generated by frictional heating along slip surfaces (Sibson, 1975; Swanson, 1992). Thin section and SEM analyses of pseudotachylytes demonstrate a melt origin for these rocks where compositional and textural characteristics of glass or rapidly quenched melt can be

identified (Maddock, 1983; Magloughlin, 1992). Pseudotachylytes are well documented in faults such as the Outer Hebrides fault zone (Sibson, 1975) Alpine fault, New Zealand (Barker, 2005), and the Gole Larghe fault zone, Italian Alps (Di Toro *et al.*, 2005a; Di Toro and Pennacchioni, 2004). Melt lubrication is inferred to have been active during seismic slip events along these faults, and pseudotachylytes are assumed to be indicative of this slip weakening mechanism.

Flash heating involves heat generation at asperity contacts across a sliding surface (e.g. Rice, 2006). The physical products of flash heating should be deformed asperity contacts and small (micro- to nano-scale) pockets of quenched melt at asperity boundaries (Goldsby, 2007). These potential signatures of flash heating are exceptionally fine-scale, and the likelihood of small amounts of amorphous melt remaining undeformed or unaltered in a fault zone seems small. Similarly, silica gel, which is composed of an amorphous silica-water mix, might form thin films of amorphous material coating a fault surface (Goldsby, 2007). Any silica gel films would become brittle after rapid slip and could easily be re-worked or altered.

Thermal pressurization and elastohydrodynamic lubrication both require fluidized slipping zone materials. Fluidized gouges are observed in some fault zones (Lin, 1996; Miller and Cowan, 1998; Rowe *et al.*, 2005), and are thought to be indicative of high pore pressures during slip events, but injection veins containing gouge are very rarely reported. The fluid transport properties of fault zones have been studied in outcrop and through permeability measurements (e.g. Wibberley and Shimamoto, 2005), but thin section evidence describing the active slipping zone is only partly developed (e.g. Noda and Shimamoto, 2005).

7.3.2 Evidence for slip weakening in the Sierra Nevada

7.3.2.1 Pseudotachylytes and melt lubrication

Five of the faults in the central Sierra Nevada described in this study contain pseudotachylytes. Pseudotachylytes are accepted as the only evidence for slip events occurring at seismic velocities (Cowan, 1999; Sibson, 1975). Earthquakes were thus common on these faults, and melt lubrication was likely significant during the rupture events.

The DBF is a small displacement (<1m) fault in the Mount Abbot Quadrangle that contains pseudotachylytes. The conventional interpretation of pseudotachylytes implies that the

DBF experienced earthquake ruptures at seismic velocities. The conditions during co-seismic slip on this fault were such that the onset of melting was reached for small slip magnitudes (likely <10mm, see section 5.7.3). However, pseudotachylyte generation on the DBF did not occur by bulk melting; the composition of the melt is not similar to the host rock composition suggesting that melting is extremely localised, and that melt mixing is limited (section 5.5.2.2). The scale of the melt (millimetre-scale thickness) suggests that frictional heating occurred at much greater spatial scales than that inferred to be generated at the micro-asperities associated with flash heating. Slip weakening by melt lubrication might be inferred, but whether slip weakening was achieved is unclear as the inferred magnitude of coseismic slip is smaller than any previously reported slip weakening distance (see section 5.7.3).

Various studies analyse the environmental and slipping zone properties under which melting can be achieved, including for low slip magnitudes (Kanamori and Heaton, 2000; Rempel and Rice, 2006). In general, thermal processes are thought to become increasingly important for larger earthquakes since the heat is continuously produced during slip. However, the permeability structure of a fault zone is critical to the heat production and transport during slip (Rempel and Rice, 2006). Rempel and Rice (2006) show that the onset of melting during slip is promoted by more efficient fluid escape associated with high permeabilities, and by larger increases in pore pressure associated with higher initial values of the effective stress. The DBF permeability properties have not been measured in this study, but it is clear that a sharp contrast must be present between the fault rock and the wall rock. This confinement of the slipping zone suggests that the initial effective stress must have been high (i.e. the fault contained little pore fluid).

The GPF (displacement <100m) is a relatively mature seismogenic fault that has undergone multiple slip events, and has hosted extensive fluid flow and hydrothermal mineralisation through much of its deformation history. Sibson (1973) suggested that melt generation is unlikely to occur in mature fault zones in which fault-hosted fluids decrease the effective normal stress across the slipping zone (i.e. thermal pressurization is prevalent). Pseudotachylytes are present in the GPF as undeformed veins of quenched melt and as fragments in fault breccias and cataclasites. Evidence for syn-deformation fluid-related alteration is present in the form of chlorite and epidote mineralisation in the cataclasites, some of which were subsequently cross-cut by pseudotachylytes. Chlorite is also a significant constituent of fault rocks containing pseudotachylyte fragments. Fluids were therefore present in the faults before, after, and potentially during slip events, but

clearly did not preclude melt generation. Melting of fluidized material has been previously reported (Rowe *et al.*, 2005), supporting the conclusion that fluids do not always inhibit heat production sufficiently to inhibit melting.

A single through-going pseudotachylyte generation surface cannot be identified in the GPF. Field observations of pseudotachylytes in the GPF are inevitably limited in scale by exposure. However, multiple pseudotachylytes have been observed in several localities demonstrating that there is no systematic spatial distribution of the pseudotachylytes with respect to the fault architecture. The spatial distribution of pseudotachylytes mapped in the fault suggests that melt is developed in patches that are of the order of metres long. This implies that although melt generation occurred along the GPF, the concept of an earthquake rupture being defined in the field by a continuous generation surface is not valid for the GPF. A similar inference can be made directly for the SKF where a single outcrop contains one pseudotachylyte patch ~4m long. In the SKF, there is an apparent correlation with the fault core thickness; where the fault core is narrower (<1cm), pseudotachylytes are developed but where it is wider cataclasites are present. As with the DBF, melt lubrication is not necessarily an effective slip-weakening mechanism for the GPF and SKF.

7.3.2.2 Cataclasites, injection veins and pressurized fluids

Fluidized fault breccias in the GPF were likely produced during co-seismic slip. In particular the fault breccia in sample GPF10 (see section 4.4.1) has several characteristics indicative of a seismically-induced texture. The injection-vein like geometry of the breccia-wall rock irregularity is similar to injection veins associated with pseudotachylytes and fluidized gouge in shallow faults that cut sedimentary rocks, both of which are inferred to form in response to slip events (Lin, 1996; Miller and Cowan, 1998). The fault breccia also contains angular fragments of cataclasite, suspended in an incohesive, gouge-like, chlorite-rich matrix. These fragments have undergone little comminution both during and since the brecciation event, and the chlorite matrix demonstrates that fluid was associated with the brecciation event. Distributed cataclastic flow or brittle comminution cannot explain these features of the GPF fault breccia.

The fluidized breccias therefore formed by rapid dilation events, associated with high fluid pressures. In other parts of the GPF, fluid flow alteration and precipitation of hydrothermal minerals has occurred without brecciation. Elevated pore pressures, as well as perhaps temperatures, must therefore be associated with the fluidized breccia in GPF10.

These conditions are implied by the models of thermal pressurization and elastohydrodynamic lubrication. The fault breccia may therefore represent the direct product of these slip-weakening mechanisms. If the fluidized breccia in GPF10 is the product of coseismic slip, then the slipping zone thickness defined by the breccia is ~20mm thick. The thickness of the coseismic slipping zone inferred from the fluidized breccia is therefore consistent with the thicknesses predicted by both elastohydrodynamic lubrication (1 to 5mm; Brodsky and Kanamori, 2001) and thermal pressurization (less than several centimetres; Wibberley and Shimamoto, 2005).

Other breccias developed in the GPF fault are not associated with injection veins (e.g. the unfoliated cataclasite in GPF11, section 4.4.3). Identifying these fault rocks as the product of co-seismic slip is therefore more difficult, but they still likely result from elevated pore pressures and could result from thermal pressurization. The fault breccias represent catastrophic failure, and consistently contain a significant component of chlorite. Fragments of cataclasite within the breccias show that previously deformed rock has been brecciated. The brecciation event therefore represents a change in the rheological response of the fault rock to deformation, otherwise cataclasites would continue to deform and accommodate slip by cataclastic-flow. There is little evidence in the composition of the cataclasite fragments for strengthening or healing of the fault rock by cementation. Strain-hardening behaviour might explain a change in the deformation response of the rock. However, where strain-hardening is inferred in other rocks deformation is thought to transfer laterally away from the hardened material. The most likely explanation for the brecciation is a change in the strain rate, which would change the mechanical response of the fault rock. Seismic slip occurs at rapid velocities; the GPF is a seismogenic fault and so it seems likely that brecciation is caused by rapid slip events.

The northern strand of the SKF at locality 1 contains pseudotachylytes juxtaposed laterally along strike with cataclasites. Earthquake ruptures are therefore be inferred to have occurred on this strand of the fault zone. Similar cataclastic or brittle fault rock textures to those in the GPF that are inferred to develop in response to co-seismic slip might be expected to develop in the cataclasites immediately adjacent to pseudotachylytes. However, the cataclasites adjacent to the SKF pseudotachylyte are either foliated cataclasites, or random fabric cataclasites. These textures are typical of cataclasite fault rocks, and cannot be unequivocally associated with earthquake ruptures. The spatial distribution of the fault rocks in outcrop suggests that these typical fabrics must be

associated with rapid slip events. In the case of the cataclasites of the northern strand of the SKF, no particular slip weakening mechanism can be recognised as being active.

Field and thin section observations of brittle fault rocks from the Sierra Nevada demonstrate that recognising active slip weakening mechanisms is difficult. Pseudotachylytes and fluidized fault breccias are likely the products of melt lubrication and thermal pressurization respectively. However, cataclasites that are laterally adjacent to patches of pseudotachylyte do not contain diagnostic evidence for any particular slip weakening mechanism, or slip events that occurred at high velocities, even though their spatial association with pseudotachylytes suggests they are likely to be coseismic.

7.3.3 Implications for earthquake rupture processes

Field and microstructural evidence show that no single slip weakening mechanism can account for the dynamic reduction in shear strength associated with ruptures in the Sierra Nevada faults. This implies that active slip weakening mechanisms are spatially heterogeneous during a rupture event. The best evidence for this is the limited extent of friction-induced melting inferred from pseudotachylytes. Pseudotachylytes and cataclasites are mixed along strike at both outcrop and thin section scales, and are shown to have deformed in the same slip event. The earthquake rupture that formed these pseudotachylytes therefore required multiple active slip weakening mechanisms, which were spatially variable. Additionally, brecciated pseudotachylytes attest to slip-weakening mechanisms progressively changing from melt lubrication to thermal pressurization or elastohydrodynamic lubrication. This change in process may be during a single slip event, or from rupture to rupture. Heterogeneous slip weakening mechanisms in space and time suggest that the inherently heterogeneous properties of fault zones (slipping zone thickness and geometry, fluid-flow history, permeability properties) dictate which slip weakening mechanism is active during slip. At any point on a rupture surface, it might therefore be inferred that slip weakening mechanisms are competing; the mechanism that reduces frictional strength the most rapidly for the fault properties at that point is likely to be active. This also shows that extrapolating experimental data that constrain the slip weakening distance up to the scales of natural faults is likely not appropriate unless a particular fault is shown to have consistent properties in three dimensions with progressive slip.

Progressively changing deformation conditions during coseismic slip are recorded by pseudotachylytes (melt generation), injection veins containing melt or fluidized fault

breccias (mass transfer and/or pore pressure changes or adiabatic heat transfer), and progressively more comminuted cataclasites. The changes in deformation conditions provide feedbacks to the conditions under which seismic slip is occurring. For example, Rice (2006) uses slipping zone thicknesses measured from the Punchbowl and Median Tectonic Line faults in models of thermal pressurization. However, brecciation and injection of fluidized material into the wall rock in response to elevated pressures in fault zones suggest that where the response of the fault rock to elevated pore pressure is non-elastic, a drastic rapid decrease in pressure after some peak value will occur. As noted by Noda and Shimamoto (2005), there is no direct evidence for localised seismic slip on the most comminuted ultracataclasites in major faults, but they are assumed to be the product of many localized slip events. A simple measurement of the thickness of a prominent ultracataclasite cannot account for changes in the properties of the slipping zone induced during slip. Such changes in permeability properties of fault rocks during slip might mask the processes that occur during the early stages of slip.

7.4 Conclusions

- Field and microscope observations have constrained the intrinsic controls on the GPF architecture: the fault cuts isotropic crystalline host rock, is at least 8km, has approximately 80m of left-lateral strike slip displacement, and fluid-fault rock interaction has been extensive during the lifetime of the fault.

- Extrinsic controls on fault zone architecture require the deformation history of the fault to be reconstructed. The GPF deformation progressed from high temperature ductile deformation to low temperature brittle deformation as the host rock pluton was exhumed.

- The controls on the GPF model architecture have been defined and show that the model is likely transferrable to faults in other plutonic or basement rocks that are undergoing cooling and/or exhumation.

- The GPF model is similar to a model based on the Carboneras fault, but is not similar to the Punchbowl-type model. This is likely due to the geometry of the fault imposed by the earliest deformation structures that are strongly influenced by the host rock lithology.

- Due to the differences in exhumed fault architectures, investigations into the fluid flow properties or processes associated with co-seismic slip should utilise appropriate fault

zone models. However, processes that are generic to faults or earthquake ruptures must be transferrable between the different models.

- The left-lateral Glacier Lakes fault, Sierra Nevada, CA, has been exhumed from ~6-8 km depth. Field observations show that the western termination of the fault is defined by a series of splay faults, up to 3km long, forming dihedral angles of 13-60 ° with the main fault trace, that extend into the dilational quadrant of the fault.

- Pseudotachylytes identified within the fault core of the GLF indicate that the fault was at least in part seismically active.

- The geometry of the GLF termination is similar to those of other exhumed faults in the Sierra Nevada and elsewhere, and to the terminations of earthquake ruptures observed at the Earth's surface.

- Field observations of the exhumed GLF demonstrate that the complexity observed in association with the terminations of fault traces at the surface can also be expected at seismogenic depths.

- Splay fault geometry at the tip of the GLF is well-predicted by quasi-static models of fault growth. The zone of deformation at the fault tip defined by the splays also appears to match the predictions of off-fault damage associated with dynamic rupture propagation.

- The elastic properties of host rocks are different at fault terminations and stepovers due to the accumulation of damage structures in these regions, and must be accounted for in models of dynamic rupture propagation beyond fault terminations, or across other structural discontinuities.

- Aftershock distributions and focal mechanisms may be controlled by the size, geometry and kinematics of structures present at fault terminations.

- Theoretical analyses of slip weakening mechanisms make few explicit predictions as to the micro-scale structures or textures that might be used to identify active slip weakening mechanisms in natural fault zones.

- Pseudotachylytes are observed along small faults in the Sierra Nevada, as well as more mature fault zones in which both pre-seismic and post-seismic fluid flow can be identified.

- In the Sierra Nevada faults, pseudotachylytes are difficult to relate to a slip weakening distance where the coseismic slip is inferred to be small. Melt lubrication cannot account for dynamic slip weakening in more mature fault zones as there are no continuous generation surfaces at the scale of the fault zones.

- Multiple slip weakening mechanisms must have been active during single rupture events. Slip weakening mechanisms also change at a given point on the fault in response to continued deformation. This suggests active slip weakening mechanisms compete during earthquake ruptures.

- The spatial heterogeneity on fault zone properties likely controls the extent of active slip weakening mechanisms during coseismic slip. Extrapolating modelling and lab predictions of the slip weakening distance to natural faults is therefore problematic

8

Further Work

8.1 Fieldwork

Further fieldwork in the Granite Pass study area could be beneficial in a number of ways. Defining the lengths of the GPF and GPF-parallel faults would allow the faults to be related to earthquakes through scaling relations between length and magnitude. Determining the length of the GLF by defining the termination of the fault in the east would allow the fault geometry to be more confidently compared to models of earthquake rupture processes. Identifying the terminations of the GPF and GPF-parallel faults would be essential to defining the fault lengths. If the terminations are well-exposed, the structures in the end zones of the faults could be mapped and compared to the GLF splays as an additional measure for understanding the fault architectures of the GLF and GPF fault systems.

Identifying more offset markers for each of these faults would provide a much more precise estimate of the magnitude of total displacement. The number of earthquakes experienced by each fault could then be inferred, and the changes that occur in fault zone architecture with increased displacement might be clarified. Cumulative slip profiles would also show how much the faults are interacting with each other. The GPF and GPF-parallel faults are relatively closely spaced so the lateral extent of interaction through stress intensification near fault terminations could be constrained by constructing accurate slip profiles near the fault terminations. The interaction of the GLF splays and the GPF-parallel faults could also be highlighted with better-defined slip profiles. If these two systems of faults were coeval then the slip profiles along the GPF-parallel faults might show a slip deficit in the vicinity of the splays. If the systems of faults were in part coeval, displacement data would also provide constraints for models of rupture propagation through stepover zones.

Reconnaissance fieldwork undertaken in this study suggests that there are more faults to the south of the GPF that might be well exposed to the south of Granite Pass in Granite Basin. The orientation of these faults suggests that they are likely an extension of the GPF system of faults. Elevation falls rapidly to the south of Granite Pass, so faults to the south of the GPF could provide exposures exhumed from deeper structural levels. Comparing faults exposed from deeper in the crust with the GPF and GPF-parallel faults would provide massive insight into earthquake rupture propagation as the system of faults was apparently active near the base of the seismogenic zone (defined by the frictional-viscous transistion; Sibson, 1982). Faults exposed at lower modern elevations would also provide insight into the 3D architecture of the fault zones.

Data and observations describing The GLF architecture are limited in this study as the internal portions of the fault are generally poorly exposed. If further exposures of the GLF could be found, most likely to the east of Glacier Lakes, this would show how realistic the model of GLF architecture proposed in this study is. Similarly, samples of the GLF were difficult to collect because the fault was not exposed. More samples would illustrate the reliability of the interpretation of the fault deformation history. In general, more exposures would be useful for all of the faults to ascertain the variability in the along-strike architecture of the faults, and to add more confidence to the models of fault architecture.

8.2 Microfractures

The damage zones of the faults in the Granite Pass study area likely comprise numerous microfractures (e.g. Faulkner *et al.*, 2006). Previous studies have shown that the damage zone width is a function of the deformation element used to define the damage zone (Schulz and Evans, 2000; Wilson *et al.*, 2003). The damage zone width is greater when defined by microfractures in these studies, so given the likely microfractures in the damage zones of GPF, GLF and GPF-parallel faults the measured widths would change if micro-scale analyses were conducted. If oriented samples are collected for microfracture analysis, the orientations of the fractures can be measured as well as density and compared to the predictions of models of fault processes to distinguish between processes such as process zone propagation or rupture propagation (Vermilye and Scholz, 1998; Yamashita, 2000). Oriented microfracture analyses would also be useful for the small faults in the Mount Abbot Quadrangle where the identification of pseudotachylytes in this study suggests dynamic rupture propagation is an important process in these faults. Previous models that predict the faults behaved quasi-statically (e.g. Martel and Boger, 1998) could

be tested by analysing the microfracture density, distribution and orientation around small faults; reactivated joints should have fewer microfractures near the centre of the faults as microfractures develop in response to stress intensification at fault tips. Propagating rupture fronts might leave a wake of damage that could explain such a fracture distribution.

Measurements of microfracture orientations and distributions applied to fault rocks can show how cataclasites develop, and can be used to infer the slip mechanisms, and grain-scale controls on fault strength (e.g. Evans, 1990). Evans (1990) measured fracture lengths, densities and orientations along ten transects across fault rocks in each of two mutually perpendicular thin sections. Applying this technique to GPF and GLF cataclasites might provide added insight into the style of deformation and interactions between fault rocks and fault-hosted fluids in the two faults.

Significant microfracture densities have been observed immediately adjacent to many of the slip surfaces studied in thin section. Recent work has defined pulverized fault zone rocks (PFZRs) as a deformation element in the damage zone of the San Andreas fault, and other faults in California (Dor *et al.*, 2006). These rocks are defined as 'mainly to crystalline plutonic and metamorphic rocks that were mechanically pulverized to the micron or finer scale, while preserving most of their original fabric and crystal boundaries'. Many of the intensely fractured rocks adjacent to slip surfaces in the Granite Pass faults retain their original crystalline texture, and their crystal shape can be easily defined because the amount of shear on the fractures is small (often <10μm). As such, these rocks might be classified as PFZRs. However, Dor *et al.* (2006) show that PFZRs are limited to the top few kilometres of the crust, which does not correlate well with the deformation history of the Pyramid pluton faults. Analysing the fractured rocks from the Pyramid pluton faults using the techniques of Dor (2007) and Dor *et al.* (2007) would determine whether these rocks are 'pulverized', and if so would imply that the rupture processes inferred to cause pulverization apply to these faults.

8.3 Fault rock compositions

The fault core deformation elements analysed for the GPF show variable chlorite and epidote content, despite cross-cutting relations evident in hand specimen and outcrop. It is therefore apparent that the cataclasites and ultracataclasites of the GPF fault cores are not well mixed with respect to the products of hydrothermal mineralisation, and that some deformation elements were susceptible to cementation, whilst others were not. Whole rock X-ray fluorescence (XRF) of major, minor and trace elements applied to samples of

different deformation elements would quantitatively measure the composition of the samples. As the cataclasites and ultracataclasites are all derived from a single host rock, differences between deformation elements would likely represent different fluid-flow histories. The localisation of fluid flow could therefore be constrained within the fault cores, and correlated with cataclastic processes. Distinctive trace element data might also provide a signature to 'track' the progressive comminution of some deformation elements, or to map coeval fluid flow pathways. Samples of the damage zone could also be incorporated into these analyses. Fluid inclusions in the distinctive quartz veins in the ultracataclasites could be analysed to show the temperature, pressure and fluid composition accompanying cataclastic flow in the ultracataclasites.

8.4 Slip surfaces

Slip surfaces are defined in this study by inferring localised cataclasite from extremely fine-grained material that localised in seams that cross-cut other fault rocks. A wide range of fracture types, orientations with respect to the fault zone and magnitudes of displacement have been observed. A technique for quantifying the poro-elastic properties of slip surface material could be to accurately measure the grain size distribution; the surfaces are defined by a large proportion of 'matrix' in thin section. Analysing a suite of slip surfaces with a range of displacements would show if a characteristic grain size distribution could be recognized and be used as a quantitative identification criteria for a slip surface where cross-cutting relations are not obvious.

Slip surface permeability is closely related to grain size distribution, and plays a significant role in controlling the slip weakening mechanism for a particular rupture event (Rempel and Rice, 2006; Rice, 2006; Segall and Rice, 2006). Recent studies are providing more data to estimate the permeability of the slipping zone (Noda and Shimamoto, 2005; Wibberley and Shimamoto, 2005), but measuring permeabilities for the Granite Pass faults would provide the first data set from a single host rock fault, and from faults with small seismogenic faults. In particular, measurements would be useful in combination with the observations of fault architecture which show lateral heterogeneity in slip surface geometry, and apparently patchy active slip weakening mechanisms. Permeabilities could also be measured for cataclasites, fault breccias and the host rock so that a detailed model of the permeability structure of the fault could be constructed. This would place constraints on thermal and hydrological boundary layer thicknesses, and could be related to fault-valve behaviour (Sibson, 1985).

The northern fault core strand has a slip surface thickness that can be confidently shown to vary within metres along strike. Where the slip surface is thick (>1mm) cataclastic flow occurred, whereas melting was induced in the narrow portion (<1mm). Particle-based models have been used to investigate cataclastic flow and also rupture processes (Abe *et al.*, 2006) by embedding a slip surface with rough edges between two planar blocks. If the SKF north strand slipping zone geometry, in which the slip surface thickness changes by an order of magnitude, could be inserted into the model parameter it might demonstrate how the localization of slip is effects slip processes. In particular, localization might cause strain rate variations and/or changes in the slip velocity of particles in the slipping zone, which could induce local melting. This could also explain the limited extent of pseudotachylyte generation surfaces observed in other faults in the area. Such models would also indicate how a slip surface geometry such as the one defined for the SKF would change with continued deformation, and could constrain how fault core rocks mix. Differential fluid-flow may also by a product of changes in the slipping zone thickness.

8.5 Thermochronology

The K-Ar dating technique has been partially successful when applied to pseudotachylytes in this study. The close agreement in the K-Ar ages of each of the three samples suggests that the results might be useful, but as discussed numerous factors make interpreting the ages difficult. Potentially, constraining the proportion of clasts and compositions of the clasts through BSE imaging could be used to estimate the maximum input of inherited Ar to the measurements made during the analysis. Subtracting clast-sourced Ar, and K, from the age calculations could be achieved easily if these quantities were known.

Many recent studies have applied ^{39}Ar-^{40}Ar dating to pseudotachylytes, and have argued that the results can be rigorously interpreted (e.g. Pennacchioni *et al.*, 2006; Sherlock and Hetzel, 2001; Warr *et al.*, 2007). The ^{39}Ar-^{40}Ar technique could readily be applied to the SKF samples already dated in this study and would show how accurate the K-Ar method is for dating pseudotachylytes. An interesting comparison could be made by applying both techniques to experimentally-formed pseudotachylytes which have a known age of recent. Reliable pseudotachylyte ages would define the onset of brittle slip episodes on the SKF (given no crystal-plastic deformation of pseudotachylyte is observed), and therefore show the time and temperature at which the deformation mechanisms switched from crystal-plastic to brittle.

The temperature variation accompanying exhumation of the Pyramid pluton could be much better constrained by combined apatite (U-Th)/He and apatite fission track analysis. A vertical profile from the floor of Kings Canyon to the study area could be easily sampled as the route into the area follows a suitable path. The elevation gain is around 1500m. Inverse and forward modelling techniques can be applied to the fission track length distributions to ascertain the most likely exhumation path for the pluton (e.g. Persano *et al.*, 2005b), and would therefore allow lithostatic pressure and temperature variations to be calculated.

8.6 Earthquake energy partitioning

Wilson *et al.* (2005) and Chester *et al.* (2005) used grain size distribution analyses to investigate the development of fault gouge by earthquake rupturing and to infer the magnitude of the fracture energy component of the seismic energy budget. The fracture linkage model (Martel, 1990) could be used as a basis to further these two investigations. Similar grain size distribution analyses for samples of faults at each stage of fault development, combined with detailed maps of fault core and damage zone would provide two additional insights to the earthquake rupture process: firstly, recent studies have concluded that slip surfaces and slipping zones nucleate early in the history of a fault, which are then long-lived. This suggests that an early, large input of fracture energy is required to develop fault gouge, which is then re-pulverised continuously by repeated rupture propagation. The amount of energy consumed in creating new fracture surface area might therefore be small for later ruptures, and the radiation efficiency would change. The FLM provides a basis to investigate this as samples representative of various stages of fault evolution can be collected. Secondly, mapping the fault zones in detail at each stage of fault evolution could define the proportion of energy that has been consumed along the slipping zone, fault core and damage zone. Comparing different stages of evolution would therefore show whether the fracture energy is partitioned between the fault zone components differently as faults develop.

References

ABE, S., LATHAM, S. and MORA, P., 2006. Dynamic rupture in a 3-D particle-based simulation of a rough planar fault. *Pure And Applied Geophysics*, 163(9): 1881-1892.

AGUE, J.J. and BRIMHALL, G.H., 1988. Magmatic Arc Asymmetry and Distribution of Anomalous Plutonic Belts in the Batholiths of California - Effects of Assimilation, Crustal Thickness, and Depth of Crystallization. *Geological Society of America Bulletin*, 100(6): 912-927.

AKI, K., 1979. Characterization Of Barriers On An Earthquake Fault. *Journal Of Geophysical Research*, 84(NB11): 6140-6148.

ANDERSON, E.M., 1942. *The dynamics of faulting and dyke formation with applications to Britain*. Edinburgh : Oliver and Boyd, 1942.

ANDREWS, D.J., 1976. Rupture Propagation with Finite Stress in Antiplane Strain. *Journal of Geophysical Research*, 81(20): 3575-3582.

ANDREWS, D.J., 2002. A fault constitutive relation accounting for thermal pressurization of pore fluid. *Journal of Geophysical Research-Solid Earth*, 107(B12).

ANDREWS, D.J., 2005. Rupture dynamics with energy loss outside the slip zone. *Journal of Geophysical Research-Solid Earth*, 110(B1): art. no.-B01307.

AOCHI, H. and FUKUYAMA, E., 2002. Three-dimensional nonplanar simulation of the 1992 Landers earthquake. *Journal Of Geophysical Research-Solid Earth*, 107(B2).

AYDIN, A. and DU, Y.J., 1995. Surface Rupture at a Fault Bend - the 28-June-1992 Landers, California, Earthquake. *Bulletin of the Seismological Society of America*, 85(1): 111-128.

AYLING, M.R., MEREDITH, P.G. and MURRELL, S.A.F., 1995. Microcracking During Triaxial Deformation Of Porous Rocks Monitored By Changes In Rock Physical-Properties .1. Elastic-Wave Propagation Measurements On Dry Rocks. *Tectonophysics*, 245(3-4): 205-221.

BALDWIN, S.L., HARRISON, T.M. and FITZ GERALD, J.D., 1990. Diffusion of Ar-40 in Metamorphic Hornblende. *Contributions to Mineralogy and Petrology*, 105(6): 691-703.

BARKA, A., 1996. Slip distribution along the north anatolian fault associated with the large earthquakes of the period 1939 to 1967. *Bulletin of the Seismological Society of America*, 86(5): 1238-1254.

BARKER, S.L.L., 2005. Pseudotachylyte-generating faults in Central Otago, New Zealand. *Tectonophysics*, 397(3-4): 211-223.

BARTON, C.A., ZOBACK, M.D. and MOOS, D., 1995. Fluid-Flow Along Potentially Active Faults in Crystalline Rock. *Geology*, 23(8): 683-686.

BATEMAN, P.C., 1992. Plutonism in the central part of the Sierra Nevada Batholith, California. *U.S. Geological Survey Professional Paper*, 1483: 186pp.

BAYASGALAN, A., JACKSON, J., RITZ, J.F. and CARRETIER, S., 1999. Field examples of strike-slip fault terminations in Mongolia and their tectonic significance. *Tectonics*, 18(3): 394-411.

BERGBAUER, S. and MARTEL, S.J., 1999. Formation of joints in cooling plutons. *Journal of Structural Geology*, 21(7): 821-835.

BERGER, G.W. and YORK, D., 1981. Geothermometry From Ar-40-Ar-39 Dating Experiments. *Geochimica Et Cosmochimica Acta*, 45(6): 795-811.

BIZZARRI, A. and COCCO, M., 2006. A thermal pressurization model for the spontaneous dynamic rupture propagation on a three-dimensional fault: 1. Methodological approach. *Journal of Geophysical Research-Solid Earth*, 111(B5).

BLENKINSOP, T.G., 1991. Cataclasis and Processes of Particle-Size Reduction. *Pure and Applied Geophysics*, 136(1): 59-86.

BOUCHON, M., SEKIGUCHI, H., IRIKURA, K. and IWATA, T., 1998. Some characteristics of the stress field of the 1995 Hyogo-ken Nanbu (Kobe) earthquake. *Journal of Geophysical Research-Solid Earth*, 103(B10): 24271-24282.

BRODSKY, E.E. and KANAMORI, H., 2001. Elastohydrodynamic lubrication of faults. *Journal of Geophysical Research-Solid Earth*, 106(B8): 16357-16374.

BRUHN, R.L., PARRY, W.T., YONKEE, W.A. and THOMPSON, T., 1994. Fracturing and Hydrothermal Alteration in Normal-Fault Zones. *Pure and Applied Geophysics*, 142(3-4): 609-644.

BRUNE, J.N., BROWN, S. and JOHNSON, P.A., 1993. Rupture Mechanism and Interface Separation in Foam Rubber Models of Earthquakes - a Possible Solution to the Heat-Flow Paradox and the Paradox of Large Overthrusts. *Tectonophysics*, 218(1-3): 59-67.

BURGMANN, R. and POLLARD, D.D., 1992. Influence of the State of Stress on the Brittle-Ductile Transition in Granitic Rock - Evidence from Fault Steps in the Sierra-Nevada, California. *Geology*, 20(7): 645-648.

BURGMANN, R. and POLLARD, D.D., 1994. Strain accommodation about strike-slip fault discontinuities in granitic rock under brittle-to-ductile conditions. *Journal of Structural Geology*, 16(12): 1655-1674.

BURGMANN, R., POLLARD, D.D. and MARTEL, S.J., 1994. Slip Distributions On Faults - Effects Of Stress Gradients, Inelastic Deformation, Heterogeneous Host-Rock Stiffness, And Fault Interaction. *Journal Of Structural Geology*, 16(12): 1675-1690.

CAINE, J.S., EVANS, J.P. and FORSTER, C.B., 1996. Fault zone architecture and permeability structure. *Geology*, 24(11): 1025-1028.

CAINE, J.S. and TOMUSIAK, S.R.A., 2003. Brittle structures and their role in controlling porosity and permeability in a complex Precambrian crystalline-rock aquifer system in the Colorado Rocky Mountain Front Range. *Geological Society of America Bulletin*, 115(11): 1410-1424.

CARTWRIGHT, J.A., TRUDGILL, B.D. and MANSFIELD, C.S., 1995. Fault Growth by Segment Linkage - an Explanation for Scatter in Maximum Displacement and Trace Length Data from the Canyonlands Grabens of Se Utah. *Journal of Structural Geology*, 17(9): 1319-1326.

CHEN, J.H. and MOORE, J.G., 1982. Uranium-Lead Isotopic Ages From The Sierra-Nevada Batholith, California. *Journal Of Geophysical Research*, 87(NB6): 4761-4784.

CHESTER, F.M. and CHESTER, J.S., 1998. Ultracataclasite structure and friction processes of the Punchbowl fault, San Andreas system, California. *Tectonophysics*, 295(1-2): 199-221.

CHESTER, F.M., EVANS, J.P. and BIEGEL, R.L., 1993. Internal Structure and Weakening Mechanisms of the San-Andreas Fault. *Journal of Geophysical Research-Solid Earth*, 98(B1): 771-786.

CHESTER, F.M., FRIEDMAN, M. and LOGAN, J.M., 1985. Foliated Cataclasites. *Tectonophysics*, 111(1-2): 139-146.

CHESTER, F.M. and LOGAN, J.M., 1986. Implications for Mechanical-Properties of Brittle Faults from Observations of the Punchbowl Fault Zone, California. *Pure and Applied Geophysics*, 124(1-2): 79-106.

CHESTER, J.S., CHESTER, F.M. and KRONENBERG, A.K., 2005. Fracture surface energy of the Punchbowl fault, San Andreas system. *Nature*, 437(7055): 133-136.

CHRISTIANSEN, P.P. and POLLARD, D.D., 1997. Nucleation, growth and structural development of mylonitic shear zones in granitic rock. *Journal of Structural Geology*, 19(9): 1159-1172.

CICCOTTI, M. and MULARGIA, E., 2004. Differences between static and dynamic elastic moduli of a typical seismogenic rock. *Geophysical Journal International*, 157(1): 474-477.

CLARK, M.K., MAHEO, G., SALEEBY, J. and FARLEY, K.A., 2004. The non-equilibrium landscape of the southern Sierra Nevada, California. *GSA Today*, 12(9): 4-10.

COLLETTINI, C. and TRIPPETTA, F., 2007. A slip tendency analysis to test mechanical and structural control on aftershock rupture planes. *Earth and Planetary Science Letters*, 255(3-4): 402-413.

COOKE, M.L., 1997. Fracture localization along faults with spatially varying friction. *Journal of Geophysical Research-Solid Earth*, 102(B10): 22425-22434.

COWAN, D.S., 1999. Do faults preserve a record of seismic slip? A field geologist's opinion. *Journal of Structural Geology*, 21(8-9): 995-1001.

COX, A. and DALRYMPL.GB, 1967. Statistical Analysis of Geomagnetic Reversal Data and Precision of Potassium-Argon Dating. *Journal of Geophysical Research*, 72(10): 2603-&.

CRUIKSHANK, K.M., ZHAO, G.H. and JOHNSON, A.M., 1991. Analysis of Minor Fracture Associated with Joints and Faulted Joints. *Journal of Structural Geology*, 13(8): 865-886.

CUREWITZ, D. and KARSON, J.A., 1999. Ultracataclasis, sintering, and frictional melting in pseudotachylytes from East Greenland. *Journal of Structural Geology*, 21(12): 1693-1713.

D'ALESSIO, M.A. and MARTEL, S.J., 2004. Fault terminations and barriers to fault growth. *Journal of Structural Geology*, 26(10): 1885-1896.

DALGUER, L.A., IRIKURA, K. and RIERA, J.D., 2003. Simulation of tensile crack generation by three-dimensional dynamic shear rupture propagation during an earthquake. *Journal Of Geophysical Research-Solid Earth*, 108(B3).

DALRYMPLE, G.B. and LANPHERE, M.A., 1969. *Potassium-Argon Dating; Principles, Techniques and Applications to Geochronology*. W. H. Freeman and Company, 258 pp.

DALRYMPLE, G.B. and MOORE, J.G., 1968. Argon-40 - Excess in Submarine Pillow Basalts from Kilauea Volcano Hawaii. *Science*, 161(3846): 1132-&.

DAVIES, R.K. and POLLARD, D.D., 1986. Relations between Left-Lateral Strike-Slip Faults and Right- Lateral Monoclinal Kink Bands in Granodiorite, Mt Abbot Quadrangle, Sierra-Nevada, California. *Pure and Applied Geophysics*, 124(1-2): 177-201.

DECARITAT, P., HUTCHEON, I. and WALSHE, J.L., 1993. Chlorite Geothermometry - a Review. *Clays and Clay Minerals*, 41(2): 219-239.

DENG, Q.D., WU, D.N., ZHANG, P.Z. and CHEN, S.F., 1986. Structure And Deformational Character Of Strike-Slip-Fault Zones. *Pure And Applied Geophysics*, 124(1-2): 203-223.

DEPOLO, C.M., CLARK, D.G., SLEMMONS, D.B. and RAMELLI, A.R., 1991. Historical Surface Faulting In The Basin And Range Province, Western North-America - Implications For Fault Segmentation. *Journal Of Structural Geology*, 13(2): 123-136.

DI TORO, G., GOLDSBY, D.L. and TULLIS, T.E., 2004. Friction falls towards zero in quartz rock as slip velocity approaches seismic rates. *Nature*, 427(6973): 436-439.

DI TORO, G., HIROSE, T., NIELSEN, S., PENNACCHIONI, G. and SHIMAMOTO, T., 2006. Natural and experimental evidence of melt lubrication of faults during earthquakes. *Science*, 311(5761): 647-649.

DI TORO, G., NIELSEN, S. and PENNACCHIONI, G., 2005a. Earthquake rupture dynamics frozen in exhumed ancient faults. *Nature*, 436(7053): 1009-1012.

DI TORO, G. and PENNACCHIONI, G., 2004. Superheated friction-induced melts in zoned pseudotachylytes within the Adamello tonalites (Italian Southern Alps). *Journal of Structural Geology*, 26(10): 1783-1801.

DI TORO, G. and PENNACCHIONI, G., 2005. Fault plane processes and mesoscopic structure of a strong-type seismogenic fault in tonalites (Adamello batholith, Southern Alps). *Tectonophysics*, 402(1-4): 55-80.

DI TORO, G., PENNACCHIONI, G. and TEZA, G., 2005b. Can pseudotachylytes be used to infer earthquake source parameters? An example of limitations in the study of exhumed faults. *Tectonophysics*, 402(1-4): 3-20.

DI VINCENZO, G., ROCCHI, S., ROSSETTI, F. and STORTI, F., 2004. Ar-40-Ar-39 dating of pseudotachylytes: the effect of clast-hosted extraneous argon in Cenozoic fault-generated friction melts from the West Antarctic Rift System. *Earth and Planetary Science Letters*, 223(3-4): 349-364.

DIETERICH, J.H., 1978. Time-Dependent Friction and Mechanics of Stick-Slip. *Pure and Applied Geophysics*, 116(4-5): 790-806.

DOBLAS, M., 1998. Slickenside kinematic indicators. *Tectonophysics*, 295(1-2): 187-197.

DODGE, G.C.W. and MOORE, J.G., 1968. Occurrence and composition of biotites from the Cartridge Pass pluton of the Sierra Nevada batholith, California. *U.S. Geological Survey Professional Paper*, 600-B: 6-10.

DODSON, M.H., 1973. Closure Temperature in Cooling Geochronological and Petrological Systems. *Contributions to Mineralogy and Petrology*, 40(3): 259-274.

DOR, O., 2007. *Symmetry Properties, Pulverized Rocks and Damage Architectures in Fault Zones as Signatures of Earthquake Ruptures*. PhD Thesis Thesis, University of Southern California.

DOR, O., BEN-ZION, Y., CHESTER, J.S., BRUNE, J. and ROCKWELL, T., 2007. Damage characterization in sandstones along the Mojave section of the San Andreas Fault with a new method: initial results and implications for the depth and mechanism of dynamic rock fragmentation *American Geophysical Union Fall 2007 Meeting*

DOR, O., BEN-ZION, Y., ROCKWELL, T.K. and BRUNE, J., 2006. Pulverized rocks in the Mojave section of the San Andreas Fault Zone. *Earth And Planetary Science Letters*, 245(3-4): 642-654.

DUCEA, M. and SALEEBY, J., 1998. Crustal recycling beneath continental arcs: silica-rich glass inclusions in ultramafic xenoliths from the Sierra Nevada, California. *Earth and Planetary Science Letters*, 156(1-2): 101-116.

DUCEA, M.N. and SALEEBY, J.B., 1996. Buoyancy sources for a large, unrooted mountain range, the Sierra Nevada, California: Evidence from xenolith thermobarometry. *Journal of Geophysical Research-Solid Earth*, 101(B4): 8229-8244.

DUYSTER, J., 2000. StereoNett v. 2.46.

EVANS, J.P., 1990. Textures, deformation mechanisms, and the role of fluids in the cataclastic deformation of granitic rocks. In: R.J. KNIPE and E.H. RUTTER (Editors), *Deformation Mechanisms, Rheology and Tectonics*, pp. 29-39.

EVANS, J.P. and CHESTER, F.M., 1995. Fluid-Rock Interaction In Faults Of The San-Andreas System - Inferences From San-Gabriel Fault Rock Geochemistry And Microstructures. *Journal Of Geophysical Research-Solid Earth*, 100(B7): 13007-13020.

EVANS, J.P., SHIPTON, Z.K., PACHELL, M.A., LIM, S.J. and ROBESON, K.R., 2000. The structure and composition of exhumed faults, and their implications for seismic processes. In: G.H.R. BOKELMANN and R.L. KOVACH (Editors), *The 3rd conference on the tectonic problems of the San Andreas fault system*. Geological Sciences. Stanford University Publications, pp. 67-81.

EVERNDEN, J.F. and KISTLER, R.W., 1970. Chronology of emplacement of of Mesozoic batholithic complexes in California and western Nevada. *U.S. Geological Survey Professional Paper*, 632: 42pp.

FAULKNER, D.R., LEWIS, A.C. and RUTTER, E.H., 2003. On the internal structure and mechanics of large strike-slip fault zones: field observations of the Carboneras fault in southeastem Spain. *Tectonophysics*, 367(3-4): 235-251.

FAULKNER, D.R., MITCHELL, T.M., HEALY, D. and HEAP, M.J., 2006. Slip on 'weak' faults by the rotation of regional stress in the fracture damage zone. *Nature*, 444(7121): 922-925.

FAURE, G., 1986. *Principles of Isotope Geology*. John Wiley & Sons, Inc., 589pp pp.

FIALKO, Y. and KHAZAN, Y., 2005. Fusion by earthquake fault friction: Stick or slip? *Journal of Geophysical Research-Solid Earth*, 110(B12).

FISHER, D.E., 1981. Quantitative Retention of Magmatic Argon in a Glassy Basalt. *Nature*, 290(5801): 42-43.

FISHER, R.A., 1953. Dispersion on a sphere. *Proceedings of the Royal Society, London*, v. A17: pp. 295-305.

FLISS, S., BHAT, H.S., DMOWSKA, R. and RICE, J.R., 2005. Fault branching and rupture directivity. *Journal Of Geophysical Research-Solid Earth*, 110(B6).

FREED, A.M., 2005. Earthquake triggering by static, dynamic, and postseismic stress transfer. *Annual Review of Earth and Planetary Sciences*, 33: 335-367.

GILBERT, G.K., 1883. A theory of the earthquakes of the Great Basin, with a practical application. *Salt Lake City Tribune, reprinted in the American Journal of Science*, 3rd ser., 27: 49-53.

GOLDSBY, D.L., 2007. Fault zone structure and strength during coseismic and slow slip in laboratory experiments. *Geological Society of America Abstracts with Programs*, 39(6): 373.

GOLDSBY, D.L. and TULLIS, T.E., 2002. Low frictional strength of quartz rocks at subseismic slip rates. *Geophysical Research Letters*, 29(17).

GRANIER, T., 1985. Origin, damping and pattern of faults in granite. *Tectonics*, 4: 721-737.

GROVE, M. and HARRISON, T.M., 1996. Ar-40(*) diffusion in Fe-rich biotite. *American Mineralogist*, 81(7-8): 940-951.

GUPTA, A. and SCHOLZ, C.H., 2000. A model of normal fault interaction based on observations and theory. *Journal of Structural Geology*, 22(7): 865-879.

HANKS, T.C. and BAKUN, W.H., 2002. A bilinear source-scaling model for M-log A observations of continental earthquakes. *Bulletin of the Seismological Society of America*, 92(5): 1841-1846.

HARDEBECK, J.L., 2006. Homogeneity of small-scale earthquake faulting, stress, and fault strength. *Bulletin Of The Seismological Society Of America*, 96(5): 1675-1688.

HARRIS, R.A. and DAY, S.M., 1999. Dynamic 3D simulations of earthquakes on en echelon faults. *Geophysical Research Letters*, 26(14): 2089-2092.

HARRISON, T.M., 1981. Diffusion of Ar-40 in Hornblende. *Contributions to Mineralogy and Petrology*, 78(3): 324-331.

HARRISON, T.M., DUNCAN, I. and MCDOUGALL, I., 1985. Diffusion of Ar-40 in Biotite - Temperature, Pressure and Compositional Effects. *Geochimica Et Cosmochimica Acta*, 49(11): 2461-2468.

HEILBRONNER, R. and TULLIS, J., 2002. The effect of static annealing on microstructures and crystallographic preferred orientations of quartzites experimentally deformed in axial compression and shear. In: S. DE MEER, M.R. DRURY, J.H.P. DE BRESSER and G.M. PENNOCK (Editors), *Deformation Mechanisms, Rheology and Tectonics: Current Status and Future Perspectives*. The Geological Society of London, pp. 191-218.

HESS, J.C., LIPPOLT, H.J., GURBANOV, A.G. and MICHALSKI, I., 1993. The Cooling History of the Late Pliocene Eldzhurtinskiy Granite (Caucasus, Russia) and the Thermochronological Potential of Grain-Size Age Relationships. *Earth and Planetary Science Letters*, 117(3-4): 393-406.

HIROSE, T. and SHIMAMOTO, T., 2003. Fractal dimension of molten surfaces as a possible parameter to infer the slip-weakening distance of faults from natural pseudotachylytes. *Journal of Structural Geology*, 25(10): 1569-1574.

HIROSE, T. and SHIMAMOTO, T., 2005a. Growth of molten zone as a mechanism of slip weakening of simulated faults in gabbro during frictional melting. *Journal Of Geophysical Research-Solid Earth*, 110(B5).

HIROSE, T. and SHIMAMOTO, T., 2005b. Slip-weakening distance of faults during frictional melting as inferred from experimental and natural pseudotachylytes. *Bulletin Of The Seismological Society Of America*, 95(5): 1666-1673.

HIRTH, G. and TULLIS, J., 1992. Dislocation Creep Regimes in Quartz Aggregates. *Journal of Structural Geology*, 14(2): 145-159.

HOUSE, M.A., WERNICKE, B.P. and FARLEY, K.A., 1998. Dating topography of the Sierra Nevada, California, using apatite (U-Th)/He ages. *Nature*, 396(6706): 66-69.

HOUSE, M.A., WERNICKE, B.P. and FARLEY, K.A., 2001. Paleo-geomorphology of the Sierra Nevada, California, from (U-Th)/He ages in apatite. *American Journal Of Science*, 301(2): 77-102.

IDA, Y., 1972. Cohesive Force across Tip of a Longitudinal-Shear Crack and Griffiths Specific Surface-Energy. *Journal of Geophysical Research*, 77(20): 3796-&.

IDE, S., 2002. Estimation of radiated energy of finite-source earthquake models. *Bulletin of the Seismological Society of America*, 92(8): 2994-3005.

IDE, S. and TAKEO, M., 1997. Determination of constitutive relations of fault slip based on seismic wave analysis. *Journal of Geophysical Research-Solid Earth*, 102(B12): 27379-27391.

JEFFERIES, S.P. et al., 2006. The nature and importance of phyllonite development in crustal-scale fault cores: an example from the Median Tectonic Line, Japan. *Journal of Structural Geology*, 28(2): 220-235.

JEFFREYS, H., 1942. On the Mechanics of Faulting. *The Geological Magazine*, 79: 291-295.

JONES, C.H., FARMER, G.L. and UNRUH, J., 2004. Tectonics of Pliocene removal of lithosphere of the Sierra Nevada, California. *Geological Society Of America Bulletin*, 116(11-12): 1408-1422.

KAME, N. and YAMASHITA, T., 2003. Dynamic branching, arresting of rupture and the seismic wave radiation in self-chosen crack path modelling. *Geophysical Journal International*, 155(3): 1042-1050.

KANAMORI, H. and BRODSKY, E.E., 2004. The physics of earthquakes. *Reports on Progress in Physics*, 67(8): 1429-1496.

KANAMORI, H. and HEATON, T.H., 2000. Microscopic and Macroscopic Physics of Earthquakes. In: J.B. RUNDLE, D.L. TURCOTTE and W. KLEIN (Editors), *Geocomplexity and the Physics of Earthquakes*. Geophysical Monograph. American Geophysical Union, pp. 147-163.

KANAMORI, H. and RIVERA, L., 2006. Energy partitioning during an earthquake. In: R.E. ABERCROMBIE, A. MCGARR, H. KANAMORI and G. DI TORO (Editors), *Earthquakes, Radiated Energy and the Physics of Faulting*. Geophysical Monograph. American Geophysical Union, pp. 3-13.

KASE, Y. and KUGE, K., 2001. Rupture propagation beyond fault discontinuities: significance of fault strike and location. *Geophysical Journal International*, 147(2): 330-342.

KELLER, J.V.A., HALL, S.H., DART, C.J. and MCCLAY, K.R., 1995. The Geometry and Evolution of a Transpressional Strike-Slip System - the Carboneras Fault, Se Spain. *Journal of the Geological Society*, 152: 339-351.

KING, G. and NABELEK, J., 1985. Role Of Fault Bends In The Initiation And Termination Of Earthquake Rupture. *Science*, 228(4702): 984-987.

KING, G.C.P., STEIN, R.S. and LIN, J., 1994. Static Stress Changes and the Triggering of Earthquakes. *Bulletin of the Seismological Society of America*, 84(3): 935-953.

KISTLER, R.W., BATEMAN, P.C. and BRANNOCK, W.W., 1965. Isotopic Ages Of Minerals From Granitic Rocks Of Central Sierra Nevada And Inyo Mountains California. *Geological Society Of America Bulletin*, 76(2): 155-&.

KLINGER, Y. et al., 2005. High-resolution satellite imagery mapping of the surface rupture and slip distribution of the M-W similar to 7.8, 14 November 2001 Kokoxili Earthquake, Kunlun Fault, northern Tibet, China. *Bulletin Of The Seismological Society Of America*, 95(5): 1970-1987.

LACHENBRUCH, A.H., 1980. Frictional Heating, Fluid Pressure, and the Resistance to Fault Motion. *Journal of Geophysical Research*, 85(NB11): 6097-6112.

LAWN, B., 1993. *Fracture of Brittle Solids - Second Edition*. Cambridge Solid State Science Series. Cambridge University Press, 378 pp.

LIM, S.J., 1998. *Small strike-slip faults in granitic rock: implications for three-dimensional models*, Utah State University, Logan, Utah.

LIN, A.M., 1996. Injection veins of crushing-originated pseudotachylyte and fault gouge formed during seismic faulting. *Engineering Geology*, 43(2-3): 213-224.

LIN, A.M. et al., 2005. Propagation of seismic slip from brittle to ductile crust: Evidence from pseudotachylyte of the Woodroffe thrust, central Australia. *Tectonophysics*, 402(1-4): 21-35.

LIN, A.M. and SHIMAMOTO, T., 1998. Selective melting processes as inferred from experimentally generated pseudotachylytes. *Journal Of Asian Earth Sciences*, 16(5-6): 533-545.

LOCKNER, D., NAKA, H., ITO, H. and IKEDA, R., 2000. Permeability and strength of core samples from the Nojima fault of the 1995 Kobe earthquake, *Proceedings of the International Workshop on the Nojima Fault Core and Borehole Analysis*. USGS Open File Report 00-129, pp. 147-152.

LOCKWOOD, J.P. and LYDON, P.A., 1975. Geological map of the Mount Abbot quadrangle, central Sierra Nevada, California. *U. S. Geological Survey Geologic Quadrangle Map*(Map GQ-1155).

MADDOCK, R.H., 1983. Melt Origin of Fault-Generated Pseudotachylytes Demonstrated by Textures. *Geology*, 11(2): 105-108.

MADDOCK, R.H., 1992. Effects of Lithology, Cataclasis and Melting on the Composition of Fault-Generated Pseudotachylytes in Lewisian Gneiss, Scotland. *Tectonophysics*, 204(3-4): 261-278.

MAGLOUGHLIN, J.F., 1992. Microstructural and Chemical-Changes Associated with Cataclasis and Frictional Melting at Shallow Crustal Levels - the Cataclasite Pseudotachylyte Connection. *Tectonophysics*, 204(3-4): 243-260.

MAGLOUGHLIN, J.F., HALL, C.M. and VAN DER PLUIJM, B.A., 2001. Ar-40-Ar-39 geochronometry of pseudotachylytes by vacuum encapsulation: North Cascade Mountains, Washington, USA. *Geology*, 29(1): 51-54.

MAGLOUGHLIN, J.F. and SPRAY, J.G., 1992. Frictional Melting Processes and Products in Geological-Materials - Introduction and Discussion. *Tectonophysics*, 204(3-4): 197-206.

MANLEY, C.R., GLAZNER, A.F. and FARMER, G.L., 2000. Timing of volcanism in the Sierra Nevada of California: Evidence for Pliocene delamination of the batholithic root? *Geology*, 28(9): 811-814.

MANSFIELD, C.S. and CARTWRIGHT, J.A., 1996. High resolution fault displacement mapping from three-dimensional seismic data: Evidence for dip linkage during fault growth. *Journal Of Structural Geology*, 18(2-3): 249-263.

MARTEL, S.J., 1990. Formation of Compound Strike-Slip-Fault Zones, Mount Abbot Quadrangle, California. *Journal of Structural Geology*, 12(7): 869-882.

MARTEL, S.J., 1997. Effects of cohesive zones on small faults and implications for secondary fracturing and fault trace geometry. *Journal of Structural Geology*, 19(6): 835-847.

MARTEL, S.J. and BOGER, W.A., 1998. Geometry and mechanics of secondary fracturing around small three-dimensional faults in granitic rock. *Journal of Geophysical Research-Solid Earth*, 103(B9): 21299-21314.

MARTEL, S.J. and POLLARD, D.D., 1989. Mechanics of Slip and Fracture Along Small Faults and Simple Strike-Slip-Fault Zones in Granitic Rock. *Journal of Geophysical Research-Solid Earth and Planets*, 94(B7): 9417-9428.

MARTEL, S.J., POLLARD, D.D. and SEGALL, P., 1988. Development of Simple Strike-Slip-Fault Zones, Mount Abbot Quadrangle, Sierra-Nevada, California. *Geological Society of America Bulletin*, 100(9): 1451-1465.

MASE, C.W. and SMITH, L., 1984. Pore-Fluid Pressures and Frictional Heating on a Fault Surface. *Pure and Applied Geophysics*, 122(2-4): 583-607.

MASE, C.W. and SMITH, L., 1987. Effects of Frictional Heating on the Thermal, Hydrologic, and Mechanical Response of a Fault. *Journal of Geophysical Research-Solid Earth and Planets*, 92(B7): 6249-6272.

MATTINSON, J.M., 1978. Age, Origin, and Thermal Histories of Some Plutonic Rocks from Salinian Block of California. *Contributions to Mineralogy and Petrology*, 67(3): 233-245.

MCGARR, A., 1999. On relating apparent stress to the stress causing earthquake fault slip. *Journal of Geophysical Research-Solid Earth*, 104(B2): 3003-3011.

MCKENZIE, D. and BRUNE, J.N., 1972. Melting on Fault Planes During Large Earthquakes. *Geophysical Journal of the Royal Astronomical Society*, 29(1): 65-&.

MCLAREN, A.C. and PRYER, L.L., 2001. Microstructural investigation of the interaction and interdependence of cataclastic and plastic mechanisms in Feldspar crystals deformed in the semi-brittle field. *Tectonophysics*, 335(1-2): 1-15.

MCLEOD, A.E., DAWERS, N.H. and UNDERHILL, J.R., 2000. The propagation and linkage of normal faults: insights from the Strathspey-Brent-Statfjord fault array, northern North Sea. *Basin Research*, 12(3-4): 263-284.

MCNULTY, B.A., 1995. Pseudotachylyte Generated in the Semibrittle and Brittle Regimes, Bench-Canyon Shear Zone, Central Sierra-Nevada. *Journal of Structural Geology*, 17(11): 1507-1521.

MELOSH, H.J., 1979. Acoustic Fluidization - New Geologic Process. *Journal of Geophysical Research*, 84(NB13): 7513-7520.

MELOSH, H.J., 1996. Dynamical weakening of faults by acoustic fluidization. *Nature*, 379(6566): 601-606.

MICKLETHWAITE, S. and COX, S.F., 2006. Progressive fault triggering and fluid flow in aftershock domains: Examples from mineralized Archaean fault systems. *Earth And Planetary Science Letters*, 250(1-2): 318-330.

MIKUMO, T., OLSEN, K.B., FUKUYAMA, E. and YAGI, Y., 2003. Stress-breakdown time and slip-weakening distance inferred from slip-velocity functions on earthquake faults. *Bulletin of the Seismological Society of America*, 93(1): 264-282.

MILLER, G.M. and COWAN, D.S., 1998. Mesoscopic ductility in fault gouges. In: A.W. SNOKE, J. TULLIS and V.R. TODD (Editors), *Fault-related rocks, a photographic atlas*. Princeton University Press.

MIZOGUCHI, K., TAKAHASHI, M., MASUDA, K. and FUKUYAMA, E., 2007. Fault strength drop due to phase transitions in the pore fluid. *Geophysical Research Letters*, 34(9).

MOORE, J.G., 1978. Geologic Map of the Marion Peak Quadrangle, Fresno County, California. *U. S. Geological Survey Geologic Quadrangle Map*(Map GQ-1399).

NASSERI, M.H.B., SCHUBNEL, A. and YOUNG, R.P., 2007. Coupled evolutions of fracture toughness and elastic wave velocities at high crack density in thermally treated Westerly granite. *International Journal of Rock Mechanics and Mining Sciences*, 44(4): 601-616.

NIELSEN, S., DI TORO, G., HIROSE, T. and SHIMAMOTO, T., 2008. Frictional melt and seismic slip. *Journal of Geophysical Research-Solid Earth*, 113(B1).

NILSEN, T.H. and CLARKE, S.H., JNR., 1975. Sedimentation and tectonics in the early Tertiary continental borderland of central California. *U. S. Geological Survey Professional Paper*, 925: 64pp.

NODA, H. and SHIMAMOTO, T., 2005. Thermal pressurization and slip-weakening distance of a fault: An example of the Hanaore fault, southwest Japan. *Bulletin of the Seismological Society of America*, 95(4): 1224-1233.

O'CONNELL, R.J. and BUDIANSKY, B., 1974. Seismic Velocities In Dry And Saturated Cracked Solids. *Journal Of Geophysical Research*, 79(35): 5412-5426.

OZAWA, K. and SHIGERU, T., 2007. Amorphous material formed by the mechanochemical effect in natural pseudotachylyte of crushing origin: A case study of the Iida-Matsukawa Fault, Nagano Prefecture, Central Japan. *Journal of Structural Geology*, 29: 1855-1869.

PACHELL, M.A. and EVANS, J.P., 2002. Growth, linkage, and termination processes of a 10-km-long strike-slip fault in jointed granite: the Gemini fault zone, Sierra Nevada, California. *Journal of Structural Geology*, 24(12): 1903-1924.

PACHELL, M.A., EVANS, J.P. and TAYLOR, W.L., 2003. Kilometer-scale kinking of crystalline rocks in a transpressive convergent setting, Central Sierra Nevada, California. *Geological Society of America Bulletin*, 115(7): 817-831.

PASSCHIER, C. and TROUW, R.A.J., 2005. *Micro-tectonics*. Springer-Verlag, Berlin, 366 pp.

PASSCHIER, C.W., 1982. Pseudotachylyte and the Development of Ultramylonite Bands in the Saint-Barthelemy Massif, French Pyrenees. *Journal of Structural Geology*, 4(1): 69-79.

PEACOCK, D.C.P., 1991. Displacements and Segment Linkage in Strike-Slip-Fault Zones. *Journal of Structural Geology*, 13(9): 1025-1035.

PENNACCHIONI, G., DI TORO, G., BRACK, P., MENEGON, L. and VILLA, I.M., 2006. Brittle-ductile-brittle deformation during cooling of tonalite (Adamello, Southern Italian Alps). *Tectonophysics*, 427(1-4): 171-197.

PERSANO, C., STUART, F.M., BARFOD, D.N., BISHOP, P. and BROWN, R.W., 2005a. Constraining denudation in Scotland by using a combination of low temperature thermochronometers. *Geochimica Et Cosmochimica Acta*, 69(10): A299-A299.

PERSANO, C., STUART, F.M., BISHOP, P. and DEMPSTER, T.J., 2005b. Deciphering continental breakup in eastern Australia using low-temperature thermochronometers. *Journal of Geophysical Research-Solid Earth*, 110(B12).

POLIAKOV, A.N.B., DMOWSKA, R. and RICE, J.R., 2002. Dynamic shear rupture interactions with fault bends and off-axis secondary faulting. *Journal Of Geophysical Research-Solid Earth*, 107(B11).

PRYER, L.L., 1993. Microstructures in Feldspars from a Major Crustal Thrust Zone - the Grenville Front, Ontario, Canada. *Journal of Structural Geology*, 15(1): 21-36.

REIMOLD, W.U., JESSBERGER, E.K. and STEPHAN, T., 1990. Ar-40-Ar-39 Dating of Pseudotachylite from the Vredefort Dome, South-Africa - a Progress Report. *Tectonophysics*, 171(1-4): 139-152.

REMPEL, A.W. and RICE, J.R., 2006. Thermal pressurization and onset of melting in fault zones. *Journal of Geophysical Research-Solid Earth*, 111(B9).

RENNE, P.R., TOBISCH, O.T. and SALEEBY, J.B., 1993. Thermochronological Record of Pluton Emplacement, Deformation, and Exhumation at Courtright Shear Zone, Central Sierra-Nevada, California. *Geology*, 21(4): 331-334.

RICE, J.R., 2006. Heating and weakening of faults during earthquake slip. *Journal of Geophysical Research-Solid Earth*, 111(B5).

RICE, J.R. and COCCO, M., 2007. Seismic Fault Rheology and Earthquake Dynamics. In: M.R. HANDY, G. HIRTH and N. HOVIUS (Editors), *Tectonic Faults, Agents Of Change On A Dynamic Earth*. The MIT Press, pp. 446.

RICE, J.R., LAPUSTA, N. and RANJITH, K., 2001. Rate and state dependent friction and the stability of sliding between elastically deformable solids. *Journal of the Mechanics and Physics of Solids*, 49(9): 1865-1898.

RICE, J.R., SAMMIS, C.G. and PARSONS, R., 2005. Off-fault secondary failure induced by a dynamic slip pulse. *Bulletin Of The Seismological Society Of America*, 95(1): 109-134.

ROSAKIS, A.J., 2002. Intersonic shear cracks and fault ruptures. *Advances in Physics*, 51(4): 1189-1257.

ROWE, C.D., MOORE, J.C., MENEGHINI, F. and MCKEIRNAN, A.W., 2005. Large-scale pseudotachylytes and fluidized cataclasites from an ancient subduction thrust fault. *Geology*, 33(12): 937-940.

ROWLAND, J.V. and SIBSON, R.H., 2004. Structural controls on hydrothermal flow in a segmented rift system, Taupo Volcanic Zone, New Zealand. *Geofluids*, 4(4): 259-283.

RUTTER, E.H., 1986. On the nomenclature of mode of failure transitions in rocks. *Tectonophysics*, 122(3-4): 381-387.

RUTTER, E.H., CASEY, M. and BURLINI, L., 1994. Preferred Crystallographic Orientation Development During the Plastic and Superplastic Flow of Calcite Rocks. *Journal of Structural Geology*, 16(10): 1431-1446.

SAGY, A., RECHES, Z. and ROMAN, I., 2001. Dynamic fracturing: field and experimental observations. *Journal Of Structural Geology*, 23(8): 1223-1239.

SALEEBY, J., 1999. On some aspects of the geology of the Sierra Nevada. In: E.M. MOORES, D. SLOAN and D.L. STOUT (Editors), *Classic Cordilleran Concepts: A View from California*. The Geological Society of America, Special Paper 338.

SCHOLZ, C.H., 2002. *The Mechanics of Earthquakes and Faulting*. Cambridge University Press.

SCHOLZ, C.H., AVILES, C.A. and WESNOUSKY, S.G., 1986. Scaling Differences between Large Interplate and Intraplate Earthquakes. *Bulletin of the Seismological Society of America*, 76(1): 65-70.

SCHULZ, S.E. and EVANS, J.P., 1998. Spatial variability in microscopic deformation and composition of the Punchbowl fault, southern California: implications for mechanisms, fluid-rock interaction, and fault morphology. *Tectonophysics*, 295(1-2): 223-244.

SCHULZ, S.E. and EVANS, J.P., 2000. Mesoscopic structure of the Punchbowl Fault, Southern California and the geologic and geophysical structure of active strike-slip faults. *Journal of Structural Geology*, 22(7): 913-930.

SEGALL, P., 1984. Formation and Growth of Extensional Fracture Sets. *Geological Society of America Bulletin*, 95(4): 454-462.

SEGALL, P., MCKEE, E.H., MARTEL, S.J. and TURRIN, B.D., 1990. Late Cretaceous Age of Fractures in the Sierra-Nevada Batholith, California. *Geology*, 18(12): 1248-1251.

SEGALL, P. and POLLARD, D.D., 1980. Mechanics Of Discontinuous Faults. *Journal Of Geophysical Research*, 85(NB8): 4337-4350.

SEGALL, P. and POLLARD, D.D., 1983a. Joint Formation in Granitic Rock of the Sierra-Nevada. *Geological Society of America Bulletin*, 94(5): 563-575.

SEGALL, P. and POLLARD, D.D., 1983b. Nucleation and Growth of Strike Slip Faults in Granite. *Journal of Geophysical Research*, 88(NB1): 555-568.

SEGALL, P. and RICE, J.R., 2006. Does shear heating of pore fluid contribute to earthquake nucleation? *Journal of Geophysical Research-Solid Earth*, 111(B9).

SEGALL, P. and SIMPSON, C., 1986. Nucleation of Ductile Shear Zones on Dilatant Fractures. *Geology*, 14(1): 56-59.

SEIDEMANN, D.E., 1977. Effects of Submarine Alteration on K-Ar Dating of Deep-Sea Igneous Rocks. *Geological Society of America Bulletin*, 88(11): 1660-1666.

SEIDEMANN, D.E., MASTERSON, W.D., DOWLING, M.P. and TUREKIAN, K.K., 1984. K-Ar Dates and Ar-40/Ar-39 Age Spectra for Mesozoic Basalt Flows of the Hartford Basin, Connecticut, and the Newark Basin, New-Jersey. *Geological Society of America Bulletin*, 95(5): 594-598.

SERONT, B. et al., 1998. Laboratory characterization of hydromechanical properties of a seismogenic normal fault system. *Journal Of Structural Geology*, 20(7): 865-881.

SHAND, S.J., 1916. The Pseudotachylyte of Parijs (Orange Free State). *Quarterly Journal Of The Geological Society Of London*, 72: 198-221.

SHEPARD, C.U., 1835. Microlite, a New Mineral Species. *American Journal of Science*, 1: 361-362.

SHERLOCK, S.C. and HETZEL, R., 2001. A laser-probe Ar-40/Ar-39 study of pseudotachylite from the Tambach Fault Zone, Kenya: direct isotopic dating of brittle faults. *Journal Of Structural Geology*, 23(1): 33-44.

SHIPTON, Z.K. and COWIE, P.A., 2001. Damage zone and slip-surface evolution over mu m to km scales in high-porosity Navajo sandstone, Utah. *Journal of Structural Geology*, 23(12): 1825-1844.

SHIPTON, Z.K., EVANS, J.P., ABERCROMBIE, R.E. and BRODSKY, E.E., 2006. The missing sinks: Slip localization in faults, damage zones, and the seismic energy budget. In: R.E. ABERCROMBIE, A. MCGARR, G. DI TORO and H. KANAMORI (Editors), *Earthquakes: Radiated Energy and the Physics of Faulting*. Geophysical Monograph. American Geophysical Union, pp. 217-222.

SIBSON, R.H., 1973. Interactions Between Temperature And Pore-Fluid Pressure During Earthquake Faulting And A Mechanism For Partial Or Total Stress Relief. *Nature-Physical Science*, 243(126): 66-68.

SIBSON, R.H., 1975. Generation Of Pseudotachylyte By Ancient Seismic Faulting. *Geophysical Journal Of The Royal Astronomical Society*, 43(3): 775-794.

SIBSON, R.H., 1977. Fault rocks and fault mechanisms. *Journal of the Geological Society (London)*, 133: 191-213.

SIBSON, R.H., 1982. Fault Zone Models, Heat-Flow, And The Depth Distribution Of Earthquakes In The Continental-Crust Of The United-States. *Bulletin Of The Seismological Society Of America*, 72(1): 151-163.

SIBSON, R.H., 1983. Continental Fault Structure and the Shallow Earthquake Source. *Journal of the Geological Society*, 140(SEP): 741-767.

SIBSON, R.H., 1985. Stopping of Earthquake Ruptures at Dilational Fault Jogs. *Nature*, 316(6025): 248-251.

SIBSON, R.H., 1986. Brecciation Processes in Fault Zones - Inferences from Earthquake Rupturing. *Pure and Applied Geophysics*, 124(1-2): 159-175.

SIBSON, R.H., 1989. Earthquake faulting as a structural process. *Journal of Structural Geology*, 11(1-2): 1-14.

SIBSON, R.H., 2003. Thickness of the seismic slip zone. *Bulletin Of The Seismological Society Of America*, 93(3): 1169-1178.

SIBSON, R.H. and TOY, V.G., 2006. The Habitat of Fault-Generated Pseudotachylyte: Presence vs. Absence of Friction-Melt. In: R.E. ABERCROMBIE, A. MCGARR, G. DI TORO and H. KANAMORI (Editors), *Earthquakes: Radiated Energy and the Physics of Faulting*. Geophysical Monograph Series. American Geophysical Union, pp. 153-166.

SPRAY, J.G., 1992. A Physical Basis for the Frictional Melting of Some Rock-Forming Minerals. *Tectonophysics*, 204(3-4): 205-221.

SPRAY, J.G., 1995. Pseudotachylyte Controversy - Fact or Friction. *Geology*, 23(12): 1119-1122.

STEIGER, R.H. and JAGER, E., 1977. Subcommission on Geochronology - Convention on Use of Decay Constants in Geochronology and Cosmochronology. *Earth and Planetary Science Letters*, 36(3): 359-362.

STERN, T.W., BATEMAN, P.C., MORGAN, B.A., NEWELL, M.F. and PECK, D.L., 1981. Isotopic U-Pb ages of zircon from the granitoids of the central Sierra Nevada. *U.S. Geological Survey Professional Paper*, 1185: 17p.

STIPP, M., STUNITZ, H., HEILBRONNER, R. and SCHMID, S.M., 2002. The eastern Tonale fault zone: a 'natural laboratory' for crystal plastic deformation of quartz over a temperature range from 250 to 700 degrees C. *Journal of Structural Geology*, 24(12): 1861-1884.

STORTI, F., ROSSETTI, F. and SALVINI, F., 2001. Structural architecture and displacement accommodation mechanisms at the termination of the Priestley Fault, northern Victoria Land, Antarctica. *Tectonophysics*, 341(1-4): 141-161.

STUNITZ, H. and FITZ GERALD, J.D., 1993. Deformation of Granitoids at Low Metamorphic Grade .2. Granular Flow in Albite-Rich Mylonites. *Tectonophysics*, 221(3-4): 299-324.

SWANSON, M.T., 1989. Sidewall Ripouts in Strike-Slip Faults. *Journal of Structural Geology*, 11(8): 933-&.

SWANSON, M.T., 1992. Fault structure, wear mechanisms and rupture processes in pseudotachylyte generation. *Tectonophysics*, 204(3-4): 223-242.

TIKOFF, B. and DE SAINT BLANQUAT, M., 1997. Transpressional shearing and strike-slip partitioning in the Late Cretaceous Sierra Nevada magmatic arc, California. *Tectonics*, 16(3): 442-459.

TOBISCH, O.T., RENNE, P.R. and SALEEBY, J.B., 1993. Deformation Resulting From Regional Extension During Pluton Ascent And Emplacement, Central Sierra-Nevada, California. *Journal Of Structural Geology*, 15(3-5): 609-&.

TOBISCH, O.T., SALEEBY, J.B., RENNE, P.R., MCNULTY, B. and TONG, W.X., 1995. Variations In Deformation Fields During Development Of A Large-Volume Magmatic Arc, Central Sierra-Nevada, California. *Geological Society Of America Bulletin*, 107(2): 148-166.

TODA, S., STEIN, R.S., REASENBERG, P.A., DIETERICH, J.H. and YOSHIDA, A., 1998. Stress transferred by the 1995 M-w = 6.9 Kobe, Japan, shock: Effect on aftershocks and future earthquake probabilities. *Journal of Geophysical Research-Solid Earth*, 103(B10): 24543-24565.

TOYOSHIMA, T., 1990. Pseudotachylite From The Main Zone Of The Hidaka Metamorphic Belt, Hokkaido, Northern Japan. *Journal Of Metamorphic Geology*, 8(5): 507-523.

TULLIS, J., STUNITZ, H., TEYSSIER, C. and HEILBRONNER, R., 2000. Deformation Microstructures in Quartzo-feldspathic Rocks. In: M.W. JESSELL and J.L. URAI (Editors), *Journal of the Virtual Explorer, v2, Stress, Strain and Structure, A volume in honour of W D Means.* .

TULLIS, J. and YUND, R.A., 1985. Dynamic Recrystallization of Feldspar - a Mechanism for Ductile Shear Zone Formation. *Geology*, 13(4): 238-241.

TULLIS, J. and YUND, R.A., 1987. Transition from Cataclastic Flow to Dislocation Creep of Feldspar - Mechanisms and Microstructures. *Geology*, 15(7): 606-609.

VAUCHEZ, A. and DASILVA, M.E., 1992. Termination of a Continental-Scale Strike-Slip-Fault in Partially Melted Crust - the West Pernambuco Shear Zone, Northeast Brazil. *Geology*, 20(11): 1007-1010.

VERMILYE, J.M. and SCHOLZ, C.H., 1998. The process zone: A microstructural view of fault growth. *Journal of Geophysical Research-Solid Earth*, 103(B6): 12223-12237.

VERNON, R.H., WILLIAMS, V.A. and DARCY, W.F., 1983. Grain-Size Reduction and Foliation Development in a Deformed Granitoid Batholith. *Tectonophysics*, 92(1-3): 123-145.

VREDEVOOGD, M.A., OGLESBY, D.D. and PARK, S.K., 2007. Fluid pressurization due to frictional heating on a fault at a permeability contrast. *Geophysical Research Letters*, 34(18).

WALSH, J.B., 1965. Effect Of Cracks On Uniaxial Elastic Compression Of Rocks. *Journal Of Geophysical Research*, 70(2): 381-389.

WARR, L.N., VAN DER PLUIJM, B.A. and TOURSCHER, S., 2007. The age and depth of exhumed friction melts along the Alpine fault, New Zealand. *Geology*, 35(7): 603-606.

WELLS, D.L. and COPPERSMITH, K.J., 1994. New Empirical Relationships among Magnitude, Rupture Length, Rupture Width, Rupture Area, and Surface Displacement. *Bulletin of the Seismological Society of America*, 84(4): 974-1002.

WENK, H.R., JOHNSON, L.R. and RATSCHBACHER, L., 2000. Pseudotachylites in the Eastern Peninsular Ranges of California. *Tectonophysics*, 321(2): 253-277.

WERNICKE, B. et al., 1996. Origin of high mountains in the continents: The southern Sierra Nevada. *Science*, 271(5246): 190-193.

WESNOUSKY, S.G., 2006. Predicting the endpoints of earthquake ruptures. *Nature*, 444(7117): 358-360.

WIBBERLEY, C.A.J. and SHIMAMOTO, T., 2003. Internal structure and permeability of major strike-slip fault zones: the Median Tectonic Line in Mie Prefecture, Southwest Japan. *Journal of Structural Geology*, 25(1): 59-78.

WIBBERLEY, C.A.J. and SHIMAMOTO, T., 2005. Earthquake slip weakening and asperities explained by thermal pressurization. *Nature*, 436(7051): 689-692.

WILLETT, S.D., FISHER, D., FULLER, C., EN-CHAO, Y. and LU, C.Y., 2003. Erosion rates and orogenic-wedge kinematics in Taiwan inferred from fission-track thermochronometry. *Geology*, 31(11): 945-948.

WILLSON, J.P., LUNN, R.J. and SHIPTON, Z.K., 2007. Simulating spatial and temporal evolution of multiple wing cracks around faults in crystalline basement rocks. *Journal of Geophysical Research-Solid Earth*, 112(B8).

WILSON, B., DEWERS, T., RECHES, Z. and BRUNE, J., 2005. Particle size and energetics of gouge from earthquake rupture zones. *Nature*, 434(7034): 749-752.

WILSON, J.E., CHESTER, J.S. and CHESTER, F.M., 2003. Microfracture analysis of fault growth and wear processes, Punchbowl Fault, San Andreas System, California. *Journal of Structural Geology*, 25(11): 1855-1873.

WINTSCH, R.P., CHRISTOFFERSEN, R. and KRONENBERG, A.K., 1995. Fluid-Rock Reaction Weakening of Fault Zones. *Journal of Geophysical Research-Solid Earth*, 100(B7): 13021-13032.

YAMASHITA, T., 2000. Generation of microcracks by dynamic shear rupture and its effects on rupture growth and elastic wave radiation. *Geophysical Journal International*, 143(2): 395-406.

YEEND, W.E., 1974. Gold-bearing gravels of the ancestral Yuba River, Sierra Nevada, California. *U. S. Geological Survey Professional Paper*, 722: 44pp.

YIN, Z.M. and RANALLI, G., 1992. Critical Stress Difference, Fault Orientation and Slip Direction in Anisotropic Rocks under Non-Andersonian Stress Systems. *Journal of Structural Geology*, 14(2): 237-244.

A.1 Appendix 1: Geologic map of the Granite Pass study area

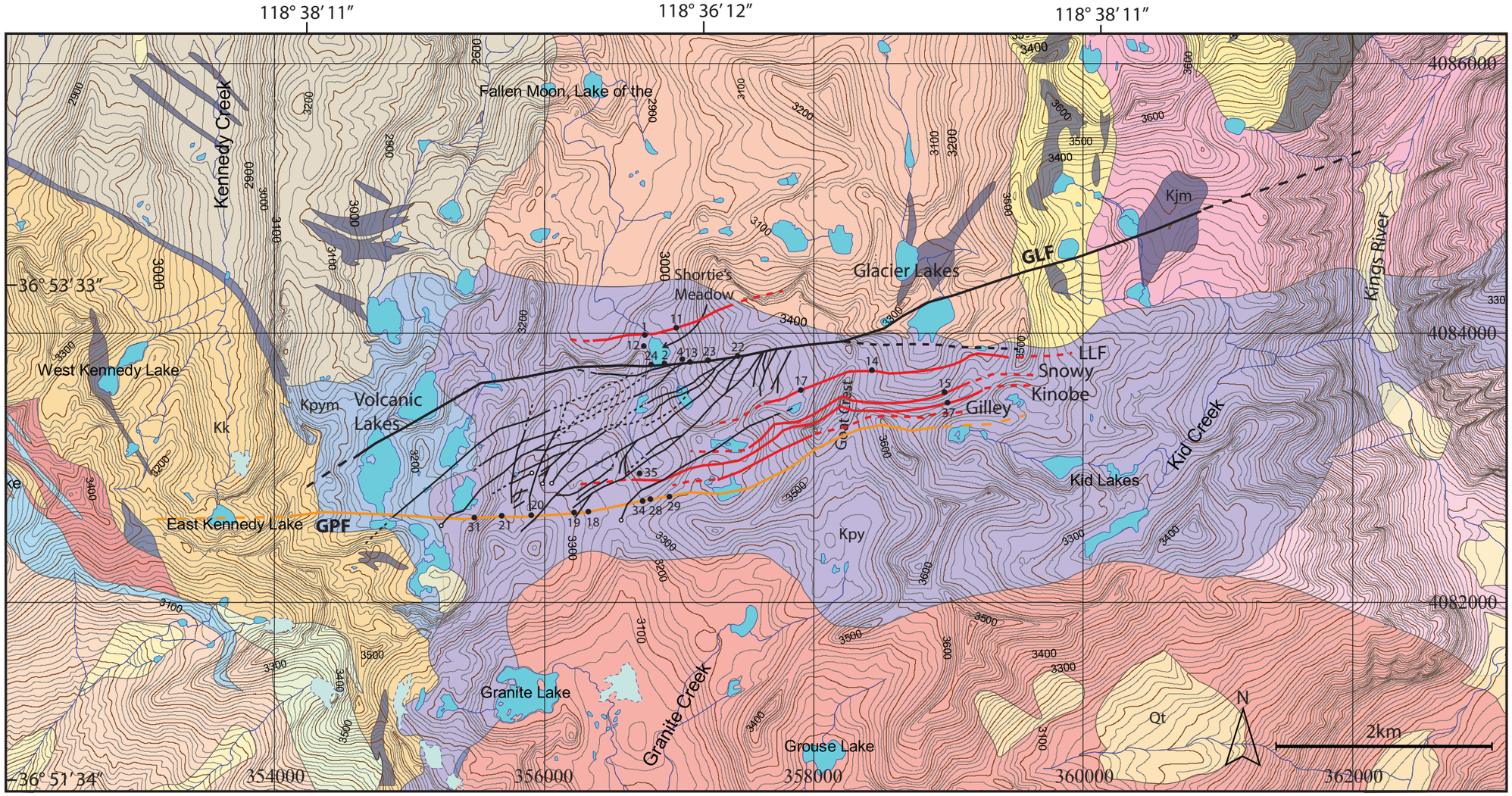

Geologic map of the Granite Pass study area in Sequoia and Kings Canyon National Park (geology from Moore, 1978; Kpy = Pyramid pluton, Kpym = Pyramid pluton mafic western facies, Kk = Granite of Kennedy Lakes, Kjm = mafic plutonic rock, Qt = Pleistocene sedimentary deposits). The faults described in this study are shown (dashed where uncertain); GLF = Glacier Lakes fault (with splays in black), GPF = Granite Pass fault, LLF = Little Lake fault. GLF, GPF and splay faults are modified from Evans *et al*. (2002). Numbers and black spots represent the localities referred to in the text. Latitude and longitude are shown top and left, and the UTM datum is labelled on the right and bottom axes.

A.2 Appendix 2: List of localities

Locality	UTM Coordinates	Fault	Samples
1	0356605 4084192 (10)	SKF	SKR, SKL, SKZS, SK8, SK9, SK10
2	0356874 4083945 (7)	GLF	GLF5
4	0356957 4083940 (7)	REACTIVATED	
11	0356957 4084275 (6)	SKF	
12	0356659 4084142 (6)	REACTIVATED	
13	0357071 4083944 (5)	GLF	
14	0358766 4083863 (6)	LLF	
15	0359412 4083692 (6)	Snowy	
17	0358098 4083674 (5)	LLF	
18	0356109 4082650 (5)	GPF	GPF2, GPF5
19	0355969 4082636 (4)	GPF	
20	0355616 4082600 (4)	GPF	
21	0355314 4082558 (5)	GPF	GPF6, GPF7
22	0357506 4084007 (7)	GLF	
23	0357253 4083951 (7)	GLF	GLF3, GLF4
24	0356722 4083953 (5)	GLF	
28	0356705 4082677 (5)	GPF	GPF10
29	0356884 4082732 (4)	GPF	
31	0355095 4082536 (7)	GPF	GPF11
34	0356643 4082651 (5)	GPF	
35	0356617 4082872 (4)	Host	GPP1, GPP3
37	0359402 4083607 (5)	Kinobe	

A.3 Appendix 3: Statistical analysis of spherical data

Defining the orientation of planes as plunge and plunge azimuth allows orientation measurements to be treated as a population of vectors. The method of Fisher (1953) has been used to characterize the statistical properties of a population of vector data. The Fisher method relies upon the vector data having a unimodal distribution (Fisher distribution). Each vector has three orthogonal components, the direction cosines (l_i, m_i, n_i), which are determined relative to axes oriented north, east and down:

$$l_i = \cos(p_i)\cos(t_i), \quad m_i = \cos(p_i)\sin(t_i), \quad n_i = \sin(p_i).$$

Where p_i and t_i are the plunge and plunge azimuth of the i^{th} observation. The vector magnitude, R, of N unit vectors is then:

$$R = \sqrt{\left(\left(\sum_{i=1}^{N} l_i\right)^2 + \left(\sum_{i=1}^{N} m_i\right)^2 + \left(\sum_{i=1}^{N} n_i\right)^2\right)}. \qquad \textbf{Equation 12}$$

The corresponding mean unit vector (l', m', n') is given by the direction cosines:

$$\begin{bmatrix} l' & m' & n' \end{bmatrix} = \begin{bmatrix} \frac{\sum_{i=1}^{N} l_i}{R} & \frac{\sum_{i=1}^{N} m_i}{R} & \frac{\sum_{i=1}^{N} n_i}{R} \end{bmatrix}. \qquad \textbf{Equation 13}$$

This may then be converted to plunge and plunge azimuth, and reported as a strike and dip as required. The radius of the 95% confidence-interval cone, α_{95}, reported in degrees, is given by:

$$\alpha_{95} = \left(\frac{180°}{\pi}\right)\arccos\left(1 - \left(\left(\frac{N-R}{R}\right)\left(\left(\frac{1}{P}\right)^{\left(\frac{1}{N-1}\right)} - 1\right)\right)\right) \qquad \textbf{Equation 14}$$

where probability $P = 0.05$. By comparing the sample mean vector with the assumed Fisher distribution of vectors for the population that the sample is drawn from, the value for α_{95} indicates that there is a 95% chance that the mean vector for the population lies in a circle of radius α_{95} degrees centred on the calculated sample mean vector. A measure of the dispersion of vectors is the spherical variance, s_s^2, given by:

$$s_s^{\,2} = \frac{(N-R)}{N}.$$ **Equation 4**

Clustered vectors give a resultant R which approaches N, and so s_s^2 is small (approaching 0). As vectors become more randomly distributed, R approaches 0 and $s_s^2 \rightarrow 1$.

The statistical analysis of field data is achieved by treating orientations of planes (faults, joints, slip surfaces etc.) as vectors by evaluating the plunge and plunge azimuth of the maximum dip direction within the plane. Each plane is therefore defined by a vector unique to that plane, allowing mean orientations to be easily calculated and converted to strikes and dips. The following discussion presents large populations of orientations that are represented on stereonets as poles to the measured planes, with mean orientations of the measurements represented by great circles. The α_{95} confidence ellipse is constructed around the maximum dip vector for the mean plane.

A.4 Appendix 4: Pseudotachylyte and biotite XRF results

Sample	SiO2	Al2O3	Fe2O3	MgO	CaO	Na2O	K2O	TiO2	MnO	P2O5	LOI	Total
SKR	56.82	16.05	7.00	3.78	5.34	3.46	4.02	0.93	0.16	0.27	1.84	99.67
SKZS	57.70	16.09	7.94	3.45	4.96	3.64	3.66	1.01	0.12	0.29	0.69	99.54
SKL	57.88	16.28	7.08	3.41	4.81	3.20	3.87	0.95	0.11	0.28	1.81	99.68
Average Melt	57.47	16.14	7.34	3.55	5.04	3.43	3.85	0.96	0.13	0.28	1.45	99.63
GPP-1	37.93	14.30	19.46	11.97	1.02	0.11	8.84	3.44	0.32	0.45	0.87	98.70
GPP3a	37.69	14.09	18.92	11.95	1.15	0.04	8.625	3.277	0.325	0.453	1.19	97.71
GPP3b	37.62	14.53	19.13	12.23	1.06	0.04	8.782	3.357	0.33	0.426	1.44	98.95
GPP3c	37.51	14.67	19.22	12.3	1	0.08	8.881	3.372	0.328	0.432	1.45	99.24
Average Biotite	37.69	14.40	19.18	12.11	1.06	0.07	8.78	3.36	0.32	0.44	1.24	98.65

Table showing the major element composition of biotite and pseudotachylyte melt samples analysed by XRF to determine the potassium contents for K-Ar dating (reported as weight %). Analytical uncertainties associated with the XRF measurements are 0.5%.